Comparison of Experimental Methods in the Measurement of Wind Turbine Wakes

by

Michael McKinnon

A thesis
presented to the University of Waterloo
in fulfillment of the
thesis requirement for the degree of
Master of Applied Science
in
Mechanical and Mechatronics Engineering

Waterloo, Ontario, Canada, 2018

I hereby declare that I am the sole author of this thesis. This is a true copy of the thesis, including any required final revisions, as accepted by my examiners.

I understand that my thesis may be made electronically available to the public.

Abstract

With the increasing development of wind energy, it has become essential to study the interactions of turbines within wind farms. Wind turbines create wakes when harnessing the energy in the wind for electricity. Reduced velocities in the wakes and increased turbulence pose problems on nearby turbines. Therefore, to better understand the behaviour of wakes, experiments were conducted at the University of Waterloo Wind Generation Facility to study the behaviour of a wake behind a 3.3 m diameter turbine.

To ensure accuracy of measurements inside the facility, the flow distribution was measured upwind of the turbine to obtain a profile. This was completed through the development of a structure to orientate pitot tubes in front of the area of the turbine. The device allowed for various fan configuration settings of the facility to be tested to attempt to obtain an even flow distribution profile. A completely uniform flow distribution could not be achieved, however improvements to the profile were made.

Experiments were conducted through the use of flow visualization techniques to gain an initial understanding of the behaviour of the wake in both un-yawed and yawed turbine configurations. This was performed in two methods, to ignite a smoke emitter upstream of the turbine blade and to ignite smoke emitters on the blade tips of the turbine. Using the upstream smoke technique, the tip vortices could be seen to shed from the blades as they moved through the stream of the smoke. The vortices propagated downstream with the movement of the flow. The helical wake distribution of the wake could be seen using the blade ignited smoke technique. An estimate of the wake characteristics were obtained from this experiment, resulting in an approximate near wake length of 1.6 rotor diameters and helix angle of 30°.

Measurements of the wake of a wind turbine in un-yawed and yawed positions were conducted using three different measurement methods to gain an understanding of the wake behaviour in the range of 3 rotor diameters downstream of the turbine. The pitot tube structure previously developed was used to measure a two-dimensional profile of the wake at various downstream positions. With this method, the wake centre could be seen as well as temporal changes in the wake. A sonic anemometer was used to traverse the wake at hub height to obtain a horizontal velocity profile at various downstream distances. The velocity profile showed the decay of the wake as well as deflection in the yawed turbine measurements. LiDAR measurements were collected by scanning the wake at hub height to obtain a flow distribution throughout the wake of the turbine. Through these measurements a clear wake profile was developed, which showed how the velocity profile progressed behind the turbine. When the turbine was yawed, the wake was seen to deflect in the direction of the yaw angle.

Acknowledgements

I would like to thank all the people who made this thesis possible. I am especially grateful to Professor Johnson whose knowledge and support greatly contributed to this thesis and my own personal growth. I would also like to thank the Wind Energy Group, including Farid Samara, Alison Zilstra, and Faegheh Ghorbanishohrat, for their encouragement and assistance in the work to complete the experiments. I am thankful to the University of Waterloo technicians is dealing with the issues that arose in the setup of equipment. Leif Falk has been an integral contributor to all of the experiments that were performed at the Wind Generation Facility. His generous help and experience made the process much smoother. I am grateful to Neil Griffet's help with the LiDAR power supply, which prevented more delays in the experiments. Finally I would like to thank my sister Michelle Chibou for tirelessly reviewing several revisions of this thesis.

Dedication

This thesis is dedicated to my mother and grandfather who will not be able to read this. My mother has given me the encouragement to pursue my dreams no matter what the situation. My grandfather's pursuit of knowledge has inspired me to do the same.

Table of Contents

List of Tables

List of Figures

Nomenclature

a	Axial induction factor
a'	Tangential flow induction factor
A_d	Rotor swept area [m^2]
A_s	Airfoil planform area [m^2]
B	Number of blades
b	Wake width [m]
c	Chord length [m]
C_D	Drag coefficient
C_L	Lift coefficient
c_l	Speed of light [m/s]
C_P	Power coefficient
C_T	Thrust coefficient
D	Rotor diameter [m]
dr/dx	Wake growth rate
Δu	Uncertainty
f	Reflected light frequency from a particle [Hz]
f_0	LiDAR laser frequency [Hz]
F_D	Drag force [N]
F_L	Lift force [N]
H	LiDAR measurement distance [m]
H_m	LiDAR measurement distance after modification [m]
h_t	Hub height [m]
I	Turbulence intensity [%]
I_+	Added turbulence
I_0	Free stream turbulence [%]
I_{wake}	Total wake turbulence intensity [%]
k_w	Wake coefficient

L_F	LiDAR laser focal length [m]
m	Initial velocity deficit [m/s]
N	Number of measurement samples
p	Distance from the laser fibre output to the lens of the LiDAR [m]
p'	Distance from the lens to the laser waist position of the LiDAR [m]
P_{atm}	Atmospheric pressure [Pa]
r_0	Expanded rotor disc close to the rotor blades [m]
$R_{9.6}$	Wake radius at 9.6 rotor diameters downstream of a turbine [m]
R	Rotor radius [m]
r	Radius of blade element [m]
R_{air}	Gas constant [J/kg·K]
R_w	Wake radius [m]
t	Time [s]
U_0	Upstream wind velocity [m/s]
u, v, w	Wind velocity in cartesian coordinates [m/s]
$\bar{u}$	Local mean velocity [m/s]
u_{wake}	Wake velocity [m/s]
v_{LOS}	Particle speed in the line-of-sight of the laser [m/s]
W	Wind velocity relative to a rotating blade [m/s]
x_n	Near wake region [m[
z_0	Roughness factor [m]

α	Angle of attack [°]
α_0	Roughness coefficient
Γ	Vortex strength [rad/s]
γ	Yaw-offset angle [°]
λ	Tip speed ratio
λ_0	LiDAR laser wavelength [nm]
Ω	Rotational speed of rotor [rad/s]
ϕ	Helix angle [°]
ψ	Azimuthal position [°]
ρ	Density [kg/m^3]
σ	Standard deviation of velocity [m/s]
θ	Blade pitch [°]

θ_{actual}	Corrected measured wind direction of the vane anemometer [°]
θ_c	LiDAR conical scan laser angle [°]
θ_{LOS}	LiDAR laser direction angle with respect to the incoming flow direction [°]
θ_{vane}	Measured wind direction of the vane anemometer [°]

ABL	Atmospheric Boundary Layer
CNC	Computer Numerical Control
DAQ	Data Acquisition
$DSLR$	Digital Single Lens Reflex
FFT	Fast Fourier Transform
$HAWT$	Horizontal Axis Wind Turbine
LE	Leading Edge
$LiDAR$	Light Detection and Ranging
LOS	Line-of-sight
NI	National Instruments
$NREL$	National Renewable Energy Laboratory
PIV	Particle Image Velocimetry
RMS	Root Mean Square
RPM	Revolutions per minute
SNR	Signal-to-Noise Ratio
TE	Trailing Edge
UW	University of Waterloo
VFD	Variable Frequency Drive
WEG	Wind Energy Group
WT	Wind Turbine

Chapter 1

Introduction

1.1 Wind Energy

Wind energy is a clean source of electricity production and a sought after technology because of this. By harnessing the energy from the wind, wind turbines convert the energy into another usable form of energy. In this process, wind is used as a resource without the emission of greenhouse gases that contribute to pollution of the atmosphere. In order to achieve a sustainable lifestyle on Earth, wind energy is a viable form of generation to provide the electricity needs of society.

Windmills have been developed for 3000 years from the use of grinding grain, pumping water on farms, and electricity generation in recent years. During this time, the technology and design of wind turbines has been maturing. One of the first wind turbines used for electricity production was developed in the 19^{th} century by Charles Brush from the United States [18]. The turbine was a 12 kW DC windmill generator.

The first commercial wind farm in Canada was installed on Cowley Ridge in Alberta in 1993 [9]. Since then, Canada used wind energy to generate 6% of the country's electricity. The development of wind energy in Canada continued to grow with an average rate of 15% between 2012 and 2017 [9].

Several types of wind turbines exist. A wind turbine can be either be orientated as a horizontal axis wind turbine (HAWT) or vertical axis turbine (VAWT). The difference between these types of turbines is the orientation of the direction of rotation and whether it rotates about a horizontal axis or a vertical axis. Horizontal axis wind turbines can be further divided into upwind or downwind facing designs. This is determined by the

orientation of the rotor and nacelle from the direction of the wind. A turbine where the incoming wind first passes through the rotor is called an upwind turbine. Contrary to this, a turbine where the incoming wind first moves over the nacelle then passes through the rotor is labelled as a downwind turbine. Upwind horizontal axis wind turbines are the most common type of turbine used for electricity generation.

Wind turbines also vary in size which determine the power production capacity. A small-scale turbine is defined as having a generation capacity of less than 50 kW, with large-scale turbines operating at a capacity higher than 50 kW [80]. Utility-scale turbines are turbines used in the production of electricity. The capacity of utility-scale turbines grow with developments in wind turbine technology. The typical capacity of wind turbines being developed in 2018 is in the range of 2 MW [68].

1.2 Project Motivation

Increasing energy demands and desire for cleaner electricity sources have spurred the development of renewable energy [55]. Wind energy is a type of renewable energy that is becoming cost competitive to fossil fuel generation, especially when compared to sources such as solar energy [2]. As a result, a high volume of wind farms are being built to accommodate this demand. Areas with a high wind resource are seeing an increase in wind farm density to utilize the available space.

The spacing, however, is limited by the wakes that are generated from the wind turbine power production. Wakes are formed behind a wind turbine with reduced velocity and higher turbulence. As a result, another wind turbine located in the wake will experience reduced production and fluctuating electricity generation [66]. Additionally, the turbulence of the wake causes blade loading issues, which leads to a need for increased maintenance of the turbine. Wind farms are therefore designed to have a distance of 6-10 rotor diameters in the predominant wind direction and 1.5 rotor diameters in the crosswind direction [61].

To alleviate the issues caused by wakes and design for increasing wind farm densities, the behaviour of the wake must first be understood. Experimental research of wind turbine wakes is typically performed by scaling a wind turbine to fit inside of a wind tunnel or by performing measurements on utility-scale turbines. In the wind tunnel experiments, the turbines are scaled to a size in the area of 15 cm [11]. The scalability of results from a wind turbine this small has concerns when applying the results on large-scale turbines, which typically have a rotor diameter in the area of 100 m. Studies on utility-scale turbines, on the other hand, have issues with the uncontrollable behaviour of the environmental wind

conditions. This makes it difficult to determine the effect that incoming wind conditions have on the wake.

1.3 Project Overview

To fulfill the gap in research on wind turbine wakes under controlled conditions while reducing the effects of scaling on the results, wake experiments were performed inside of the University of Waterloo's large scale Wind Generation Facility. The Wind Generation Facility allows for data to be obtained at specific free stream airspeeds, resulting in a more controlled collection of samples in comparison to utility wind turbines located in the outdoor environment. The UW WEG turbine was designed to operate inside of the Wind Generation Facility and has a rotor diameter of 3.3 m with a production of 1.45 kW at 11 m/s winds [31]. Therefore, scaling is closer to utility-scale turbines in comparison to wind tunnel experiments.

In order to improve the accuracy of experiments, the profile of the wind inside the Wind Generation Facility had to first be characterized. To measure the profile of the incoming wind, a structure of pitot tubes was constructed. The structure, called the Pitot Tree, allowed measurements to be taken in front of the UW WEG turbine to determine the profile at various wind speed settings of the Wind Generation Facility.

Flow visualization was performed to gain an initial understanding of the wake behaviour. This was conducted using two common methods used to visualize wind turbine wakes. The first method ignited smoke upstream of the UW WEG turbine to visualize tip vortices being formed at the turbine blade tips. The second method ignited smoke from the tips of the turbine blade to visualize the behaviour of the wake behind the turbine.

A light detection and ranging (LiDAR) measurement device was proposed to use to measure the velocity of the wake profile. The device was new to the research group and therefore testing was completed to ensure the accuracy and proper operation of the device. This was completed in two phases, the first to verify the working order of the device, and the second to ensure the accuracy of measurements are maintained after modification necessary for the use of the LiDAR in the wake measurements. To verify the working order of the device in the first phase, the LiDAR measurements were compared to a vane and cup anemometer. The second phase confirmed the laser position and measurement distance of the LiDAR, after the original conical laser scanning pattern was modified to obtain a straight laser configuration. After which, the LiDAR measurements were compared against a sonic anemometer measurement device under controlled wind speeds inside of the Wind Generation Facility.

The wake experiments were performed using three measurement methods. The Pitot Tree, developed for the wind profile characterization, could also be utilized to measure the wake at various distances from the turbine. In addition, the sonic anemometer measurement device was used to obtain traverse velocity measurements of the wake. Ultimately, wake measurements using the LiDAR was the goal of the experiments. Therefore, the research finishes with LiDAR measurement scans of the wake of the UW WEG turbine inside the Wind Generation Facility.

A background on the theory of aerodynamics of wind turbines and wakes is provided in Chapter 2. This section also covers the theory of LiDARs and wake studies in literature. Chapter 3 provides a description and details of the facilities and measurement devices used in this thesis. The experimental setup is described in the following section, Chapter 4, where details on the wind characterization of the Wind Generation Facility, flow visualization experiments, LiDAR verification process, and wake measurement experiments can be found. Finally, the results of these experiments are shown in Chapter 5, followed by concluding remarks in Chapter 6. Further details of the experiments and work completed in this thesis, not given in the previous sections, are provided in the appendices.

Chapter 2

Background

This chapter gives a theoretical background of the research of this thesis and describes previous relevant studies in literature. Section 2.1 gives an overview of the theoretical concepts of wind turbines, atmospherical boundary layer, and wind turbine wakes as well as describing the performance parameters of a turbine. Wake models have been developed to predict the behaviour of wakes based on the theory of wakes and experiments. The models discussed in this thesis are described in Section 2.2. A LiDAR was used in the experiments of this thesis, therefore the theory of LiDARs are described in Section 2.3. The behaviour of wind turbine wakes has been studied by several researchers. Some of the relevant studies are summarized in Section 2.4.

2.1 Wind Turbines

2.1.1 Airfoil Aerodynamics

Wind turbines use the principles of aerodynamics of airfoils to rotate the blades from an incoming wind source. Lift and drag forces generate torque to create the rotation. Figure 2.1 shows a picture of a wind turbine blade and the cross sectional airfoil of the blade. The front of an airfoil, located at the point where the airfoil hits the relative wind, W, is known as the leading edge (LE). The opposite end, where the incoming air exits the airfoil, is known as the trailing edge (TE). The chord, c, is defined as the straight distance between the leading edge and trailing edge of the airfoil.

The driving force of the wind turbine rotor rotation is caused by a lift force, F_L, that is generated on the airfoil. The direction of the lift force is defined to be perpendicular to

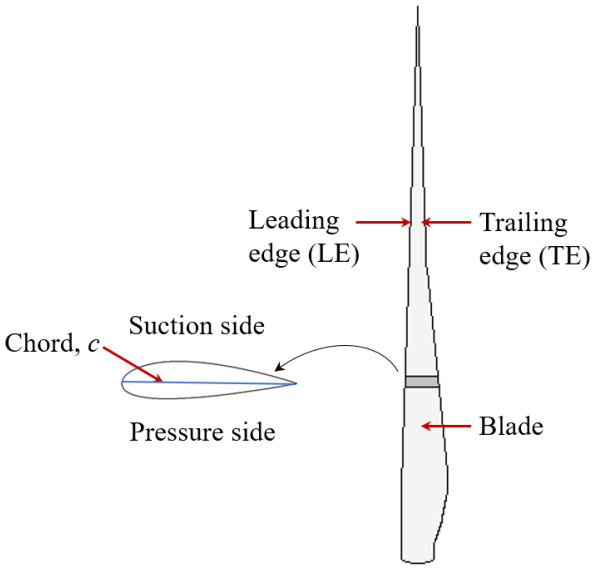

Figure 2.1: Schematic of wind turbine blade and section two-dimensional airfoil

the incoming flow. A drag force, F_D, also results due to the aerodynamics of the airfoil. The direction of the drag force is defined to be in the direction of the incoming flow.

Lift occurs when air moves over the airfoil causing a difference in pressure forces over the surface between the top and bottom sides of the airfoil [8]. The side with the lowest pressure forces is known as the suction side, whereas the side with the highest pressure forces is referred as the pressure side. A two-dimensional airfoil is depicted in Figure 2.2 showing the forces due to lift and drag. The lift and drag forces act at the aerodynamic centre of the airfoil. This is typically located at a distance of $c/4$ from the leading edge.

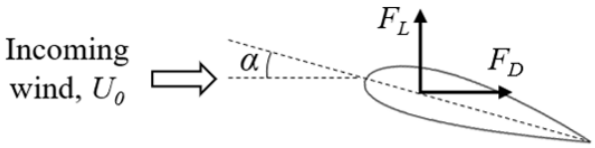

Figure 2.2: Schematic of lift and drag forces on a non-rotating two-dimensional airfoil

Drag on the airfoil is caused by two forces, friction on the airfoil and a pressure difference between the high stagnation at the front and low pressure that forms behind the airfoil [79]. Due to the shape and surface area of the airfoil, surface friction dominates the drag created by these two forces for most design conditions.

The lift and drag forces can be non-dimensionalized based on the incoming, U_0, or relative wind speed, W, and dimensions of the airfoil to form the lift and drag coefficients. The lift coefficient, C_L, and drag coefficient, C_D, are calculated from Eq. 2.1 and 2.2, where ρ is the air density and A_s is the planform area of a two-dimensional airfoil [8].

$$C_L = \frac{F_L}{\frac{1}{2}\rho U_0^2 A_s}, \qquad C_{L_W} = \frac{F_L}{\frac{1}{2}\rho W^2 A_s} \tag{2.1}$$

$$C_D = \frac{F_D}{\frac{1}{2}\rho U_0^2 A_s}, \qquad C_{D_W} = \frac{F_D}{\frac{1}{2}\rho W^2 A_s} \tag{2.2}$$

The amount of lift generated depends on the type of airfoil and the angle of attack, α, of the airfoil, which is the angle of the airfoil relative to the incoming flow. The angle of attack can be increased to generate increasingly higher lift up to the point of stall, which occurs when the flow separates from the airfoil, as shown in Figure 2.3. Stall occurs after the point of maximum lift.

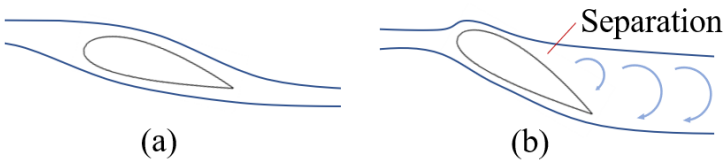

Figure 2.3: Schematic of a two-dimensional airfoil with (a) attached flow and (b) stalled flow

Several types of airfoils have been developed to achieve different aerodynamic effects. One way this can be achieved is by adjusting the camber of the airfoil, which is defined as the distance between the centre of the suction and pressure sides of the airfoil and the chord line, causing a curved shape of the airfoil [8]. Cambering the airfoil allows lift to be generated at a zero angle of attack. Another method is to adjust the thickness relative to the chord length of the airfoil. The thickness affects the stall angle of the airfoil and maximum lift achievable.

A finite airfoil, in which the span of the airfoil has an end, such as a wind turbine blade, has additional affects at the tips. At the ends of a blade, there is a difference between the high pressure at the pressure side of the airfoil and the low pressure at the suction side of the airfoil. Therefore, this difference causes the air flow to move from the pressure side to

the suction side of the blade. This is known as the tip effect. The movement of air flow at the tip causes the lift to decrease, drag to increase, and tip vortices form as a result. The vortices propagate downstream with the movement of the air. Figure 2.4 shows the formation of tip vortices on a finite blade. The movement of the tip vortices downstream forms a vortex cylinder.

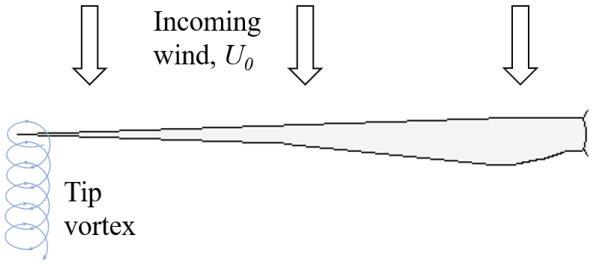

Figure 2.4: Schematic of the formation of a tip vortex on a blade

2.1.2 Wind Turbine Aerodynamics

A wind turbine is comprised of several components. The main components are the nacelle, rotor, tower, and blades. A diagram shown in Figure 2.5 shows the components of a wind turbine. The size of a turbine is usually noted by the rotor diameter, D, and the hub height, h_t, relative to the ground. The rotor radius, R, is also defined as half the rotor diameter.

The nacelle houses the generation components of the wind turbine, such as the gearbox and generator, and attaches to the tower and rotor. The nacelle will yaw to position the turbine in the direction of the wind. The yaw angle, γ, is the angle of the rotor axis with respect to the incoming wind direction.

The rotor is attached to the nacelle and is comprised of the rotational components while the wind turbine is in operation. The air flow is either described as upwind, when the direction of the wind source is coming towards the rotor, or downstream, which is the opposite side of upwind direction when the air flow moves away from the rotor. When the wind turbine is in operation, the turbine will face in the direction of the wind with upwind orientated in front of the turbine towards the wind source.

Blades are attached to the hub of the turbine which are used to rotate the rotor from the incoming wind speed. As mentioned before, the cross section of the blade has an

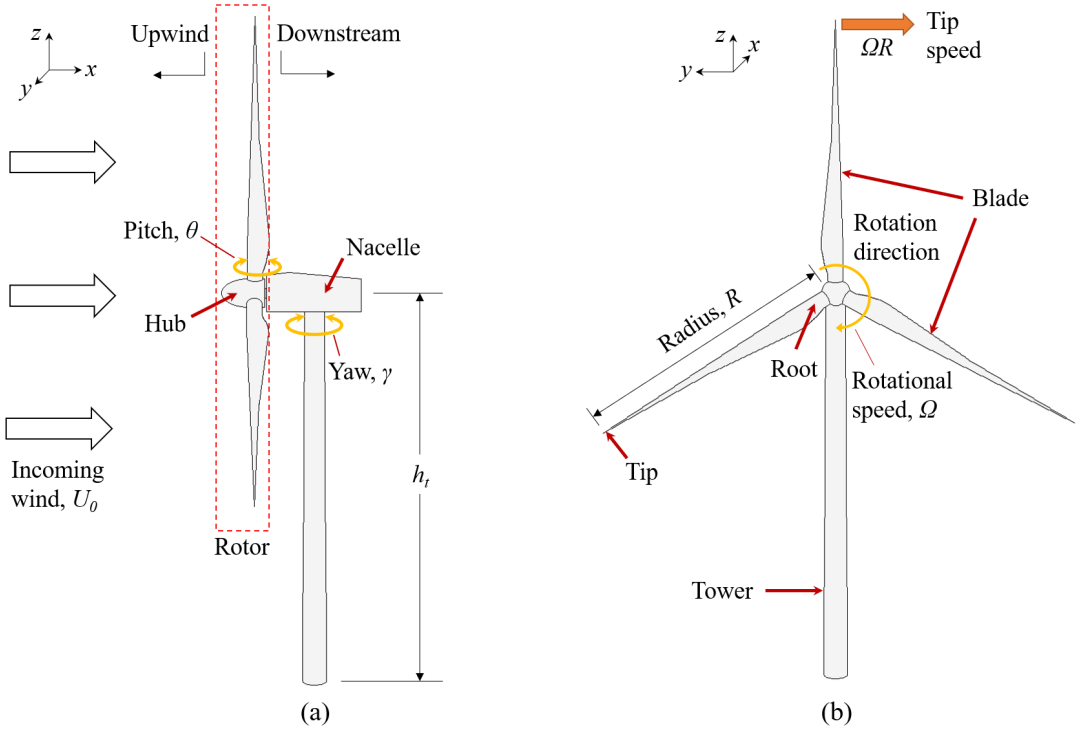

Figure 2.5: Schematic of a horizontal axis wind turbine from the (a) side view and (b) front view

airfoil shape, to generate lift from the angle of attack positioned to the air direction. The swept area, A_d, of the turbine is the rotational area of the blades. The blades are typically designed to have a twist to account for the change in relative airspeed as the blades rotate.

The blade tip is located at the end of the wind turbine blade away from the hub. The tip is the end of the blade and usually has the smallest dimensions of the blade. The root is the opposite end of the wind turbine blade attached to the hub. The root provides structural support for the blade. Typically, the blades of the turbine can pitch, θ, to change the angle of attack depending on wind conditions.

Due to the rotational movement of the blade, the wind speed seen at the leading edge of the airfoil is actually a combination of the incoming wind and the velocity caused from the angular velocity of the blade. Therefore, a resultant relative velocity, W, is seen at the leading edge of the airfoil. Figure 2.6 shows the change in the aerodynamic components of the airfoil as a result of the resultant relative velocity, where a is the axial induction factor and a' is the tangential flow induction factor, which will be defined later. The angle

of the relative velocity is dependant on the angle of attack of the airfoil relative to the free stream velocity and the pitch of the blade.

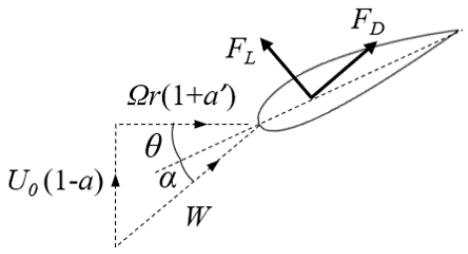

Figure 2.6: Schematic of an airfoil aerodynamics due to resultant relative velocity

The relative velocity component can be determined by looking at the actuator disc model of a wind turbine. A wind turbine can be represented without the components and simply by the energy extraction from the incoming wind [18]. The energy extraction is represented by an actuator disc with the area of the rotor diameter area. Incoming air approaches the actuator disc and once the air passes through the disc, energy is extracted from the wind and subsequently reduces the velocity. The airflow that has passed through the actuator disc forms a wake that is propagated downstream. The air passing through an actuator disc is shown in Figure 2.7, with the boundary of the air shown by the streamtube.

According to the conservation of mass, a decrease in velocity causes an increase in the area of the air stream. Therefore, the reduced velocity in the wake of the actuator disc causes the wake to increase, this is known as the wake expansion. In order to maintain a continuing air stream, the area of the incoming wind increases as it approaches the actuator disc and continues to increase to an expansion area denoted from the conversation of mass equation. This is shown in Eq. 2.3.

$$\rho A_\infty U_\infty = \rho A_D U_D = \rho A_W U_W \tag{2.3}$$

The pressure, as a result, increases as it approaches the actuator disc, with a sharp drop immediately after. The pressure then recovers relative to the expansion area of the downstream air. The pressure as the air moves through the actuator disc can also be seen in Figure 2.7.

The reduction in velocity is represented by the axial induction factor, a. Using the axial induction factor, the velocity at the actuator disc is defined as in Eq. 2.4 [18]. Therefore, applying conservation of momentum, the wake velocity, U_W, when the area is fully expanded can be derived to obtain Eq. 2.5.

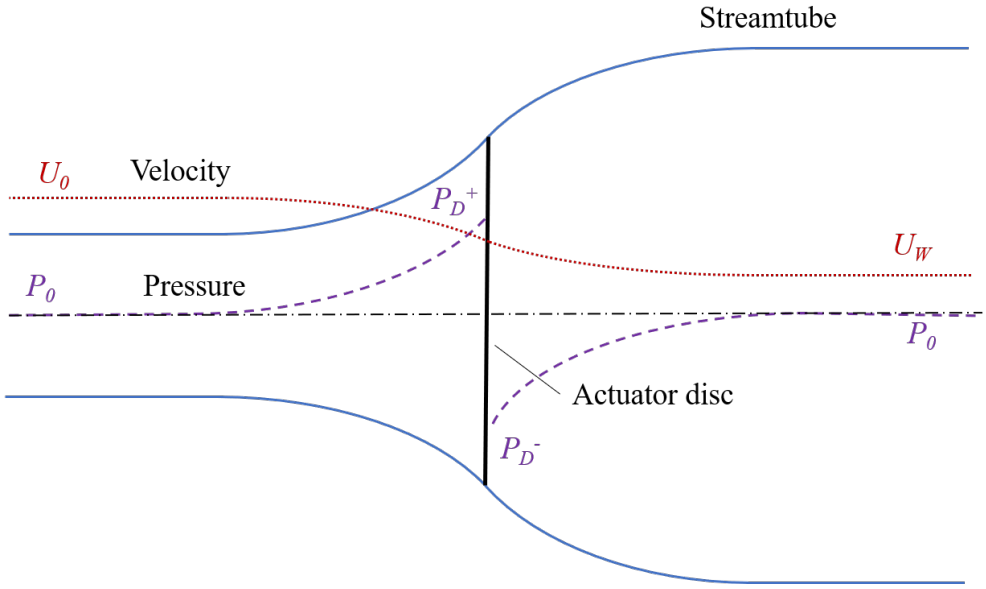

Figure 2.7: Schematic of air passing through an actuator disc adapted from Burton et al. [18]

$$U_D = U_0(1 - a) \tag{2.4}$$

$$U_W = U_0(1 - 2a) \tag{2.5}$$

Since the blades of the turbine are rotating, the actuator disc model also induces rotation on the airflow moving through the disc. The incoming air has no rotation and develops a tangential velocity component associated with the rotation as it exits the disc. The tangential velocity component can be related to the rotation of the blades by the tangential flow induction factor, a' [18]. Therefore, the tangential velocity component on a blade section is given in Eq. 2.5, where r is the local radius of the blade element.

$$U_t = \Omega r(1 + a') \tag{2.6}$$

Applying this theory to an airfoil section on the blade of the turbine, the resultant relative velocity can be determined. The relative velocity is the resultant of the incoming velocity approaching the blade and the tangential velocity. This relation is given in Eq. 2.7.

$$W = \sqrt{U_D^2 + U_t^2} \tag{2.7}$$

2.1.3 Performance Parameters

Several parameters are used to describe the performance of a wind turbine. The parameters are non-dimensionalized to allow comparison of turbines with different dimensions under various conditions.

One such performance parameter is the tip speed ratio, λ. The tip speed ratio is defined as the ratio between the speed seen at the tip of the blade, or tip speed, and the incoming wind velocity. This results in the equation given in Eq. 2.8.

$$\lambda = \frac{\Omega R}{U_0} \tag{2.8}$$

The main function of a wind turbine is to produce power. Therefore, another parameter is the power coefficient, C_P, which non-dimensionalizes the power based on the potential power in the incoming wind over the swept area of the turbine. This is given in Eq. 2.9.

$$C_P = \frac{Power}{\frac{1}{2}\rho U_0^3 A_d} \tag{2.9}$$

Applying conservation of momentum and energy to the actuator disc model, the power coefficient can also be related to the axial induction factor by Eq. 2.10.

$$C_P = 4a(1-a)^2 \tag{2.10}$$

The pressure drop through the blade swept area of the wind turbine results in a thrust force acting on the rotor. The thrust can also be non-dimensionalized to obtain the thrust coefficient, C_T using Eq. 2.11,

$$C_T = \frac{Thrust}{\frac{1}{2}\rho U_0^2 A_d} \tag{2.11}$$

Similar to the power coefficient, the thrust coefficient can also be related to the axial induction factor using Eq. 2.12.

$$C_T = 4a(1-a) \tag{2.12}$$

The actuator disc model breaks down when $a \geq 0.5$. When a is 0.5 the wake velocity, U_W, becomes 0 and at values of $a > 0.5$ the wake velocity becomes negative. Therefore, the actuator disc model no longer applies at values of a above 0.5.

When a turbine is yawed at angle γ, however, the previous momentum model on the actuator disc must be modified. Therefore, the power and thrust coefficients can be related to the axial induction factor by Eq. 2.13 and 2.14 respectively.

$$C_P = 4a(\cos\gamma - a)^2 \tag{2.13}$$

$$C_T = 4a(\cos\gamma - a) \tag{2.14}$$

2.1.4 Wind Turbine Wakes

Wakes are formed behind wind turbines as energy is extracted from the incoming wind. As a result, the wake contains reduced wind speeds and increased levels of turbulence. The wake of the turbine can be modeled by modifying the actuator disc model from Section 2.1.2.

As shown in the actuator disc model, a wake is formed downstream of the turbine due to the extraction of energy and rotation of the blades. The wake propagates downstream with the airflow. Additionally, as mentioned in Section 2.1.1, vortex cylinders form at the tip of the blade due to the tip effect. The vortex cylinders also move and rotate in the wake of the turbine due to the rotation of the blades and movement of the air. The actuator disc model can therefore be modified to incorporate the vortex cylinder model.

The vortex cylinder model represents the blades of a turbine by a radial line and circulation with a strength noted by $\Delta\Gamma$ [18]. The tips of the blades shed a vortex cylinder also with strength $\Delta\Gamma$, which move downstream with the wake velocity. This is shown in Figure 2.8. The vortex cylinders form a helical distribution as they move downstream in the wake. The helical path is distributed at an angle called the helix angle, ϕ, also noted as the flow angle at the blade tip. At the root, the vortex of each blade form a total root vortex of strength Γ. As seen in the actuator disc model, the vortex tubes expand with the wake.

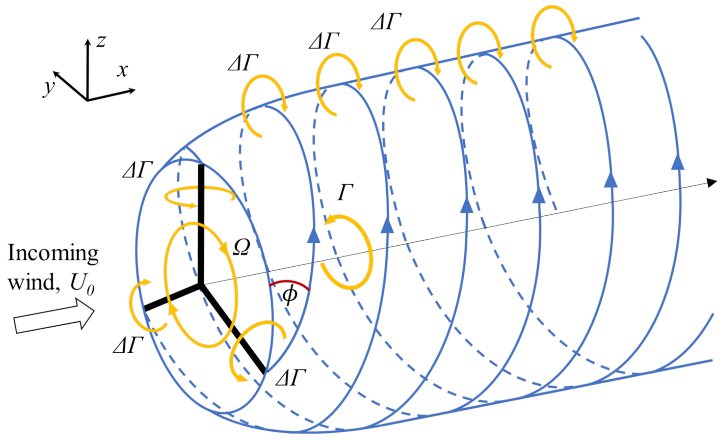

Figure 2.8: Schematic of a helical vortex formation in the wake of a turbine adapted from Burton et al. [18]

Using the Biot-Savart law, the tangential flow induction factor can be calculated from the root vortex as shown in Eq. 2.15 [18].

$$a' = \frac{\Gamma}{4\pi r^2 \Omega} \tag{2.15}$$

The velocity in the wake is not evenly distributed as seen in the actuator disc model. The energy extracted from the incoming wind causes a reduction in velocity in the wake of the turbine, however an additional shearing effect from the free stream velocity outside of the wake creates a velocity distribution inside of the wake. The shearing causes additional turbulence which allows the transfer of momentum to mix the wake with the surrounding free stream flow. This mixing spreads towards the centre of the wake as well as outwards, increasing the width of the wake. Therefore, the reduced velocity of the wake in comparison to the free stream velocity, known as the velocity deficit, recovers as the flow moves downstream. The mixing of the flow and eroding of the wake velocity can be seen in Figure 2.9.

Areas of the wake can then be defined based on this mixing. The near wake region begins immediately after the flow passes through the rotor and extends until the shear layer increases to the centre of the wake. After this point, the far wake region begins and extends for the length of the wake. The regions of the wake are also depicted in Figure 2.9.

The wake velocity, u_{wake}, is directly related to the thrust coefficient as it is determined by the momentum extracted from the flow. In addition, the velocity deficit is dependant

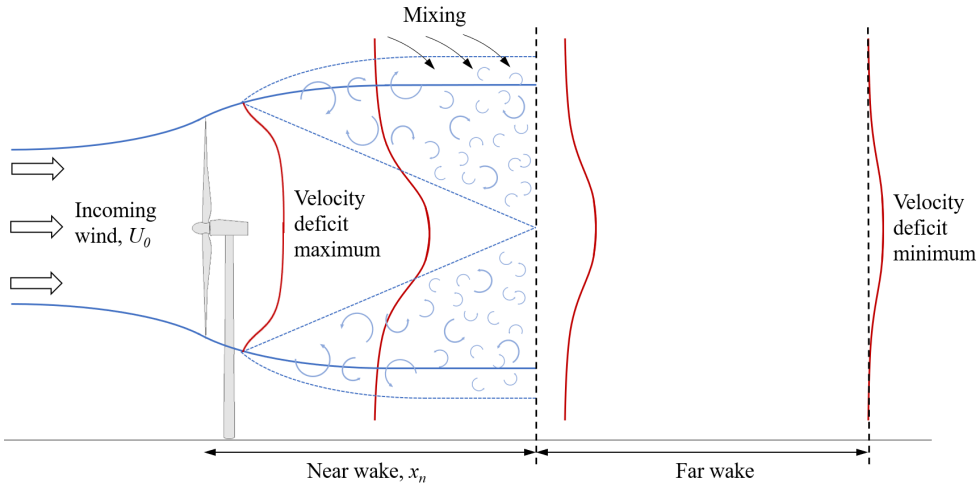

Figure 2.9: Schematic of the velocity profile in the wake of a wind turbine adapted from Sanderse [61]

on the turbulence levels of the wake, I_{wake}. The incoming turbulence in the wind, I_0, along with turbulence from the tip vortices and flow disturbance from the blades, nacelle, and tower also contribute to the overall turbulence in the wake. This causes increased mixing of the shear layer, increasing the rate of decay and recovery of the wake velocity.

Vermeulen [75] developed an empirical model to estimate the length of the near wake region, x_n, of the wake based on the thrust coefficient and rotor radius. This can therefore be calculated from the formula given in Eq. 2.16.

$$x_n = \frac{\sqrt{0.214 + 0.144m}(1 - \sqrt{0.134 + 0.124m})}{(1 - \sqrt{0.214 + 0.144m})\sqrt{0.134 + 0.124m}} \frac{r_0}{(\frac{dr}{dx})} \tag{2.16}$$

where r_0 is the expanded rotor disc close to the rotor blades [37] calculated from:

$$r_0 = R\sqrt{\frac{m+1}{2}} \tag{2.17}$$

m is the initial deficit [37] calculated from:

$$m = \frac{1}{\sqrt{1 - C_T}} \tag{2.18}$$

and the growth rate, $\frac{dr}{dx}$, is given by:

$$\frac{dr}{dx} = \sqrt{\left(\frac{dr}{dx}\right)_a^2 + \left(\frac{dr}{dx}\right)_m^2 + \left(\frac{dr}{dx}\right)_\lambda^2} \tag{2.19}$$

where $(\frac{dr}{dx})_a$ is the growth rate due to ambient turbulence, I_0:

$$\left(\frac{dr}{dx}\right)_a = 2.5I_0 + 0.005 \tag{2.20}$$

$(\frac{dr}{dx})_m$ is the growth rate due to shear generated turbulence:

$$\left(\frac{dr}{dx}\right)_m = \frac{(1-m)\sqrt{1.49+m}}{(1+m)9.76} \tag{2.21}$$

and $(\frac{dr}{dx})_\lambda$ is the growth rate due to mechanical turbulence:

$$\left(\frac{dr}{dx}\right)_\lambda = 0.012B\lambda \tag{2.22}$$

with B being the number of blades.

The wake is typically characterized by the velocity deficit, wake centre, wake radius, and added turbulence. The wake velocity is defined by the reduction of velocity in the wake in relation to the free stream velocity. This is defined using Eq. 2.23.

$$\Delta u_{wake} = U_0 - u_{wake} \tag{2.23}$$

With an un-yawed turbine, the wake centre is noted to be in line with the turbine hub. However, for a yawed turbine, the wake is deflected. In the far wake region, the centre can be determined by the minimum velocity. The wake radius is defined as the distance from the rotor centre to the first point in the radial direction that the wake speed reaches the free stream values [70].

The wake can also be characterized by the added turbulence, I_+, defined by Crespo & Hernández [22]. The added turbulence is the total turbulence added to the wake by the shearing and mechanical sources and removes the effects of the incoming turbulence, I_0.

It is defined as the square root of the additional wind speed variance normalized by the mean wind speed [18]. The added turbulence is therefore:

$$I_+ = \sqrt{I_{wake}^2 - I_0^2} \tag{2.24}$$

where I_{wake} is the total wake turbulence intensity at a given downstream distance and the incoming turbulence, I_0.

The turbulence, I, is calculated from the standard deviation of the wind velocity, σ, with respect to the local mean wind velocity, $\bar{u}$, as shown in Eq. 2.25 [26].

$$I = \frac{\sigma}{\bar{u}} \tag{2.25}$$

Some characteristics of the wake regions have been noted in various studies [61]. Based on experimental results, Schepers [62] notes that the wake reaches full expansion at 2.25 downstream rotor diameters (D) through simulations validated on a 35 m turbine. The velocity deficit is maximum after 1 to 2 D according to Ainslie [4]. The tip vortices present in the shear layer are fully broken down after 4 D [3]. The expansion region length is estimated to be 1 D by Crespo et al. [23]. Also Crespo et al. [23] determined that the end of the near wake region, where the shear layer extends to the centre of the wake, is reached between 2 and 5 D.

The variation in wake characteristics is due to the large contribution that the thrust coefficient and incoming turbulence levels have on the wake as mentioned before [61]. Increased thrust coefficient causes more energy extraction and therefore results in higher velocity deficits and a larger wake expansion. The incoming turbulence levels of the wake affect the wake recovery rate. Increased turbulence results in more mixing and therefore reduces the distance for the deficit to recover.

2.1.5 Atmospheric Boundary Layer

The wind in the atmosphere is not uniformly distributed and in actuality forms a distribution of increasing velocity with elevation, known as the atmospheric boundary layer (ABL). The atmospheric boundary is caused by friction as the wind moves over the Earth's terrain. This effect causes the velocity near the surface of the Earth to be reduced and gradually recovers at higher altitudes. A typical profile is shown in Figure 2.10.

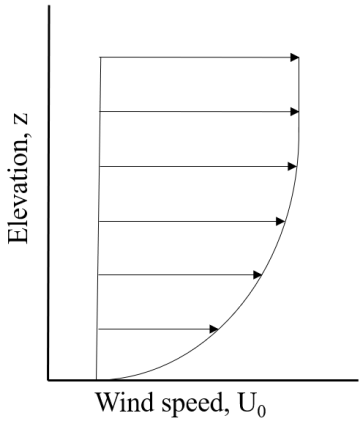

Figure 2.10: Typical atmospheric boundary layer velocity profile

The atmospheric boundary layer usually extends to at least 300 m, however this and the profile of the velocity change based on wind conditions and the terrain [18]. The atmospheric boundary layer also changes frequently with different levels of shear and turbulence [45]. The effects of the atmospheric boundary layer are reduced at higher altitudes. Therefore, it is desirable to place wind turbines outside of the boundary or as high as possible to increase the incoming wind speed and reduce ground effect turbulence. The structure and behavior of a wind turbine wake is also affected by the atmospheric boundary layer [38].

The terrain can be empirically characterized based on the roughness exponent, α_0, and the roughness factor, z_0. Both factors are estimated based on features of the land, such as shrubs, trees, and buildings. Using these factors, the boundary layer profile can be approximated using the power law, shown in Eq. 2.26, or the log law, shown in Eq. 2.27, where h_1 and h_2 are the different elevation heights, and u_1 and u_2 are the wind speeds at those heights [18]. The relationship between the heights and corresponding velocities depend on either the roughness exponent or roughness factor.

$$\frac{u_2}{u_1} = \left(\frac{h_2}{h_1}\right)^{\alpha_0} \tag{2.26}$$

$$\frac{u_2}{u_1} = \frac{\ln\left(\frac{h_2}{z_0}\right)}{\ln\left(\frac{h_1}{z_0}\right)} \tag{2.27}$$

2.2 Wind Turbine Wake Models

Wake models have been developed and improved over time to model the wake velocity and added turbulence. The models are related to the thrust coefficient, incoming turbulence intensity, and dimensions of the turbine.

2.2.1 Wake Models

Jensen Model

One of the original and well known empirical models to calculate the wake velocity was proposed by Katic et al. [40]. The model, called the Jensen model, calculates the wake velocity in relation to the thrust coefficient and incoming turbulence intensity for various downstream distances. This model uses the "top hat" distribution in which the wake velocity is seen to be constant. The empirical Jensen model is calculated as:

$$\frac{u^*_{wake}}{U_0} = 1 - \frac{1 - \sqrt{1 - C_T}}{(1 + 2k_w \frac{x}{D})^2} \tag{2.28}$$

where u^*_{wake} represents the one-dimensional wake velocity in the Jensen model and the wake coefficient, k_w, is:

$$k_w = 0.3837 I_0 + 0.0037 \tag{2.29}$$

A two-dimensional variation of the Jensen was proposed by Tian et al. [70] to replace the "top hat" distribution, called the 2D_k Jensen model. This is calculated as:

$$\frac{u_{wake}}{U_0} = \left(1 - \frac{u^*_{wake}}{U_0}\right) \cos\left(\frac{\pi}{R_w} y + \pi\right) + \frac{u^*_{wake}}{U_0} \tag{2.30}$$

where the wake radius, R_w, is;

$$R_w = R + k_w x \tag{2.31}$$

Ainslie Model

Another model proposed by Ainslie [4] is commonly used. This model is based on the initial velocity deficit of the wake and applies a Gaussian distribution to obtain the radial velocity profile seen at the hub height. This model is used to determine the wake profile at a downstream distance of 2 rotor diameters (D). It also uses the wake width in the calculation. The Ainslie empirical model is therefore:

$$\frac{u_{wake}}{U_0} = 1 - m \exp\left(-3.56(y/b)^2\right) \tag{2.32}$$

where the initial velocity deficit, m, is:

$$m = C_T - 0.05 - (16C_T - 0.5)I_0/10 \tag{2.33}$$

and the wake width, b, is:

$$b = \left(\frac{3.56C_T}{8m(1 - 0.5m)}\right)^{\frac{1}{2}} \tag{2.34}$$

Larsen Model

A model developed by Larsen [43] was later proposed. The Larsen model is recommended by the European Wind Turbine Standard II [26]. The model is calculated as:

$$\frac{u_{wake}}{U_0} = 1 + \frac{1}{9}(C_T A(x + x_0)^{-2})^{\frac{1}{3}}\left[y^{\frac{3}{2}}(3c_1^2 C_T A(x + x_0))^{-\frac{1}{2}} - \left(\left(\frac{35}{2\pi}\right)^{\frac{3}{10}}(3c_1^2)\right)^{-\frac{1}{5}}\right]^2 \tag{2.35}$$

where c_1 is a parameter given by:

$$c_1 = r_0^{\frac{5}{2}}\left(\frac{105}{2\pi}\right)^{-\frac{1}{2}}(C_T A x_0)^{-\frac{5}{6}} \tag{2.36}$$

and x_0 is also a parameter calculated as:

$$x_0 = \frac{9.6D}{\left(\frac{R_{9.6}}{r_0}\right)^3 - 1} \tag{2.37}$$

where r_0 is calculated as from Section 2.1.4 and $R_{9.6}$ is the empirically estimated radius of the wake at a downstream distance of 9.6 D:

$$R_{9.6} = a_1 \exp\left(a_2 C_T^2 + a_3 C_T + a_4\right)(b_1 I + 1)D \tag{2.38}$$

with empirical constants shown in Table 2.1.

Table 2.1: Empirical constants for $R_{9.6}$ of the Larsen model [43]

Constant	**Value**
a_1	0.435449861
a_2	0.797853685
a_3	-0.124807893
a_4	0.136821858
b_1	15.6298

The wake radius, R_w, is also modeled using the formula:

$$R_w = \left(\frac{105 c_1^2}{2\pi}\right)^{\frac{1}{5}} \left(C_T A (x + x_0)\right)^{\frac{1}{3}} \tag{2.39}$$

2.2.2 Turbulence Intensity Models

Several models have been developed to model the added turbulence in the wake of a turbine, however these are not as well developed as the velocity profile models [18] [26]. The added turbulence is the turbulence added to the wake with respect to the incoming turbulence, as defined in Section 2.1.4.

Quarton & Ainslie Model

An empirical model, based on wind tunnel measurements and full-size turbine experiments, was developed by Quarton & Ainslie [59] to calculate the added turbulence at various downstream distances. This model is calculated as:

$$I_+ = 4.8 C_T^{0.7} I_0^{0.68} (x/x_n)^{-0.57} \tag{2.40}$$

where I_+ and I_0 are expressed as percentages.

Hassan Model

An improvement to the Quarton & Ainslie model was later proposed by Ainslie et al. [5] called the Hassan model. The proposed improvement is:

$$I_+ = 5.7 C_T^{0.7} I_0^{0.68} (x/x_n)^{-0.96} \tag{2.41}$$

Larsen Model

Larsen et al. [44] proposed a turbulence model, as shown in Eq. 2.42. This model is also recommended by the European Wind Turbine Standard II [26], similar to the velocity profile model described previously.

$$I_+ = 0.29 (\frac{x}{D})^{-\frac{1}{3}} \sqrt{1 - \sqrt{1 - C_T}} \tag{2.42}$$

2.2.3 Wake Model Comparison

Duckworth & Barthelmie [26] compare the wake models described and additional models against field measurements using two Siemens turbines with rotor diameters of 62 m and 82.4 m. Information of the turbines are collected using Supervisory Control and Data Acquisition (SCADA) and a power performance mast set in the wake of the turbines. Both the wake and turbulence models were considered in the comparison of Duckworth & Barthelmie.

The comparison of the wake models and field measurements can be seen in Figure 2.11 with additional models added by Stevens & Meneveau [66]. The field measurements by Duckworth & Barthelmie appear to have a larger velocity than the Ainslie, Larsen, and Jensen models at 2.5 D, however the Larsen model develops a larger deficit with further downstream distances. The Ainslie model is the closest related model to the field measurements for each distance. It was determined that the Ainslie model had an absolute

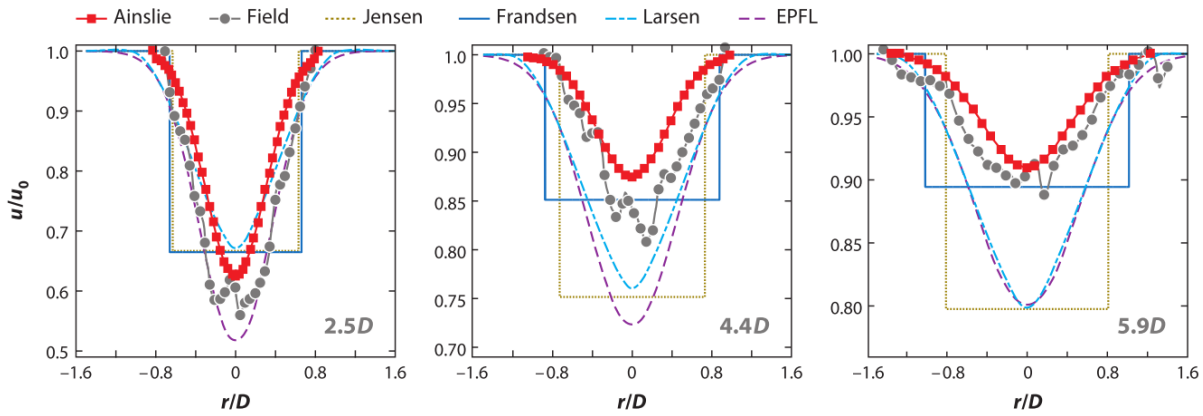

Figure 2.11: Comparison of Jensen [40], Ainslie [4], Frandsen [27], Larsen [43], and EPFL [57] models against Duckworth & Barthelmie [26] field measurements at $I_0 = 11\%$ and $C_T = 0.78$ (Taken from Stevens & Meneveau [66])

deviation from the field measurements of 12.8%, the Jensen model had a deviation of 22.7%, the Larsen model at 33.9% [26].

The wake width was also measured and compare to the width predicted by the Ainslie, Jensen, and Larsen models. It was found that the Ainslie model had a deviation from the field measurements of 7.5%, the Jensen model deviated by 12.0%, and the Larsen model deviated by 8.6%.

The turbulence intensity in the centreline of the wake in the field measurements of Duckworth & Barthelmie were also compared to the turbulence models by Quarton & Ainslie [59] and Larsen et al. [44]. These models showed a difference of 19% and 13% for the Quarton & Ainslie and Larsen models respectively.

In both the wake models and turbulence intensity models, the agreement was not ideal. Therefore, there is room for improvement.

2.3 LiDAR

Light Detection and Ranging (LiDAR) technology can be used to measure the wind speeds at heights above ground level. LiDARs use a single laser beam to measure distances of various objects and particles. There are several types of LiDARs that are utilized for various applications. The basic operation of the LiDAR consists of a laser and receiver

[76]. The laser is projected to an object in which the light is back scattered and detected by the receiver. Wavelengths of the laser, analysis of the information, and exposure of the laser all vary depending on the application type.

One type of LiDAR is the Doppler LiDAR which uses the Doppler effect to detect the movement of objects. The Doppler effect was described initially for acoustic waves, but also occurs in electromagnetic waves. When a laser strikes an object, the laser is reflected off the object if it has the ability to reflect electromagnetic waves. The movement of the object affects the frequency of the reflection in the line-of-sight of the laser. If the frequency of the reflected laser is known then the speed of the object can be determined. The observed frequency of the particle reflection, f, and frequency of the laser, f_0, is related to the velocity of the particle by Eq. 2.43, where v_{LOS} is the velocity of the particle moving in the line-of-sight of the laser and c_l is the speed of light [78].

$$f = f_0\big(1 + \frac{v_{LOS}}{c_l}\big) \tag{2.43}$$

The initial laser frequency of the LiDAR is a function of the speed of light and the laser wavelength, λ_0, shown by Eq. 2.44 [78].

$$f_0 = \frac{c_l}{\lambda_0} \tag{2.44}$$

One of the applications of Doppler LiDAR is to measure wind speeds. It achieves this by detecting the movement of aerosols in the air such as dust and pollen. The aerosols are used as seeding material to predict the movement of the air, based on the movement of particles with the wind.

The seeding material must follow the flow of the wind and also be able to scatter light [69]. Ideally the seeding material is neutrally buoyant to neglect the effects of buoyancy and gravity. Small particles follow the flow better, but may not be able to scatter the light appropriately. Figure 2.12 shows the sizes of various aerosols in the wind that the LiDAR would be able to use to measure the wind speed.

The LiDAR measures the particles that pass through the focal point of the laser. A lens inside of the laser adjusts the focal point distance by adjusting the minimum width of the laser at the desired measurement point, this is known as the waist position [24]. This is shown in Figure 2.13, where p is the distance from the laser fibre output to the lens and p' is the distance from the lens to the waist position. Minimizing the laser width maximizes the power at the focal point and therefore particles are detected when passing through this section.

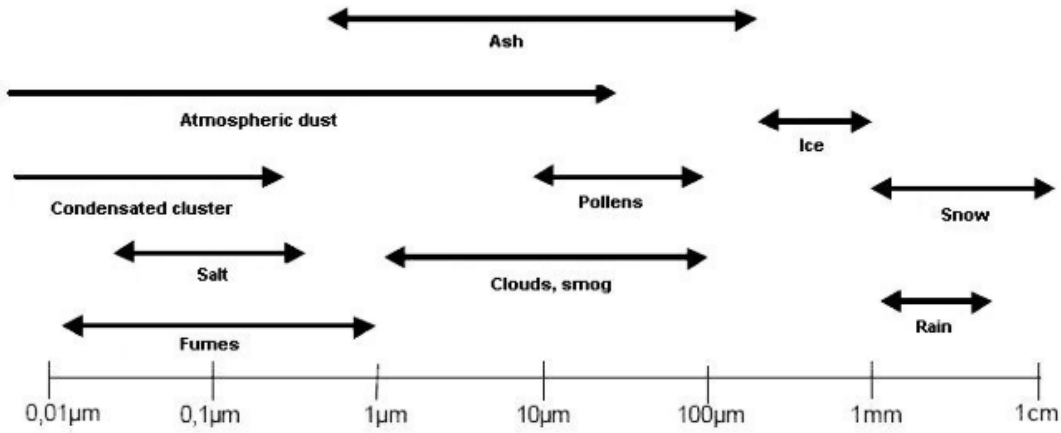

Figure 2.12: Size of aerosols [16]

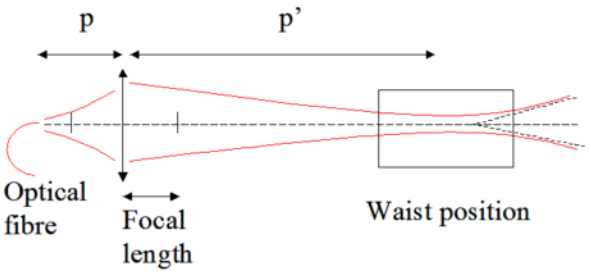

Figure 2.13: LiDAR laser propagation [24]

2.4 The Study of Wakes in Literature

There are several methods to study the effects of wind turbine wakes. Experimental methods to measure the velocity in the wake of the turbine have been conducted in both wind tunnels and field measurements. Studies vary on whether a single turbine is measured or an array of turbines. Various regions of the wake are also examined in different experiments, with a focus on either the near wake or far wake regions. This thesis focuses on the study of a single turbine and therefore relevant studies pertaining to a single turbine wake will be discussed.

2.4.1 Wake Flow Visualization

Visual flow behaviour can be obtained through flow visualization. Flow visualization methods for turbines can be performed in at least two methods, by applying flow indicators upstream of the turbine directed at the blade tips, to look at the tip effects, and by applying flow indicators on the blades of the turbines themselves. These methods are typically performed through the use of smoke.

Upstream smoke emission was conducted by Vermeer [74] and Alfredsson & Dahlberg [6] to visualize the vortex shedding from the blades of a turbine. The results of these experiments are shown in Figure 2.14a and b respectively. The vortex can clearly be seen in both experiments. The experiments by Vermeer [74] have a visualization of the vortices that form from the tips and propagate downstream. In the experiments of Alfredsson & Dahlberg, the vortex cylinders can be seen as the smoke gets sucked into the cylinders.

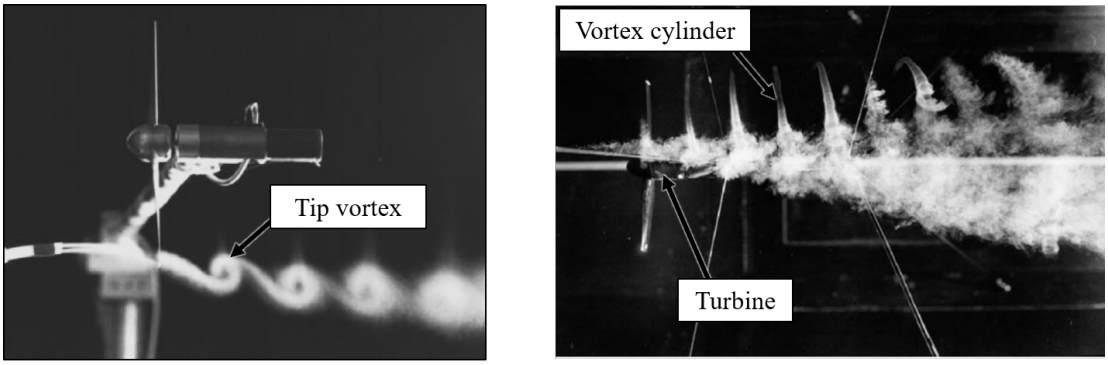

Figure 2.14: Upstream smoke visualization by (a) Vermeer on a 0.2 m turbine (taken from [73]) and (b) Alfredsson & Dahlberg (taken from [6])

Blade ignited smoke visualization was conducted at the National Renewable Energy Laboratory (NREL) by Hand et al. [35] on a 10 m diameter turbine inside a wind tunnel. The experiment was performed for both un-yawed and yawed angle of 30° of the turbine. The results from the experiment are shown in Figure 2.15. The helical vortex formation is seen to be emitting from a single blade. The wake of the yawed turbine is seen to deflect as it moves downstream.

During the experiment, the turbine extract little energy from the flow. Hence, no expansion in the wake was seen. Since only a small amount of energy was extracted, the flow is not representative of a turbine in production.

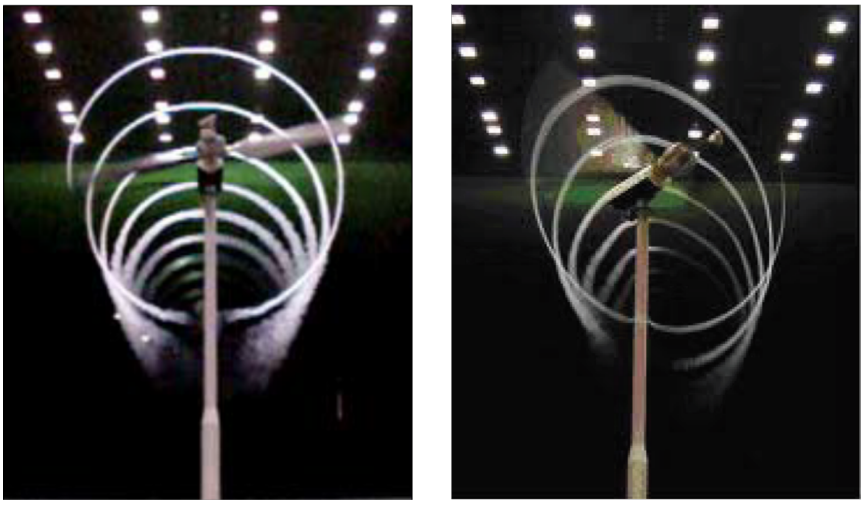

(a) (b)

Figure 2.15: Blade ignited flow visualization performed by Hand et al. [35] on a 10 m turbine for (a) $\gamma = 0°$ and (b) $\gamma = 30°$

2.4.2 Wind Tunnel Wake Measurements

Bastankhah & Porté-Agel conducted measurements on a scaled 3 bladed HAWT turbine inside a wind tunnel [11]. The measurements were conducted using PIV inside of a wind tunnel 2 m high, 2.57 m wide, and 28 m long. To fit inside of the tunnel, the wind turbine used had a rotor diameter of 15 cm. Compared to utility-scale turbines, the scaled turbine in this experiment has a 1 to 600 ratio. Scaling a turbine to such small measures has implications in the scaling of flow parameters, such as Reynolds number and Mach number. Therefore, the results may not properly relate under full scale conditions.

Measurements were performed to compare the effects of tip speed ratio and turbine yaw on the wake behavior. Figure 2.16 shows the results of the velocity profile at tip speed ratios of 6.34 and 3.9. At a lower tip speed ratio the velocity deficit was found to be higher and the near wake was more pronounced.

Additionally, lateral velocity profiles at various downstream distances were obtained for the different tip speed ratios. The profiles are shown in Figure 2.17. The profile of the far wake region can be seen at distances greater than 4 D, which develops a Gaussian distribution. At distances of 1 D and 2 D, the near wake profile is seen, which is more sensitive to the rotor dynamics.

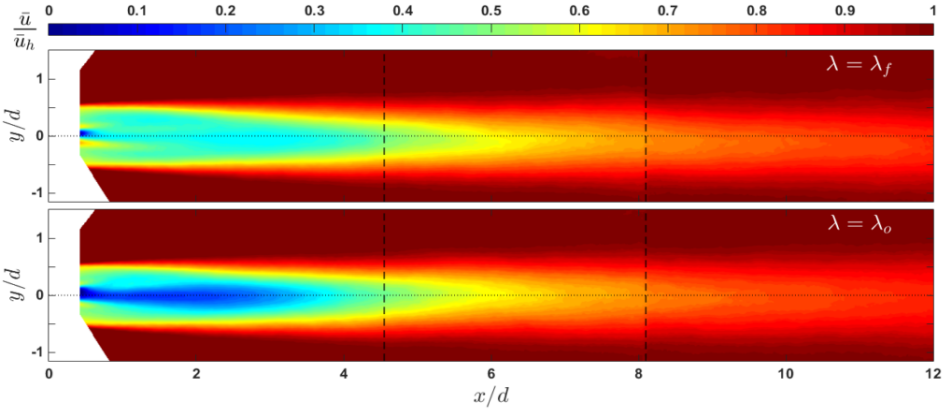

Figure 2.16: Contours of the normalized mean streamwise velocity from the results of wake experiments performed by Bastankhah & Porté-Agel for tip speed ratios of $\lambda_f = 6.34$ and $\lambda_o = 3.9$ [11]

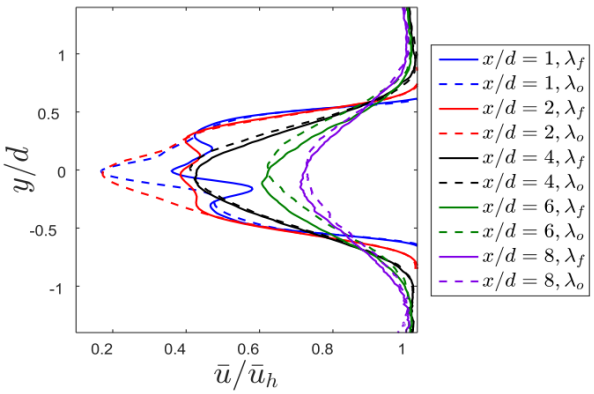

Figure 2.17: Lateral profiles of the normalized mean streamwise velocity from the results of wake experiments performed by Bastankhah & Porté-Agel for tip speed ratios of $\lambda_f = 6.34$ and $\lambda_o = 3.9$ [11]

The effects of the yaw angle on the wake from the results of the experiment are shown in Figure 2.18. With increasing yaw angle, the deflection of the wake increases. The wake was found to be less pronounced with increasing yaw angles as a results of the reduced thrust coefficient. The wake recovery is also accelerated when the turbine is yawed due to the momentum flux of the lateral velocity from the deflection of the wake.

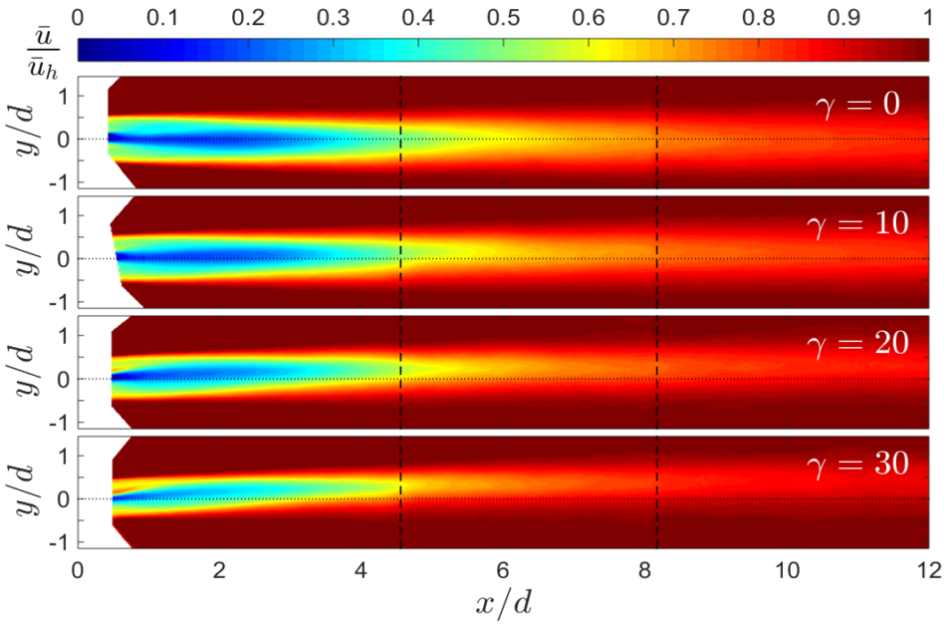

Figure 2.18: Contours of the normalized mean streamwise velocity from the results of PIV measurements from the wake experiments performed by Bastankhah & Porté-Agel for different yaw angles [11]

2.4.3 Large Wind Tunnel Wake Measurements

Larger wind tunnel experiments were performed by Krogstad & Adaramola [41] on a 0.9 m turbine. Velocity measurements were taken in the wake of the turbine using a Pitot-static pressure probe. The wind tunnel has significantly low turbulence with an average turbulence intensity of 0.2% [10].

The experiment investigated various tip speed ratios and yaw angles for the effect on the velocity profile. Figure 2.19 shows the results of the axial velocity profiles of various tip speed ratios at several downstream distances. A decreasing velocity deficit was seen at further downstream distances. The wake width was shown to increase with further distance as well, irrespective of the tip speed ratio.

Figure 2.20 shows the results of the axial velocity profile at various yaw angles. A deflection in the wake was seen when the turbine was in the yawed direction. It was determined that the wake width decreased with increasing yaw angles.

Due to the significantly low turbulence levels of the tunnel, the velocity profile is ex-

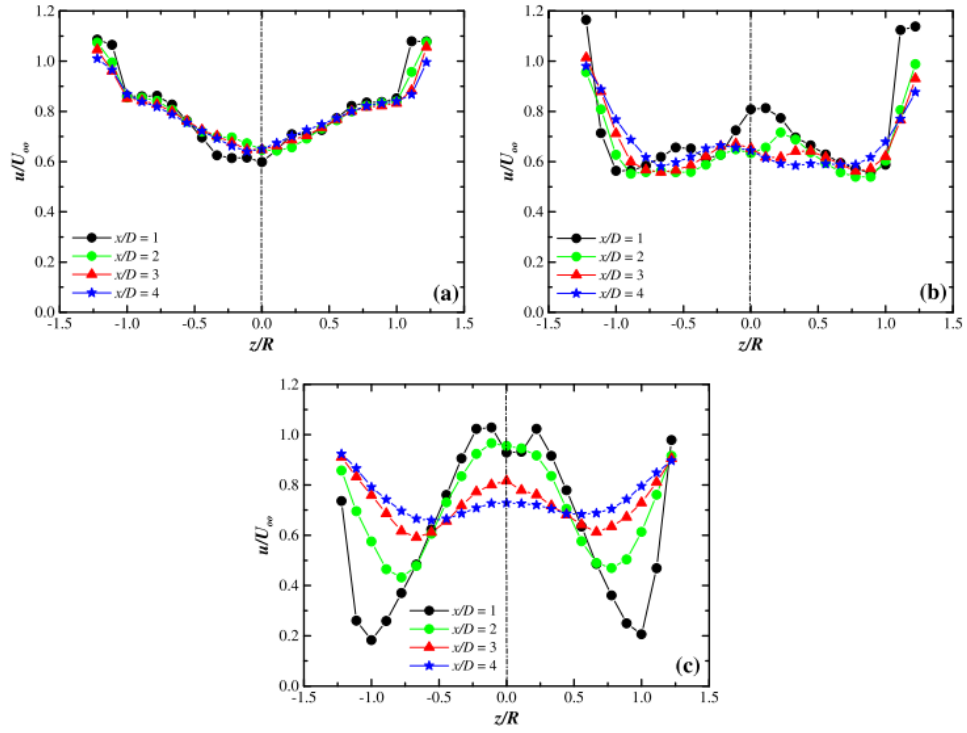

Figure 2.19: Axial velocity profiles at the hub height of a 0.9 m turbine for four positions downstream of the rotor plane for (a) $\lambda = 3.35$, (b) $\lambda = 5.79$ and (c) $\lambda = 9.15$ from the experiments of Krogstad & Adaramola [41]

pected to be much more pronounced with an extended wake recovery time. The lack of turbulence in the wake reduced the mixing that occurs to recover the wake. In comparison to utility turbines, this level of turbulence is not seen in atmospheric conditions and therefore is difficult to relate to external wake behaviour.

2.4.4 LiDAR Wake Measurements

Wind Doppler LiDAR's primary use have been to evaluate wind conditions, however in recent years they have been used to measure the incoming wind of a wind turbine as well as to study the wake behaviour behind the turbine.

Experiments performed by Bingöl [16] modified a wind Doppler LiDAR to make wake measurements on a full-scale wind turbine. The experiments were conducted in a 2 part

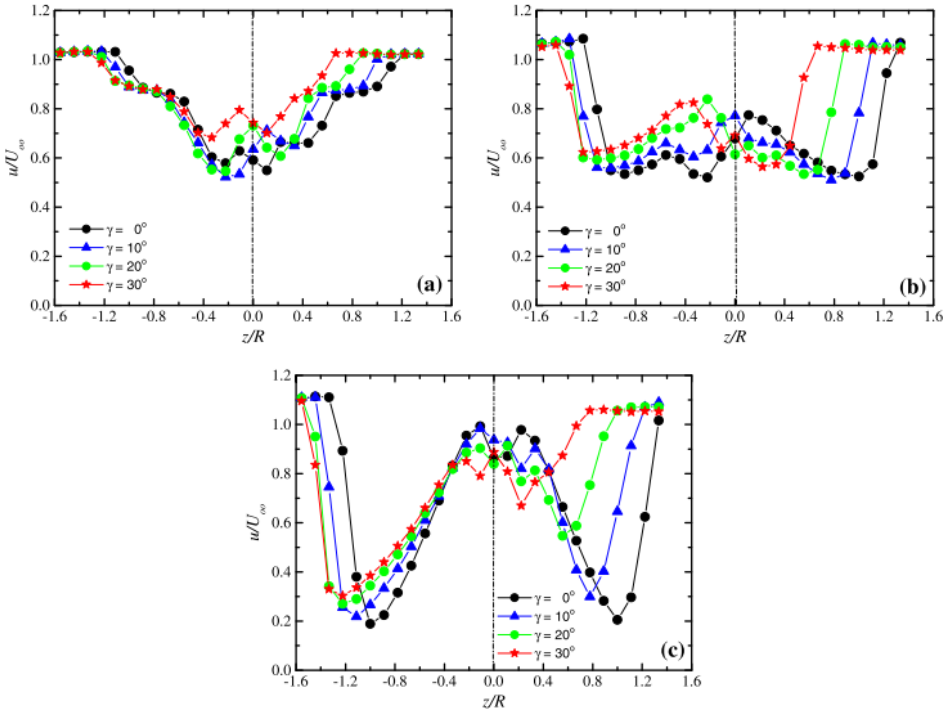

Figure 2.20: Axial velocity profiles at the hub height of a 0.9 m turbine and a downstream distance of 1 D at various yaw angles for (a) $\lambda = 3.35$, (b) $\lambda = 5.79$ and (c) $\lambda = 9.15$ from the experiments of Krogstad & Adaramola [41]

measurement campaign, divided into one-dimensional LiDAR scanning by Bingöl et al. [17] and two-dimensional scanning by Trujillo et al. [72].

A ZephIR LiDAR was used and modified in the experiments. The ZephIR LiDAR's conical laser scan was adapted to incorporate a straight line-of-sight (LOS) laser position. The LiDAR was then mounted onto a tilt-and-pan head to control the laser scan position. The mechanism was then mounted to the back of a Tellus 95 kW wind turbine for the use of velocity measurements behind the turbine.

Part 1 of the experiments took measurements with the adapted LiDAR mechanism completing horizontal scans at $\pm 30°$ for various distances from the turbine. This was labelled as line scan mode for the experiments. In addition, a deep line scan mode, was performed by changing the focus distance of the LiDAR during the pan from the line scan mode. Results of the experiment obtained velocity profiles for the measurement scans.

Part 2 of the experiments used the LiDAR's conical scanning mode in combination with the tilt-and-pan head to obtain measurements in two-dimensions at various distances away from the turbine.

The results of these measurements provided velocity deficit profiles, which were compared to the Ainslie model at a distance of 4 D. This is shown in Figure 2.21. The results shown are for the wake profile with the nacelle as the reference point (Nac. frame) and also the wake corrected for meandering (Meand. frame). In this experiment, the velocity deficit obtained is defined by Eq. 2.23. In Figure 2.21a, the turbine changed yaw position to orientate the hub with the changing wind direction. This caused a spread in the velocity profile of the nacelle reference frame. The velocity profile was corrected using the meandering reference frame, however the velocity deficit is much higher in comparison to the Ainslie model. The measurements in Figure 2.21b did not have a change in yaw direction and therefore the velocity profiles correlate better to the Ainslie model, although the measurements still show a slightly higher deficit.

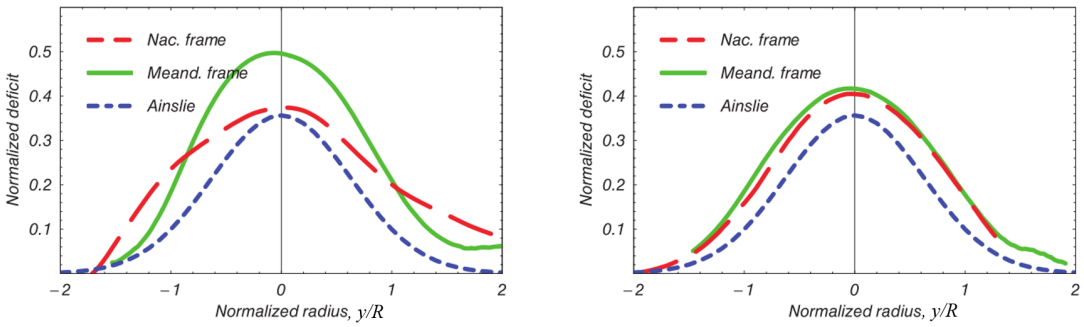

Figure 2.21: Normalized wind speed deficit in a nacelle and meandering reference frame compared against the Ainslie model at 4 D for (a) $U_0 = 4.9$ m/s and (b) $U_0 = 5.2$ m/s with $I_0 = 8\%$ from experiments by Trujillo et al. [72]

Finally, the turbulence intensity was measured and is shown in Figure 2.22. A higher turbulence level is seen in the centre of the wake with the larger velocity deficit and recovers at the edges of the profile. The turbulence intensity in Figure 2.22a shows higher values for the nacelle reference frame than the meandering reference frame and is also offset from the centre of the hub. This is a result of the change in yaw direction of the turbine causing increased turbulence from the movement of the wake. The meandering reference frame corrects this and provides a more symmetric turbulence profile. Figure 2.22b shows similar profiles for both the meandering and nacelle reference frames since the turbine did not

yaw during the measurements. This is therefore the more representative profile, which the meandering reference frame was able to provide in Figure 2.22a.

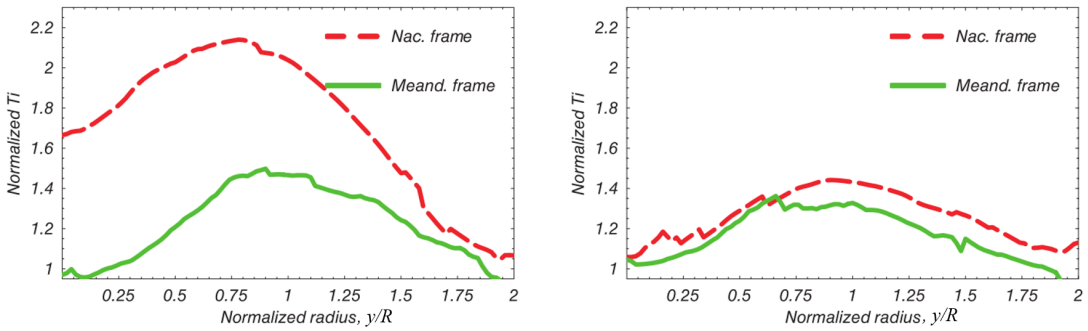

Figure 2.22: Normalized turbulence intensity (T_i) at 4 D for (a) U_0 = 4.9 m/s and (b) U_0 = 5.2 m/s with I_0 = 8% from experiments by Trujillo et al. [72]

The results of the experiments conducted on a turbine open to environmental conditions show the difficulties in providing accurate measurements from the changing atmospheric conditions. The wind speed and direction are constantly changing, causing the variability in the measurements and the need to provide corrections to the directional changes of the turbine.

Chapter 3

Experimental Equipment

This chapter will cover the facilities and equipment used in the research experiments. Details of the Wind Generation Facility and UW WEG wind turbine follow in Section 3.1. Measurement equipment, including the design and development of the Pitot Tree, sonic anemometer, and LiDAR are described in Sections 3.2 to 3.4.

3.1 Experimental Facilities

The University of Waterloo Wind Energy Group has a 3.3 m diameter wind turbine operated inside a large controlled wind facility that will be studied for wake characteristics. Using the turbine under controlled wind conditions will give an idea of the wake characteristics without environmental effects and allow for a better understanding of the behavior of the wake.

3.1.1 Wind Generation Facility

The University of Waterloo Fire Testing Research Facility, which will be referred as the Wind Generation Facility, is a large-scale open circuit wind tunnel for indoor wind turbine testing that allows for controlled wind condition testing. The facility, shown in Figure 3.1, is located in the Region of Waterloo.

The facility is equipped with six 75 kW variable frequency drive fans that produce variable airspeeds up to 11.1 m/s inside the test area of the facility [31]. It was determined

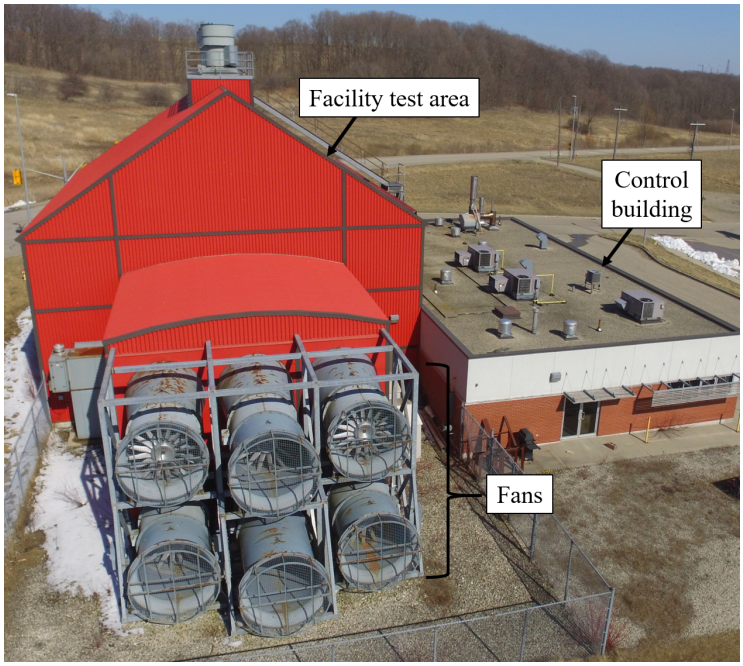

Figure 3.1: UW Wind Generation Facility

by Gertz [31] that the turbulence intensity inside the facility ranged between 5.9% and 6.2%. The fans are orientated with three fans across and two fans high. The orientation and naming of the fan positions are shown in Table 3.1. Specifications of the fans are given in Table 3.2.

Table 3.1: UW Wind Generation Facility fan naming and orientation view towards the upwind direction

Top South	Top Middle	Top North
Bottom South	Bottom Middle	Bottom North

A fan discharge plenum connects the fans to the test area of the facility with an array of flow straightening ducts to condition the incoming flow [39]. The plenum expands to the flow entering the test area. The fans and flow straightening ducts can be seen in Figure 3.2 with a size scale for reference. Following the inlet of the fans is the facility test section where experiments are conducted. An exit area then follows at the end of the test area, which is equipped with large doors to open the area to the atmosphere. Specifications on the facility geometry are given in Table 3.3.

Table 3.2: UW Wind Generation Facility fan specification [28]

Specification	**Value**	**Details**
Type	Vane axial fans	Howden-Buffalo Model 78-26 Series 1000
Size	1.98 m	Diameter
Number (arrangement)	6 (3 x 2)	-
Volume Flow Rate	78.8 m^3/s	Maximum per fan
Pressure	413.5 Pa	At a maximum flow rate
Control	VFD	Individual operation

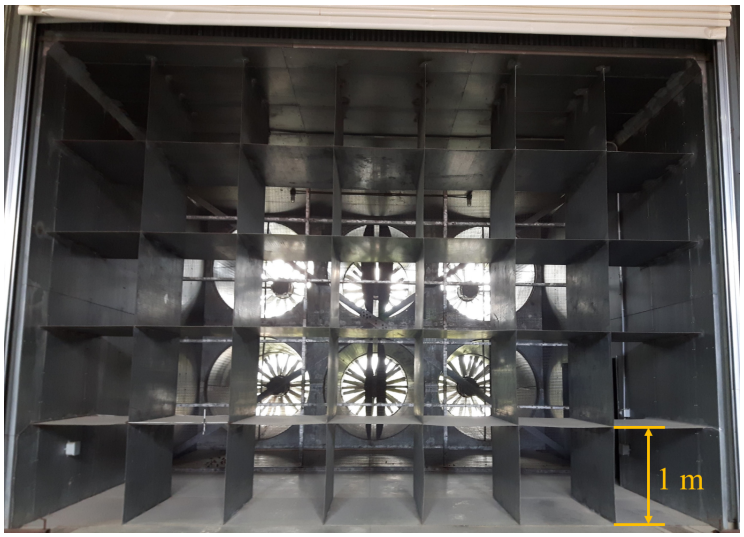

Figure 3.2: UW Wind Generation facility fans

More details on the facility can be found in Devaud [25], Gaunt [29], and Gertz [31]. The facility is therefore ideal for wind turbine testing as the high turbulence makes the wind representative to environmental conditions while being able to control the wind speeds [28].

3.1.2 UW WEG Turbine

A 3.3 m diameter turbine developed within the Wind Energy Group is used in the Wind Generation Facility and produced a rated power of 1.45 kW in 11 m/s wind conditions [31]. The turbine, named the UW WEG turbine, is shown inside of the facility in Figure 3.3. The UW WEG turbine is an upwind horizontal axis wind turbine (HAWT) with a

Table 3.3: UW Wind Generation Facility geometry specification [28]

Area	**Geometry**
Fan discharge plenum	8.23 m long, 8.54 m wide 5.9 m high
Plenum exit plane	Rectangular 8.0 m wide, 5.9 m high
Flow conditioning	Two settling screens and a 7 x 5 array of steel flow-straightening ducts in the discharge plenum
Test area	15.4 m wide, 19.5 m long, 7.8 m high along the sides and 13 m high at the peak
Flow exit	Squared, 7.9 m x 7.9 m

hub height of 3.05 m and designed to attach 3 blades to the rotor hub [1].

Figure 3.3: UW WEG wind turbine inside the Wind Generation facility

The turbine is equipped with a Marathon Electric Y287 184TC frame vector motor to act as either a motor or generator [28]. The motor attaches to a drive shaft, which

incorporates an encoder to measure the rotational speed of the turbine. The encoder relays information to an SP2203 Control Techniques Vector Drive to control the speed of rotation. A sub-panel, located in the control room of the Wind Generation Facility, communicates with the controller to set the desired rotational speed, start and stop the motor, and provide an emergency brake activation [31]. The sub-panel also displays the actual rotational speed from the encoder and the power generated or consumed. A block diagram of the communication is provided by Gallant [28] shown in Figure 3.4. More details of the turbine specifications can be found in Abdelrahman [1] and Gallant [28].

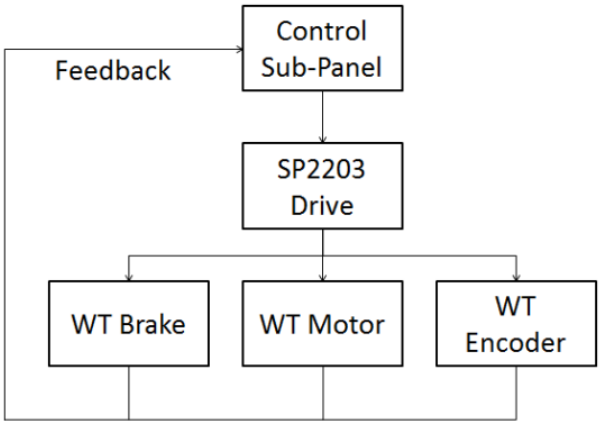

Figure 3.4: Block diagram of the UW WEG turbine control communication connections from Gallant [28]

The UW WEG turbine is equipped with 3 custom designed blades designed by and manufactured by Gertz [31] out of fibre-reinforced plastic material. The blades were designed using NREL S83X series airfoils [65]. The length of the blades are 1.6 m, together with the rotor dimensions makes the total radius of the blade 1.65 m. The blade was designed for interchangeable winglets. For the purpose of experiments performed in this thesis, standard winglets were used from Gertz [31], which were CNC milled from maple wood. Further details on the specifications, design, and manufacturing of the blades can be found in Gertz [31]. With the blades from Gertz, the blockage ratio of the turbine inside the Wind Generation Facility was found to be 7%, which is relatively low for wind turbine tests inside of a wind tunnel [39].

The turbine nacelle can be yawed between $\pm 40^\circ$ at 10° increments. A diagram of the yaw angle conventions used in this thesis in relation to the incoming wind direction is shown in Figure 3.5 for reference. The figure also depicts the direction of rotation of the rotor.

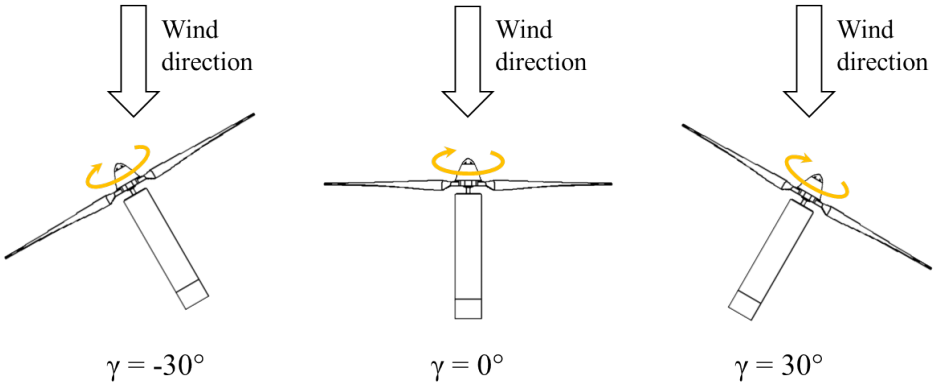

Figure 3.5: Diagram of the yaw angle conventions of the UW WEG turbine and corresponding rotational direction (viewed from above)

3.2 Pitot Tree

As part of an effort to characterize the wind profile inside the Wind Generation Facility, a structure to hold 16 pitot tubes was developed in order to measure the velocity profile of the incoming flow upstream of the UW WEG turbine. The pitot tube structure, referred to as the Pitot Tree, was designed to provide a single device that can be placed in front of the UW WEG turbine to capture the flow in front of the turbine with a single measurement. This allowed changes in the velocity profile to be observed as a result of changing the facility fan speeds and a simple method to evaluate the flow profile before performing experiments with the UW WEG turbine.

3.2.1 Design

The Pitot Tree was designed to capture a representation of the flow upstream of the blade swept area of the UW WEG turbine. The design was limited by the amount of pressure transducers available, resulting in 16 pitot tubes being placed on the structure. To use the limited number of pitot tubes effectively, it was devised to place the pitot tubes in line of 3 circles of varying diameters with the centres at the hub position of the UW WEG turbine.

The circles and relative pitot tube placement on the structure are depicted in Figure 3.6a. The outer circle had a diameter near the diameter of the 3.3 m blade, set to 3.2 m. The inner circles were then set to diameters decreasing by 1 m, resulting in diameters of 2.2 m and 1.1 m. The tips of the blade are of highest concern of the wind turbine as

the end 20% of the blade provides a large portion of the power extraction and the tips of the blades generate tip vortices important in the formation of the wind turbine wake [18]. In addition to the importance of the outer area, it was discovered that this area had the highest velocity variability during the experiments of Gallant [28]. Therefore, the highest number of pitot tubes was placed in the outer circle of the Pitot Tree design, with 8 pitot tubes evenly distributed across the circle circumference. The inner circles were given 4 pitot tubes each, evenly distributed, and in opposite configurations to each other, to fill the remaining area of the blade swept area.

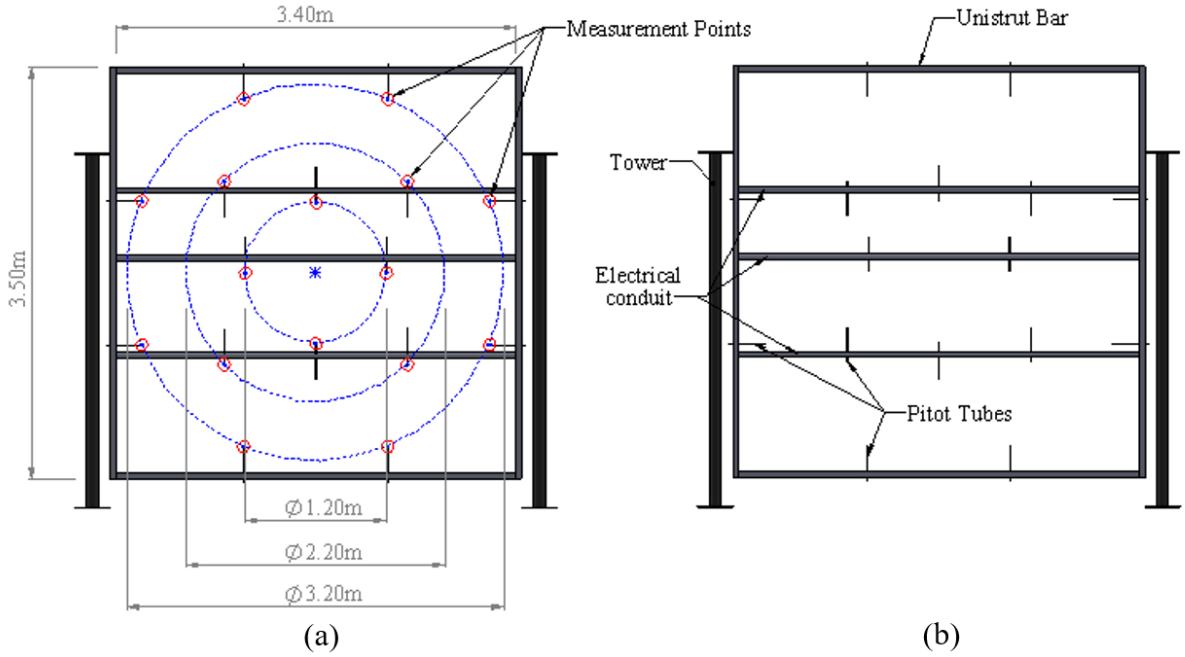

Figure 3.6: Pitot Tree design showing (a) measurement points and pitot tube circle alignment, and (b) components of the structure

The structure was designed to be constructed using Unistrut steel bars for ease of assembly and availability of material. The bars were configured in a rectangular fashion with legs extending down to lift the structure to the desired height, and used to fasten the outer pitot tubes. The Unistrut structure was mounted to 2 towers to hold it upright and provide stability. Electrical conduit was used to provide a connection structure for the placement of the remaining inner pitot tubes. The construction components of the Pitot Tree design are shown in 3.6b. The towers were placed on 8 wheels to be able to relocate the structure as needed. Figure 3.7 shows the final construction of the Pitot Tree.

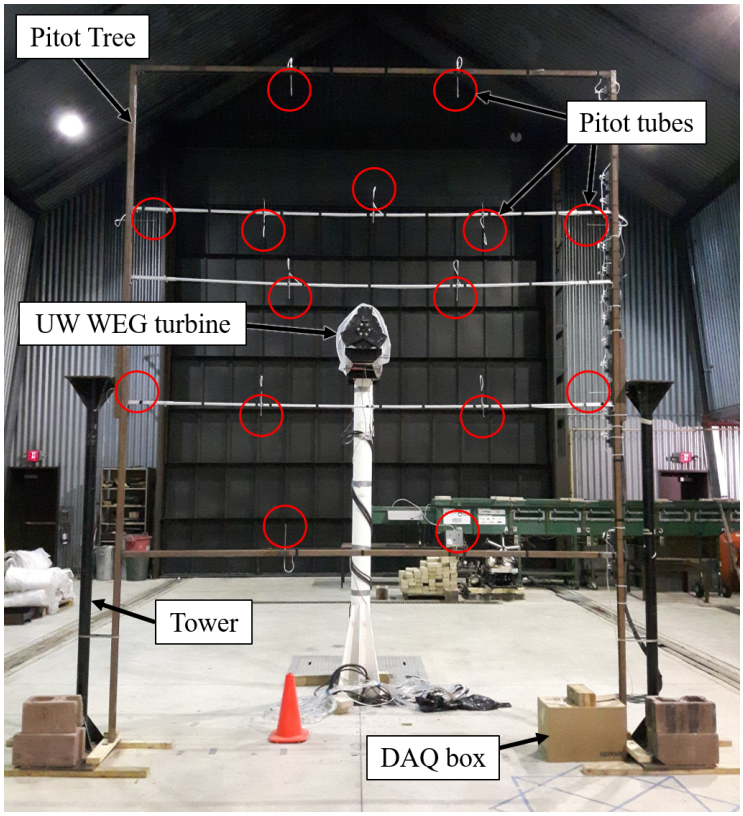

Figure 3.7: Pitot Tree seen in the Wind Generation Facility

3.2.2 Instrumentation

Pitot-static probes were fabricated for the Pitot Tree structure. Each pitot probe was attached to a Setra 267 pressure transducer using 1/16" tubing with a central 1/8" tubing connecting all transducers and running to a box at the base of one of the towers to provide a static pressure reading for each transducer. Details of the Setra 267 pressure transducers are shown in Table 3.4.

The pressure transducers are all located on the outer structure of the Unistrut assembly, with wires running to a National Instruments (NI) 9205 data acquisition (DAQ) analog to digital converter located at the bottom of the tower. The NI 9205 DAQ is attached to a NI 9191 chassis to transmit the signal through a WiFi signal from inside the Wind Generation Facility to a router inside the control area of the facility. The router then connects to a computer for data collection and operation of the DAQ. A block diagram of

Table 3.4: Setra 267 pressure transducer specifications [63]

Specification	**Value**
Pressure Range	0 Pa to 250 Pa
Output	0 to 10 VDC
Accuracy	±1.0% FS
Non-Linearity	±0.98% FS
Hysteresis	±0.10% FS
Non-Repeatability	±0.05% FS

the communication connection is shown in Figure 3.8.

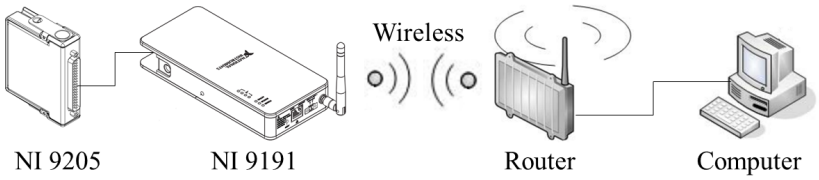

Figure 3.8: DAQ and communication block diagram

Calibration

The Setra 267 transducers were calibrated using a GE Druck DPI 610 Pressure Calibrator. All 16 pressure transducers were connected to the pressure calibrator and the pressure was increased by 50 Pa from 0 Pa to 250 Pa and then reduced by 50 Pa from 225 Pa to 75 Pa to capture any error associated with hysteresis. The results of the calibration for each transducer are shown in Figure 3.9 below. A fit was used to calculate the slope and intercept of the calibration results to use to convert the voltage data of the transducers to the corresponding pressure measurement. The fit results are shown in Table 3.5 with the corresponding root mean square (RMS) values. From the RMS values, it was determined that any error due to the fit was negligible.

Prior to each use of the Pitot Tree, a zero reading is taken as used as the intercept in the calibration equation to ensure accuracy of the information.

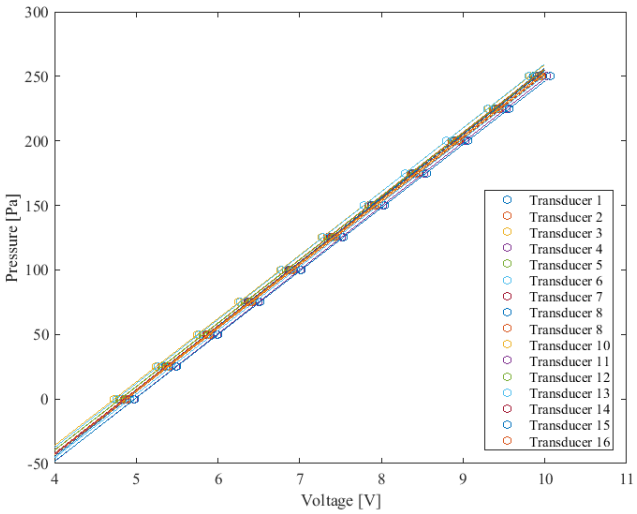

Figure 3.9: Calibration results for the Setra 267 pressure transducers

Table 3.5: Calibration results for the Setra 267 pressure transducers

Transducer	**Slope**	**Intercept**	**RMS**
1	50.22	-245.58	1.000
2	49.08	-239.76	1.000
3	49.19	-232.81	1.000
4	49.48	-246.38	1.000
5	49.27	-236.64	1.000
6	49.43	-243.47	1.000
7	49.04	-238.44	1.000
8	49.11	-244.75	1.000
9	49.28	-236.92	1.000
10	49.23	-239.95	1.000
11	49.66	-241.62	1.000
12	49.18	-236.53	1.000
13	49.56	-235.86	1.000
14	49.49	-240.13	1.000
15	49.49	-240.51	1.000
16	49.26	-239.42	1.000

3.3 Sonic Anemometer

The University of Waterloo Wind Energy Group used a CSAT3 Three Dimensional Sonic Anemometer for measurements of single point velocities. The CSAT3 Sonic Anemometer is an ultrasonic anemometer with the capability of measuring wind speeds in three dimensions [19]. The sonic anemometer has three pairs of transducers orientated non-orthogonally to transmit and receive ultrasonic signals. The time of the ultrasonic signal is related to the wind speed along the transducer axis, speed of sound, and air density. The wind speeds can then be calculated and divided into the x, y, and z directions due to the orientation of the transducers. The directions are associated with the sonic anemometer head, which is equipped with a level and mounted onto a leveling mount to ensure accuracy of direction. A schematic of the sonic anemometer's transducers is shown in Figure 3.10.

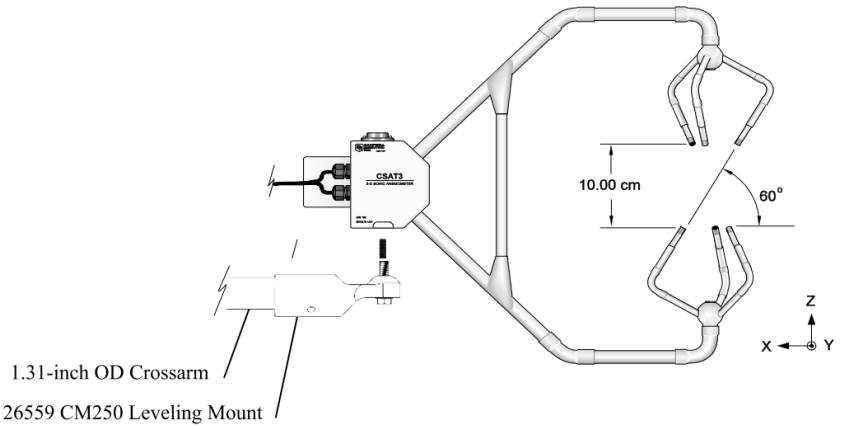

Figure 3.10: CSAT3 Three Dimensional Sonic Anemometer Schematic [19]

The specifications of the CSAT3 Sonic Anemometer can be found in Table 3.6. More details of the CSAT3 Sonic Anemometer can be found in the CSAT3 Three Dimensional Sonic Anemometer instruction manual [19].

Table 3.6: CSAT3 Three Dimensional Sonic Anemometer Specifications [19]

Measurement rate	Programmable from 1 to 60 Hz
Measurement resolution	1 mm/s RMS resolution
Offset error	±8 cm/s
Direction accuracy	±0.7° at 1 m/s for horizontal wind

The sonic anemometer was mounted on an adjustable stand to be able to adjust the height of the measurement up to the hub height of the UW WEG turbine [1].

3.4 ZephIR LiDAR

The ZephIR z150 LiDAR model is used by the University of Waterloo Wind Energy Group for collecting wind speed and direction measurements. The LiDAR, sold by ZephIR Lidar, is a wind Doppler LiDAR as described in Section 2.3. The LiDAR is primarily used for wind farm applications as a replacement for met towers. They are designed to operate in offshore conditions due to the high cost of installing a met tower offshore. The LiDAR uses a pulsed laser that measures aerosols in the air to determine the wind speed.

The LiDAR has several components as shown in Figure 3.11. The optics pod houses the laser and sensors. The internal component details of this pod are discussed later in Figure 3.12. The electronics pod runs the electronics in the LiDAR and contains the data storage. The battery pod powers the LiDAR either by internal batteries or an external power supply. The met station measures the pressure, humidity, and temperature in the ambient air. The louvres protect the cables while allowing for cooling of the electrical components of the LiDAR.

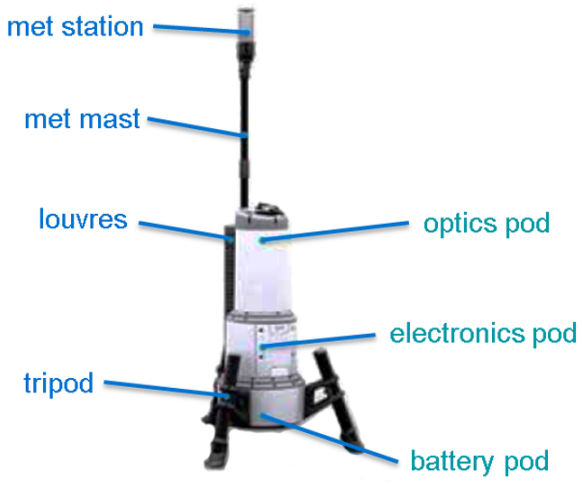

Figure 3.11: ZephIR z150 LiDAR components [56]

Figure 3.12 shows a cross-sectional view of ZephIR Lidars first model. A laser is shown

through a lens to converge the laser to a relatively wide cross-sectional area. The laser is then deflected using a prism lens which rotates to give the laser the conical pattern. The lens is set to deflect the laser to 30.6° from the vertical position.

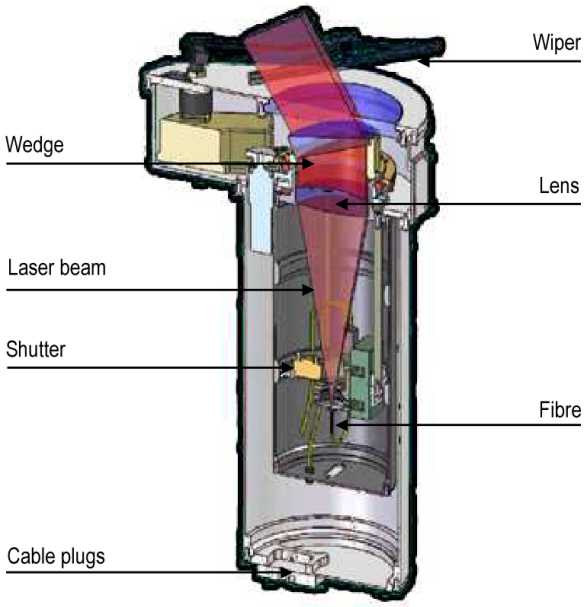

Figure 3.12: Cross sectional view of the prototype ZephIR [16]

The details of the system specification are given in Table 3.7. A 28 V external power supply is used to power the LiDAR. The LiDAR can measure 5 different heights during a run from a range of 12 m to 200 m from ground level. The laser has a wavelength of 1575 nm and power of 1 W. Due to the rotating prism lens, the laser is considered a class I and eye safe because it is a defocussed collimated beam. Without the rotating lens, the laser would be increased to a class IV and eye protection is needed to handle the device according to e-mail communication with ZephIR Lidar [46].

The conical laser pattern of the LiDAR is used to determine the direction of the wind speed. The LiDAR determines the direction of the wind by measuring the velocity for two perpendicular points in the conical scan. Then using the formula relation in Eq. 3.1 to 3.3, where θ_c is the laser cone angle and u_{θ_c} is the velocity of the particle in the direction of the laser, the direction can be determined. Since at both measurement points the vertical velocity, w, is the same, the horizontal velocity component, u, can be analyzed to determine the direction [16]. Figure 3.13 shows the components of two perpendicular measurement

Table 3.7: ZephIR z150 LiDAR system specifications [56]

LiDAR	Model	ZephIR z150
	Unit number	135
System Power Requirements	28V DV at 100W continuous	
	Max. power draw: 250W	
Measurement Range	Min. height	11 m
	Max. height	200 m
	5 user programmable heights	
Wind Speed	Max.	70 m/s
	Min.	4 m/s
Laser	Class	I (eye safe)
	Wavelength	1575 nm
	Peak power	< 1 W (25 mm aperture)
	Pulse length	< 1 m/s
	Pulse frequency	< 1 Hz
	Conical angle	30.6°
Data output	Wind data (3 s average)	
	1, 5, 10 minute wind speed averages	

points within the conical scan, where P_1 and P_2 are the particles within the laser scan and $\vec{B}$ is the direction of the laser.

$$u_{\theta_c} = u \sin\theta_c + w \cos\theta_c \tag{3.1}$$

$$u_{-\theta_c} = -u \sin\theta_c + w \cos\theta_c \tag{3.2}$$

$$u = \frac{u_{\theta_c} - u_{-\theta_c}}{2 \sin\theta_c} \tag{3.3}$$

The LiDAR uses the program Waltz to operate and record data [56]. Waltz has two modes for data collection and outputting data files [48]. The first option is the wind data collection, which uses the built-in calculations of the program to convert the measurement data to wind speed and direction in 3 second averages. The second option outputs the raw spectral data in the form of Fast Fourier Transforms (FFT) for each data point collected from particles moving through the path of the laser focal point. The doppler shift is

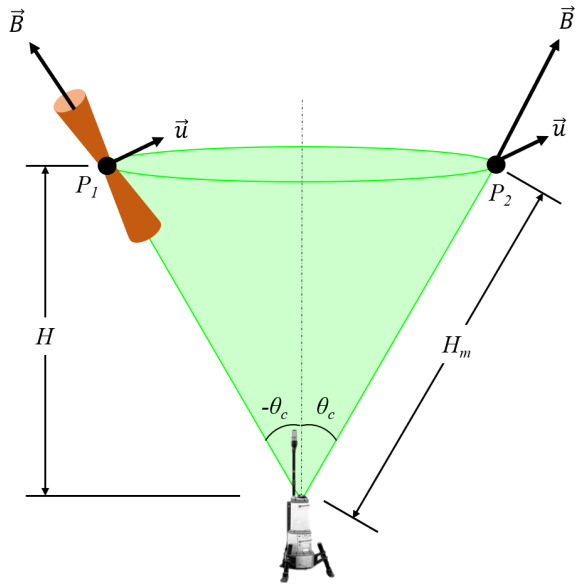

Figure 3.13: LiDAR conical scanning mode adapted from Bingöl [16]

registered for the line-of-sight (LOS) direction of the laser. The signal-to-noise ratio (SNR) is displayed in each bin of the FFT. For this mode, the LiDAR takes 50 readings per second as specified by the ZephIR Lidar Waltz user's guide [48]. Details of processing the raw data are described in the following section.

3.4.1 Measurement Frequency Processing

Measurements for the raw spectral data of the ZephIR LiDAR are output in Fast Fourier Transforms (FFT) with the signal-to-noise ratio (SNR) displayed in each bin. The FFT bins correspond to the velocity that is calculated from the Doppler frequency shift. The velocity is dependant on sampling rate, the size of the FFT, the laser wavelength, and the speed of light, which under normal operation corresponds to a velocity of 0.1538 m/s for each bin number excluding bin 0, according to e-mail communications with ZephIR Lidar [53]. The SNR seen in the FFT forms a peak for a measurement point. Therefore, the true velocity aligns with the peak of the SNR distribution. Any single bin measurements should be disregarded as outlined by the ZephIR CSV file user's guide [47]. An example of the SNR seen in a series of FFT bins is shown in Figure 3.14.

The FFT data can be processed to remove any objects in the path of the laser, such as a

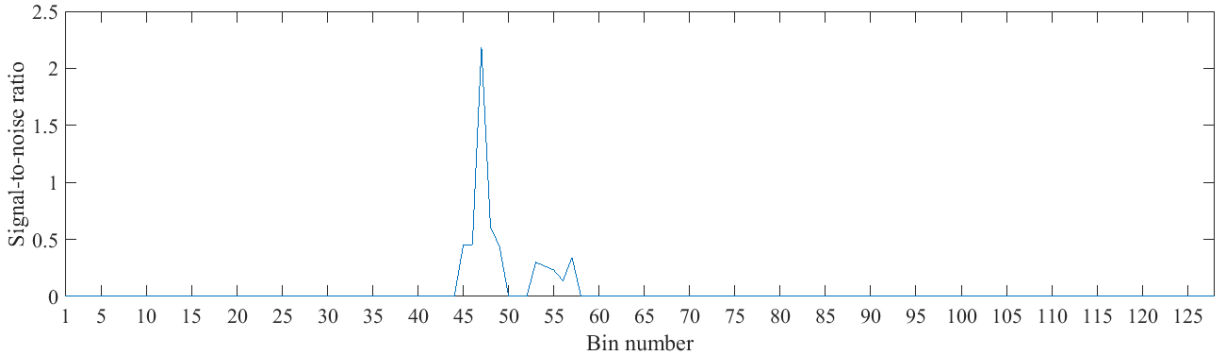

Figure 3.14: Typical SNR distribution in the FFT of the ZephIR LiDAR raw data

wind turbine blade. Large physical objects are detected with a SNR that is approximately 10 times the SNR detected from a seeding particle. Therefore, these measurements can be omitted by applying a low-pass filter, removing any SNR above the range of the seeding particles. In addition, a wind turbine blade that passes through the laser measurement area shows a cyclic pattern in the data with data being recorded for every pass seen at the laser LOS velocity direction and no information seen at any other velocity, since the blade blocks the laser from reaching any further. Therefore, processing the data for the LiDAR laser passing through the swept area of a wind turbine is achievable.

Chapter 4

Experimental Methods

This chapter will discuss the experimental setup and methods used in characterization of the flow of the Wind Generation Facility, verification of LiDAR measurements, and wake measurements of the UW WEG turbine. The process to characterize the velocity profile inside the Wind Generation Facility is described in Section 4.1. Following the wind characterizing, the LiDAR verification process is shown in Section 4.2. Initial experiments using flow visualization were performed to study the wake. The setup for these experiments are described in Section 4.3. Finally, the wake velocity experimental setups for the Pitot Tree, sonic anemometer, and LiDAR are described in Section 4.4.

4.1 Wind Characterization

During the experiment of Gallant [28] it was determined that there is non-uniformity of the velocity profile in the Wind Generation Facility seen at the UW WEG turbine location. This was noted by an increase in the velocity profile seen at an azimuth angle of 120° clockwise from a 6 O'clock position at the wind turbine from previous experiments conducted in the facility. This non-uniformity is problematic to perform accurate experiments inside of the facility. Therefore, in order to ensure accurate experiments, steps were completed to determine the cause of this non-uniformity and attempt to alleviate the issue.

The velocity non-uniformity was also determined from previous work of Weisinger to characterize the flow throughout the test enclosure when the facility was built by traversing pitot probes throughout the facility to obtain velocity profiles at various distances from the test enclosure opening [77]. Similar to Weisinger's work, Best also provided a velocity

contour at various wind speeds and positions in his thesis [15]. In each of the velocity contours of the facility provided by Weisinger and Best, it is seen that around the position that the wind turbine is set, approximately 8 m downstream of the fan outlet, there is evidence of the non-uniformity. At the top middle position of the wind turbine there shows to be a velocity deficit from the average. Moving the turbine to another position inside the facility will also have uniformity issues according to the results of Best.

Several potential causes of the issue were explored. This included measuring the fan blade angles, adjusting the fan back draft dampers, measuring the flow rate of each fan, and providing additional measurements of the flow in front of the UW WEG turbine. Details of work done to explore these causes are given in Appendix B. The final solution to this issue was to develop the Pitot Tree described in Section 3.2 to adjust the facility fan speeds to attempt to obtain a uniform profile. The Pitot Tree allowed real-time measurements to be able to validate each fan speed setting configuration for the profile uniformity achieved.

4.1.1 Fan Frequency Adjustment

Using the Pitot Tree developed in Section 3.2, real-time measurements could be obtained while adjusting the fan frequencies in the Wind Generation Facility. With this method it could be determined whether a uniform flow profile in front of the UW WEG turbine was achievable by adjusting the flow from the fans.

The test was conducted in three parts. Initially, with an average VFD frequency of 30 Hz set across the fans, the frequency was set based on known characteristics, such as flow rate, fan current, and velocity profiles taken from previous measurements in Appendix B. Once the results of the characteristic based settings were determined, the data collected from the velocity readings and fan settings were entered as training data into an optimization program which uses artificial neural networks to predict the fan settings that will achieve uniform flow. In conjunction with this program, the fan settings were also determined by a visual inspection and trial and error. The last part was to adjust the average fan frequency to determine whether the results from the 30 Hz average case could be scaled to other frequencies. This was conducted at an average frequency of 40 Hz and the maximum possible fan frequency settings.

For part 1 of the testing, the following test fan frequency settings in Tables 4.1 to 4.4 were used based on known flow characteristics. Tables 4.1 to 4.4 represent the fan frequency settings of the fan orientation shown in Table 3.1.

To determine the next fan frequency configuration, the previous tests were used as training data for a neural network optimization program. The neural network optimization

Table 4.1: Test 1 Wind Generation Facility base case fan frequency settings at 30 Hz

30 Hz	30 Hz	30 Hz
30 Hz	30 Hz	30 Hz

Table 4.2: Test 2 Wind Generation Facility fan frequency settings adjusted for flow rate with a 30 Hz average

28 Hz	30 Hz	27 Hz
33 Hz	31 Hz	30 Hz

Table 4.3: Test 3 Wind Generation Facility fan frequency settings adjusted for fan current readings with a 30 Hz average

29 Hz	28 Hz	29 Hz
30 Hz	29 Hz	28 Hz

Table 4.4: Test 4 Wind Generation Facility fan frequency settings adjusted for Pitot tube array velocity profile measurements with a 30 Hz average

30 Hz	36 Hz	25 Hz
25 Hz	30 Hz	30 Hz

program used a standard MATLAB neural network function with details outlined in the MATLAB user's guide [13]. The neural network used 10 hidden layers with 16 inputs from the velocity data of the pitot tube readings and 6 outputs for the fan frequency settings. All the inputs and outputs were non-dimensionalized based on the total average of the velocities and frequency. Initially, with only a few training data samples the program did not converge, although the outputted fan frequencies were still tested to obtain more training data. More tests were performed based on the results of previous tests through human visualization. Eventually, with enough training data the program was able to converge. However, the program was still not able to predict a total uniform setting.

A total of 27 tests were performed at an average VFD frequency of 30 Hz. The test configurations are given in Appendix B.8. Three of the 27 tests were repeated configurations to determine the repeatability of the velocity profile in response to the fan settings.

To determine the scalability of the fan settings to reach the same relative velocity profile, the fans were set to a base setting across the fans of 40 Hz and 50 Hz. Additionally, based on test 1 and the best uniformity case for the average 30 Hz fan settings, the settings were scaled proportionally to determine the frequencies at averages of 40 Hz and 50 Hz. An

addition test on the 50 Hz average setting scaled the 30 Hz settings by magnitude. These fan frequency settings are given in Appendix B.8.

4.2 LiDAR Verification

To determine its ability to provide sufficient measurements for wake measurements, the ZephIR z150 LiDAR was verified in several methods to ensure the accuracy of measurements. The methods described in Sections 4.2.1 and 4.2.2 were to verify the LiDAR was performing accurately under normal operations and to ensure the reliability of measurements after modifications that were completed to be able to use the LiDAR in further wake measurement experiments.

4.2.1 Comparison to Cup and Vane Anemometer

To verify the performance of the LiDAR under normal operations, it was decided to compare the LiDAR's velocity and wind direction measurements against a cup and vane anemometer equipped on the University of Waterloo Wind Energy Group's Wenvor turbine. The Wenvor turbine was equipped with a vane and a cup anemometer attached to the tower. The heights of the anemometers from ground level are 20 m and 10 m respectively. The LiDAR was used to measure the wind velocity at the heights of the anemometers next to the wind turbine tower to compare the wind speeds and direction. The cup anemometer was used to measure the wind speed and the vane anemometer was used to measure the direction of the wind.

The LiDAR is able to measure 5 different heights for a single run. Due to the limitation of the LiDAR, the minimum measurable ground height is 12 m. In addition to measuring the wind speeds at the heights of the anemometers, the LiDAR was also used to measure the wind speeds at the hub height of the turbine as well as the maximum and minimum heights of the blade sweep. This amounts to the heights and corresponding reference on the turbine shown in Table 4.5.

The conical movement of the laser has an angle of 30.6°. Therefore, at a measurement height of 30 m the minimum distance away from the turbine is 18 m to avoid interference of the turbine tower. Figure 4.1 shows the setup of the LiDAR measurements and anemometers on the Wenvor turbine tower.

To setup the LiDAR properly, the body was aligned to true north using a compass adjusted for the declination angle of -9.6° [49] to get an accurate direction reference. The

Table 4.5: LiDAR measurement heights

Measurement Height	Turbine Reference
36 m	Blade maximum position
31 m	Hub height
26 m	Blade minimum position
20 m	Vane anemometer
12 m	Cup anemometer (actual 10 m)

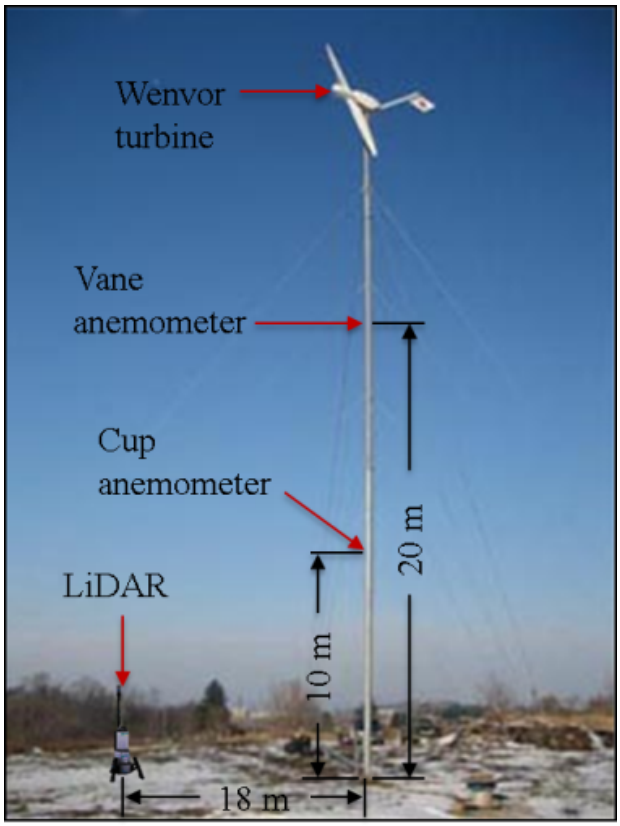

Figure 4.1: LiDAR and anemometer verification setup

base was leveled to ensure accuracy of the velocity components in the measurements. The LiDAR was positioned approximately upstream of the Wenvor wind turbine with a similar relative distance to the tree line of an adjacent forest to ensure similar wind effects from the landscape. The LiDAR position was chosen to keep a constant elevation relative to

the wind turbine base. Figure 4.2 shows the positioning of the LiDAR in relation to the Wenvor turbine and surrounding landscape.

Figure 4.2: LiDAR position and surrounding landscape [33]

Measurement data was taken for approximately 1 hour during a period of high wind speeds for the area using the LiDAR and anemometers. The LiDAR collects data approximately every 20 seconds for all measurement heights, while the anemometers give 10 minute averages of 1 second data [60].

4.2.2 Laser Position and Measurement Verification

The LiDAR was modified to allow for a straight line-of-sight laser position in place of the default conical laser pattern. The line-of-sight configuration will be used for later wake profile measurements to position the laser at precise locations. To achieve the desired line-of-sight laser position, the rotating prism lens in the optical pod was removed. Details of the modifications can be found in Appendix E. Removing the lens therefore changes the measurement distance of the LiDAR based on the angle of the deflection. Therefore, the actual measurement distance, H_m, is calculated as is in Eq. 4.1, where H is the focal point distance from the LiDAR with the conical laser configuration.

$$H_m = H \cos(30.6°) \tag{4.1}$$

Before using the LiDAR with the line-of-sight laser measurement in experiments, the measurement location was first verified in order to properly position the LiDAR for the desired measurement points in the experiment. This was done in two steps, the first to locate the laser position, and the second to determine the measurement location.

The LiDAR laser operates in the infrared spectrum, with a wave length of 1575 nm. Therefore, the laser is not visible to the eye, creating challenges in locating and aligning the laser position. To locate the position of the laser, a power meter was used, which shows a power increase on the display when the laser is directed at the detection area. The laser has a power of 1 W, which will be registered by the power meter if the laser is aligned with the power meter location. This process was performed inside a laboratory by orientating the LiDAR in a horizontal position and directing the laser at the power meter. Due to space constraints and the minimum LiDAR focal distance of 11.6 m, a mirror was used inside of the laboratory in order to position the power meter beyond the 11.6 m mark. The setup of the LiDAR in the laboratory is shown in Figure 4.3.

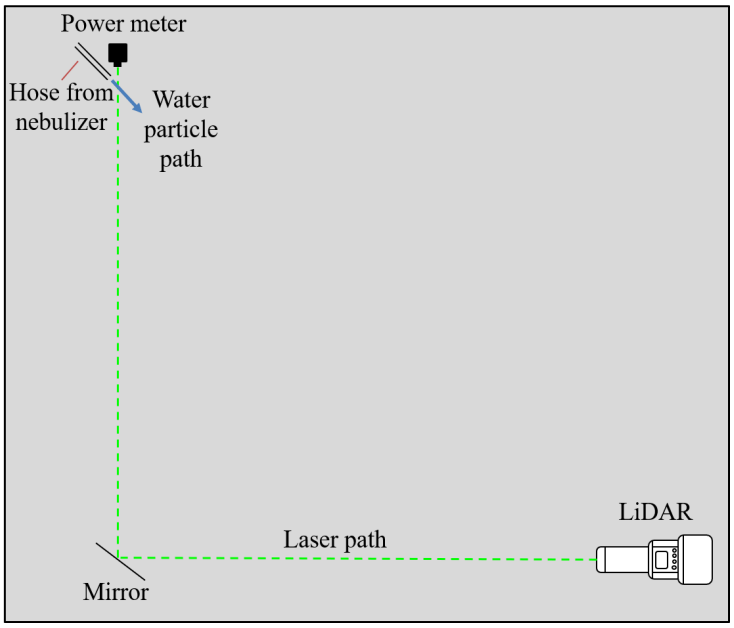

Figure 4.3: Setup of the LiDAR laboratory verification

Once the laser location was determined, the measurement location where the laser is

focused was determined by adding water particles to an area of the flow with a nebulizer. The LiDAR would then be able to measure the particle speed from the Doppler technique in the laser beam convergence area. Therefore, the position where measurements are read is the measurement location. A hose attached to the nebulized directed the water particles in front of the power meter. As to not have the hose in the path of the laser, the hose was offset to the side and directed the particles at an angle towards the laser location while allowing the particles to have a velocity component in the line-of-sight direction of the laser path. The direction of the particles in front of the power meter can be seen in Figure 4.4.

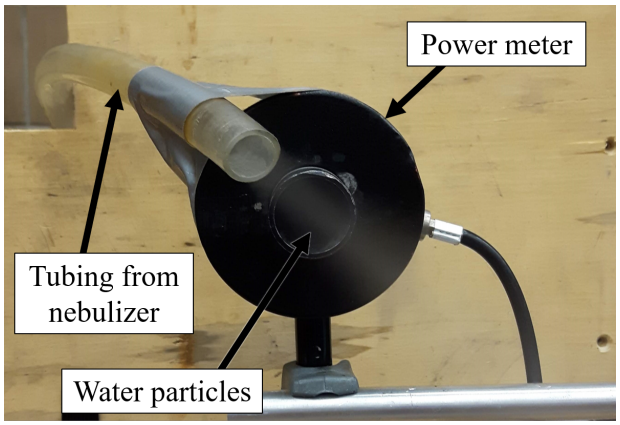

Figure 4.4: Water particles from the nebulizer directed in front of the power meter

After the LiDAR verification tests in the laboratory with the power meter and nebulizer, it was relocated to the Wind Generation Facility to test under wind conditions. In addition, the LiDAR was compared with the sonic anemometer. The LiDAR was aligned to position the laser through the sonic anemometer detection space at 12.77 m, the equivalent of the LiDAR's 11 m height setting. The position of the LiDAR laser in the sonic anemometer detection space was verified with the power meter as seen in Figure 4.5.

The test was performed at 2 wind speeds of approximately 8.4 m/s and 9.6 m/s to match the wind speeds that will be used in the wake measurement experiments. Measurements were taken at the same time for both the sonic anemometer and the LiDAR and results compared to each other.

Once the verification process was completed, a visible laser was installed on the LiDAR, level with the LiDAR laser and at 10 cm above the actual LiDAR laser location. The visible laser was used to align the laser in future experiments to eliminate the need to align the laser with the power meter.

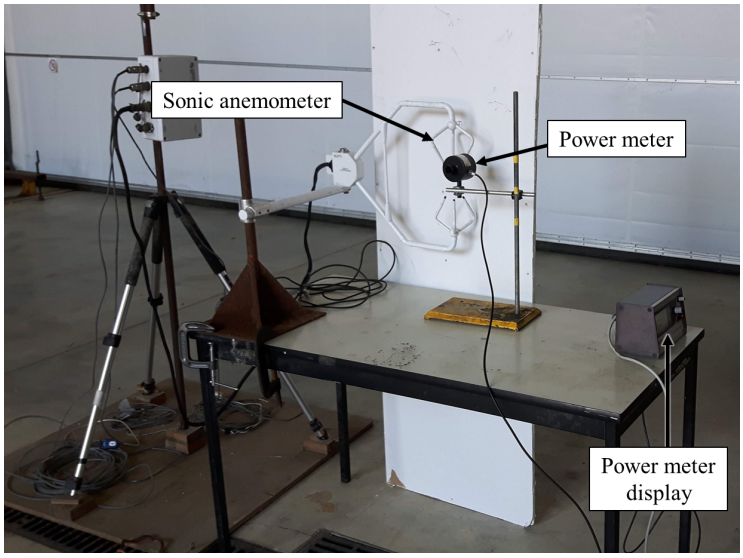

Figure 4.5: Power meter positioned to align the LiDAR laser inside the sonic anemometer measurement area

4.3 Wake Flow Visualization

Flow visualization techniques are used to gain a practical understanding of the wake of a wind turbine. Two techniques can be performed to visualize the wake characteristics of wind turbines [73]. The first technique emits smoke upstream of the turbine, directed in the path of the blade tip. The blade tip passes through the stream of smoke, showing the tip vortices being formed and propagating downstream. The second technique ignites smoke on the blade of the turbine. With this method, characteristics such as the helical wake formation and wake expansion can be seen.

Both techniques were explored to visualize the behaviour of the UW WEG turbine wake inside the Wind Generation Facility. The setup of the upstream smoke ignition is described in Section 4.3.1, and the blade ignited smoke visualization is described in Section 4.3.2.

4.3.1 Upstream Smoke Ignition

Smoke for the upstream smoke ignition experiment was produced using an Enola Gaye EG18 smoke emitter, which produces 60,000 cubic feet of smoke in 90-100 seconds [30].

The experiment used a yellow smoke emitter ignited upstream of the UW WEG wind turbine inside the Wind Generation Facility test area, directed at the blade tip. A DSLR camera pointed at the path of the smoke and blade rotation was used to capture the vortices being shed with each blade pass. The sonic anemometer was placed in the flow to get a measurement of the incoming velocity during the experiment. The experiment was performed at an upstream wind speed of 6 m/s and a blade rotational speed of 100 RPM, which resulted in a tip speed ratio, λ, of 2.9. This experiment was only performed at a yaw angle of 0°. A setup of the experiment is shown in Figure 4.6 and a picture of the smoke emitter producing smoke upstream of the UW WEG turbine is shown in Figure 4.7.

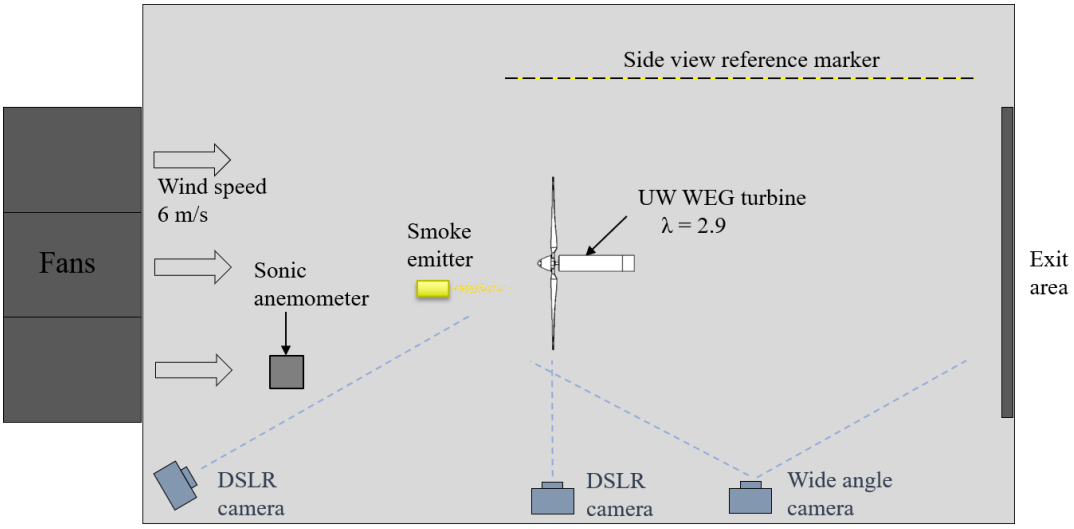

Figure 4.6: Upstream smoke ignition visualization experiment setup

4.3.2 Blade Ignited Smoke

Initial experiments using the second blade ignited technique were performed with one smoke emitter attached to the end of the UW WEG turbine blade. The tip speed ratio and speeds were set the same as the upstream smoke ignition experiment. After the experiments it was determined that a better visualization could be obtained with a smoke emitter on each of the three blades of the turbine with different colours to better see the interaction between blades. In addition, having the smoke emitters on the tips of the blade disturbed the aerodynamics of the blade and created turbulence from the flow moving around the smoke emitter body. Therefore, it was determined that having the smoke emitters located at the

Figure 4.7: Single colour smoke visualization experiment setup

hub of the turbine with tubing directing the smoke to each blade of the turbine would provide better results. Details of these initial experiments can be found in Appendix C.

For the multi-blade ignited smoke experiment, the smoke was housed at the hub of the turbine with tubing running down to the blade tip to eliminate the back flow that occurred around the smoke emitter during the initial smoke experiment. This method allowed a more concentrated and smooth smoke stream. The smoke emitters were ignited remotely as to ignite all three emitters simultaneously. More details of the smoke emitters, configuration, and the instrumentation for the remote ignition are described in Section 4.3.2. The smoke colours were chosen as blue, yellow, and red to distinguish the colours from each other and the background of the test facility.

The experiment was designed to run at the UW WEG turbine tip speed ratio of 4.0 used by Gallant [28]. The incoming velocity profile was measured with the Pitot Tree as described in Section 4.1 before performing the experiment. With the wind speed set to an average of 5 m/s, the rotational speed of the turbine was set to 125 RPM to obtain an approximate desired design tip speed ratio, which actually resulted in a tip speed

ratio of 4.3. Although the wind speed is typically seen as low, it was set in order to properly visualize the smoke traveling downstream and prevent turbulence from dispelling the smoke. In addition, the experiment was performed at yaw angles of 0° and -30° to visualize the differences in flow in varying yaw angles of the turbine.

Cameras were set to get a picture of the flow as seen from a frontal view, back view, crosswise view, top view, and wide angle side view. The frontal and back views were located at the hub height of the turbine and faced downstream and upstream respectively. Reference markers were placed at the side of the turbine and on the ground to obtain quantitative measurements from the photos. The reference markers show a 10 cm measurement resolution. Therefore, the error in quantitative measurements in the x and z-direction is ±5 cm. The experimental setup with the reference markers and camera setup are shown in Figure 4.8.

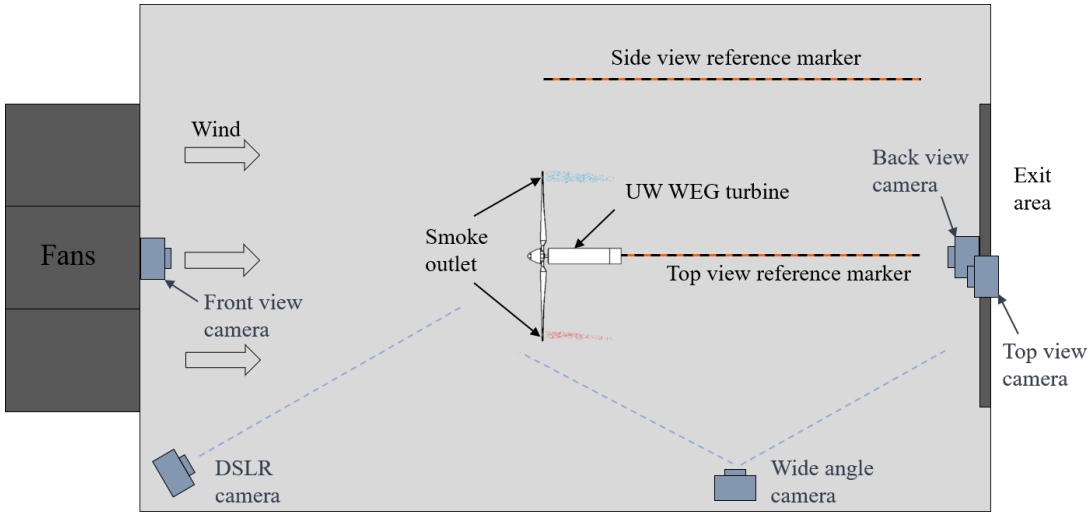

Figure 4.8: Multi-colour smoke visualization experiment setup

The reference markers were positioned directly behind the turbine in horizonal and various vertical arrangements in initial pictures to provide a reference in the area of the smoke path. The setup of a horizontal reference behind the turbine is shown in Figure 4.9. The Pitot Tree is also seen in the picture in the position to determine the initial velocity profile in front of the turbine.

After the experiment was conducted with the smoke emitters located at the turbine hub, an additional experiment under the same wind conditions was performed with the smoke emitter located at the tip of the blade similar to the initial single-colour experiment

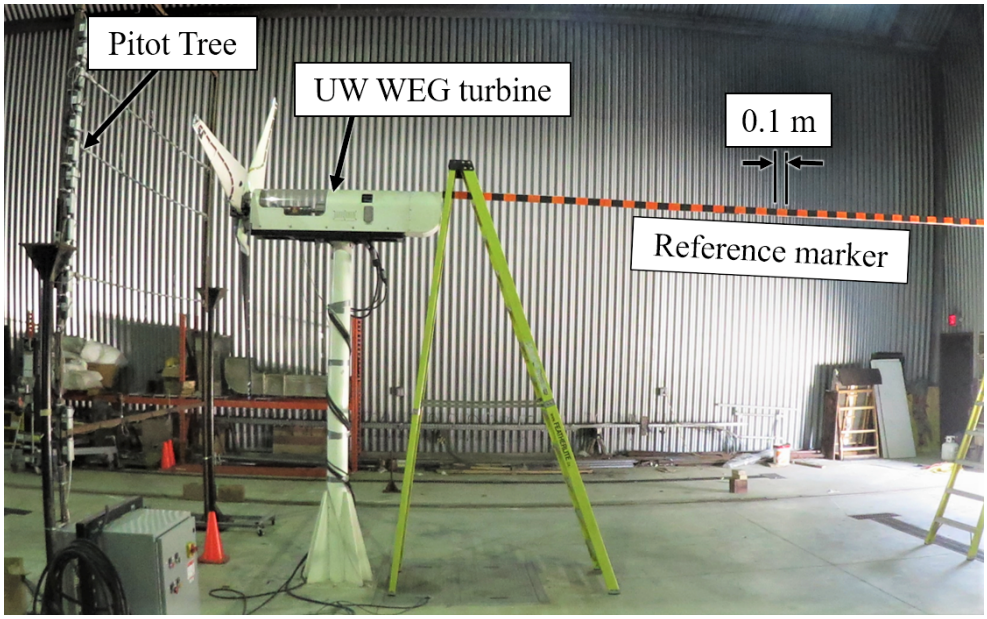

Figure 4.9: Initial horizontal reference marker placement for the multi-colour smoke visualization experiment

with the turbine at a yaw angle of -30°. Due to ignition complications, the blue smoke emitter was ignited separately from the yellow and red smoke emitters.

The load power was recorded with the turbine off and in operation to determine the effect of the tubing and ignition wires on the performance of the turbine. Load power readings from the turbine controller sub-panel were recorded at a yaw angle of -30° with the various ignition setups. The readings are shown in Table 4.6, for a bare blade, silicone tubing attached to the blade during the hub located smoke emitter experiments, and a wire running down the blade during the tip located smoke experiments. The results from the power readings showed that the introduction of the tubing on the turbine blade greatly affected the aerodynamics and power production, which may impact of the results of the visualization. Adding a wire to the blade, however, did not have much of an effect on the load power.

Instrumentation

Smoke for the visualization experiment was produced using Enola Gaye WP40 smoke emitters. The emitters have the capability to produce 20,000 cubic feet of smoke for 100-

Table 4.6: Load power readings at a yaw angle of -30°

Setup	Power
Normal operation	0.3 kW
Tubing	0.08 kW
Wire	0.28 kW

120 seconds [30]. Multiple colours were used to distinguish the smoke from the test area background and between several emitters being used at once.

For the blade ignited smoke technique, it was decided to ignite three smoke emitters of different colours simultaneously for each blade. In order to achieve this, the smoke emitters were to ignite simultaneously using a remote ignition system. That way the smoke emitters can be ignited while the wind conditions are set and the wind turbine is in operation. The ignition system used nichrome wire to ignite the fuse on the smoke emitters by generating heat through resistance in the wire with electricity using a 12 V battery. The batteries and nichrome ignition were connected to a remote relay to ignite the fuse with a remote. All three nichrome ignition wires were connected to a single relay to ensure all smoke emitters ignite simultaneously. The single relay to ignite the smoke emitter was then connected to another relay as a safety precaution as to not ignite the smoke emitters prematurely. The circuit diagram of the system is shown in Figure 4.10.

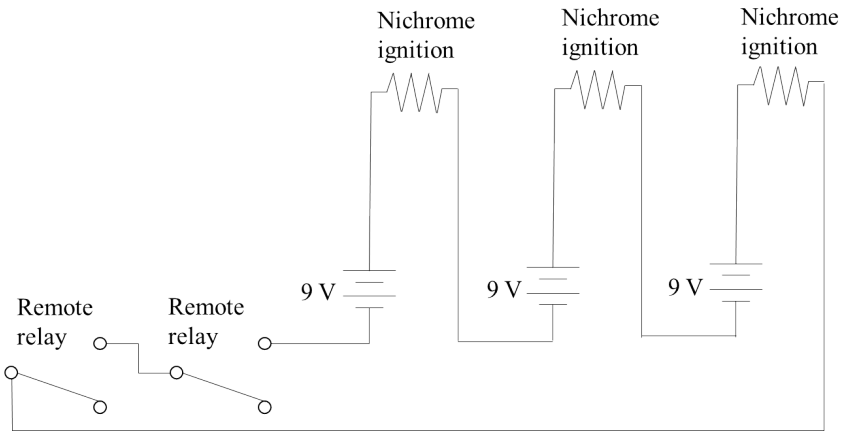

Figure 4.10: Circuit diagram for smoke emitter remote relay nichrome ignition

To be able to transfer the smoke from the emitter located at the hub of the turbine to the blade tips, a smoke housing was designed to prevent leakage from occurring. The

smoke housing is shown in Figure 4.11 along with the electrical housing, which contains the relay and batteries. The relay connects the batteries to the nichrome ignitions inside each of the smoke housings. The smoke housing used exhaust piping and silicone caulking to seal the smoke and withstand the temperature of the smoke emitter. When ignited, the smoke emitter has a maximum temperature of 130°C at the outlet [30]. The smoke housing released the smoke through a nozzle to high temperature silicone tubing, which then ran down the blade of the turbine to release the smoke at the tip of the blade. The silicone tubing was rated for 260°C.

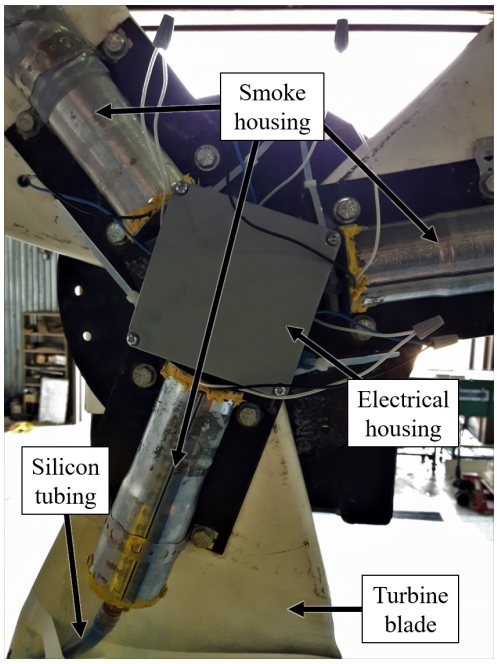

Figure 4.11: Smoke emitter housing and remote ignition configuration on the UW WEG turbine

4.4 Wake Measurements

Experiments inside of the Wind Generation Facility were performed using three different methods to measure the wake of the UW WEG turbine. These methods include placement of the Pitot Tree at various downstream locations described in Section 4.4.1, crosswind traverse measurements using a sonic anemometer described in Section 4.4.2, and LiDAR

scans described in Section 4.4.3. Each method provides different results of the wake while allowing a comparison of each method for validation.

The experiments for each method were conducted to measure the wake behaviour under several conditions. The tip speed ratio, λ, of the turbine was desired to be set at tip speed ratios of 3.5 and 4.0 as in the experiments of Gallant [28]. The additional tip speed ratio would provide information for higher relative wind speeds. The tip speed ratio was obtained by setting the UW WEG turbine to a constant rotational speed of 200 RPM and adjusting the fan speed inside the facility to get the desired tip speed ratio. In additional to looking at the change of the wake with the turbine tip speed, it was also determined to look at the behaviour of the wake with different yaw angles. Yaw angles, γ, of 0° and -30° were used to measure the wake in un-yawed and yawed cases respectively. In the wake experiments with the LiDAR, a yaw angle of 30° was used. Figure 3.5 depicts the yaw angle of the UW WEG turbine in relation to the incoming wind direction.

4.4.1 Pitot Tree Structure Measurements

Using the Pitot Tree developed in Section 3.2, initial wake measurements were obtained to gain an understanding of the flow. The Pitot Tree was positioned 1 m upstream of the UW WEG turbine to obtain desired wind speeds inside the Wind Generation Facility and determine initial incoming flow measurements. The incoming flow measurements using the Pitot Tree were used to obtain upstream wind velocities and turbulence for each tip speed ratio to be used for the other measurement methods in Sections 4.4.2 and 4.4.3.

Measurements were taken by positioning the Pitot Tree at downstream positions, x/D, of 0.75, 1, 1.5, 2, 2.25, 3, and 4 at a yaw angle of 0°. To move the Pitot Tree to each downstream position, the facility fans needed to be shutdown. Therefore, while the Pitot Tree was set to each position, the facility wind speed was set to the configuration to generate approximately the desired tip speed ratios of 4.2 and 3.5.

The closest position, at a rotor diameter distance, D, of 0.75 downstream, was determined to gain a profile close to the turbine. Since the back of the nacelle extends to approximately 0.6 D, the first position was chosen to measure close to the nacelle while allowing some flow to develop. The next measurements of 1 D, 1.5 D, and 2 D were determined to measure the wake at enough positions to get an understanding of the development while limiting the number of measurements taken. The next position of 2.25 D was chosen due to a research structure, called the Steiner Tunnel, that was located in the Wind Generation Facility test area blocked the positioning of the Pitot Tree at 2.5 D. Therefore the next obtainable positions were at 2.25 D and 3 D. Figure 4.12 shows the

Steiner Tunnel position relatively to the Pitot Tree. The position of 3 D is at the exit of the facility, therefore the position at 4 D was chosen to determine whether measurements outside of the facility are useful.

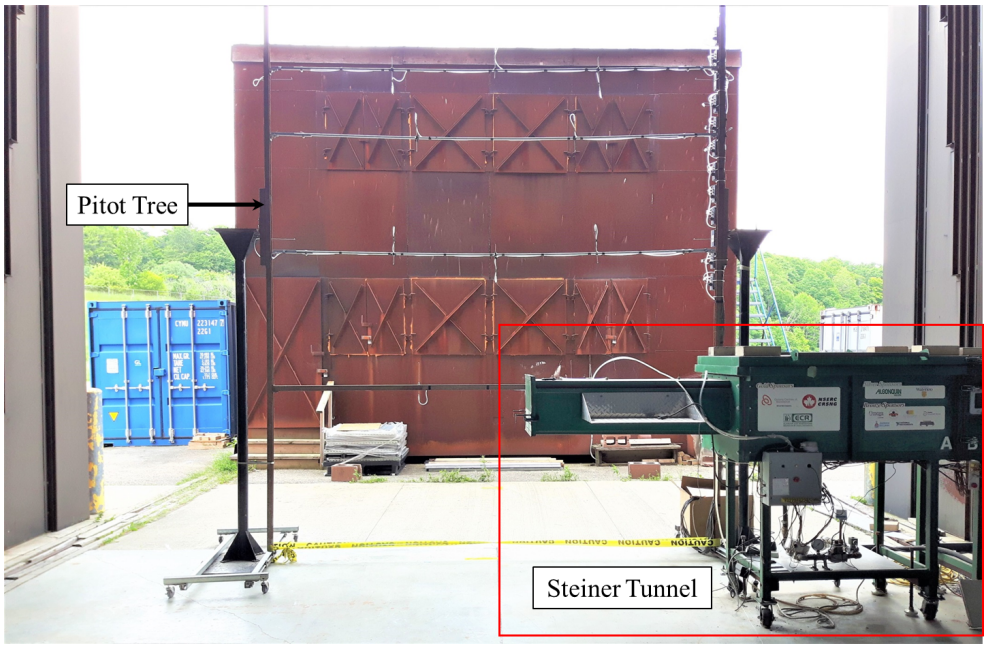

Figure 4.12: Steiner Tunnel relative to the Pitot Tree at 3 D

Once the initial testing was completed, it was determined necessary to only look at downstream positions at x/D of 1, 2, and 3 for further Pitot Tree measurements and following sonic anemometer experiments. Therefore, the experiment was repeated at a yaw angle of -30° with the Pitot Tree at the aforementioned positions while adjusting the facility fans to produce tip speed ratios of 4.2 and 3.5. Figure 4.13 shows the Pitot Tree during the experiment with the UW WEG turbine at a yaw angle of -30°. Data was collected for 60 seconds at a sample rate of 1000 Hz.

4.4.2 Sonic Anemometer Traverse

Experiments using the sonic anemometer, described in Section 3.3, were conducted by traversing the device across the wake. This was completed by setting the height of the sonic anemometer to the hub height of UW WEG turbine and positioning the sonic anemometer

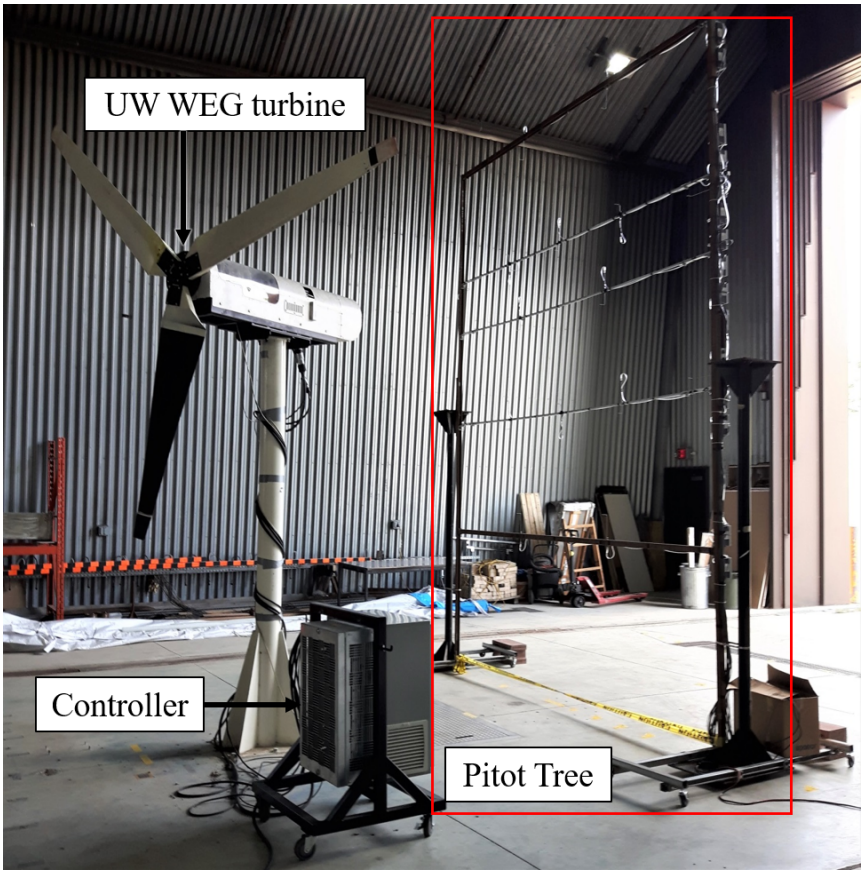

Figure 4.13: Pitot Tree positioned behind the yawed UW WEG turbine during the wake measurement experiments

at various positions in the crosswind direction along a certain rotor diameter distance downstream of the turbine.

Since the initial experiments with the Pitot Tree did not capture the ends of the wake where it recovered to free stream velocities due to expansion of the wake, an initial traverse was completed with the sonic anemometer to determine at which point the flow recovered to free stream values and where the minimum velocity occurs. The minimum velocity is the point of the wake centre which is a characteristic of interest, therefore more measurements should be taken in this area to more accurately determine the location. The initial traverse was performed by traversing the sonic anemometer from the centre of the hub outwards. The traverse was conducted at a downstream distance of 2 D and measurement points were concentrated at the centre of the hub and at the ends of the traverse to capture the wake's

key aspects. The measurement points taken for the initial testing are shown in Figure 4.14.

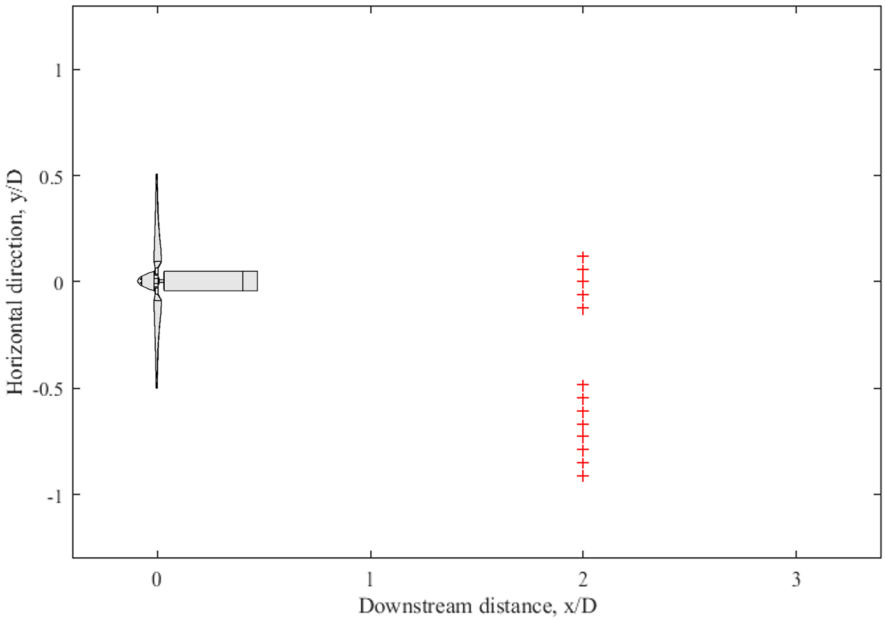

Figure 4.14: Initial sonic anemometer measurement points at hub height behind the UW WEG turbine

With the general wake size known, the traverse distance for the sonic anemometer wake measurements could be determined. Due to space constraints and the development of the wake expansion size, the measurement points at 1 D were limited on the ends. This spacing was determined to place more measurement points at the centre and ends of the wake, while limited the amount of points needed. Therefore, important areas of the wake could be determined.

The experiments were conducted with traverses at downstream distances of 1 D, 2 D, and 3 D as determined from the Pitot Tree measurements in Section 4.4.1. Each traverse was repeated for desired tip speed ratios of 4.0 and 3.5 as well as yaw angles of 0° and -30°. For experiments at a yaw angle of -30°, the position of the measurement points were adjusted due to the change in the hub position, which moved due to the yaw point of the turbine being about the tower attached to the nacelle. The measurement points taken with the sonic anemometer relative to the UW WEG turbine inside the Wind Generation Facility are shown in Figure 4.15.

Measurements were taken for 60 seconds at a sampling rate of 20 Hz for each point.

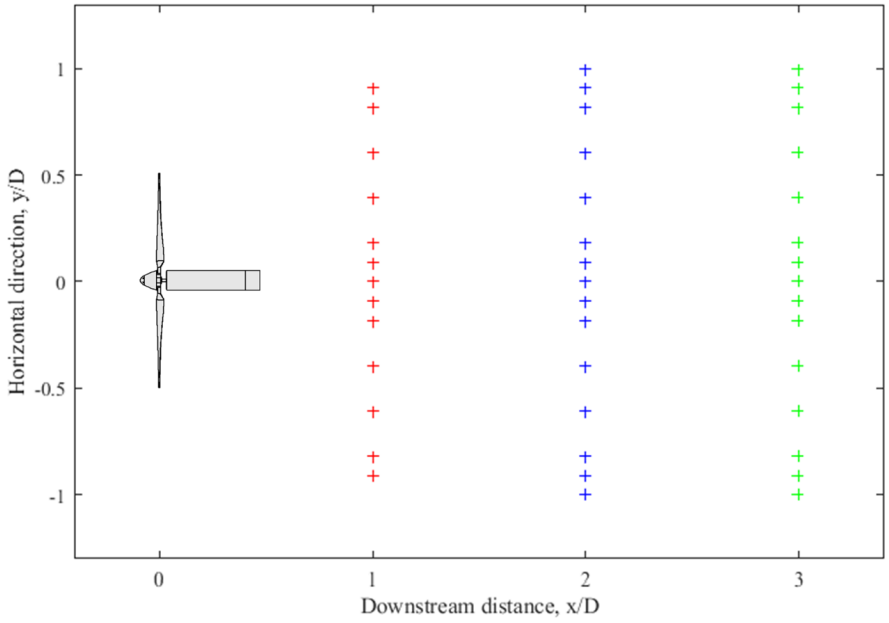

Figure 4.15: Sonic anemometer measurement points at hub height behind the UW WEG turbine

The sonic anemometer positioned behind the UW WEG turbine during the experiments is shown in Figure 4.16.

4.4.3 LiDAR Scans

Using a ZephIR z150 LiDAR, as discussed in Section 3.4, the velocity profile behind the UW WEG turbine inside of the Wind Generation Facility was measured. The LiDAR, directed in the wake of the UW WEG turbine, can gain information about the airspeed of particles in the wake. However, the LiDAR laser has a minimum focal length of 11.6 m. Therefore, special considerations were taken to place the LiDAR is the optimal position to be able to measure as much as the wake as possible.

Due to space limitations inside of the Wind Generation Facility it was decided to place the LiDAR upstream of the UW WEG turbine to the side of the fan outlet as to not block any of the flow as shown in Figure 4.17. The LiDAR was placed on a portable staircase to raise the LiDAR to the approximate hub height of the UW WEG turbine. The LiDAR was placed on its side to have a horizontal laser direction and mounted on a milling rotor

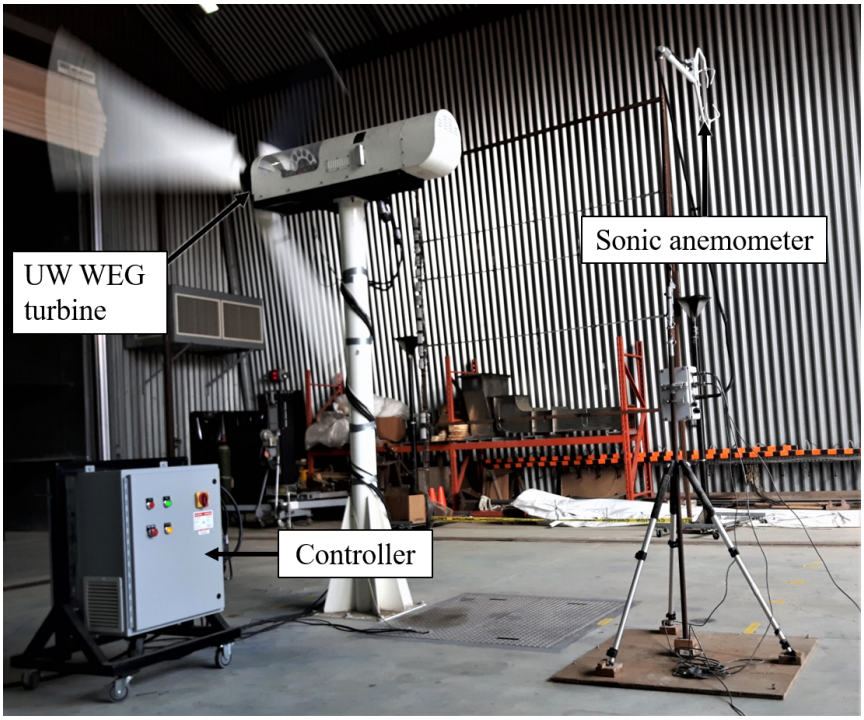

Figure 4.16: Sonic anemometer positioned at a measurement point behind the UW WEG turbine during the wake measurement experiments

platform in order to control the angular position of the LiDAR. The milling rotor platform had an accuracy of $\pm 0.008°$. The milling rotor platform was bolted to the portable staircase to ensure the setup was secure. The setup and relative position of the LiDAR assembly can be seen in Figure 4.18.

The LiDAR was mounted to the milling rotor platform by securing two Unistrut bars to the platform to make a surface for the LiDAR to sit. The bars were positioned to balance the approximate centre of gravity of the LiDAR to be close to the milling rotor platform, but positioned further to the back as a safety precaution to avoid the LiDAR from falling forward off the portable staircase. The LiDAR was then strapped to the assembly and leveled to ensure laser accuracy. The LiDAR mounted to the milling rotor platform can be seen in Figure 4.19. The entire assembly put the LiDAR laser height at 3.6 m, 0.6 m above the hub height. Although the measurements are not perfectly aligned with the turbine hub height, the height difference allowed the laser to pass through the blade swept area to allow for further measurements along the sweep without the hub interfering.

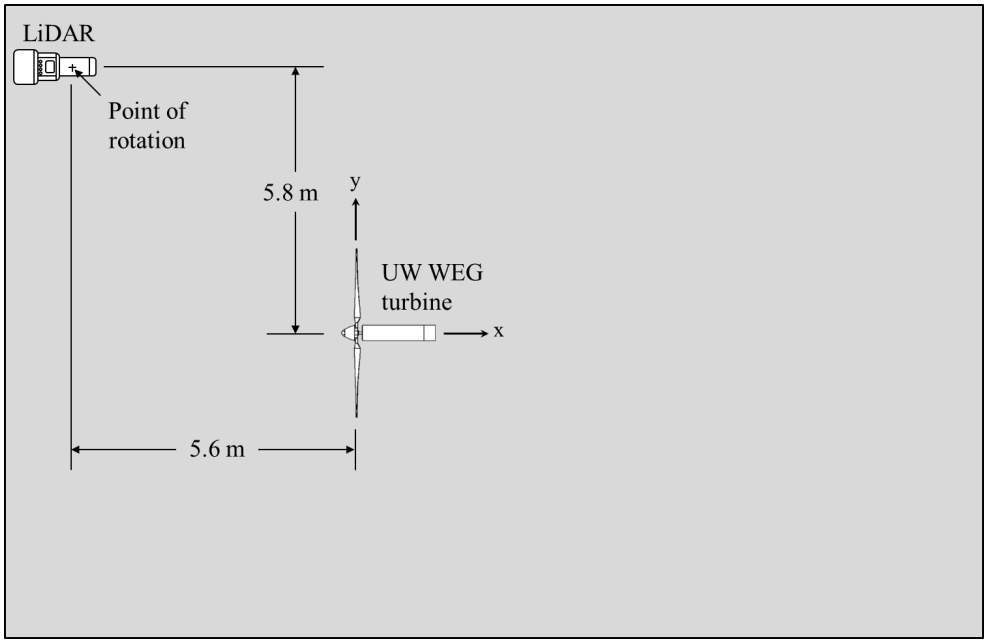

Figure 4.17: LiDAR setup and distance relative to the UW WEG turbine inside the Wind Generation Facility

The laser position was aligned by placing a gridded surface at the laser height, in the desired starting position 11.6 m away from the LiDAR resulting in a position of x/D of 1.74 and y/D of 0.88. The milling rotor platform was then used to align the visible laser, that was mounted on the LiDAR as described in Section 4.2.2, with the starting position mark. An error of ±2.5 cm in the x and y-direction is associated with this alignment.

During the experiment, the LiDAR was configured to measure at distances, H_m, of 11.6 m, 12.8 m, 13.9 m, 15.1 m, 16.2 m, and 17.4 m. At each distance, the milling rotor would be adjusted to position the laser focal point at approximately y/D of 1 and evenly rotated to take approximately 20 measurement points along the sweep until the laser focal position was at approximately y/D of -1. Due to the relation of the actual distance between points and the rotation angle, the spacing of the points, increments of the rotational angle, and number of measurement points varied for each measurement distance, H_m. Increments of 2° were used for the measurement distances of 11.6 m and 12.8 m, increments of 1.5° were used for 13.9 m and 16.2 m, and increments of 1° were used for 16.2 m and 17.4 m. Figure 4.20 shows the data points taken in relation to the UW WEG turbine. The actual data point positions are given in Appendix D.

Figure 4.18: LiDAR position relative to the UW WEG turbine inside the Wind Generation Facility during wake measurements

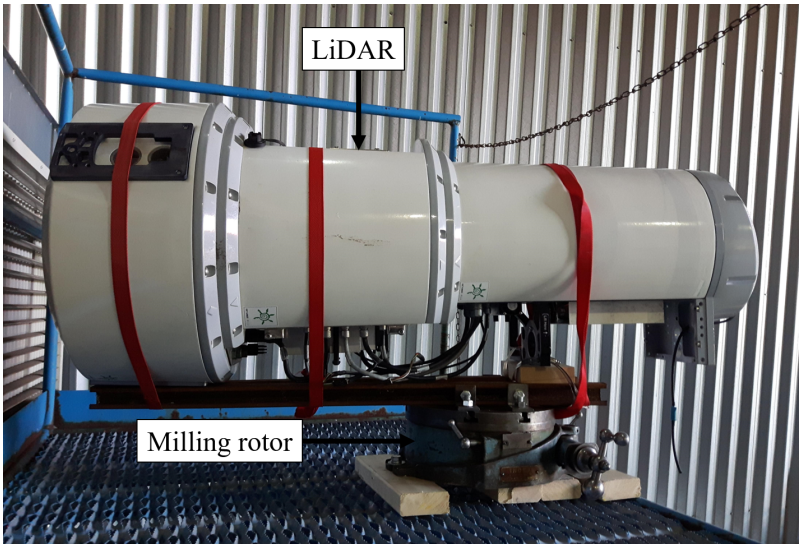

Figure 4.19: LiDAR mounted to the milling rotor platform

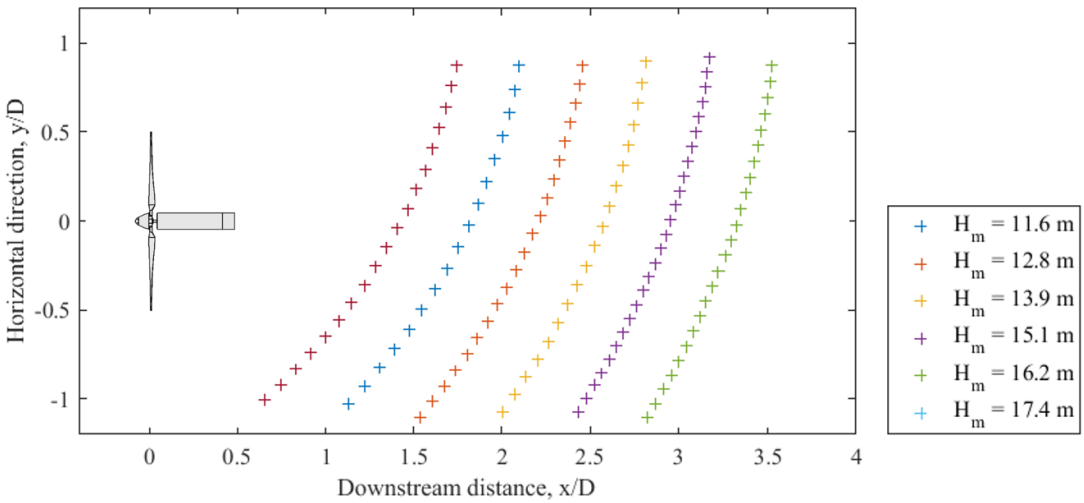

Figure 4.20: LiDAR measurement points behind the UW WEG turbine during the wake experiments

Due to the angle of the laser directed at the incoming flow, the measurements were corrected to assume the velocity of the particles are solely in the x-direction. This was calculated by using the angle of the LiDAR laser for each measurement position to correct the corresponding velocity measurement, as shown in Eq. 4.2, where u is the measurement velocity in the x-direction, v_{LOS} is the velocity measurement in the direction of the laser, and θ_{LOS} is the angle of the LiDAR laser with respect to the incoming flow direction. The correction of the velocity direction is shown in Figure 4.21. This method assumes the largest velocity component is in the x-direction.

$$u = \frac{v_{LOS}}{\cos\left(\theta_{LOS}\right)} \tag{4.2}$$

The turbulence intensity, however, was calculated from the total turbulence seen in the measurements of LiDAR. It was assumed that the turbulence measured by the LiDAR in the direction of the laser represented the total turbulence of the wake. Therefore the turbulence intensity was calculated using Eq. 4.3, where σ_{LOS} is the standard deviation of the velocity from the measurements of the LiDAR.

$$I = \frac{\sigma_{LOS}}{v_{LOS}} \tag{4.3}$$

The experiment was performed for desired tip speed ratios of 4.0 and 3.5. Due to safety

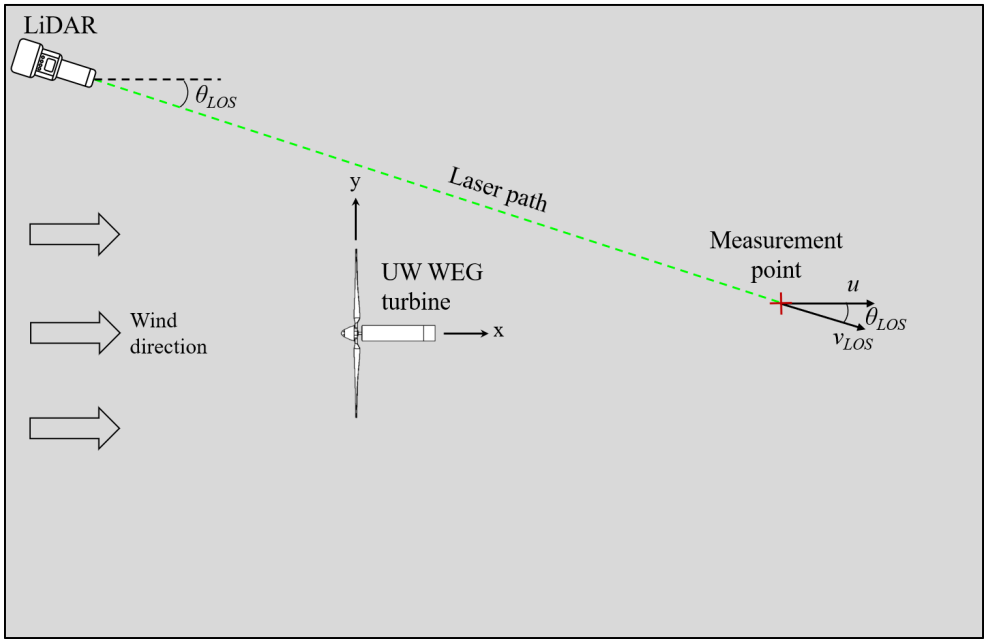

Figure 4.21: Line-of-sight velocity correction for the LiDAR wake measurements behind the UW WEG turbine inside the Wind Generation Facility

conditions to avoid aligning the LiDAR position within the rotation path, the yaw angle of the turbine was set in the opposite direction as the Pitot Tree and sonic anemometer experiments. Therefore, the LiDAR experiments were conducted at yaw angles of 0° and 30°. Each measurement point was taken for at least 20 seconds. The times of each measurement were recorded for later extraction of data by matching with the LiDAR data timestamps.

4.5 Uncertainty Analysis

Uncertainty is associated with measurements and calculations of velocity, turbulence intensity, spatial positioning, air density, tip speed ratio, and thrust coefficient. Uncertainty in velocity, turbulence intensity, and positioning are provided for the Pitot Tree measurements, sonic anemometer, and LiDAR devices, with a summary described in the following sections. The uncertainty analysis calculation for all parameters are provided in Appendix A.2.

4.5.1 Pitot Tree Structure Uncertainty Analysis

The Pitot Tree incorporates the use of pitot tubes in various positions connected to transducers with a central DAQ as described in Section 3.2. Therefore, uncertainty in instrument precision arises from the transducers and DAQ specification. Specification of the transducers are given in Table 3.4. Additional error is created in the calibration of the transducers. The calibration results are shown in Section 3.2.2. Uncertainty associated with the fit of the calibration results is neglected since it is insignificant compared to the calibration.

Random error occurs in the measurements during the experiments. The uncertainty in the random error is taken from a 95% confidence level.

Error is also associated with the orientation of pitot tube positions on the structure, as well as alignment of the Pitot Tree position for the measurement location. Therefore the corresponding position error is ± 0.014 m in the x-direction, ± 0.010 m in the y-direction, and ± 0.011 m in the z-direction.

4.5.2 Sonic Anemometer Uncertainty Analysis

The CSAT3 sonic anemometer has error associated with instrument precision. This is due to an offset error of ± 8 cm/s and resolution of 1 mm/s from Table 3.6.

Again, random error occurs in the measurements of the device, which is also calculated based on a 95% confidence level.

The leveling of the sonic anemometer head has an error of $\pm 0.5^\circ$ in the alignment. An error of ± 1 cm is associated with the position of the sonic anemometer at the measurement point in the x and y-direction. In addition, the measurement height of the sonic anemometer has an error of ± 0.5 cm in the z-direction. Finally, an error of $\pm 5^\circ$ is associated with aligning the device in the direction of the flow.

The sonic anemometer measurements were also non-dimensionlized from measurements taken by the Pitot Tree. Therefore, the Pitot Tree uncertainty is included in the final uncertainty of the sonic anemometer.

4.5.3 LiDAR Uncertainty Analysis

Error in the LiDAR measurements is caused by the laser focal area, laser alignment, and random error.

Random error of the LiDAR measurements is calculated on a 95% confidence interval, similar to the sonic anemometer and Pitot Tree uncertainty analysis.

Error in the measurement position of the LiDAR arises from the laser alignment process. The error in the alignment was found to be ± 2.5 cm in the x and y-direction. An additional position error due to the placement of the LiDAR relative to the turbine adds an extra error of ± 1 cm in the x and y-direction. This translates to a rotation error of $\pm 0.1°$. Uncertainty associated with the rotor angle precision in neglected as it has an accuracy of $\pm 0.008°$, which is insignificant in comparison to the laser alignment. The LiDAR also has an error in the measurement height due to leveling of $\pm 0.5°$ in the z-direction.

In addition, the focal length of the laser depends on the measurement distance. In the case of the measurement heights of this experiment, the maximum focal length was determined to be 0.82 m at the furthest distance from the LiDAR and the minimum was 0.39 m at the closest distance. The maximum width of the laser focal point was 1 mm, which is insignificant in comparison to the focal length.

Similar to the sonic anemometer measurements, the LiDAR measurements were also non-dimensionlized from measurements taken by the Pitot Tree. The Pitot Tree uncertainty is therefore included in the total LiDAR uncertainty.

Chapter 5

Results

This chapter shows the results of the experiments to characterize the flow of the Wind Generation Facility, validate the measurement accuracy of the LiDAR, and wake experiments performed with various measurement devices. The results of the Wind Generation Facility velocity profile characterization in front of the UW WEG turbine are detailed in Section 5.1. Flow visualization results to visualize the wake behind the UW WEG turbine are shown in Section 5.2. The ZephIR LiDAR verification results are given in Section 5.3. Finally, the wake measurement results for experiments performed using the Pitot Tree, sonic anemometer, and LiDAR are given in Section 5.4.

5.1 Wind Characterization Results

The cause of the source of the uneven flow distribution inside the Wind Generation Facility could not be solved by the work done to adjust the dampers, measure the fan blade angles, and measure the individual fan flow rates. The results of the attempts are described in Appendix B. Therefore, it was concluded to measure the flow profile while adjusting the facility fan configurations to attempt to achieve a completely uniform distribution or try to determine a setting to minimize the variation.

5.1.1 Fan Frequency Adjustment

The results of the fan frequency test configuration tests 1 to 4 from the Wind Generation Facility fan frequency adjustment experiment in Section 4.1.1 are shown in Figure 5.1. The

velocity readings for the remaining tests are given in Appendix B.9. The titles of Figure 5.1 include the corresponding standard deviation of all velocity positions, Std, and the difference between the maximum and minimum non-dimensional velocity, Diff. In order to determine the best profile, the standard deviation and difference were minimized while trying to get a visually even distribution of velocities.

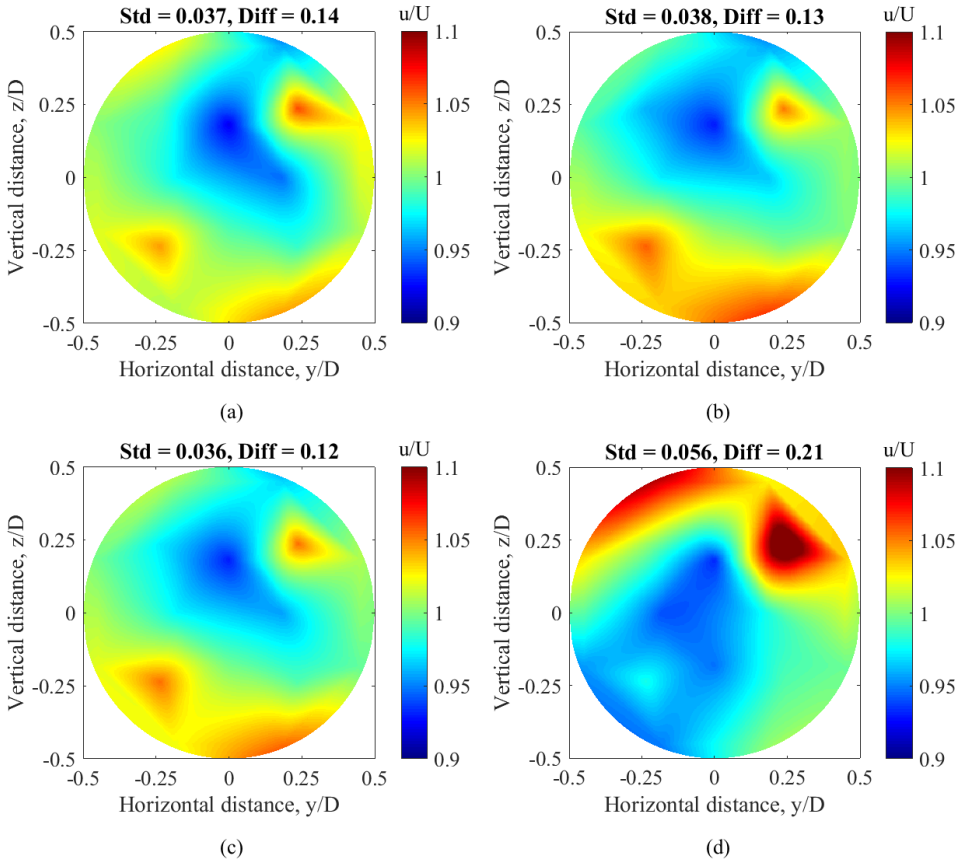

Figure 5.1: Velocity profile at 0.3 D upstream of the UW WEG turbine for (a) Test 1, (b) Test 2, (c) Test 3, and (d) Test 4

It was found that test 25, shown in Table 5.1, resulted in the most uniform flow, although did not perfectly achieve uniformity. The fan frequency setting was derived from test 2, which adjusted for the fan flow rates that had previously shown the best results.

Figure 5.2 shows the resulting velocity profile for test 25, which can be compared against the velocity profiles of the initial tests completed in Figure 5.1 for contrast. It was found

Table 5.1: Test 25 Wind Generation Facility best scenario fan frequency settings with a 30 Hz average

30 Hz	30 Hz	27 Hz
36 Hz	27 Hz	30 Hz

that adjusting the fan frequency on the bottom south resulted in a more uniform flow in the velocity profile of the top north section. The main challenge was to balance the low measurement in the top middle with the high measurement immediately next to it in the top north side. Adjusting the top middle and top north fans only seemed to increase this difference.

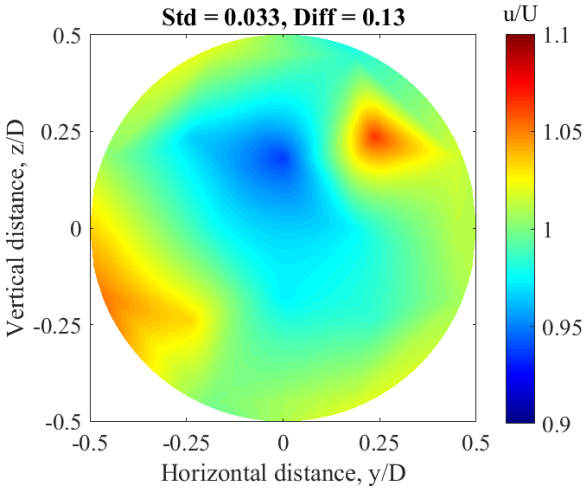

Figure 5.2: Velocity profile at 0.3 D upstream of the UW WEG turbine for Test 25

Uniformity could not be completely achieved, however, therefore future experiments will measure the velocity profile in front of the UW WEG turbine using the Pitot Tree to account for any discrepancies in the data due to the flow profile. Although there was improvement in adjusting the fan frequencies, in comparison to the base case scenario in test 1, the variation is only slight. Therefore, depending on the need for uniformity, it may not be beneficial to divert from the base case fan frequency setting.

Repeatability and Scalability

To determine the repeatability of the tests, three tests were repeated in the morning and afternoon. It was determined that the same velocity profile was able to be repeated with the same fan settings resulting in the confirmation that the tests can be repeated.

The settings of the base case, test 1, and the optimal case, test 25, were scaled to average fan frequency settings of 40 Hz by adjusting the frequencies to be proportional to the average setting. Figure 5.3a and b show the profiles of tests 1 and 25 respectively, which are compared to the scaled results in tests 28 and 32 in Figure 5.4a and b respectively. The results of the scalability tests showed that similar results were able to be achieved by adjusting the frequencies relative to the fan settings.

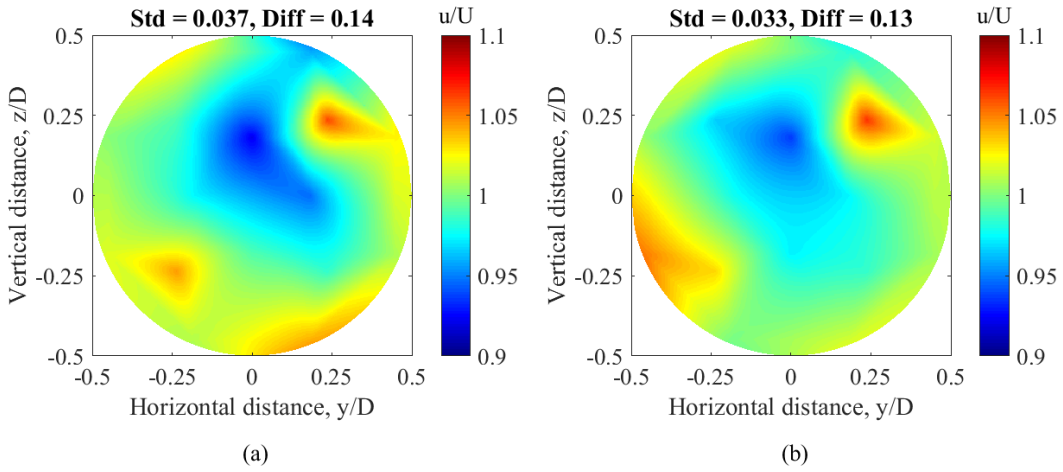

Figure 5.3: Velocity profile at 0.3 D upstream of the UW WEG turbine for (a) Test 1 and (b) Test 25

At an average setting of 50 Hz, it was tested whether adjusting the frequencies according to proportion or magnitude of the differences provided better scaling. Figure 5.5a and b show the scaling based on proportion and magnitude respectively. It was therefore determined that the magnitude of the differences showed better scaling. However, this was not tested for an average setting of 40 Hz and Figure 5.4 only shows the proportional frequency scaling.

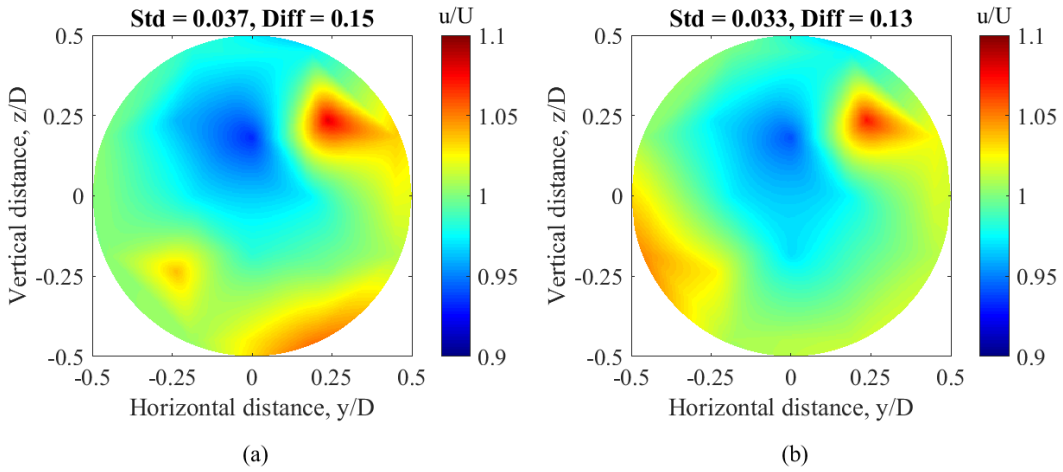

Figure 5.4: Velocity profile at 0.3 D upstream of the UW WEG turbine for (a) Test 28 with a 40 Hz average setting and (b) Test 29 with a 40 Hz average setting

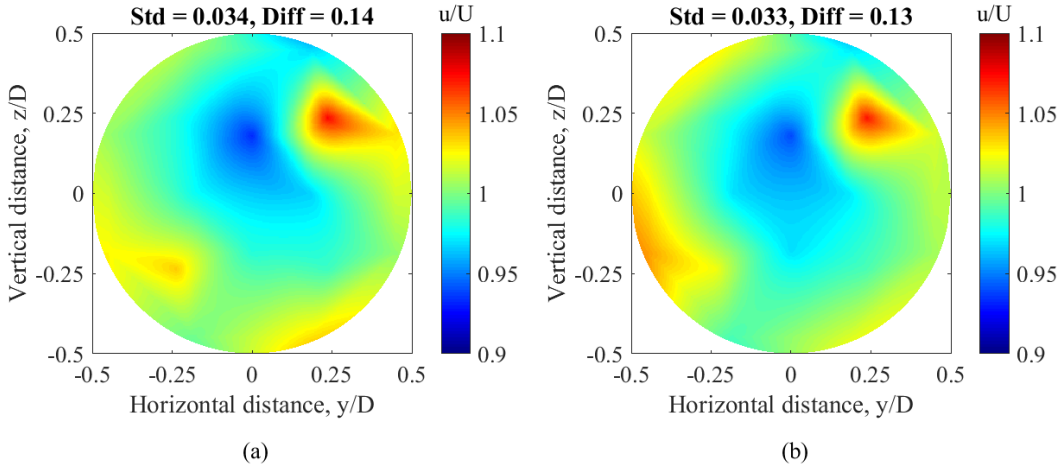

Figure 5.5: Velocity profile at 0.3 D upstream of the UW WEG turbine for (a) Test 30 with a proportional scaled 50 Hz average setting and (b) Test 32 with a magnitude scaled 50 Hz average setting

5.2 Wake Flow Visualization Results

Results of the flow visualization[1] are shown using the two methods described in Section 4.3. The results of the upstream smoke ignition method provided visualization of the tip vortices that shed from the blades of the turbine, shown in Section 5.2.1. The blade ignited smoke technique is described in Section 5.2.2 and shows the helical vortex distribution of the wakes.

5.2.1 Upstream Smoke Ignition

The result of the upstream smoke ignition visualization is shown in Figure 5.6, which was conducted at a tip speed ratio of 2.7 as described in Section 4.3.1. A tip vortex can be seen as the blade passes through the smoke. Another vortex is seen further downstream as it moves with the air flow. The distance between the vortices is related to the helical path of the vortex cylinders.

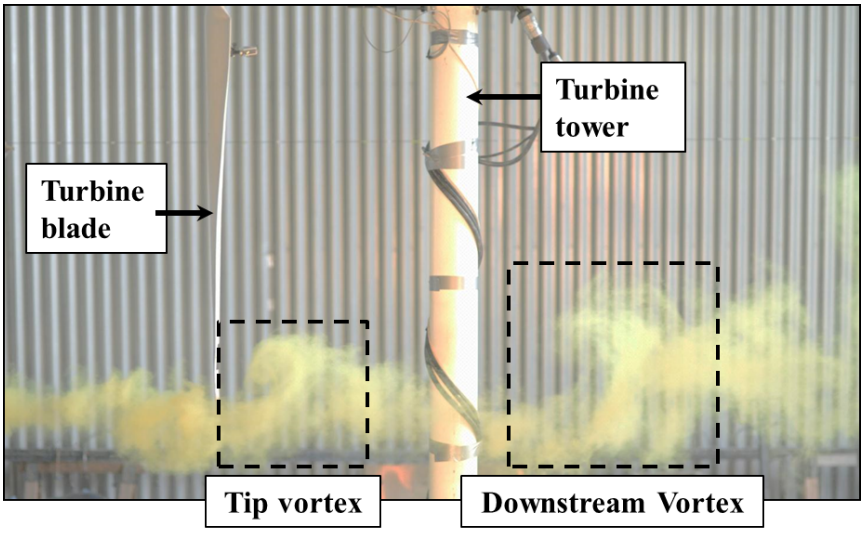

Figure 5.6: Upstream smoke visualization of the UW WEG turbine for $\lambda = 2.9$

Quantitative measurement estimations from Figure 5.6 resulted in a distance between vortices of 0.38 rotor diameters, D. The size of the vortices shown in Figure 5.6 were 0.12 D for the upstream vortex and 0.18 D for the downstream vortex.

[1]Presented at the Canadian Congress of Applied Mechanics in Victoria, Canada, May 31, 2017 [51]

5.2.2 Blade Ignited Smoke

Before starting the experiment, the flow profile in front of the turbine was obtained using the Pitot Tree method described in Section 4.1. The velocity profile and average turbulence intensity for the experiment are shown in Figure 5.7. The profile resulted in an average velocity of 5.0 m/s, desired to attain an approximate tip speed ratio of 4.0, and turbulence intensity of 5.4%.

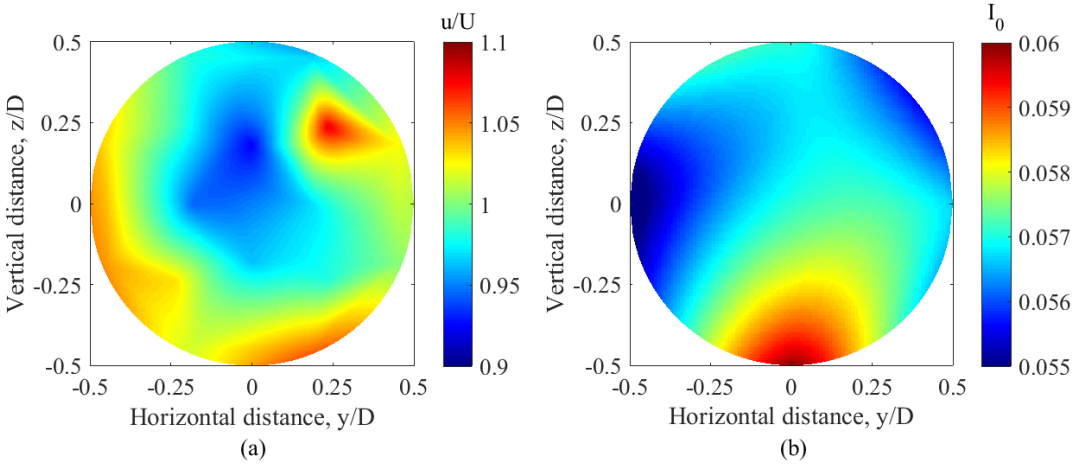

Figure 5.7: Profile of the (a) free stream velocity profile and (b) free stream turbulence intensity upstream of the UW WEG turbine using the Pitot Tree method with $U_0 = 5.0$ m/s and $I_0 = 5.4\%$

During the experiment, complications arose while performing the experiment. Several attempts were made to ignite the smoke simultaneously, however simultaneous ignition was only achieved once for each yaw angle. The experiment was performed during the daylight in partly cloudy weather, which reduced the quality of photos due to lighting. A cloudier day would have been ideal.

Results from the simultaneous ignitions were captured and are depicted in the following figures. Figure 5.8 shows the smoke exiting the outlet of the tubing at the tip of the blade as well as each smoke colour moving downstream in the flow at a yaw angle of 0°. This photo shows the typical helical path due to the vortex cylinders shedding from the tips and following the rotation of the blade.

The wide angle view from the side of the turbine, extracted from video footage, is shown in Figures 5.9 and 5.10 for yaw angles of 0° and -30° respectively. From the side view, the

Figure 5.8: Crosswise view of the blade ignited smoke visualization of the UW WEG turbine for $\lambda = 4.3$ and $\gamma = 0°$

top portion of the helical vortex wake distribution can be seen. The smoke can be best seen when it is travelling close to the same plane of the camera. The -30° yaw angle shows more of a helical formation rather than wave like feature as seen in the 0° yaw angle figure due to the deflection of the wake.

The upstream view, also extracted from video footage, is shown in Figures 5.11 for yaw angles of 0° and -30° respectively. This view shows the difference of the shape of the flow traveling downstream. In the case of the 0° yaw angle, the shape of the flow is nearly perfectly circular, whereas the -30° yaw angle flow has a narrower wake with a oval shape. The change in wake shape with different yaw angles was also seen in the velocity measurements of Bastankhah & Porté-Agel [12]. These shapes change the downstream profile of the wake. The features of the difference between the 0° and -30° yaw angles will be confirmed later during the wake measurement in Section 5.4.

Quantitative results can be analyzed from the photos of the experiment using the reference markers. Using the reference markers it was determined from Figure 5.9 that the angle at which the smoke leaves the blade, known as the helix angle, ϕ, was approximately

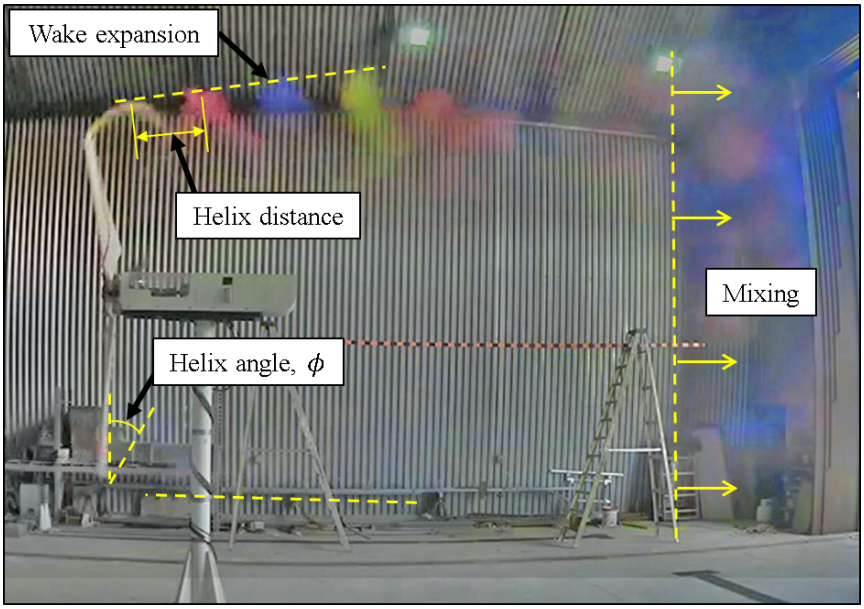

Figure 5.9: Side view of the blade ignited smoke visualization of the UW WEG turbine for $\lambda = 4.3$ and $\gamma = 0°$

30°. It could also be seen from Figure 5.9 that mixing occurred at a downstream distance, x/D, of 1.6. This is a representation of the end of the near wake region, previously shown in Figure 2.9, which is determined when the shear layer, formed due to the interaction between the tip vortices and free stream flow, reaches the centre of the wake [61]. Crespo et al. [23] determined that the end of the near wake occurs between 2 D to 5 D, however this distance is dependant on the incoming turbulence level and thrust coefficient [18]. The helix distance, which is the distance between the vortex cylinders, was estimated to be 0.18 D in both the un-yawed and yawed flow visualization. The wake radius was measured to be 0.64 D, 0.70 D, and 0.82 D at downstream distances of 0.4 D, 1.5 D, and 2.25 D for a yaw angle of 0°. For a yaw angle of -30° the wake radius was estimated to be 0.70 D, 0.73 D, 0.88 D at the same downstream distances.

Blade Ignited Smoke Literature Comparison

The results of the blade ignited smoke measurements in the previous section were compared to the NREL experiments from Hand et al. [35] shown in Section 2.4.1. In both experiments, the helical wake formation is visualized as it moves downstream. Hand et al. was able to achieve a smoother stream of smoke emitting from the blade of the turbine.

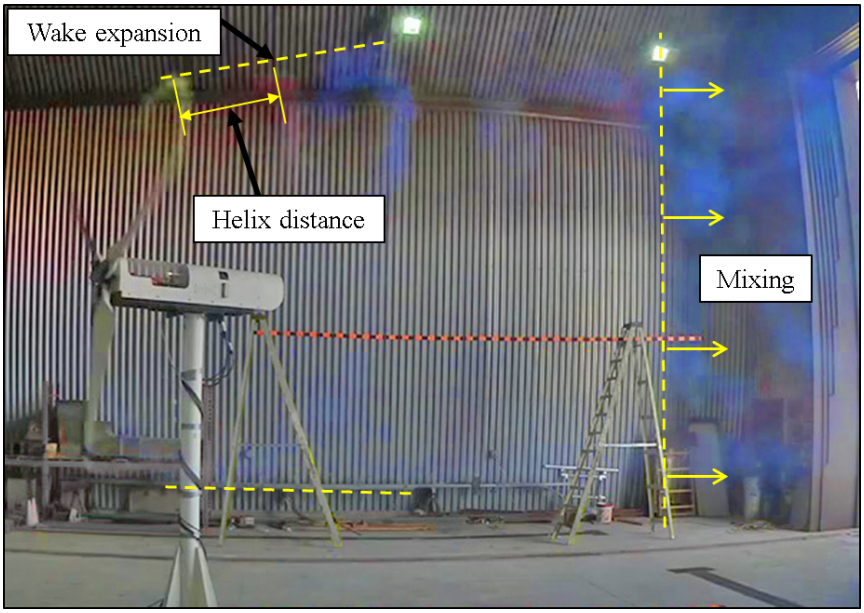

Figure 5.10: Upstream view of the blade ignited smoke visualization of the UW WEG turbine for $\lambda = 4.3$ and $\gamma =$ -30°

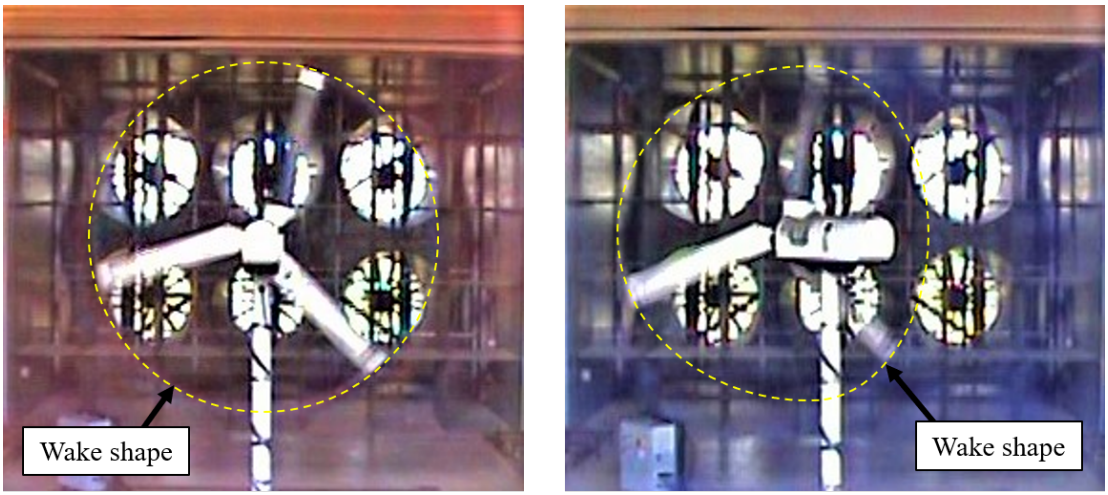

Figure 5.11: Upstream view of the blade ignited smoke visualization of the UW WEG turbine for $\lambda = 4.3$ with (a) $\gamma = 0°$ and (b) $\gamma =$ -30°

This was due to their setup of the smoke emitter, which was embedded in the blade of the turbine. A 1 mm diameter opening in the blade allowed the smoke to escape in a smooth stream [35]. This in combination with a low rotational speed of the turbine at 72 RPM allowed for a smooth visualization of the helical wake formation.

A difference can be noted in the expansion of the wake. Wake expansion cannot be visualized in the Hand et al. experiments, however it is seen in the side view of this study shown in Figure 5.9. During the Hand et al. experiments, the configuration of the turbine was set at low thrust values resulting in a small wake expansion [73]. The experiment was conducted at wind speeds varying from 5 to 15 m/s at a rotational speed of 72 RPM [35]. Therefore, the wake is mainly a result of the rotational motion of the blades and tip vortices.

The Hand et al. experiments for a yawed turbine showed the wake deflection in the direction of the turbine yaw. However, the wake deflection was difficult to see in the photos of this study when the turbine was in the yawed position. This was mainly a result of the lighting in the facility.

5.3 LiDAR Verification Results

Results of the LiDAR verification process are shown in the following sections. The LiDAR was verified for accuracy under normal operations against a cup and vane anemometer, described in Section 5.3.1[2]. The LiDAR was then modified to provide a line-of-sight measurement, detailed in Appendix E, and the accuracy and measurement position were verified with results shown in Section 5.3.2.

5.3.1 Comparison to Cup and Vane Anemometer

A velocity profile was obtained from the average horizontal wind speeds at each measurement height of the LiDAR. The profile is shown in Figure 5.12. A correlation of the data is also shown using the power law and log law. Using the power law equation shown in Eq. 2.26 and the average wind speeds at the heights 12 m and 31 m, the value of the roughness exponent, α_0, was determined. From the log law equation, Eq. 2.27, at the same measurement heights, the roughness length, z_0, was also found.

[2]Presented at the CSME International Congress in Toronto, Canada, May 28, 2018 [50]

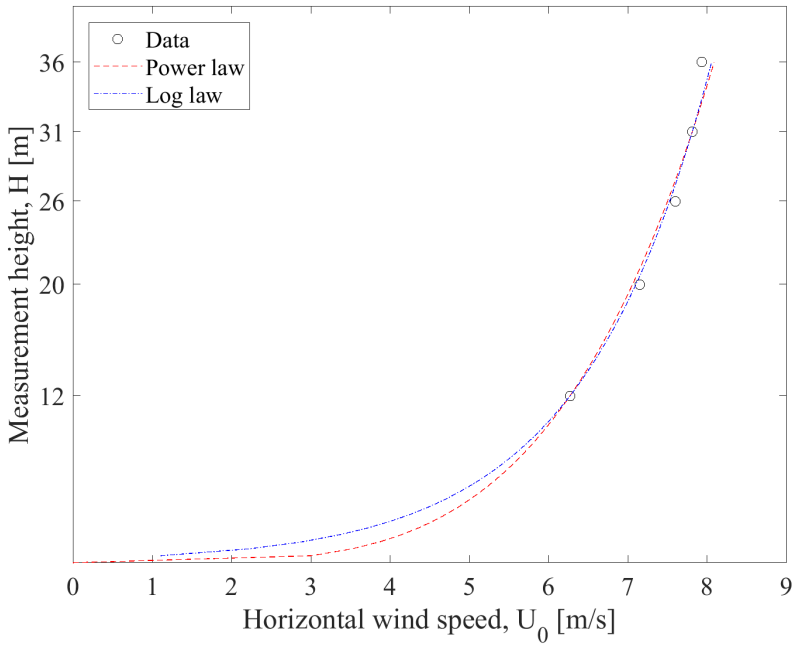

Figure 5.12: 1 hour averaged LiDAR horizontal velocity profile on November 29, 2017

From Figure 4.2, the landscape can be seen to be a grass field with a forest located in the proximity. It can be estimated that the roughness factor, z_0, of the landscape is approximately 0.2 m chosen due to the several trees and bushes in the area [71] and a roughness exponent, α_0, of 0.2 is estimated based on IEC standards for onshore normal wind conditions [20]. In addition, the wind shear was measured by Lam [42] using a meteorological tower in the vicinity. The wind shear was determined by measuring the velocity at heights of 20 m to 50 m using cup anemometers. The LiDAR measured roughness exponents and roughness lengths are shown in Table 5.2 with the values determined by Lam [42] and the estimated values shown for comparison.

Table 5.2: Wind shear data

	LiDAR	Lam measurement [42]	Estimated
Roughness exponent, α_0	0.235	0.35	0.2
Roughness length, z_0 [m]	0.268	1.74	0.2

Compared to the LiDAR wind shear, the value of the roughness length and roughness exponent LiDAR wind shear previously had a difference of 25% and 15% respectively.

However, compared to the roughness determined by Lam, the LIDAR measurements were significantly different. The measurements performed by Lam were over a 2 year period, whereas the LiDAR measurements were only performed for an hour, which is a possible contributor to the significant difference. Additionally, the roughness exponent and length were determined from an average of the wind conditions, which varied in direction throughout the year, whereas the LiDAR measurements had a predominate wind direction from the northwest. Therefore, an increase in the roughness exponent and length could occur when the wind direction is from the northeast, which from Figure 4.2 shows a forested area. A distribution of the roughness exponent was provided by Lam, which showed the variation of the values. From this distribution it was seen that the highest frequency of the roughness exponent resulted in a value of approximately 0.22, which was much closer to the roughness exponent determined from the LiDAR measurements.

The data from the LiDAR measurements seem to follow a similar trend to the power and log law trends, however there are some discrepancies for both methods seen in Figure 5.12. The measured velocity profile shows an expected trend with an increase in wind speeds at higher heights from the shearing effect of the atmospheric boundary layer.

The profiles for the average vertical wind speed and horizontal wind direction are also shown in Figures 5.13 and 5.14. Similar to the horizontal wind speed, the vertical wind speed also increases with increased height. However the difference between the speeds is 0.16 m/s, a negligible difference. This distribution is most likely due to misalignment in leveling the LiDAR, causing it to capture some of the horizontal effects. This is especially evident in the negative wind speeds seen at lower heights. However, the low vertical wind speeds give evidence that the effects of the misalignment of the LiDAR level were negligible.

The results of the horizontal wind direction profile show a small variation of direction between the heights. This is also promising since the wind direction should not change significantly for the heights measured. The direction changed by approximately 18° from each directional extreme. This may be a cause of the timing of the recorded measurements and variability of the wind.

Looking at the LiDAR measurements with time, Figure 5.15 shows the horizontal wind speed. Data is collected approximately every 20 seconds. The heights shown are for the relative positions of the cup anemometer at 10 m, vane anemometer at 20 m, and Wenvor hub height at 31 m. The data shows promising results in the collection abilities of the LiDAR, showing the variability of the wind speed as well as the increase in wind speeds for higher heights.

Similar to the wind speeds, the horizontal wind direction with time is shown in Figure 5.16. The direction shows the same variability of the wind with similar trends between

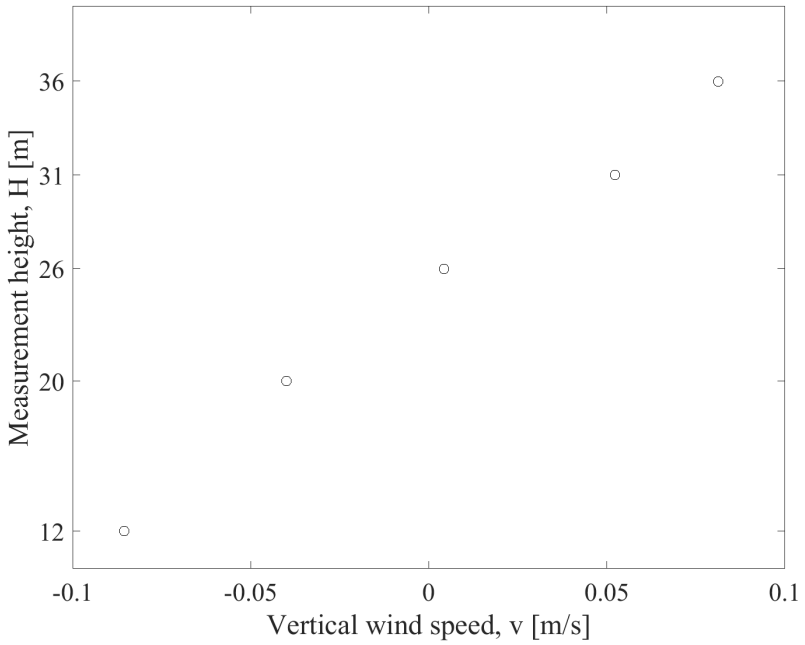

Figure 5.13: 1 hour averaged LiDAR horizontal wind direction profile on November 29, 2017

each measurement height. However, the wind at 12 m had more variability between 12:00 and 12:30, which is a possible result of the land effects in the surrounding terrain.

The LiDAR measurements for 10 minute averages were compared with the data collected from the anemometers of the Wenvor tower. The results are shown in Figures 5.17 and 5.18. Uncertainty calculations in the measurements are detailed in Appendix A.1. The LiDAR measurements were adjusted using the power law from Eq. 2.26 and the calculated total roughness exponent to get the wind speeds at 10 m for a better comparison to the cup anemometer located at 10 m.

It can be seen in Figure 5.17 that the trends of both the LiDAR and cup anemometer data are similar. However, the data shows the LiDAR measurements to have higher speeds than measured by the cup anemometer. This difference, however, could also be a result of scaling the LiDAR measurement data from 12 m to 10 m. An error analysis was performed from the random error of both measurements which are shown by the error bars in Figure 5.17. Comparing the plots with the error bars included, it can be seen that the values are within the error of the measurements. The error in the LiDAR measurements were quite large when converting the data to 10 minute averages, however, due to the 20 second

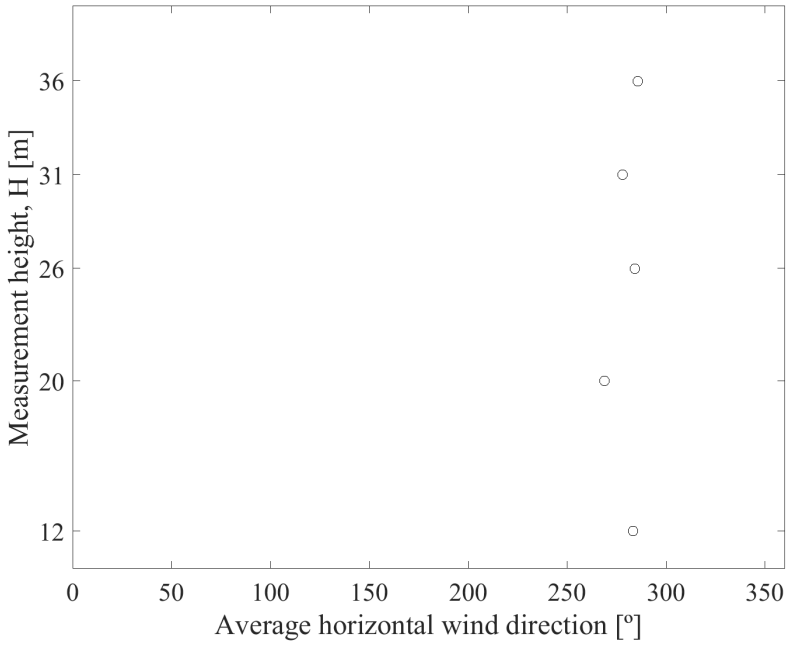

Figure 5.14: 1 hour averaged LiDAR vertical velocity profile on November 29, 2017

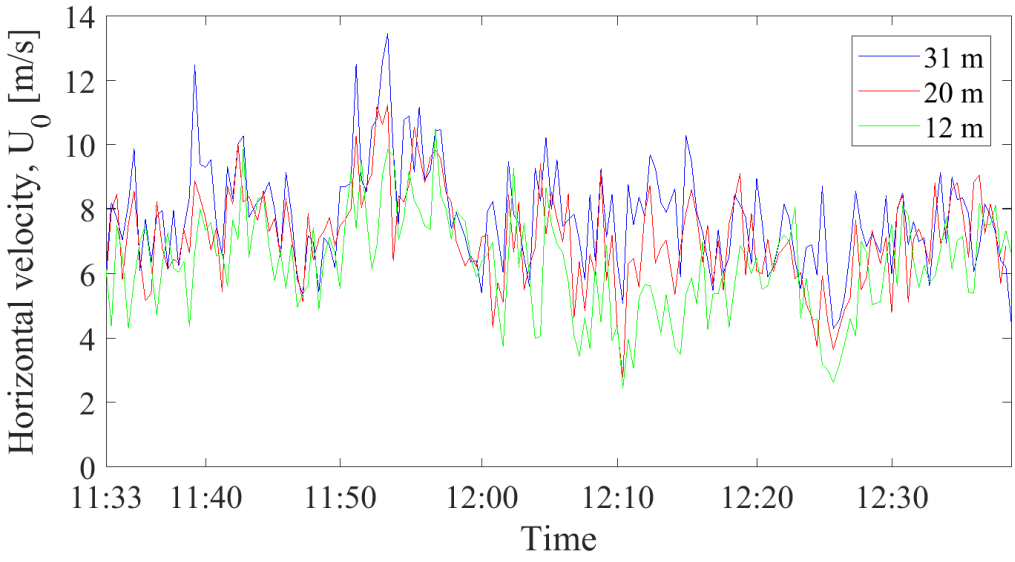

Figure 5.15: LiDAR horizontal velocity, U_0, vs. time on November 29, 2017

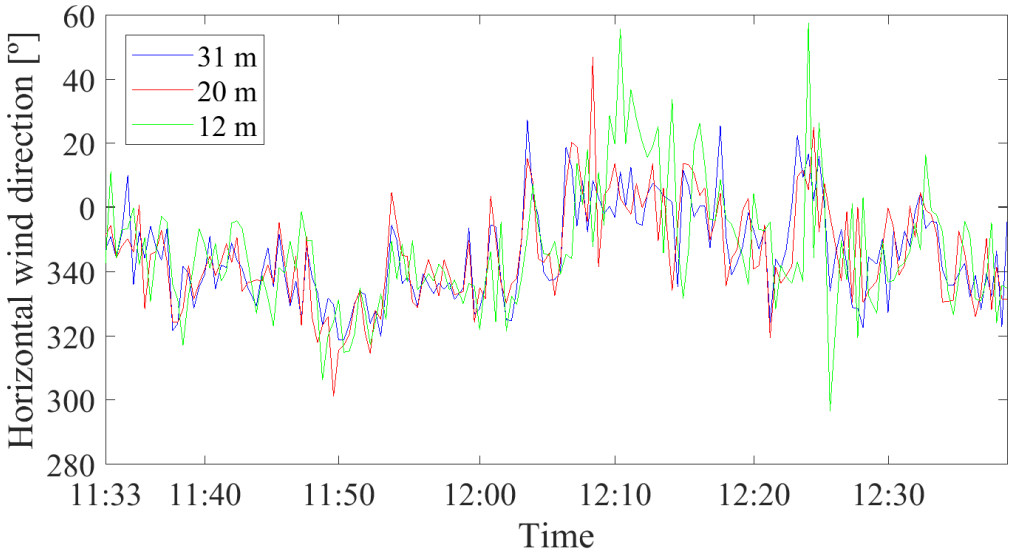

Figure 5.16: LiDAR horizontal wind direction vs. time on November 29, 2017

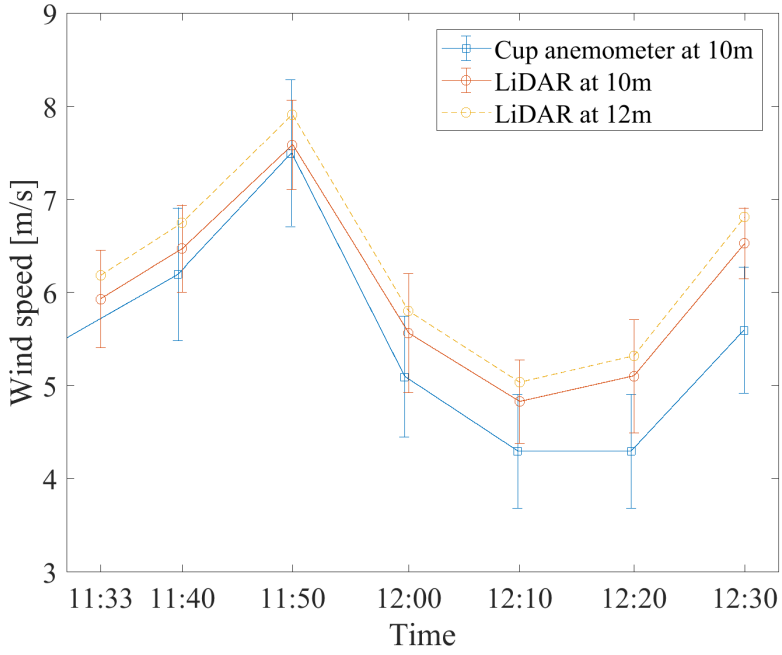

Figure 5.17: Cup anemometer and LiDAR horizontal velocity comparison

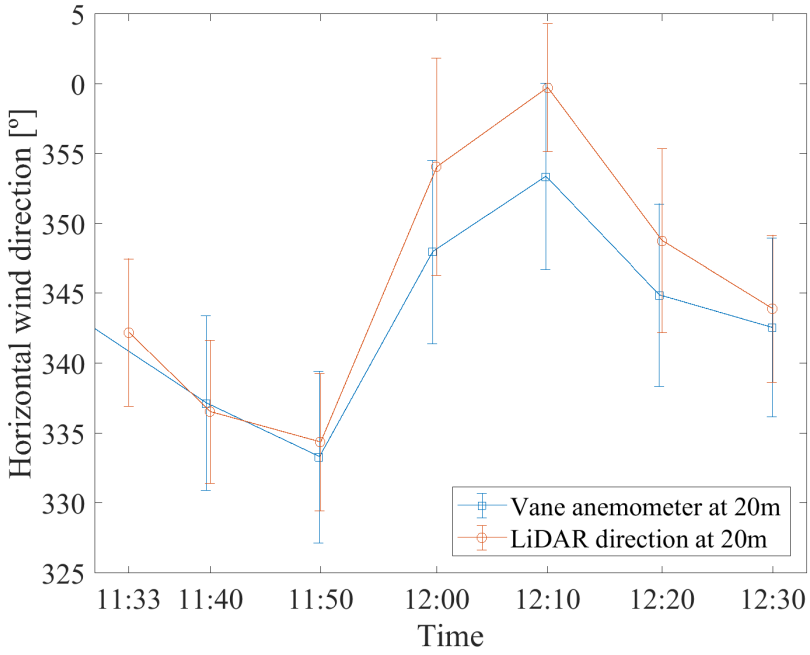

Figure 5.18: Vane anemometer and LiDAR horizontal wind direction comparison

sampling rate. The cup anemometer had a 1 second sampling rate, making the error smaller, but still large due to the variability of the wind in the 10 minute period. Details of the uncertainty can be found in Appendix A.

The vane anemometer direction measurements were corrected to adjust the recorded direction with the actual direction measured using a compass. The correlation is shown in Figure 5.19.

From the comparison of the LiDAR and vane anemometer measurements in Figure 5.18, a similar trend can also be seen. The LiDAR measurements showed values more towards north than the vane anemometer. Since both measurements were taken at heights of 20 m it was expected that the results would be more similar, but still show a reasonable correlation. The discrepancy in this case could be caused by the correction of the vane direction. When calculating the error of the vane measurements, the correlation of the correction fit was included with the random error. Therefore, from the error bars in Figure 5.18 it can be seen that the measurements of the LiDAR and vane anemometer are within reason.

The results of comparisons show that the LiDAR is able to provide reliable measurements for both wind speed and direction. The LiDAR is an excellent and easily set up

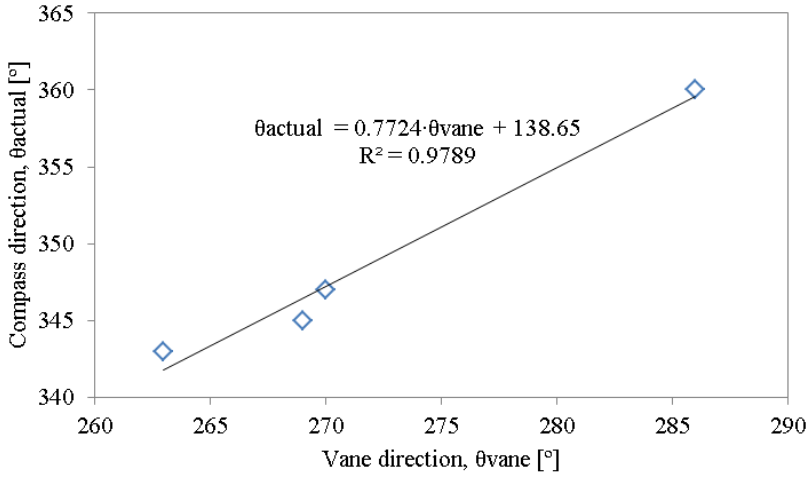

Figure 5.19: Vane anemometer correction

measuring tool to get wind characteristics at various heights.

5.3.2 Laser Position and Measurement Verification

The results from the laboratory test with the nebulizer showed that the LiDAR was able to detect the particles from the nebulizer at all heights from 11.6 m to 230 m. However, the SNR from the raw data, as described in Section 3.4.1, was larger at the measurement distance closer to the nebulizer location. Using a high-pass filter method to eliminate low SNR signals, the measurement distance of the LiDAR could be verified within 0.2 m. It was therefore determined to continue to the next phase of the verification with the sonic anemometer.

Comparing the LiDAR against the sonic anemometer inside of the Wind Generation Facility, the average velocities and standard deviations were determined. This was calculated by adjusting the start and end of the measurement times for both devices to be the same using the timestamps of the data. The results of the test are shown in Table 5.3.

The comparison between the measured velocities is close, with a difference of 0.9% and 4.4% for both velocity measurements. However, the standard deviation calculated from both velocity measurements have a higher difference at 33% and 18%, although they are in a comparable range. From the results of the comparison, it was determined that the measurements from the LiDAR were accurate enough to provide velocity measurements for

Table 5.3: Comparison of LiDAR and sonic anemometer measurements inside the Wind Generation Facility

	Measured Average Velocity [m/s]		**Standard Deviation [m/s]**	
LiDAR	8.16	9.16	0.69	0.97
Sonic anemometer	8.24	9.59	1.04	1.18
% Difference	0.9%	4.4%	33.4%	18.1%

the wake experiments of the UW WEG turbine. Additional comparisons of the devices will be conducted to ensure accuracy of measurements. This is shown later in Section 5.4.4.

5.4 Wake Measurement Results

Measurements of the velocity in the wake of the UW WEG turbine were conducted using three different measurement techniques utilizing different measurement devices. The devices included the Pitot Tree, sonic anemometer, and LiDAR for wake measurements in each experiment campaign. Each technique served to provide different information about the wake of the turbine and as a validation with the comparison of all three methods. The results of each experiment and the comparison of the methods are described in the following sections. Each method determines the velocity profile and added turbulence, as calculated from Eq. 2.24, of the wake.

Using the incoming velocity profile method measured with the Pitot Tree from Section 4.1 it was determined that the incoming flow was within u/U of approximately ± 0.1 with average velocities of 9.6 m/s and 8.4 m/s for tip speed ratios of 3.6 and 4.1 respectively. The flow profiles are shown in Figure 5.20.

Additionally, the incoming turbulence intensity is shown in Figure 5.21. The profiles result in average turbulence intensities of 0.048 for both tip speed ratios of 3.6 and 4.1 as calculated from Eq. 2.25. The turbulence intensity varied by ± 0.005.

The axial induction factor was determined from the measurements of Johnson et al. [39]. Therefore, the axial induction factor was determined to be 0.235 and 0.260 for tip speed ratios of 3.6 and 4.1 respectively. Using these values, the thrust coefficients could be determined using Eq. 2.12 and Eq. 2.14. The calculated thrust coefficients are given in Table 5.4.

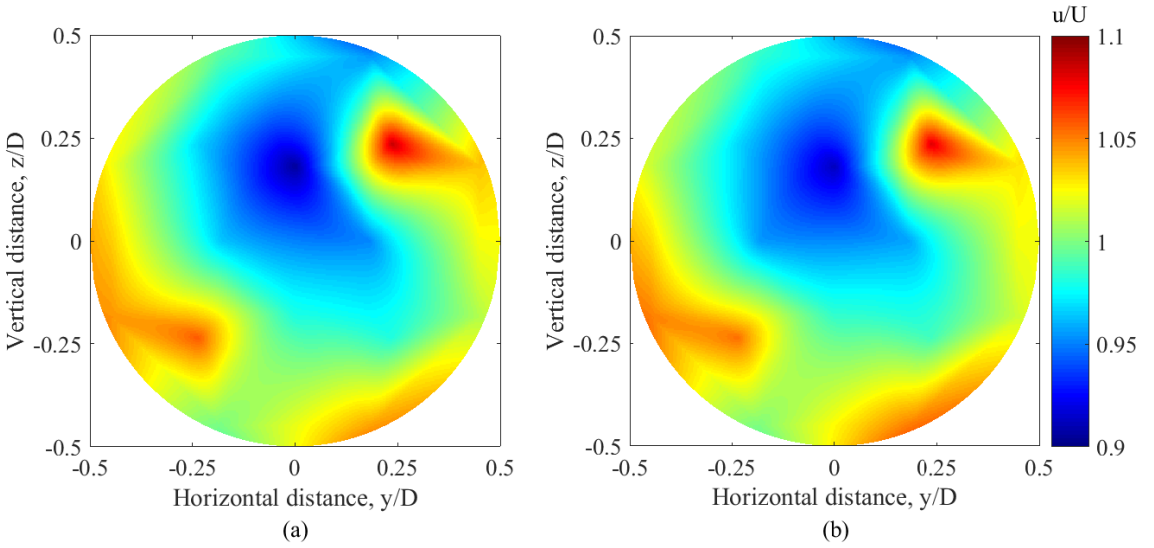

Figure 5.20: Free stream velocity profile upstream of the UW WEG turbine using the Pitot Tree method at -0.3 D with (a) $\lambda = 3.6$ and (b) $\lambda = 4.1$

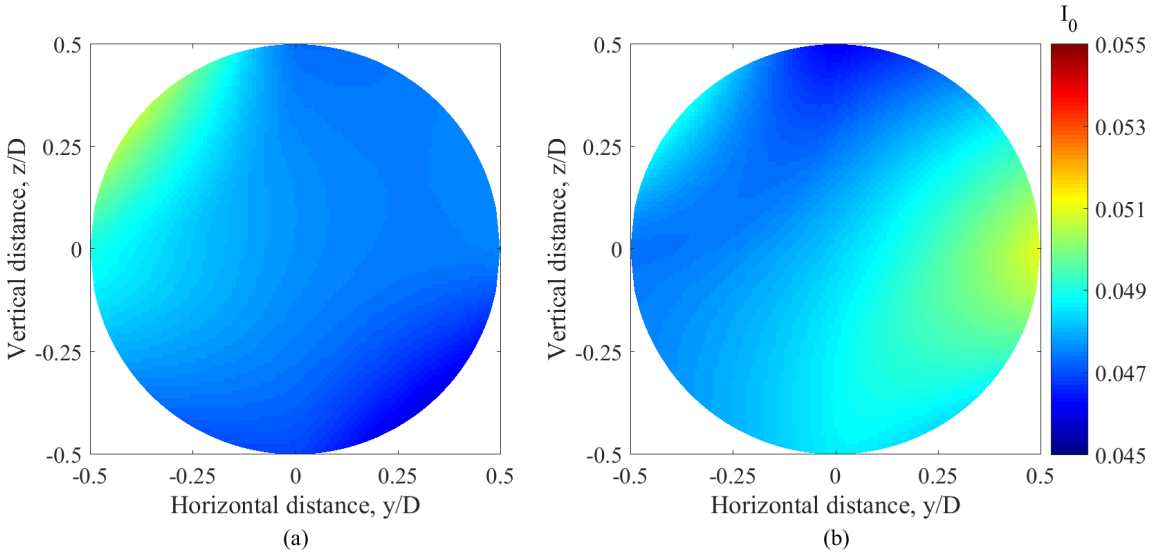

Figure 5.21: Free stream turbulence intensity profile upstream of the UW WEG turbine using the Pitot Tree method at -0.3 D with (a) $\lambda = 3.6$ and (b) $\lambda = 4.1$

Table 5.4: Thrust coefficient, C_T, of the UW WEG turbine from axial induction factor measurements of Johnson et al. [39]

Tip speed Ratio, λ	**Yaw Angle, γ**	
	0°	**±30°**
3.6	0.72	0.59
4.1	0.77	0.63

5.4.1 Pitot Tree Measurements

The Pitot Tree developed as described in Section 3.2 was used initially to measure the wake of the UW WEG turbine. As described in Section 4.4.1, the Pitot Tree was set at various downstream distances to gain an understanding of the wake, such as the location of the wake centre, the change in velocity deficit, and change in turbulence intensity as it is moved downstream.

Velocity Profile

A two-dimensional representation of the velocity profile at each downstream position was obtained using this method and is shown in Figures 5.22 to 5.25 for the various tip speed ratios and yaw angles. More downstream positions were obtained with the turbine in the un-yawed position to gain an understanding of the general wake profile shown in Figures 5.22 and 5.24. Afterwards it was determined to focus on downstream positions at x/D of 1, 2, and 3 for further experiments to get a general understanding of the wake behaviour while reducing experimental measurements. These positions were chosen from the results of Figures 5.22 and 5.24. At 4 rotor diameters, D, away, the wake appeared to be disrupted by the exit area of the facility, therefore measurements at this point are not representative of the actual wake behaviour. From the results it was determined that the wake beginning, middle, and end of the test area could be studied from positions at 1 D, 2 D, and 3 D respectively.

From the un-yawed Pitot Tree measurements in Figures 5.22 and 5.24, it can be seen that a maximum velocity deficit occurs at 1.5 D. The deficit then begins to decay as it moves further downstream as expected [61]. The wake centre position in this case, denoted by the centre of the velocity deficit, appears to be relatively stable with the position remaining at approximately hub height as the wake propagates downstream.

It should be noted that a research structure, known as a Steiner Tunnel, positioned at approximately 2.5 D extends partially into the flow. The position of the Steiner Tunnel

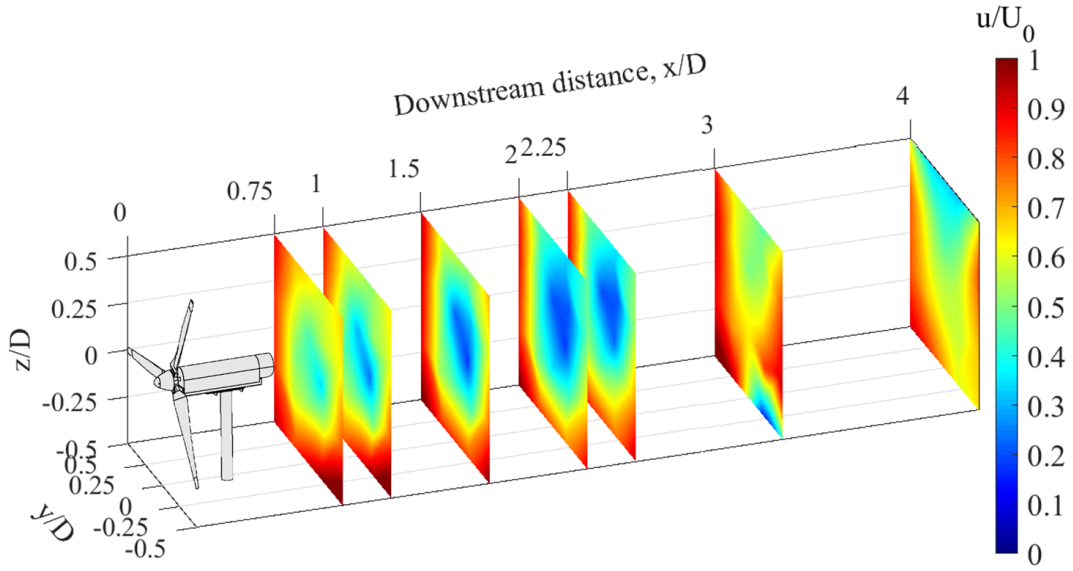

Figure 5.22: Velocity profile in the wake of the UW WEG turbine using the Pitot Tree method at $\gamma = 0°$ and $\lambda = 3.6$

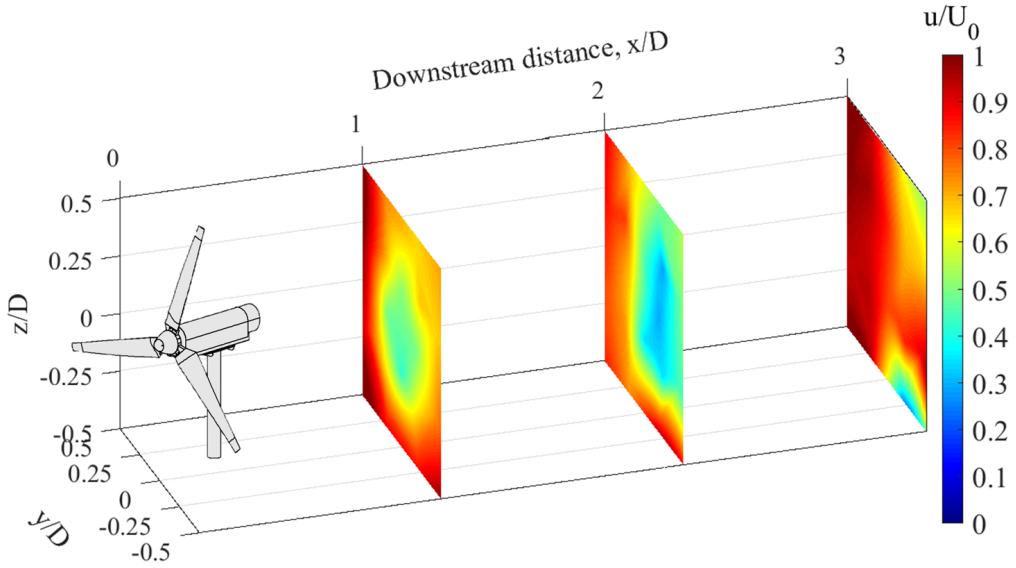

Figure 5.23: Velocity profile in the wake of the UW WEG turbine using the Pitot Tree method at $\gamma =$ -30° and $\lambda = 3.6$

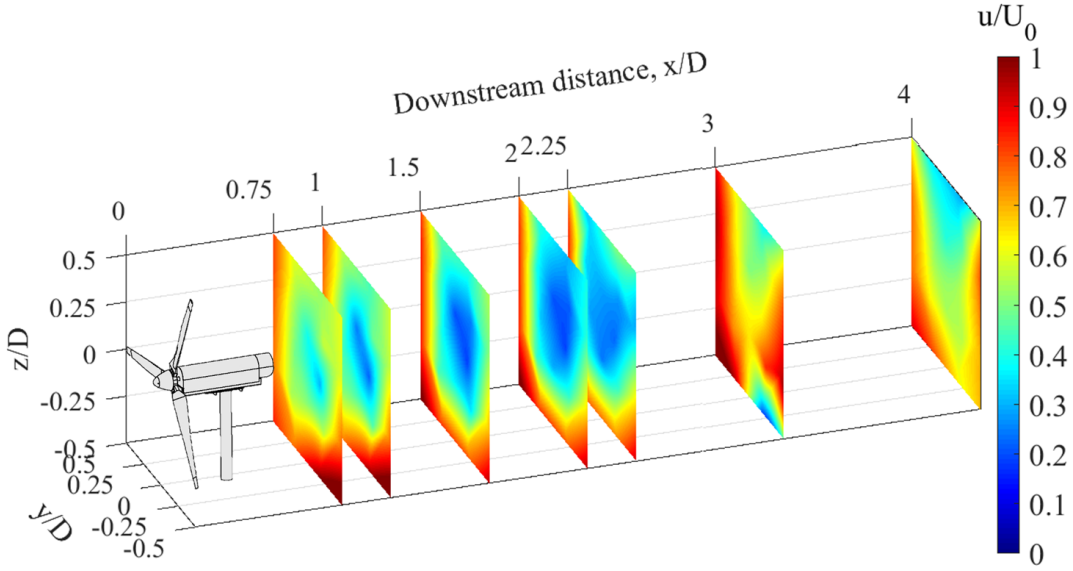

Figure 5.24: Velocity profile in the wake of the UW WEG turbine using the Pitot Tree method at $\gamma = 0°$ and $\lambda = 4.1$

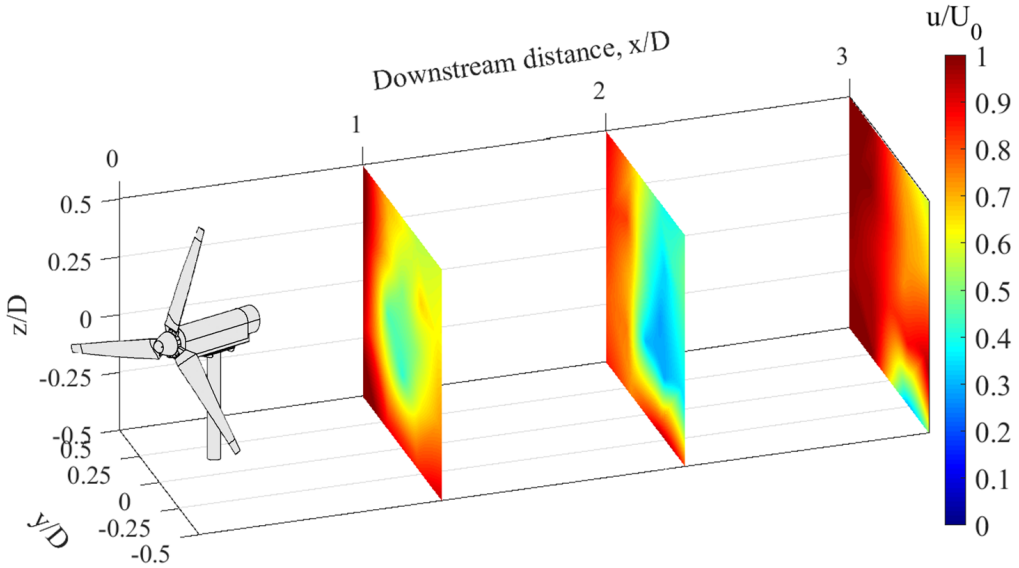

Figure 5.25: Velocity profile in the wake of the UW WEG turbine using the Pitot Tree method at $\gamma =$ -30° and $\lambda = 4.1$

can be seen as described in Section 4.4.1. The Steiner Tunnel had an effect on the flow as seen by the reduced velocity in Figures 5.22 to 5.25 at y/D between -0.25 to -0.5 and at a downstream distance of 3 D.

The wakes of the yawed turbine are shown to deflect in the direction of the yaw angle. This can be seen in Figures 5.23 and 5.25 as the position of the wake centre moves further in the negative y-direction as the flow moves further downstream. Comparing the results at different yaw directions, the yawed velocity deficit appears to be reduced in comparison to the un-yawed cases. This is a result of the reduced thrust coefficient caused when yawing the turbine as seen in Table 5.4 and increased mixing of the shear layer to accelerate the recovery of the wake as seen in the experiments of Krogstad & Adaramola [41].

From the Pitot Tree measurements, it cannot be seen whether the tip speed ratio has a significant effect on the flow. In comparison to the profile seen for both yawed and un-yawed cases, the velocity deficit and wake deflection seem to be similar in the narrow range of tip speed ratios tested. This will be further explored in the additional measurements with the sonic anemometer and LiDAR measurement devices.

Added Turbulence

The added turbulence is the turbulence added to the wake relative to the turbulence level of the incoming flow, as described in Section 2.1.4. This was calculated using Eq. 2.24. The same two-dimensional representation of the added turbulence at each downstream position is shown in Figures 5.26 to 5.29 for the Pitot Tree measurements.

It is interesting to see that the turbulence increases in the upper portion of the wake as it moves downstream. This effect is more pronounced in the un-yawed profiles of Figures 5.26 and 5.28, but also occurs when the turbine is yawed, which was observed but difficult to differentiate in comparison to the turbulence level of the wake at 2 D. The measurements for the turbine in the yawed direction were not taken at 4 D, therefore the trend cannot be seen further than 3 D. Measurements were also taken with the Pitot Tree while the turbine was not rotating, shown in Figure 5.30. The Steiner Tunnel has a significant effect on the turbulence shown in the figure, however the increase in turbulence in the upper portion of the measurements are seen to develop at 3 D and increase at 4 D. At 2 D, a turbulent wake is seen even though the turbine is not in operation as a result of the flow moving over the nacelle and non-rotating blades.

The development of the turbulence in the upper area of the facility was seen in the measurements of Best [15] during the profiling of the Wind Generation Facility. With the turbine removed from the flow, it was shown that an increase in turbulence begins

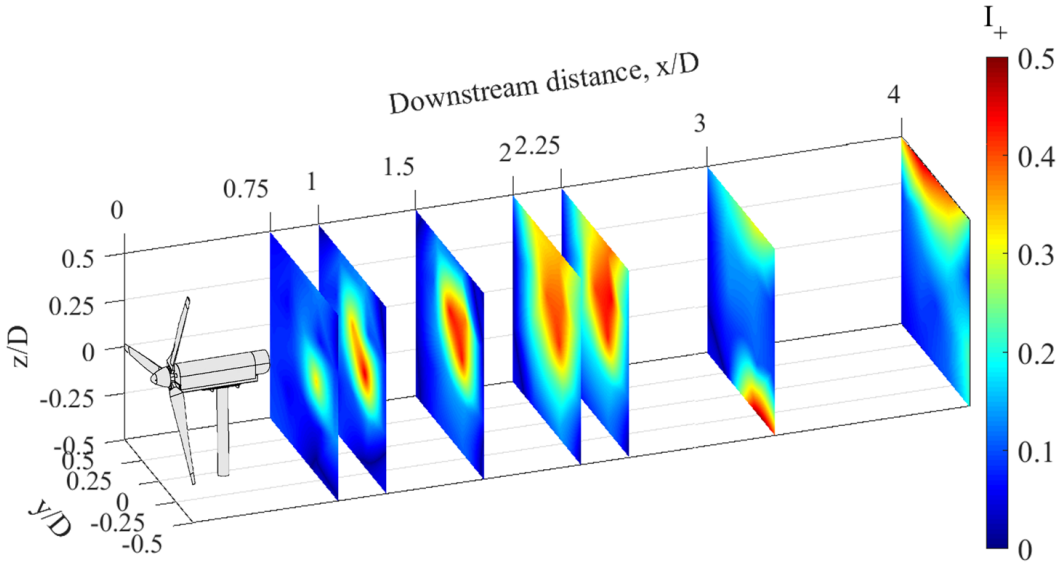

Figure 5.26: Added turbulence, I_+, in the wake of the UW WEG turbine using the Pitot Tree method at $\gamma = 0°$ and $\lambda = 3.6$

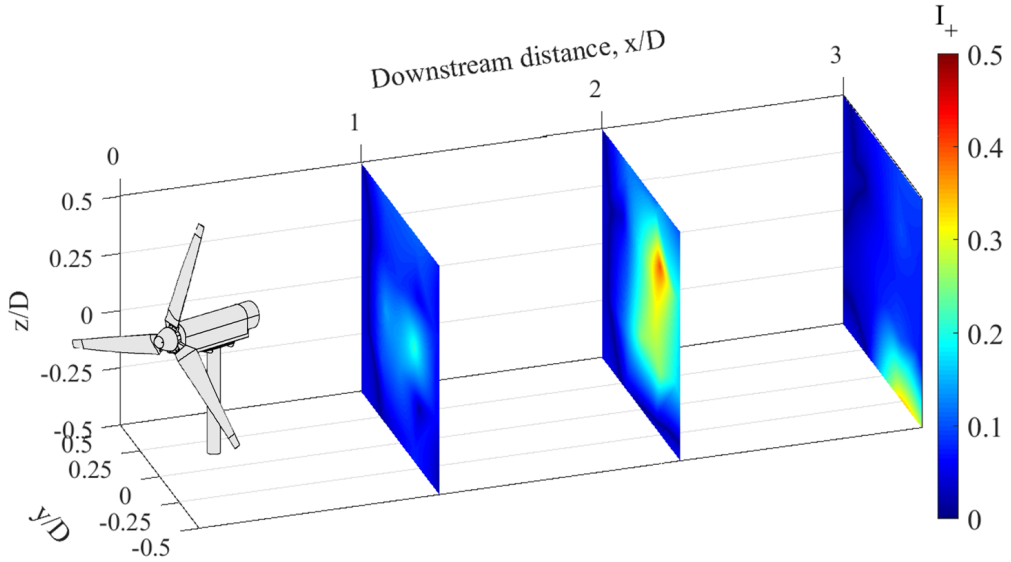

Figure 5.27: Added turbulence, I_+, in the wake of the UW WEG turbine using the Pitot Tree method at $\gamma = $ -30° and $\lambda = 3.6$

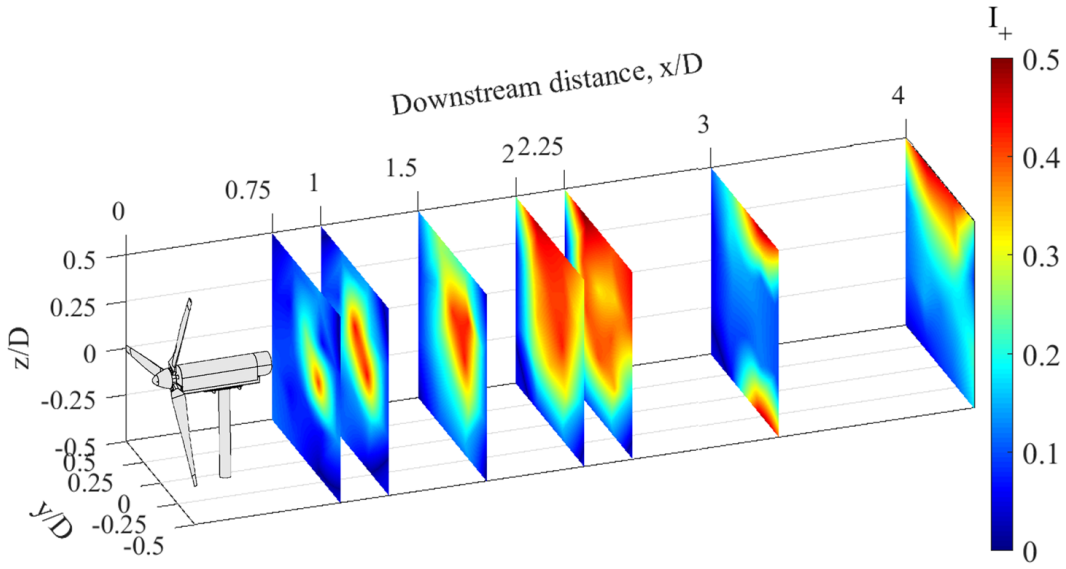

Figure 5.28: Added turbulence, I_+, in the wake of the UW WEG turbine using the Pitot Tree method at $\gamma = 0°$ and $\lambda = 4.1$

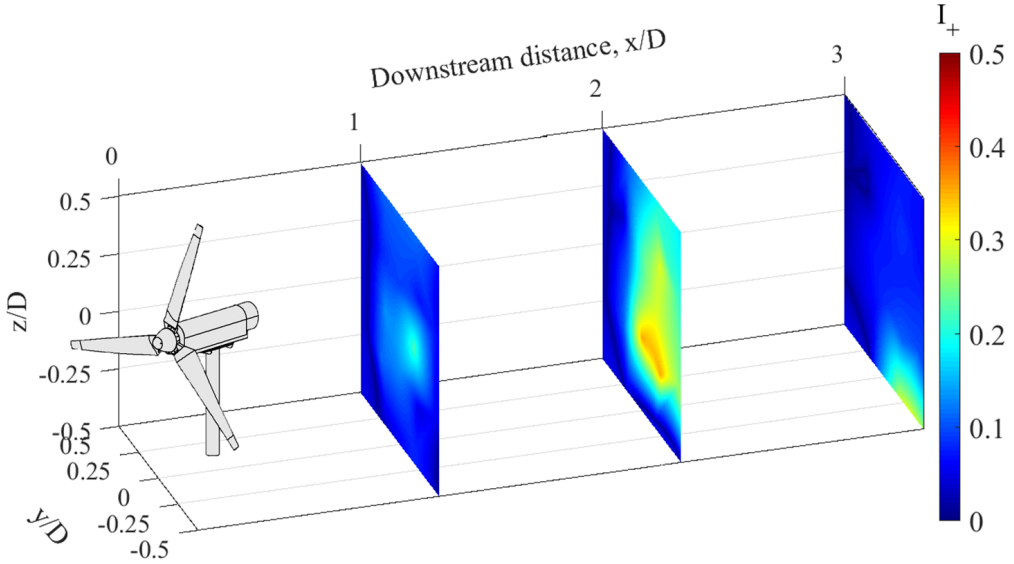

Figure 5.29: Added turbulence, I_+, in the wake of the UW WEG turbine using the Pitot Tree method at $\gamma = $ -30° and $\lambda = 4.1$

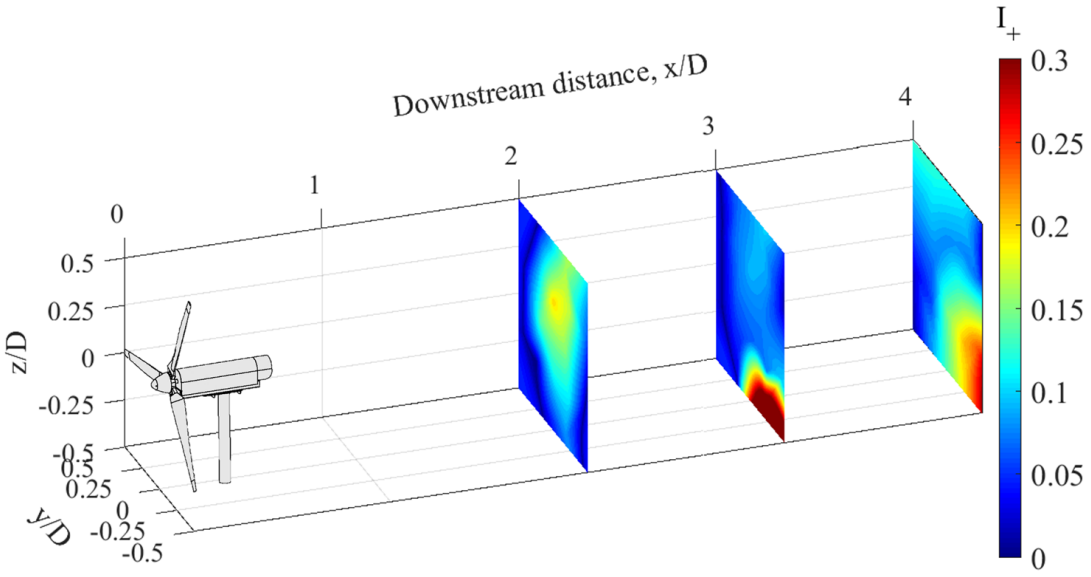

Figure 5.30: Added turbulence, I_+, in the wake of the non-rotating UW WEG turbine using the Pitot Tree method at $\gamma = 0°$ and $\lambda = 3.6$

to develop in the upper portion of the facility. This was seen starting at a downstream distance of 1 D at a height of z/D of 1.3. As the flow approached the exit of the facility, the turbulence extended downwards. At 2.2 D the increased turbulence moved to z/D of 1.0. Therefore, the unusual increase in turbulence in the upper portion of the downstream wake seen in the Pitot Tree measurements is a possible result of the flow profile of the facility.

Disregarding the unusual effect of the turbulence increase at further downstream positions, the yawed wake profiles show a much smaller level of added turbulence in comparison to the un-yawed profiles, which was on average 33% lower. This is a result of the faster wake recovery observed and lower thrust coefficient causing the overall turbulence to decrease [18]. The wake centre can still be seen in the turbulence, which shows the wake deflecting with the velocity in the yawed experiments.

Temporal Velocity Behaviour

The Pitot Tree takes measurements from all points simultaneously and therefore can be used to determine the temporal changes in the wake. The velocity profiles as the wake

changes with time, t, are shown in Figures 5.31 and 5.32 for yaw angles of 0° and 30° respectively.

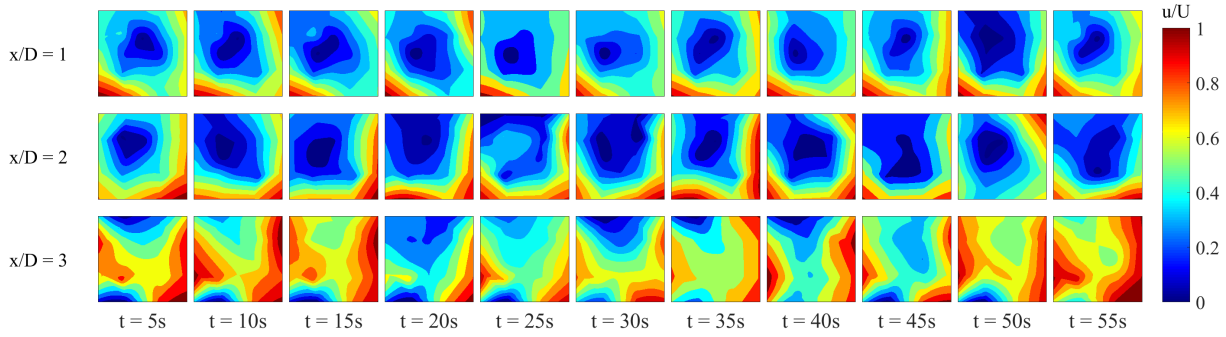

Figure 5.31: Velocity profile through time in the wake of the UW WEG turbine using the Pitot Tree method at $\gamma = 0°$ and $\lambda = 4.1$. The Pitot Tree extends to ±0.5 D in the y and z-direction

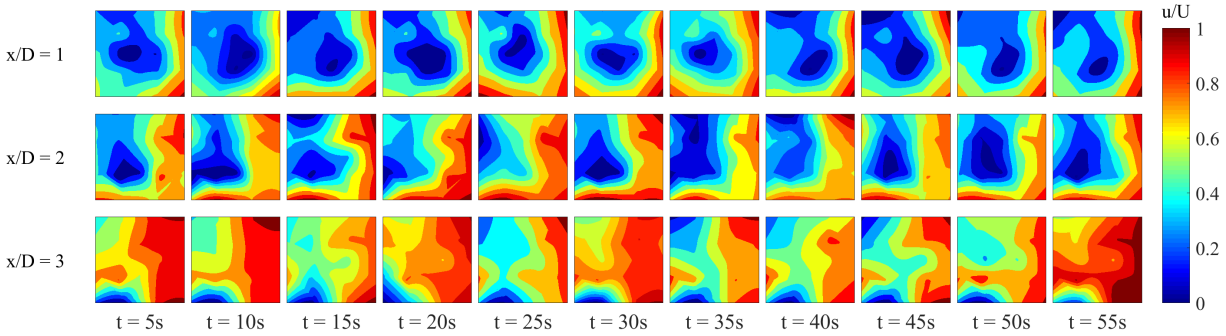

Figure 5.32: Velocity profile through time in the wake of the UW WEG turbine using the Pitot Tree method at γ = -30° and $\lambda = 4.1$. The Pitot Tree extends to ±0.5 D in the y and z-direction

At 1 D and 2 D for the un-yawed turbine, little variation is seen about the hub centre location with a strong core of slow moving fluid, as seen in Figure 5.31. This is also seen for the un-yawed turbine at 1 D in Figure 5.32. However, at 2 D for the yawed turbine profile, a diminishing of the low speed core is seen.

5.4.2 Sonic Anemometer Measurements

The sonic anemometer was used in the wake study to obtain a single line traverse at hub height for various downstream positions of the UW WEG turbine as described in Section 4.4.2. Using this method the ends of the velocity deficit in the wake could be determined as the Pitot Tree did not reach the full area of the wake expansion region. The traverses were performed for yaw angles of 0° and -30° with tip speed ratios of 3.6 and 4.1.

The sonic anemometer measures velocity in three directional components. Therefore, the measurements can be used to determine the wake behaviour in each direction. Velocity measurements were taken for both the x and y-directions. The turbulence intensity, however, is a result of the total turbulence in the wake calculated from all three directional components. This was used to calculated the added turbulence as calculated from Eq. 2.24.

Velocity Profile

The velocity measurements of the sonic anemometer traverses are shown in Figure 5.33 for each yaw angle and tip speed ratio. Lines in Figure 5.33 are shown for clarity only. The typical velocity profile in the wake is clearly seen as measured in each of the experiments of Bastankhah & Porté-Agel [11], Krogstad & Adaramola [41], and Trujillo et al. [72]. The centre of the wake has the lowest velocity and recovers to free stream values at the edges of the wake. The wake recovery appears to occur at approximately y/D of 0.7 for the un-yawed turbine. The wake from the yawed turbine has an offset wake centre due to deflection as expected [52]. It can also be seen that the velocity at the ends of the traverse begin to decline after a maximum value is reached. This is caused by the facility test section area. The incoming flow area from the fans is smaller than the test section area, therefore causing the velocity to be lower on the sides of the facility as expected in an open jet facility.

The minimum velocity deficit decreases as the flow moves further downstream, away from the turbine as expected [61]. This can be better seen in Figure 5.34 from the increase in the minimum velocity with further downstream distances, which shows the wake recovery rate. According to Ammara et al. [7], the velocity profile reaches a minimal level at a distance of 10 D. Therefore, in the measurement area, the wake should be continuing to recover, which was seen in Figure 5.34 since the velocity deficit is still significant at a distance of 3 D. Additionally, the velocity is always increasing starting at 1 D. Ainslie estimates the maximum velocity deficit to occur between 1 D and 2 D [4]. Therefore, it is shown by the continual increase in velocity of the wake that the maximum velocity has

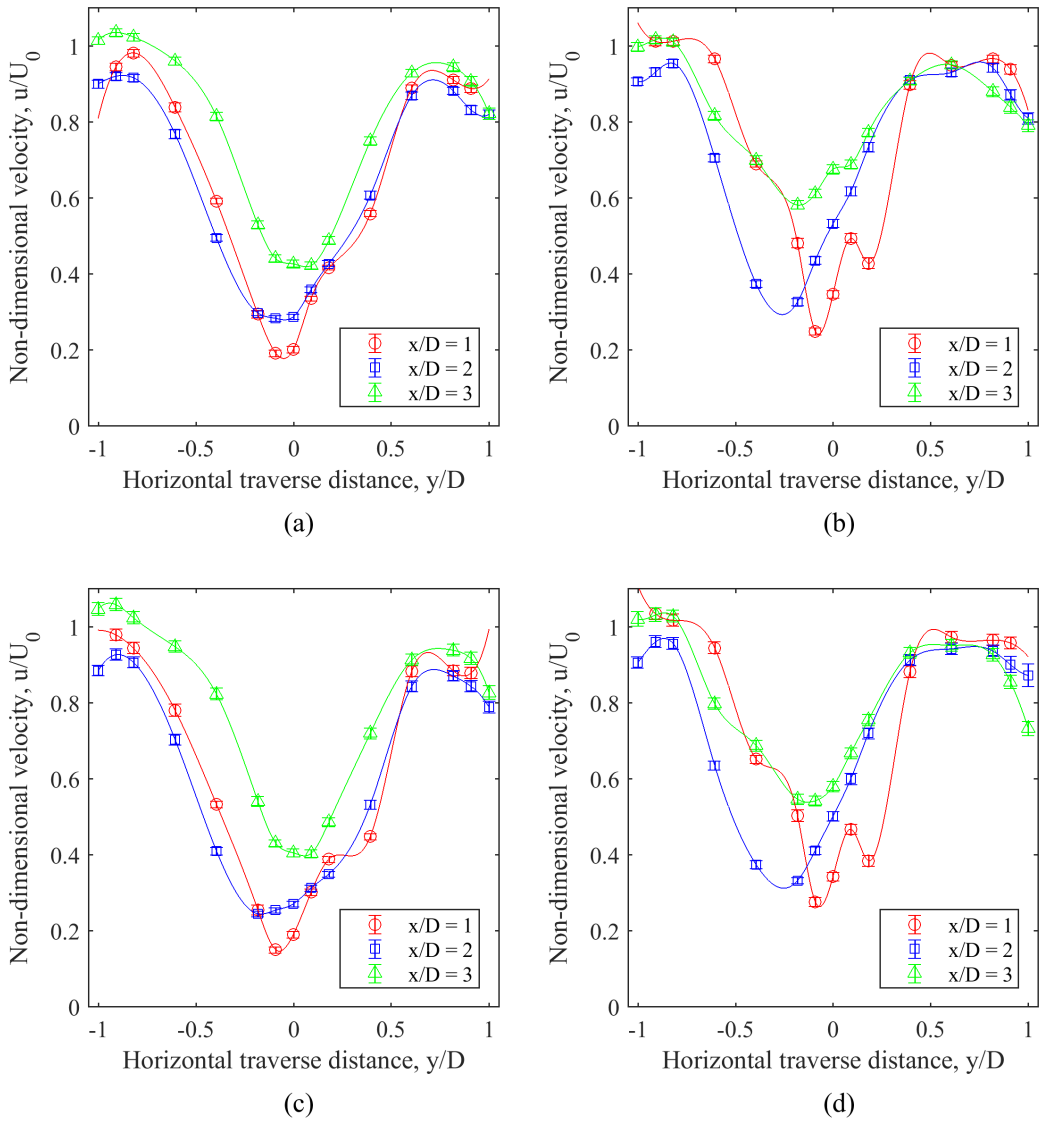

Figure 5.33: Velocity in the wake of the UW WEG turbine at z = 0 (hub height) with (a) γ= 0°, λ = 3.6, (b) γ = -30°, λ = 3.6, (c) γ = 0°, λ = 4.1, and (d) γ = -30°, λ = 4.1 (sonic anemometer traverse)

been reached, however it is unknown whether this occurs before 1 D or between 1 D and 2 D before beginning to recover.

The difference in tip speed ratios do not seem to have much of an effect on the velocity

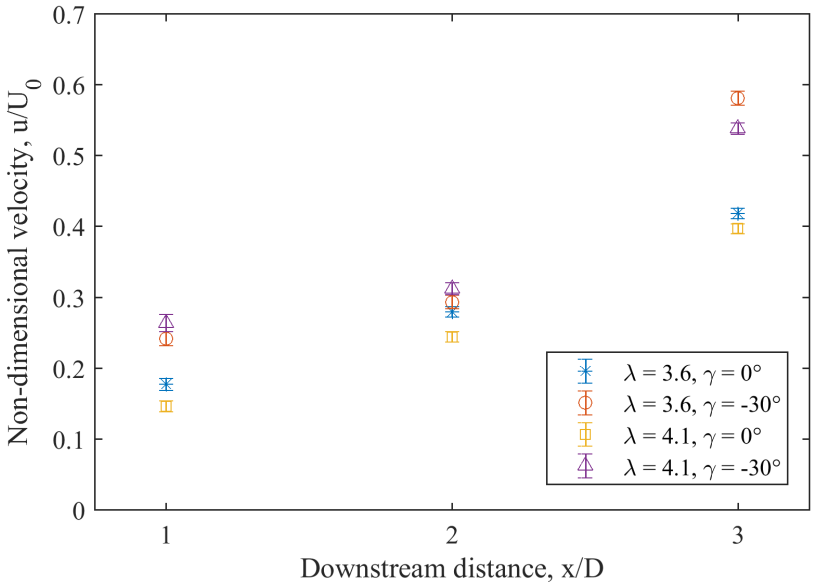

Figure 5.34: Minimum velocity in the wake of the UW WEG turbine (sonic anemometer traverse)

profile or minimum velocities, although the tested tip speed ratios resulted in only a small change in thrust coefficient as seen in Table 5.4. However, the yawed profiles show less of a deficit, which also lead to a faster recovery rate. This is a result of the reduced thrust coefficient, shown previously in Table 5.4, and reduced power extraction due to the yawed angle of the turbine as seen in the Pitot Tree measurements and experiments of Krogstad & Adaramola [41].

The velocity deficit in the yawed case, however, shows the minimum velocity at 1 D is similar to that at 2 D. In addition, the velocity profile at 1 D shows a double wake. This is the condition that occurs as a result of shearing between the velocity inside and outside of the wake, known as the shear layer [61]. Once the shear layer reaches the centre of the wake, the end of the near wake region occurs and the far wake region starts. Therefore, the double wake seen here is located in the near wake region. The transition to far wake occurs between 1 D and 2 D since the double wake transitions to a single Gaussian wake distribution. The double wake is still slightly present in the un-yawed case at 1 D showing the end of the near wake region occurring at this point [61]. Therefore, it can be concluded that the near wake region is extended in the yawed wake relative to the un-yawed wake.

The position of the minimum velocity is shown in Figure 5.35 at different downstream distances for each case. The centre of the velocity minimum, known as the wake centre,

is around zero in the un-yawed case with some variability. This is also expected since the alignment of the flow and turbine is symmetric. For the yawed tests, the wake moves away from the centre line. It is expected that the wake centre should be deflected from the hub centre with further distances downstream until it converges to an offset position, after which the wake aligns to the direction of the incoming flow, as seen in the experiments of Bastankhah & Porté-Agel [11]. However, the measurements appear to move back towards the centre after being deflected, as seen from the wake centre at 2 D being further from the hub centre than at 3 D. It is difficult to say whether the wake will continue to correct to the wake centre or remain offset from the centre. Therefore, the appearance of the wake deflection being corrected could be attributed to fluctuations in the offset position.

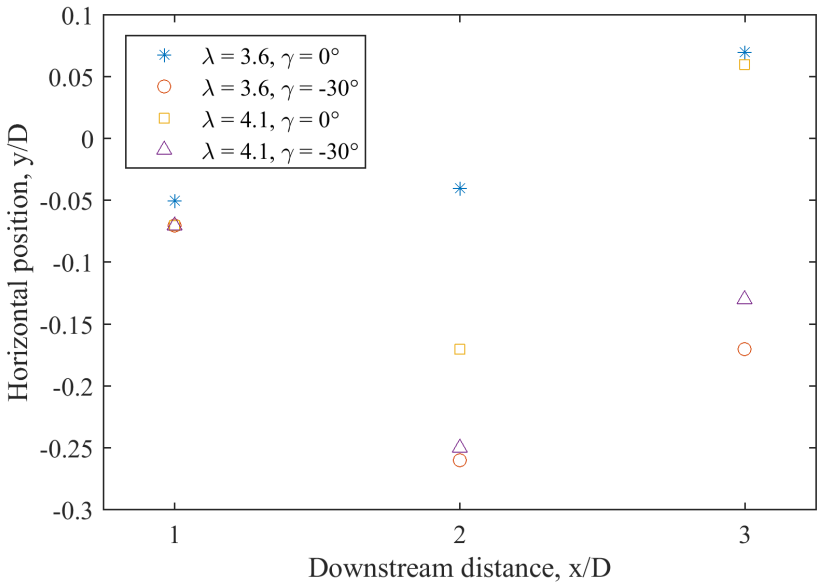

Figure 5.35: Horizontal position of minimum velocity in the wake of the UW WEG turbine (sonic anemometer traverse)

The wake centre from Figure 5.35 had similar results for the yawed turbine for each tip speed ratio, showing that the tip speed ratio did not have much of an effect. However, there is some variability between the position of the wake centre with the turbine in the un-yawed position.

The wake radius is defined as the distance of the end of the wake to the wake centre in the y-direction. The end of the wake is determined by locating the point when the velocity reaches near free stream values. Figure 5.36 shows the wake radius for each case as the flow moves downstream.

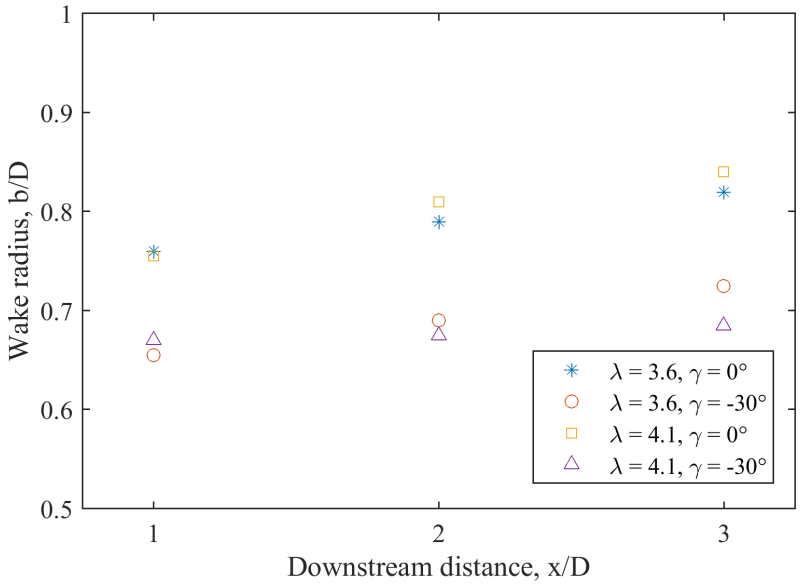

Figure 5.36: Wake radius behind the UW WEG turbine (sonic anemometer traverse)

For each case, the wake radius is shown to be increasing as the flow moves downstream, showing the continual expansion of the wake. The size of the wake radius is similar for both tip speed ratios, with a larger radius occurring at a tip speed ratio of 4.1. This is expected as a result of the higher thrust coefficient from Table 5.4. The difference between yaw angles, however, is much more pronounced. The un-yawed turbine has a larger wake radius in comparison to the yawed turbine wake. Again, this is expected as a result of the increased thrust coefficient for the un-yawed turbine [18].

Added Turbulence

The added turbulence for the measurements are shown in Figure 5.37. Lines in Figure 5.37 are shown for clarity only. The yawed direction also shows a double wake at 1 D as seen in the velocity profile. Again, this is a result of the extended near wake region as a result of the turbine being yawed. The shear layer can be seen from the increase in turbulence of the double wake peaks, which reaches the far wake region when it grows to the wake centre [22]. At 2 D, the double wake can still be seen, but is fully transitioned at 3 D. The added turbulence is seen to decay as it moves downstream as expected from the wake recovery [61]. The maximum turbulence also follows the deflection of the wake when the turbine is yawed, as seen by the change in position of the added turbulence peak. The

same movement of the wake centre is seen in the turbulence, which showed the wake centre deflect at 2 D with the appearance of a correction occurring at 3 D when the turbine is yawed. The wake centre is relatively constant about the hub centre with the un-yawed turbine.

The turbulence on the edges of the wake increased in the profile of Figure 5.37. This is due to the traverse reaching the outside of the flow in the test area as described previously in the velocity profile. Since turbulence intensity is a function of the local velocity, the decrease in velocity causes the relative variance of the flow to increase as in Eq. 2.25.

Similar to the velocity deficit, the added turbulence also decreases as the flow moves downstream with the highest level seen at 1 D. This decrease is also shown in Figure 5.38 by looking at the change in the maximum added turbulence. This is also a characteristic of the wake decay as expected [61]. According to Sanderse [61], the recovery of the velocity deficit is faster than the turbulence. Looking at the linear slope of the minimum velocity in Figure 5.34 and the maximum added turbulence in Figure 5.38, the velocity deficit had an average recovery rate of 14%, whereas the turbulence had an average recovery rate of 16% between 1 D and 3 D. However, this rate changes between distances of 2 D and 3 D to an average recovery rate of 20% for the velocity and 7% for the turbulence. It can therefore be seen that the turbulence recovery rate is decreasing whereas the velocity is increasing, which may lead to the velocity recovering faster. However, it is unknown how the velocity and added turbulence continue to progress passed a distance of 3 D.

Crosswind Velocity

The sonic anemometer measures velocity in three directional components. Therefore, the crosswind velocity can be measured to determine whether there is flow in that direction. Figure 5.39 shows the cross wind velocity for each yaw angle and tip speed ratio. It can be seen that for each case there is some crosswind velocity. Table 5.5 shows the average crosswind velocity for each case.

Table 5.5: Average crosswind velocities, v/U_0, in the wake of the UW WEG turbine (sonic anemometer traverse)

Tip speed Ratio, λ	**Yaw Angle, γ**	
	0°	**-30°**
3.6	0.0804	0.1945
4.1	0.0823	0.2013

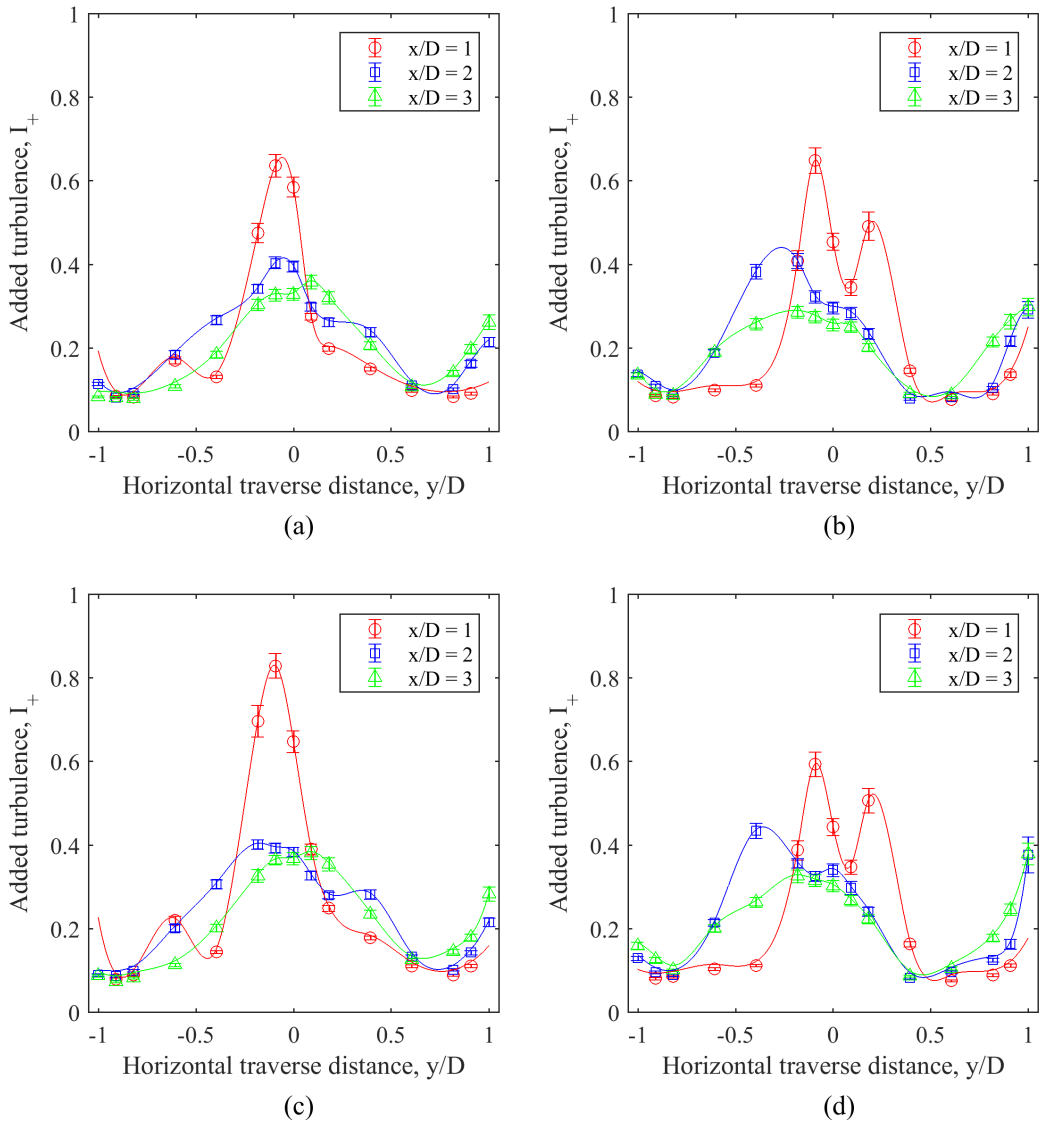

Figure 5.37: Added turbulence, I_+, in the wake of the UW WEG turbine at z = 0 (hub height) with (a) γ= 0°, λ = 3.6, (b) γ = -30°, λ = 3.6, (c) γ = 0°, λ = 4.1, and (d) γ = -30°, λ = 4.1 (sonic anemometer traverse)

For the case of a yaw angle of 0° there is cross wind velocity, however it is not significant with averages of v/U_0 approximately 0.08. The cross wind could be caused by the turbulent flow, measurement error, or misalignment of the sonic anemometer since the cross wind is

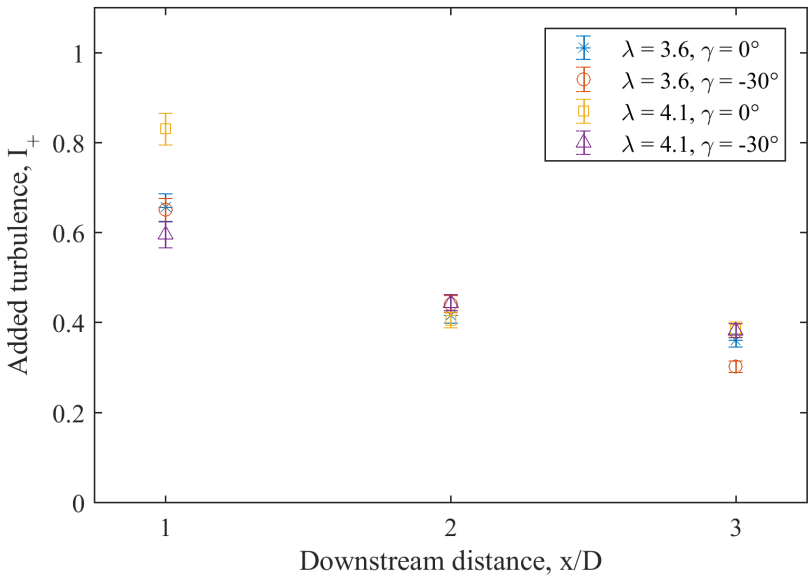

Figure 5.38: Maximum added turbulence in the wake of the UW WEG turbine (sonic anemometer traverse)

always positive. However, for the case of a yaw angle of -30°, the cross wind velocity is more significant with averages of v/U_0 around 0.2 in the direction of the turbine yaw. This is due to the directional change of the wake due to the deflection seen previously in Figure 5.33. In addition, the wake deficit profile is more pronounced in the case of the -30° yaw angle, contributing to the evidence that the cause is due to the wake direction.

5.4.3 LiDAR Wake Measurements

LiDAR measurements were the final goal of the wake measurement experiments. Using the ZephIR z150 LiDAR described in Section 2.3, which was setup upstream of the UW WEG turbine, a velocity profile could be obtained from the measurement scans downstream of the turbine. The LiDAR allowed measurements to be taken efficiently since the position of the LiDAR could be kept stationary with only the angle and LiDAR measurement height being changed. Therefore, more measurement points could be taken in the wake of the turbine.

The data was processed to remove any interference from the turbine blades and account for the line-of-sight angle of the laser relative to the direction of the flow as described in

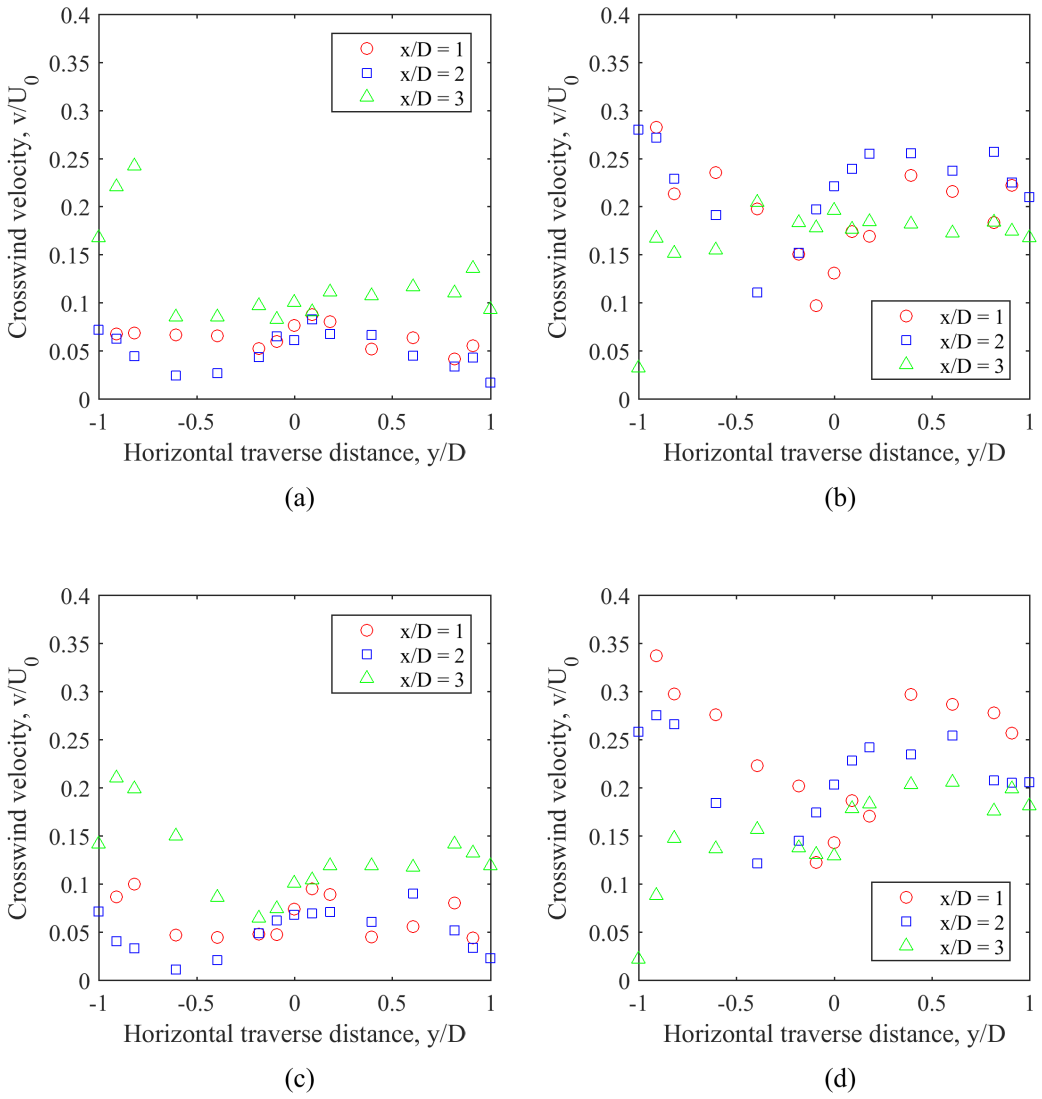

Figure 5.39: Crosswind velocity in the wake of the UW WEG turbine at (a) γ= 0°, λ = 3.6, (b) γ = -30°, λ = 3.6, (c) γ = 0°, λ = 4.1, and (d) γ = -30°, λ = 4.1 (sonic anemometer traverse)

Section 4.4.3. In this case, the flow was assumed to be completely in the downstream direction resulting in streamwise flow measurements. This method gives a measurement of the velocity deficit of the incoming flow, but does not account for any changes in direction. This assumption is backed by the measurements taken with the sonic anemometer and

results shown in Section 5.4.2. It was seen that the crosswind velocity of the un-yawed turbine was minimal and occurred due to a misalignment of the device. However, with the yawed turbine the crosswind was more significant but for the purpose of measuring the wake velocity deficit, this was sufficient. The total turbulence in the wake was taken to be the total turbulence measured by the LiDAR.

As described in Section 4.4.3, the experiment was performed for yaw angles of 0° and 30° as well as tip speed ratios, λ, of 3.6 and 4.1. Note that due to the sweeping measurements of the LiDAR experiment, in order to determine measurements for a specific downstream distance, x/D, the data needed to be interpolated, forming a grid format of the data.

Velocity Profile

The wake velocity profile contours are shown in Figure 5.40. The velocity deficit in each case can clearly be seen. The velocity deficit recovers on either side of the turbine and continues downstream of the turbine. This shows the wake path of the turbine. Due to the position inside of the facility and minimum focal distance of the LiDAR, as described in Section 4.4.3, measurements were unable to be taken in areas close to the turbine, as seen by the excluded area of the contour in Figure 5.40. The UW WEG turbine graphic in the figure is shown to give a visual representation of the turbine position and is only to scale in the y-direction.

The profiles from both tip speed ratios are seen to follow the same path while moving downstream. For both un-yawed profiles in Figure 5.40a and c, the wake aligns with the hub centre as it moves downstream. The yawed profiles, from Figure 5.40b and d, both show a wake deflection in the direction of the turbine yaw as expected from the experiments of Medici [52] and Bastankhah & Porté-Agel [11]. This shows confidence in the measurements and theory such that the wake behavior is predictable at varying tip speed ratios.

The deflection for the yawed profiles appear to begin to converge at approximately 2.7 D, at which point the wake straightens to follow the path of the flow. Therefore it can be determined that a maximum deflection from the turbine centre can be achieved and maintained as the wake moves passed this point.

In addition, the size of the wake boundaries appear to be larger with an increased tip speed ratio as seen in Figure 5.40. This is also the case for the velocity deficit seen. This pattern follows the theory which would increase the wake velocity at higher thrust coefficients, thus also causing the wake expansion to increase [18]. Looking at the thrust coefficients in Table 5.4, shows an agreement with this theory. Interestingly, the wake size appears to be reduced when the turbine is yawed, whereas the un-yawed turbine wake has

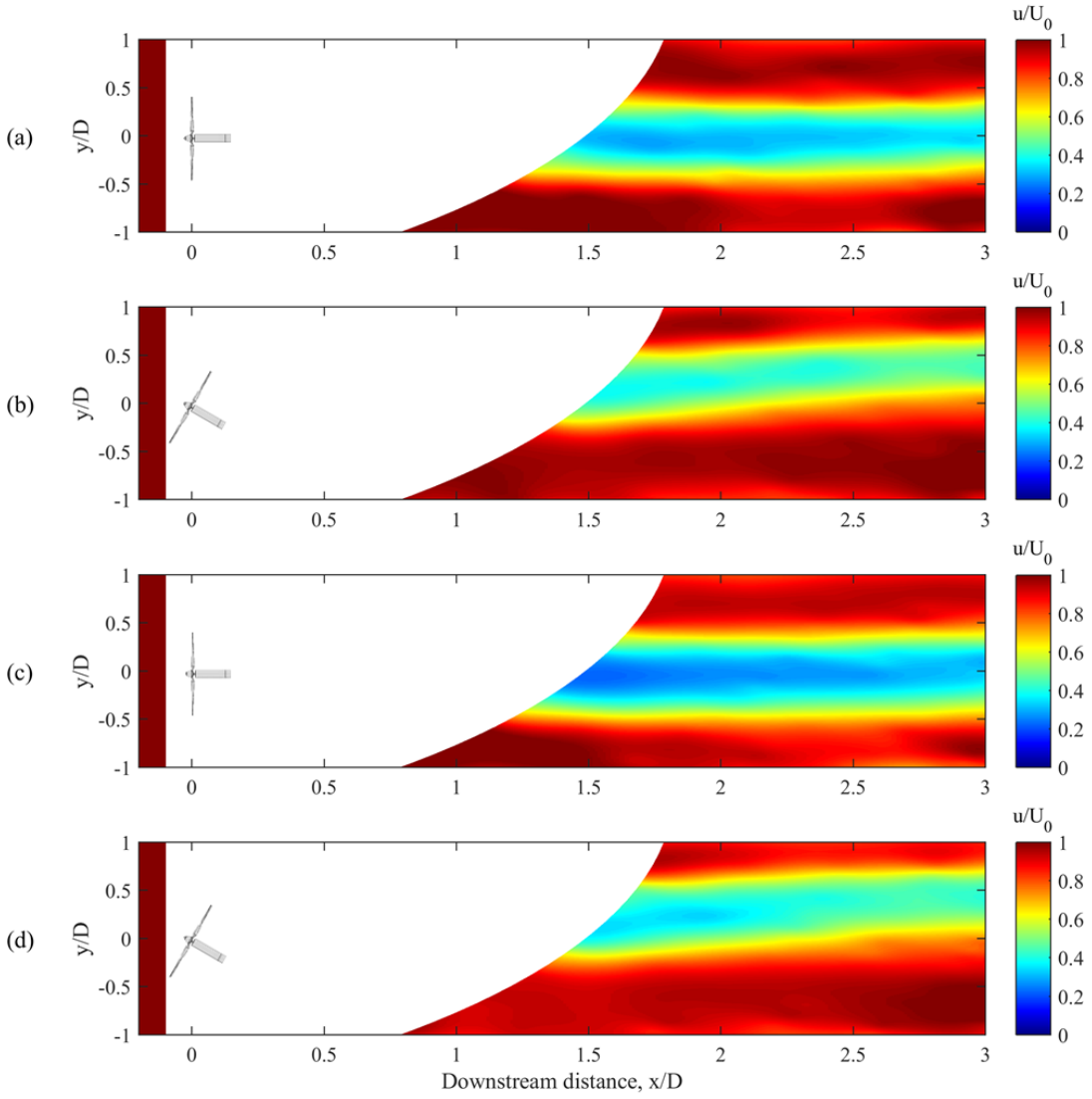

Figure 5.40: Streamwise velocity profile in the wake of the UW WEG turbine at (a) $\gamma = 0°$, $\lambda = 3.6$, (b) $\gamma = 30°$, $\lambda = 3.6$, (c) $\gamma = 0°$, $\lambda = 4.1$, and (d) $\gamma = 30°$, $\lambda = 4.1$ (LiDAR measurements)

a constant expansion size. This would relate to the recovery of the wake. Less energy is extracted in the yawed profile due to inefficiencies in the flow alignment with the turbine blades. Therefore, the recovery of the wake is seen to be accelerated in comparison to the

un-yawed velocity profile as also seen in the experiments of Krogstad and Adaramola [41].

The velocity in the wake can be seen to increase as the flow moves downstream. This trend can be seen more clearly in Figure 5.41. Although not drastic, the flow does recover the further it moves away from the turbine. As seen in the sonic anemometer experiments, the un-yawed profiles have a larger minimum velocity when compared to the yawed profiles. This again is caused by the amount of energy extracted. In addition, there is only a slight change due to the tip speed ratio, with the lower tip speed ratio showing a higher relative velocity, meaning a smaller deficit.

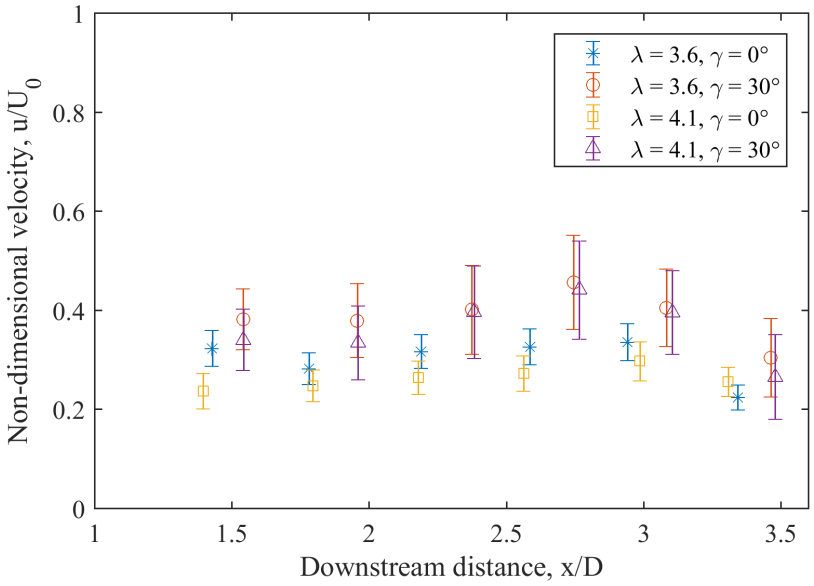

Figure 5.41: Minimum velocity in the wake of the UW WEG turbine (LiDAR measurements)

The change in the wake centre position can be seen in Figure 5.42. In this experiment, it is clear that the wake centre moves away from the centre position as it moves downstream of the yawed turbine and stays central in the un-yawed wake. In the sonic anemometer experiments from Figure 5.35, it appeared as the wake centre was realigning to the centre of the wake after deflecting, however the LiDAR measurements show the wake converging to an offset position. Therefore, the realignment in the sonic anemometer measurements is likely due to fluctuations of the measurements. Again, the tip speed ratio has little effect on the wake position due to the small difference between thrust coefficients.

The wake radius at various downstream distances is shown in Figure 5.43. The wake ends were determined by the point at which the velocity reaches free stream values or when

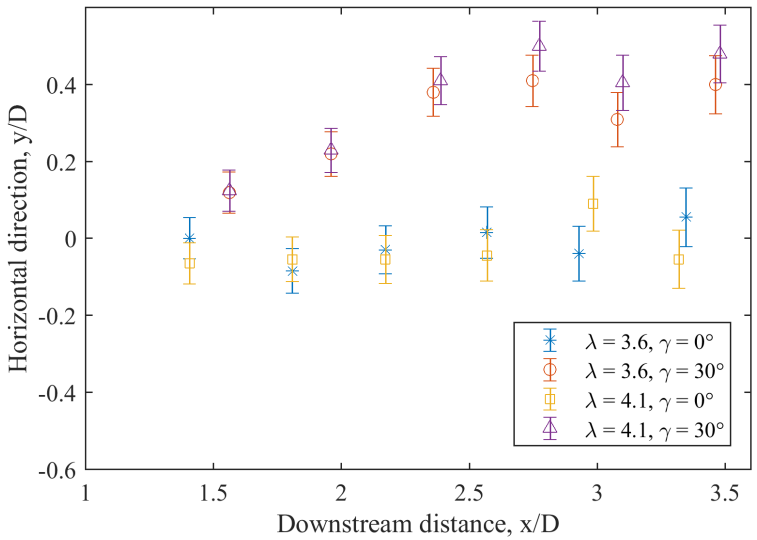

Figure 5.42: Horizontal position of minimum velocity in the wake of the UW WEG turbine (LiDAR measurements)

the slope of the horizontal velocity profile reaches 0, since the flow does not recover to free stream values at all positions. The exact location where it is fully expanded is difficult to accurately determine.

In each case, the wake radius appears to be continually increasing with the downstream distance. The wake radii appear to be higher with a tip speed ratio of 4.1 in comparison to a tip speed ratio of 3.6 for both the yawed and un-yawed turbine. This is expected due to the increase in thrust coefficient with tip speed ratio from Table 5.4 [18]. In the comparison of the wake radius of the yawed and un-yawed turbine, the radius of the yawed turbine begins at a smaller size and increases above the size of the un-yawed turbine wake. According to the values of thrust coefficient, the wake radius of the yawed turbine should be lower than the un-yawed wake radius [18]. This is possibly a result of the correction when calculating the wake radius, since the wake radius was determined by locating the end of the wake in the y-direction and subtracting the position of the wake centre.

Added Turbulence

The added turbulence from the LiDAR scans are shown in Figure 5.44. The wake profile can also be seen in the results of the added turbulence. In the wake of the turbine, the turbulence intensity increases and then recovers at the ends of the wake in the horizontal

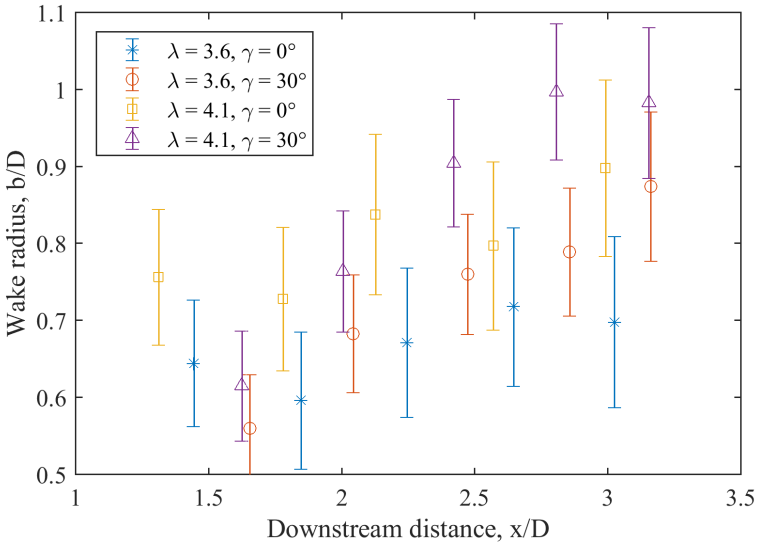

Figure 5.43: Wake radius in the wake of the UW WEG turbine (LiDAR measurements)

direction. For the yawed turbine, the deviation of the wake from the centre can also be seen from the turbulence level, similar to the velocity profile.

Contrary to expectation, the added turbulence increases the further it moves downstream in the experiments with the un-yawed turbine in Figure 5.44a and c. Extending the yawed profile further downstream, this increase can also be seen. As mentioned in Section 5.4.1, it was seen by Best [15] that there is an increase in turbulence starting from the upper area of the facility as it reaches the door. This is a possible explanation for the increase in turbulence in the LiDAR measurements. Adding to this effect, the LiDAR has an increased focal length for further measurement points as described in Section 4.5.3. This adds more variation to the particles being measured for a particular measurement location.

However, there is a point at the beginning of the LiDAR measurements, at 1.5 D, that the turbulence is high with a recovery occurring at approximately 1.8 D. This is the expected trend of the turbulence. As the wake propagates downstream, the turbulence should decrease [61]. This is a characteristic of the wake recovery.

In Figure 5.44c, there is an increase in turbulence seen at y/D of -1 and at a downstream location between 2.5 D to 3 D. This is the position of the Steiner Tunnel discussed in the Pitot Tree experiments in Section 5.4.1. Although the measurements were above the Steiner Tunnel, the effects can still be seen from the increased turbulence in that area.

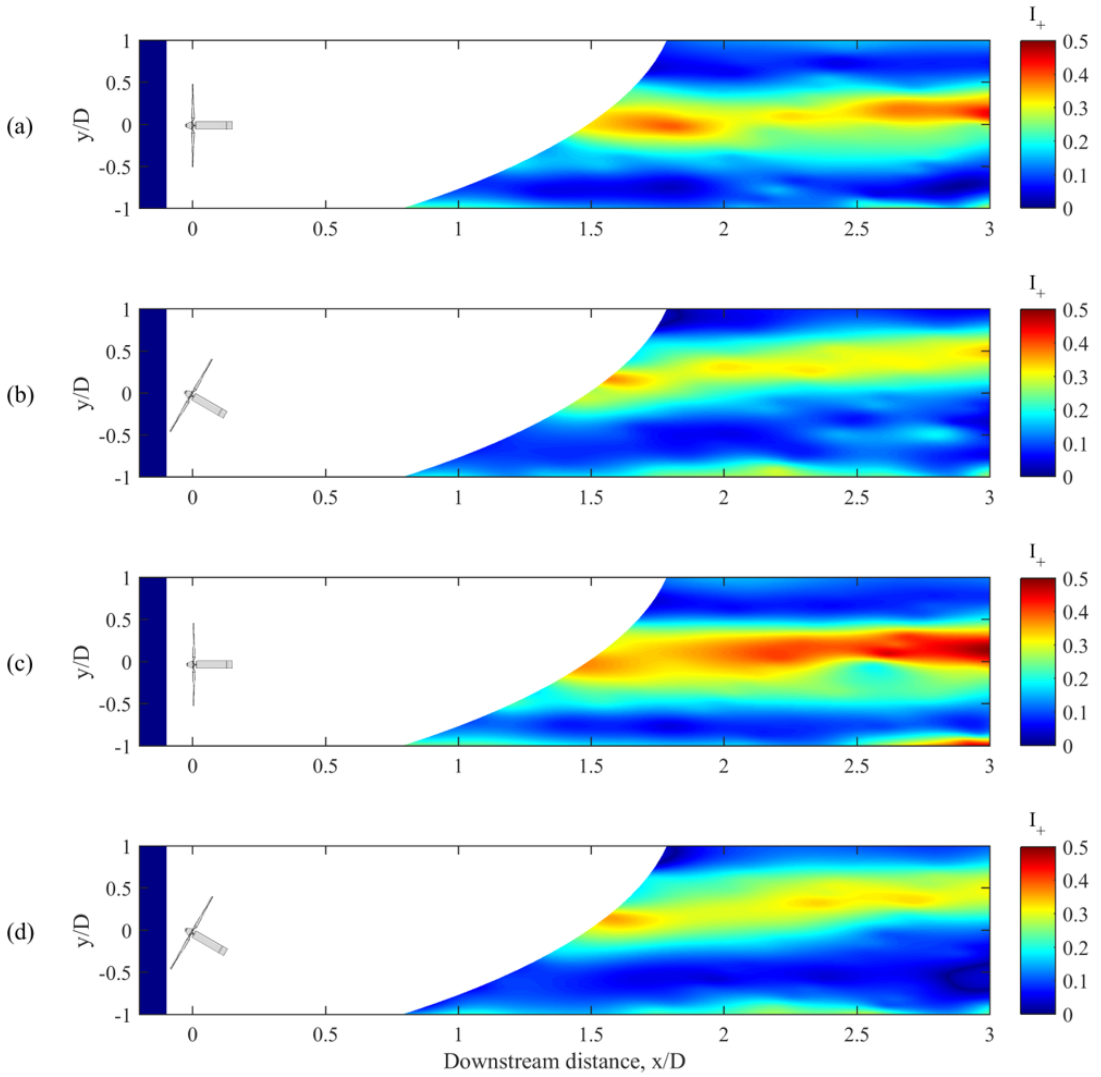

Figure 5.44: Streamwise added turbulence, I_+, in the wake of the UW WEG turbine at (a) $\gamma = 0°$, $\lambda = 3.6$, (b) $\gamma = 30°$, $\lambda = 3.6$, (c) $\gamma = 0°$, $\lambda = 4.1$, and (d) $\gamma = 30°$, $\lambda = 4.1$ (LiDAR measurements)

This trend can also be seen in Figure 5.45, which shows the maximum added turbulence as the flow moves downstream. The maximum added turbulence is seen to increase slightly as the flow moves downstream as shown in the contour plot of Figure 5.44. The highest increases occur with the un-yawed turbine, with an increase of approximately 25%. The

yawed turbine profile shows a relatively constant turbulence level has been reached in the measurement section.

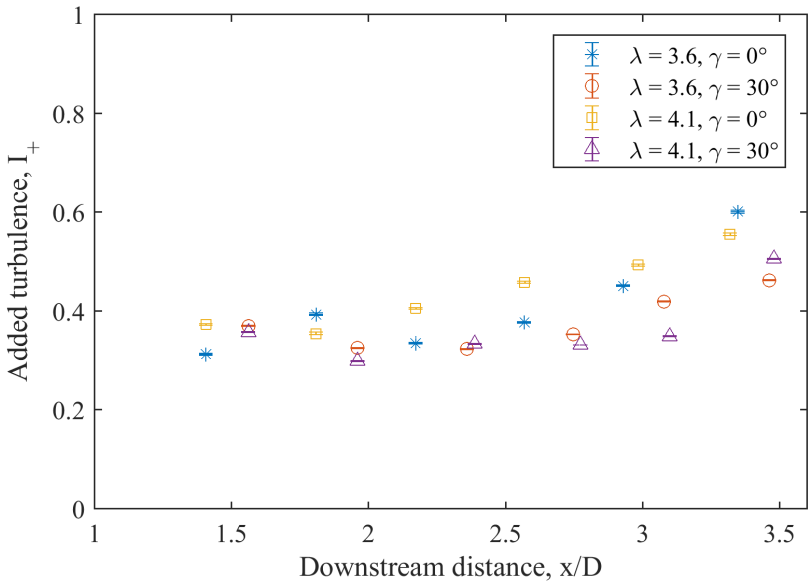

Figure 5.45: Maximum added turbulence in the wake of the UW WEG turbine (LiDAR measurements)

5.4.4 Wake Measurement Device Comparison

In order to compare each measurement technique, the effects of the yaw angle was assumed to be mirrored by the centre axis of the hub, since the Pitot Tree and sonic anemometer experiments were conducted at a yaw angle of -30° and the LiDAR experiment was conducted at a yaw angle of 30°. Therefore, whether the yaw was in the positive or negative direction it is assumed the effects are the same. The results of all three measurement techniques were compared for a single line traverse at a downstream distance of 2 D. The results were compared for yaw angles of 0° and -30° as well as tip speed ratios of 3.6 and 4.1. The comparison plots are shown in Figure 5.46 for the velocity profile and Figure 5.50 for the added turbulence.

Additionally, the minimum velocity, wake centre position, and maximum added turbulence were compared for all three methods at a tip speed ratio of 3.6 and for both yawed and un-yawed turbines. The comparison for these parameters are shown in Figures 5.47

to 5.48. The wake radius was also compared for the sonic anemometer and LiDAR experiments with quantitative results of the flow visualization experiment in Section 5.2.2 included, shown in Figure 5.49.

Velocity Profile

The comparison of the velocity profiles at 2 D are shown in Figure 5.46. Only two points were obtained for the Pitot Tree measurements due to the position of the pitot tubes at hub height. The span of the Pitot Tree is also limited and therefore does not extend to the ends of the wake expansion.

The velocity profile trend aligns for all three measurement devices. The profiles all show the velocity deficit in the wake of the turbine with the minimum velocity occurring at the same location. The sonic anemometer and Pitot Tree show slightly lower minimum velocities in each of the cases, but they are all within the uncertainty of the error. The position of the wake centre is also aligned in each case. This shows excellent agreement between the devices and shows the measurements were accurate from the repeatability of the measurements using different methods. Additionally, it shows that mirroring the profile to account for the different direction in yaw angles had a minimal impact.

Looking at the velocity deficit as it moves downstream from Figure 5.47, the magnitude of the deficit is similar, with more variation between the methods with the yawed turbine. However, the velocity of the Pitot Tree measurements in the un-yawed direction are smaller in comparison to the sonic anemometer and LiDAR measurements. Considering the large uncertainty associated with the Pitot Tree measurements, the results are still within error. With the yawed turbine, the methods are all within range at 2 D, however the Pitot Tree shows the velocity at 1 D higher than the rest, and the sonic anemometer shows a higher velocity at 3 D. It is expected that the velocity would recover as the wake develops, which was seen by the sonic anemometer.

The position of the wake centre, seen in Figure 5.48, shows a correlation between the trends of the methods. For the un-yawed turbine wake centre, all methods show the position to be constant as the flow moves downstream. However, the Pitot Tree measurements are offset from the centre, which is a possible misalignment of the device with respect to the turbine hub centre. The yawed trend shows the same deflection of the wake centre for all methods. It appears the wake is deflected between 1 D and 2.5 D then converges to a constant position at 3 D.

The wake radius is shown in Figure 5.49 as the wake moves downstream. The Pitot Tree cannot capture the full wake area and therefore was not included in the comparison.

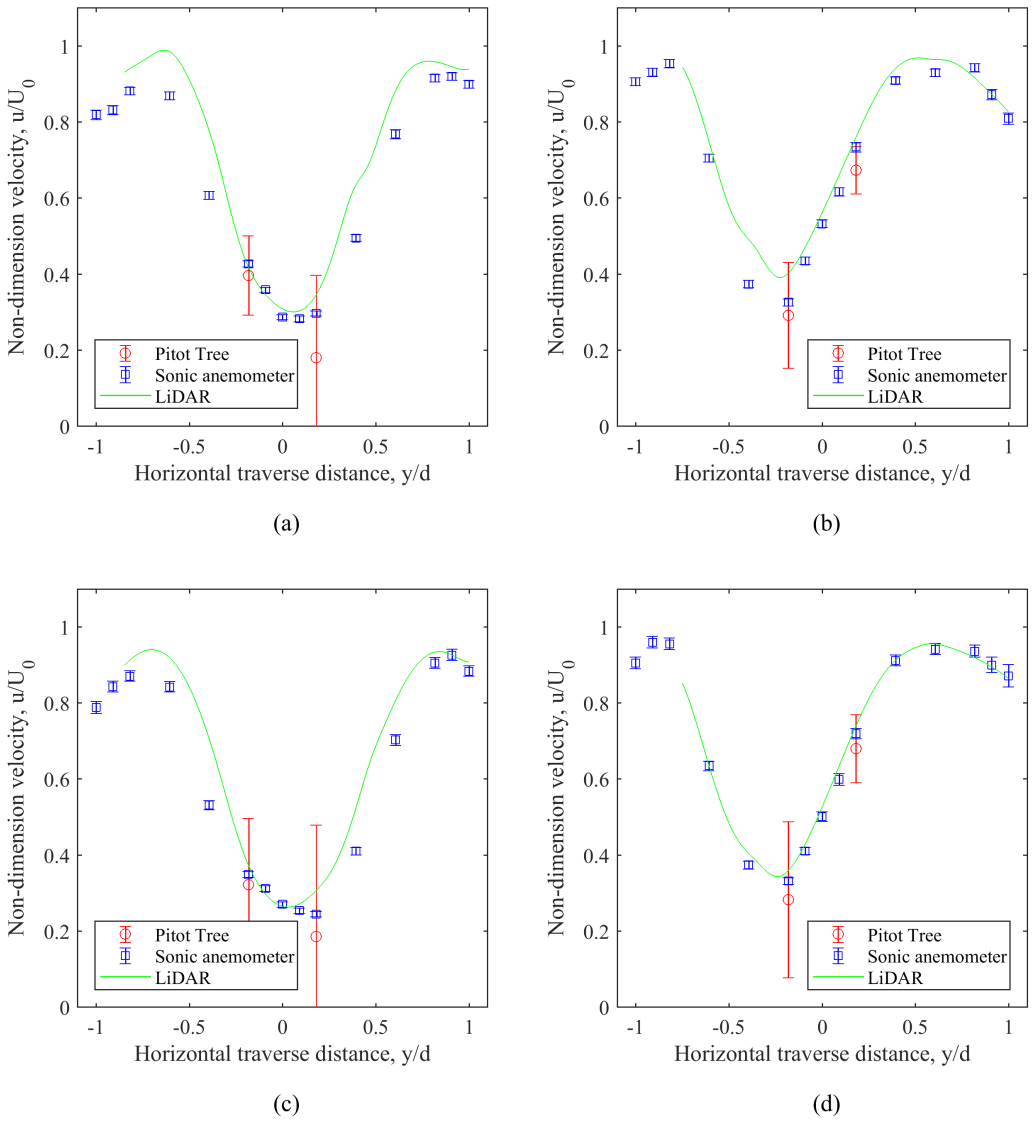

Figure 5.46: Comparison of Pitot Tree, sonic anemometer, and LiDAR velocity traverses in the wake of the UW WEG turbine at x/D = 2 with (a) $\gamma = 0°$, $\lambda = 3.6$, (b) γ = -30°, $\lambda = 3.6$, (c) $\gamma = 0°$, $\lambda = 4.1$, and (d) γ = -30°, $\lambda = 4.1$

However, quantitative measurements were obtained from the flow visualization results in Section 5.2.2 and are compared against the sonic anemometer and LiDAR measurements. The flow visualization was conducted at a tip speed ratio of 4.3, therefore the wake radius

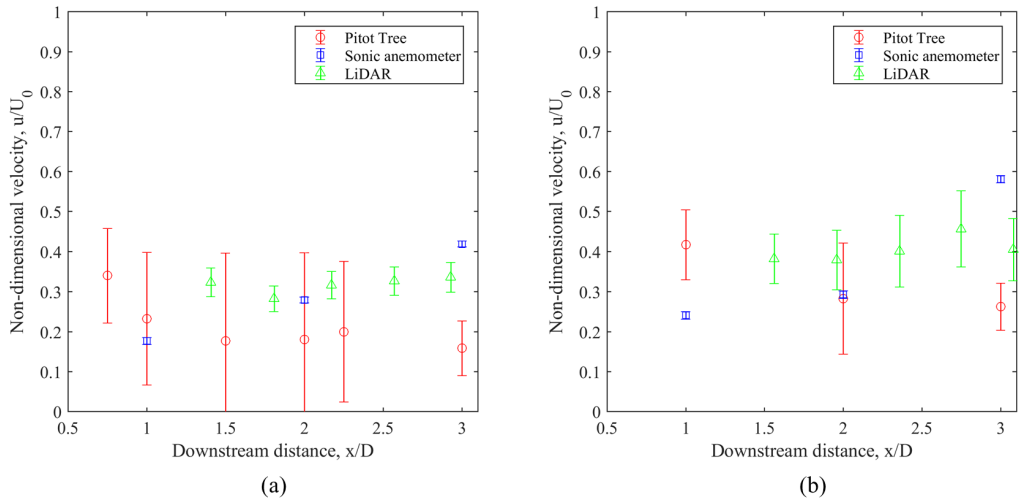

Figure 5.47: Comparison of minimum velocity in the wake of the UW WEG turbine for each measurement method at $\lambda = 3.6$ with (a) $\gamma = 0°$ and (b) γ = -30°

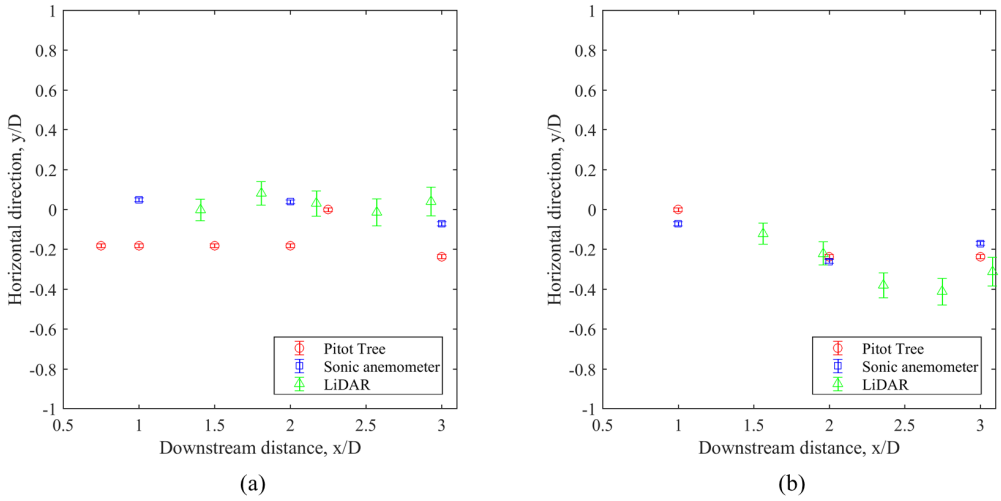

Figure 5.48: Comparison of horizontal position of minimum velocity in the wake of the UW WEG turbine for each measurement method at $\lambda = 3.6$ with (a) $\gamma = 0°$ and (b) γ = -30°

was compared for a tip speed ratio of 4.1 for the sonic anemometer and LiDAR wake measurements.

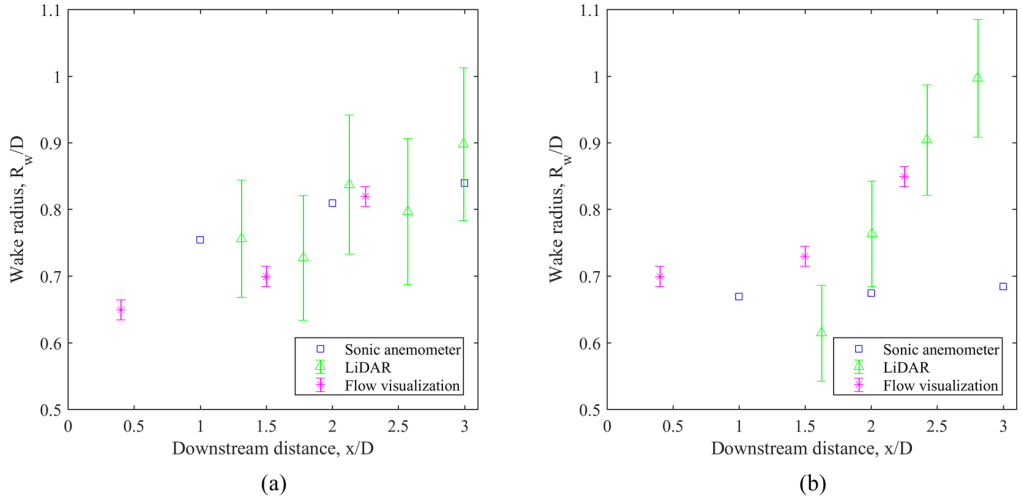

Figure 5.49: Comparison of wake radius behind the UW WEG turbine at $\lambda = 4.1$ with (a) $\gamma = 0°$ and (b) γ = -30°

The blade radius of the turbine when non-dimensionalized has a radius, R/D, of 0.5. Therefore, any values of the wake radius higher than this value shows expansion of the wake. In Figure 5.49, expansion is seen in all of the measurement methods.

At a yaw angle of 0°, all of the measurements show a similar correlation of values and trends. The wake is seen to increase as it moves downstream in all measurements, however more fluctuations are seen in the LiDAR measurements. This is a possible result of the error associated with measurements in the y-direction. At a yaw angle of -30°, however, there is more variability between measurement methods. The sonic anemometer wake radius is significantly lower than the LiDAR measurements. The flow visualization appears to follow the values of the sonic anemometer up to a distance of 1.5 D then correlates more to the LiDAR measurements. The wake size of the sonic anemometer is lower with the yawed turbine than the un-yawed, whereas both the flow visualization and LiDAR measurements have a higher radius. However, the increase in the wake radius from the flow visualization could be a result of distortion in the picture from the wake being closer to the camera from the offset of the hub centre when the turbine is yawed. It is expected that when the turbine is yawed the wake radius would be smaller as a result of the reduced thrust coefficient [18]. Additionally, the trend of the LiDAR and flow visualization measurements show the wake radius continuing to increase. Contrary to this, the sonic anemometer has a relatively constant wake radius, showing the wake is fully expanded.

Schepers [62] predicted the wake to be fully expanded at approximately 2.25 D, however this was for an un-yawed turbine under different conditions. Schepers also related the point where the wake is fully expanded to occur at the end of the near wake region. Therefore, the continual expansion of the LiDAR measurements after 1.5 D in the wake of the yawed turbine does match the behaviour as expected by Schepers. Due to the lower thrust coefficient with the yawed turbine, the wake expansion should be minimal as the flow progresses downstream, which was shown in the sonic anemometer measurements. The discrepancies of the LiDAR measurements are a possible result of the data extraction process to determine the points of the wake recovery to calculate the wake radius size.

Added Turbulence

The added turbulence is compared for each method in Figure 5.50 at 2 D. Due to significant uncertainty in the turbulence intensity measurements, the Pitot Tree measurements will not be considered in this section. It is seen from these plots that both methods have a close correlation of values and overall profile shape. The appearance of the double peak is seen in the sonic anemometer measurements, but not in the LiDAR measurements at this point. The turbulence profile appears to have similar trends, however the sonic anemometer has a higher overall turbulence level. This is possibly a result of the LiDAR measurements not being completely aligned with the hub height of the turbine as described in Section 4.4.3. The LiDAR measurements were taken at a height of 0.18 D above the hub in the z-direction, therefore the turbulence caused by the nacelle and wake centre would be reduced.

The maximum added turbulence can be seen for various downstream positions in Figure 5.51. The sonic anemometer shows a downward trend as expected from the theoretical behaviour of the wake. However, the LiDAR added turbulence is more constant with a slight increase in turbulence. It is difficult to see the actual trend of the LiDAR since the measurements begin at 1.5 D, which is the point in that the sonic anemometer measurements begin to converge. After this point, despite the differences in trends, the added turbulence levels are within the same range. Therefore, it can be expected that if the measurements of the LiDAR were to extend closer to the turbine, the same decreasing trend would be seen, with higher added turbulence occurring closer to the turbine.

Device Performance Comparison

The wake experiments performed using the Pitot Tree, sonic anemometer, and LiDAR measurement devices provided different measurement abilities for the varying devices. Each

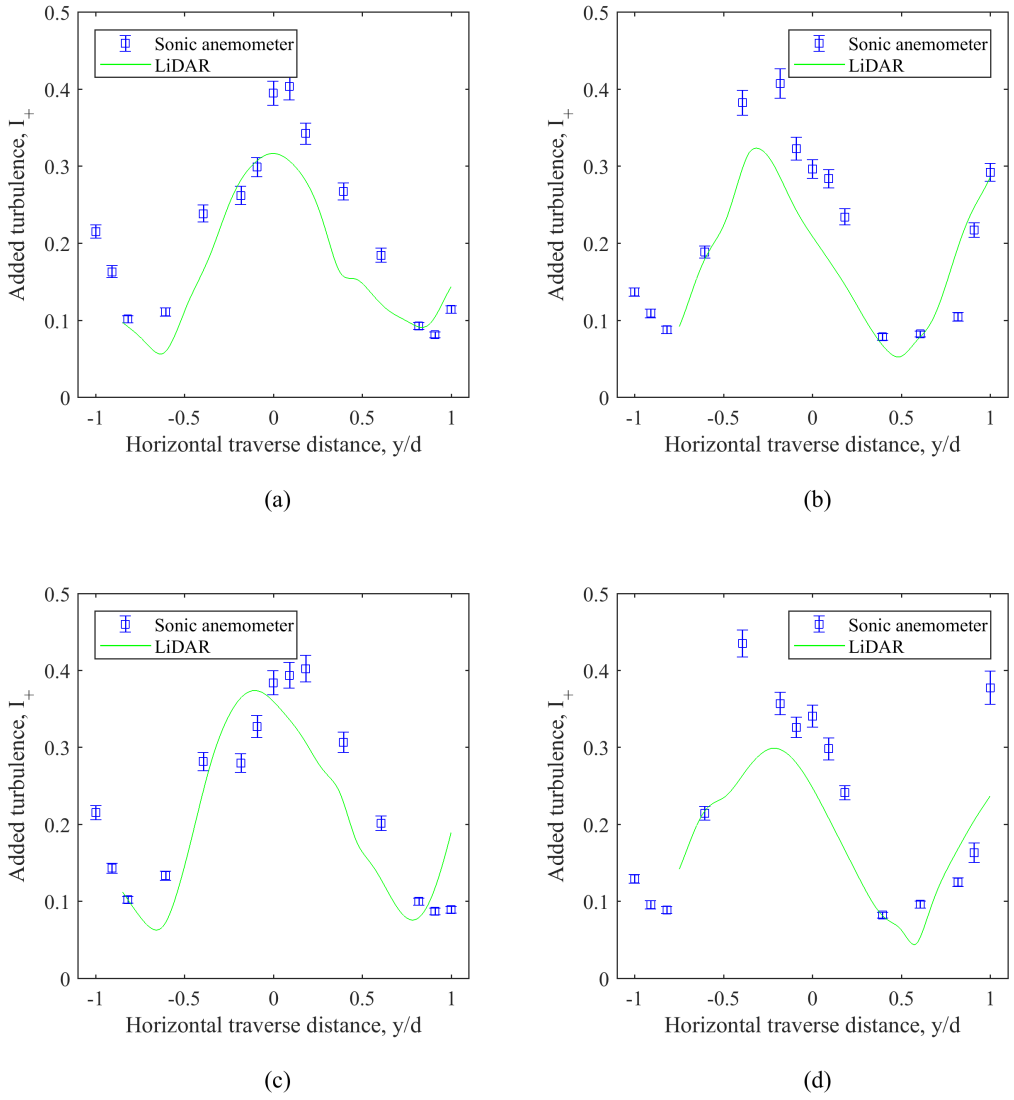

Figure 5.50: Comparison of sonic anemometer and LiDAR added turbulence traverses in the wake of the UW WEG turbine at x/D = 2 with (a) $\gamma = 0°$, $\lambda = 3.6$, (b) $\gamma = -30°$, $\lambda = 3.6$, (c) $\gamma = 0°$, $\lambda = 4.1$, and (d) $\gamma = -30°$, $\lambda = 4.1$

device showed benefits in providing useful wake measurements for different characteristics as well as differences in the ease of experimental measurements.

The Pitot Tree was able to provide a two-dimensional profile at various downstream

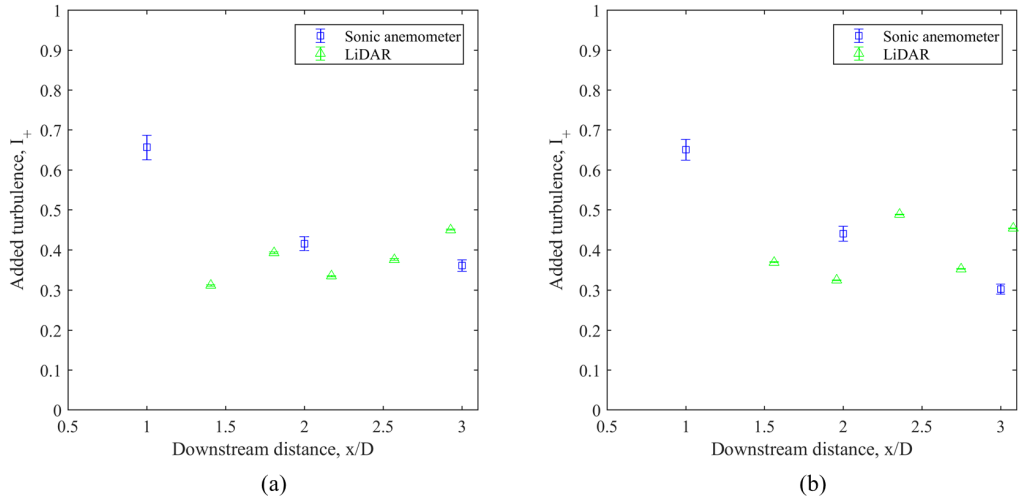

Figure 5.51: Comparison of sonic anemometer and LiDAR maximum added turbulence in the wake of the UW WEG turbine at $\lambda = 3.6$ with (a) $\gamma = 0°$ and (b) γ = -30°

positions. This allowed the vertical wake profile to be captured, whereas the other devices were only able to provide measurements at a single vertical direction. The Pitot Tree's simple setup allowed for more positions to be tested. Another benefit was the ability to provide temporal measurements of the wake profile for a particular downstream distance. The sonic anemometer and LiDAR were not able to provide this due to the traversing and sweeping measurement procedure. However, the resolution of the Pitot Tree is limited to the 16 pitot tubes on the structure. In addition, it was seen that the Pitot Tree's error is increased significantly with lower velocities due to the instrument precision. This caused issues in accurately measuring the turbulence in the wake. Therefore, the Pitot Tree is best used for initial measurements of the wake to obtain a velocity profile at various positions.

The sonic anemometer proved to be the most accurate of the devices, but also had the slowest data collection time. This allowed a better velocity and turbulence profile to be obtained. However, the experimental measurement process is time consuming and tedious, thereby limiting the amount of measurement points taken. It is possible to adjust the measurement height of the sonic anemometer, but this would increase the time to complete the experiments.

The LiDAR was able to provide a horizontal contour of the wake profile due to the sweeping measurement of the device during the experiment. With automated scanning, the device could provide full wake measurements with more ease than even the Pitot Tree. In addition, it has the ability to measure distances up to 200 m, making it a useful device

for field measurements. However, using the LiDAR inside of the Wind Generation Facility proved to be difficult due to the LiDAR's minimum measurement distance. Therefore, positioning the LiDAR inside the facility was challenging because of space constraints and the LiDAR measurements were limited in the area close to the turbine. In addition, the LiDAR's increasing focal length with the laser measurement distance introduces concerns of accuracy.

5.4.5 Wake Measurement Model Comparison

The behaviour of the wake is dependant on the thrust coefficient, C_T, and free stream turbulence intensity, I_0 [18], therefore in order to effectively compare against other experimental results in literature these parameters must be matched. However, several models have been developed to predict the velocity deficit of the wake depending on the input thrust coefficient and free stream turbulence intensity. Therefore, the models described in Section 2.2.3 can be used to validate the wake measurement experiments.

Velocity Profile

Figure 5.52 compares the results of the LiDAR wake measurements at a downstream distance of 2 D, tip speed ratio of 3.6, and yaw angle of 0° to the 2D_k Jensen [70], Ainslie [4], and Larsen [43] models described in Section 2.2.1. A thrust coefficient of 0.72 from Table 5.4 was used for the models with the measured average free stream turbulence of 4.8% from the wake experiments.

Comparing the LiDAR measurements with the models in Figure 5.52 shows an agreement of the velocity profiles. The minimum LiDAR velocity, is lower than all of the models, with a difference of 4% to the nearest model. Field measurements by Duckworth & Barthelmie [26] showed results with values of the wake deficit below each of the compared models as well at a distance of 2.5 D, as shown in Section 2.4. This adds to the confidence in the LiDAR velocity profile measurements.

The difference of the average velocity of the LiDAR measurements to the models from Figure 5.52 shows a deviation of 4% to the Ainslie model, 14% to the 2D_k Jensen model, and 8% to the Larsen model. Therefore, the Ainslie model was the best match to the experimental measurements. Compared to the results of Duckworth & Barthelmie [26], which showed a deviation of 12.8%, 22.7%, and 33.9% to the Ainslie, Jensen, and Larsen models respectively, shown in Section 2.2.3, the Ainslie model provided the best results

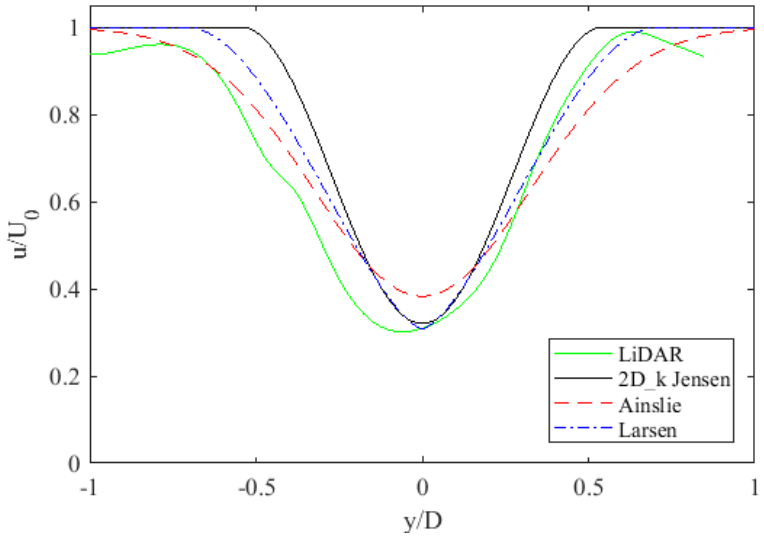

Figure 5.52: Comparison of experimental wake velocity profile to 2D_k Jensen [70], Ainslie [4], and Larsen [43] wake models for $\lambda = 3.6$ and $\gamma = 0°$ at 2 D with $C_T = 0.72$ and $I_0 = 4.8\%$

for both Duckworth & Barthelmie the LiDAR measurements. However, both experiments experience approximately the same deviation from the models.

The trend of the LiDAR velocity profile in Figure 5.52 follows closely to the profile predicted by the models. However, the LiDAR profile appears to be offset from the centre of the hub. This is a possible result of uncertainty in the measurement position. Aligning, the LiDAR profile with the centre of the hub, the velocity of the outer edges of the LiDAR profile would fit between the Ainslie and Larsen models. However, the models appear to have a sharper velocity deficit peak, whereas the LiDAR profile has a wider spread towards the centre of the wake.

Using the 2D_k Jensen and Larsen models, the minimum velocity can be compared for various downstream distances. This comparison is shown in Figure 5.53 for a tip speed ratio of 3.6 and yaw angle of 0° with the same thrust coefficient and free stream turbulence described in the previous comparison. Both the LiDAR and sonic anemometer measurements are used for comparison, since the sonic anemometer provides additional measurements closer to the turbine.

A similar velocity recovery trend is seen in both the models and the LiDAR measurements, which is also expected from theory of the wake propagation. The velocities are much closer at closer distances to the turbine, however. The LiDAR measurements ap-

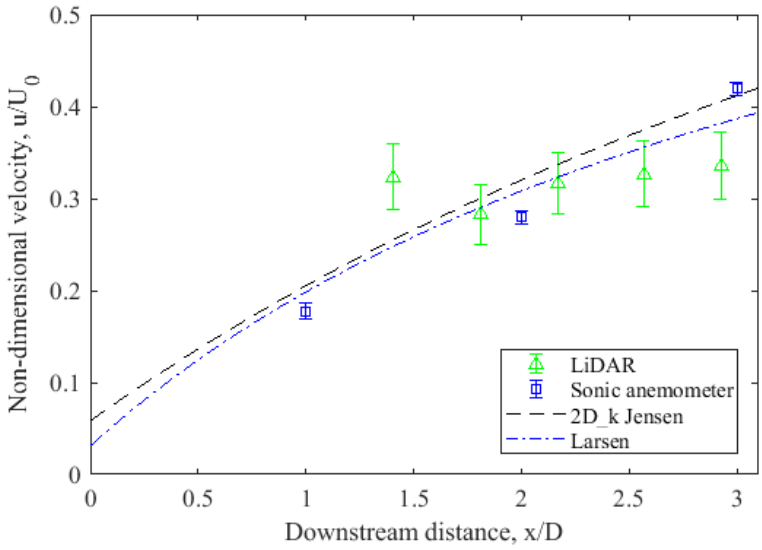

Figure 5.53: Comparison of minimum velocity measurements to 2d_k Jensen [70] and Larsen [43] wake models for $\lambda = 3.6$ and $\gamma = 0°$ against wake models with $C_T = 0.72$ and $I_0 = 4.8\%$

pear to have a slower recovery rate in comparison to the models. In addition, the LiDAR measurement at 1.4 D appears to not follow the trend.

The average deviation of the LiDAR measurements for the downstream distances was therefore determined to be 14% compared to the 2D_k Jensen model and 11% compared to the Larsen model. The sonic anemometer had a closer relation to the 2D_k Jensen model at 9% and the same deviation to the Larsen model with a 9% difference.

The models can also predict the size of the wake radius, which are compared to the LiDAR and sonic anemometer measurements in Figure 5.54 for the 2D_k Jensen and Larsen models. For consistency of the device comparison of wake radius measurements in Section 5.4.4, Figure 5.54 compares the wake radius at a tip speed of 4.1, which has a corresponding thrust coefficient of 0.77 from Table 5.4.

The models appear to significantly under predict the wake radius compared to the measurements of the LiDAR and sonic anemometer, however the increasing trend is seen in both the measurements and models. Therefore, there is an agreement that the wake is continuing to expand. The Larsen model has a higher predicted wake radius, which is closer to the values seen in the experimental measurements. An average difference of 46% and 25% was determined for the comparison of the LiDAR measurements against the 2D_k

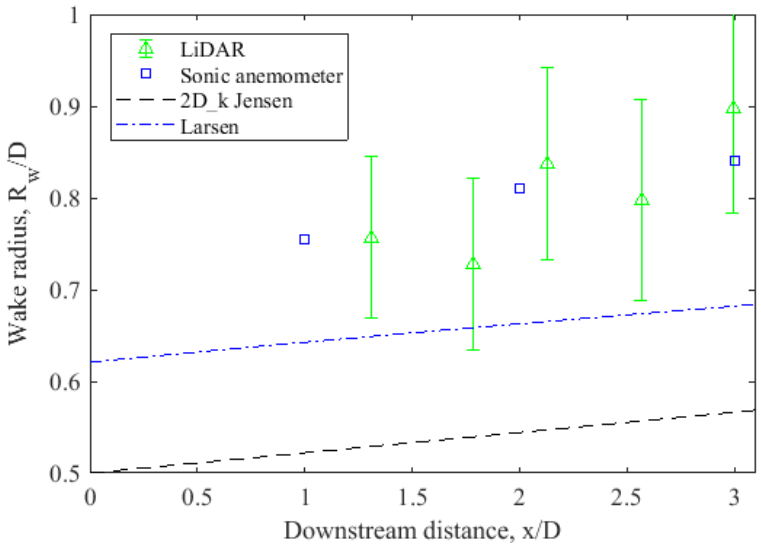

Figure 5.54: Comparison of minimum velocity measurements to 2d_k Jensen [70] and Larsen [43] wake models for $\lambda = 4.1$ and $\gamma = 0°$ against wake models with $C_T = 0.77$ and $I_0 = 4.8\%$

Jensen and Larsen models respectively. The sonic anemometer wake radius resulted in approximately the same average difference of 47% and 25% between the 2D_k Jensen and Larsen models.

Added Turbulence

The added turbulence in the wake was compared against models developed by Quarton & Ainslie [59], Ainslie et al. [5], and Larsen et al. [44] for the LiDAR and sonic anemometer measurements. The sonic anemometer was included in this comparison to show the trend of the added turbulence at closer downstream distances, since the LiDAR measurements are limited in that area. The comparison is shown in Figure 5.55.

Comparing the models to each other, the turbulence is significantly higher in the region close to the turbine. The turbulence level for each model declines at different positions, however, showing the variability in the models. From Figure 5.55, the trend of the added turbulence can be seen in the sonic anemometer measurements, which matches closest to the Hassan model, although the decline in turbulence begins at approximately 1 D in the sonic anemometer readings whereas the Hassan model shows a steep decline at

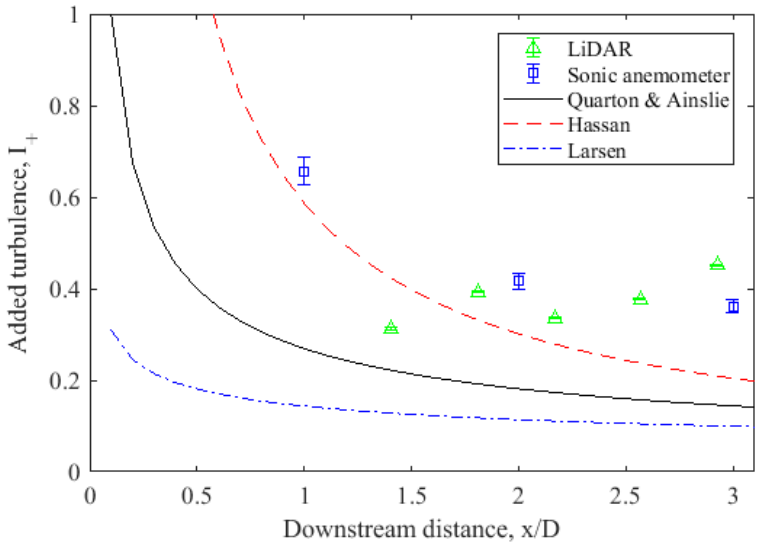

Figure 5.55: Comparison of experimental added turbulence to the Quarton & Ainslie [59], Hassan [5], and Larsen [44] turbulence models for $\lambda = 3.6$ and $\gamma = 0°$ against wake models with $C_T = 0.72$ and $I_0 = 4.8\%$

approximately 0.75 D. The LiDAR measurements have a similar trend as well, excluding the first point at 1.4 D.

After which, it is seen that each model converges to a constant value as the flow moves downstream. This is also seen in the sonic anemometer and LiDAR measurements, however the turbulence level that they converged to is over twice of that predicted by the models. As described in Section 5.4.1, this is a possible result of the facility exit area. As the flow in the facility reaches the door, an increase in turbulence was seen to start from the top of the facility and move down, therefore causing higher turbulence towards the exit area. Relating the distances of the facility to the notation in the experiments of this thesis, the exit of the facility occurs at approximately 3 D. Turbulence was seen to result in the upper portion of the facility starting at approximately 1.5 D and moving further down as it approaches the exit. Therefore, this profile is a possible result of the increased turbulence seen in the experimental measurements in comparison to the models.

The experimentally measured added turbulence was much higher than the models, however it seemed the trends had a correlation. The deviation, therefore, was significantly higher than the velocity comparison. The LiDAR had an average deviation of 160% compared to the Quarton & Ainslie model, 83% compared to the Hassan model, and the highest difference of 276% compared to the Larsen model. The sonic anemometer measurements

had a better relation, although still high. The difference was therefore 78%, 26%, and 233% compared to the Quarton & Ainslie, Hassan, and Larsen models respectively. The Larsen model correlation was significantly different, which grossly under predicted the turbulence seen in the measurements. However, the difference between the experimental turbulence and the Hassan model had a much better comparison. Duckworth & Barthelmie had a much closer relation to the models with a deviation of 19% and 13% in comparison to the Quarton & Ainslie and Larsen models respectively.

The Hassan model showed a close relation to the sonic anemometer measurements, and the best correlation to the LiDAR measurements. However, the model still had a significant difference. To improve this relation, the facility turbulence effects could be looked at more closely to determine the cause of the deviation. Additionally, the models might not be suited for the experiments as they were derived empirically from experiments under different conditions. Therefore, the models could be missing a key principle of the turbulent wake behaviour, which would also explain the noted variability between models.

Chapter 6

Conclusions

An influx of wind farms being developed has arose from the increasing demand for renewable energy. However, wakes generated from the turbines limit the placement distance of turbines within a wind farm. Wakes cause reduced production levels of downstream turbines and increase the maintenance due to increased loading from the turbulence of the wake. Therefore, the study of wind turbine wakes is essential to welcome the increasing wind energy development.

Wind turbine wakes have previously been studied, however these experiments were either conducted in wind tunnels with a scaled turbine in the order of 1:600 or in field measurements with variability and lack of control of incoming wind conditions. Therefore, this thesis provided a study of wind turbine wakes on a 3.3 m diameter turbine under controlled wind conditions. This was achieved using the University of Waterloo's Wind Generation Facility to provide adjustable and consistent wind speeds.

To ensure the accuracy of measurements, the Wind Generation Facility velocity profile was characterized to obtain a flow profile and near uniform distribution. Uneven flow distribution seen at the UW WEG turbine inside of the Wind Generation Facility prompted the need to characterize the flow of the facility. Previous attempts at determining the cause of the uneven flow resulted in the development of the Pitot Tree to measure the velocity profile in front of the UW WEG turbine. The Pitot Tree allowed for measurements to be taken and processed while changing the Wind Generation Facility fans settings to various configurations. It was found that a fully uniform distribution could not be achieved in the fan settings tested. However, a more uniform distribution was determined through the adjustment of the fan frequency settings of the facility. Since a completely uniform flow distribution could not be achieved, it is recommended to use the Pitot Tree to measure the

incoming flow profile before performing experiments. Any variation in the measurements by the flow distribution can therefore be accounted for.

Flow visualization was used to gain an initial understand of the behaviour of the wake of the UW WEG turbine. This was conducted using two methods, producing a stream of smoke upstream of the turbine and producing smoke from the tips of the blades of the turbine. The upstream smoke emission directed the stream at the rotor outer diameter to allow the blade tip to pass through the stream. As the turbine blade passed through the stream of smoke, a vortex could be seen to form. The vortex shed from the tip of the blade and propagated downstream with the flow of the wake. The blade ignited smoke technique used different coloured smoke emitters on each blade of the turbine with the smoke emitting from the tips of the blade. The smoke formed a helical wake distribution as it moved downstream. The helix angle could be estimated based on the angle of the smoke leaving the tips, which was determined to be 30°. Additionally, expansion in the wake could be seen, which appeared to converge to a fully expanded state. Mixing of the smoke from each blade occurred at 1.6 D, signalling the end of the near wake region. The different yaw angles resulted in a variation of the shape of the wake outer limits. The un-yawed flow visualization resulted in a circular wake shape, which changed to a oval shape in the yawed visualization.

Finally, measurements of the wake of the UW WEG turbine were performed inside the Wind Generation facility using three different measurement techniques. The techniques used the Pitot Tree, developed for the characterization of the flow in the facility, a sonic anemometer, and a LiDAR measurement device. The experiments were all performed at tip speed ratios of 3.6 and 4.1. The turbine was set to yaw angles of 0° and -30° for the Pitot Tree and sonic anemometer wake measurements and set to 0° and 30° for the LiDAR wake measurements.

A two-dimensional contour of the wake in the vertical and crosswind directions for several downstream positions was obtained using the Pitot Tree method. The contours provided a representation of the wake centre location and velocity deficit decay in the wake. It was seen that the wake velocity begins to decay at approximately 1 rotor diameter (D) from the turbine. The wake centre was seen to be deflected in the direction of the yaw angle, whereas the wake centre in the un-yawed angle remained relatively at the hub centre. Temporal measurements were also obtained to show the variation of the velocity distribution with time, which was seen to fluctuate about the hub centre in the un-yawed measurements and fluctuate in the deflection of the wake for the yawed measurements. The turbulence intensity in the measurements appeared to move in the vertical direction as the flow approached 3 D. This was estimated to be caused by the exit of the test facility at this position.

Sonic anemometer traverses resulted in a horizontal velocity profile distribution at various downstream positions. The velocity distribution showed a velocity deficit decay as seen in the Pitot Tree measurements. The near and far wake regions could be seen in the velocity and turbulence measurements, which was noted by the appearance of a double wake in the near region. The transition was seen to occur between 1 D and 2 D. A better representation of the turbulence decay could also be seen in these measurements.

LiDAR measurements allowed for a contour to be developed for the length of the wake. With the contour, a better result of the velocity profile could be seen as the wake moves downstream. In addition, it was seen how the expansion size and position of the wake changed. A clear deflection was seen in the yawed turbine measurements, with the un-yawed measurements showing an even distribution of the wake. The wake profile could be seen in both the velocity deficit and turbulence intensity contours.

Comparisons between each measurement device showed a reasonable correlation in the velocity and turbulence profiles for both un-yawed and yawed turbine measurements. The resolution of the Pitot Tree measurements were not as high in comparison to the sonic anemometer and LiDAR, but still matched with the profile distribution. Deflection of the wake was seen in all of the measurements from the wake of the yawed turbine. The deflection appeared to converge to consistent offset position from the centre of the turbine hub.

The LiDAR and sonic anemometer profiles were also compared against wake models for the same thrust coefficient and incoming turbulence. In comparison, the velocity profile matched the predictions of the model. The minimum velocity of the wake also matched the trend of the models, with the sonic anemometer providing closer values. The added turbulence as the flow moved downstream had a similar trend to the sonic anemometer measurement, however the LiDAR trend could not be seen clearly due to the limited measurements close the turbine. However, near the end of the wake measurements, between 1.5 D and 3 D, the turbulence levels were higher than predicted by the models. This was determined to be a result of the Wind Generation Facility since it was previously determined that the turbulence increased as the flow moved towards the exit of the facility.

Each of the measurement devices provided different information about the behaviour of the wake. The Pitot Tree was able to provide a two-dimensional profile at various downstream positions. This showed the wake in both the vertical and horizontal directions. Temporal measurements were also able to taken, showing how the wake changed with time. The sonic anemometer was able to provide accurate measurements of the horizontal velocity and turbulence profile of the wake. With this method, the characteristics of the wake regions could be determined, such as the location of the end of the near wake region.

The LiDAR scans gave an overview of the horizontal wake profile by providing a contour that extended the length of the wake. With this method, the wake behaviour could easily be seen, such as the expansion, velocity deficit, and wake deflection.

The study of a single turbine wake in this thesis provided information about the wake characteristics such as velocity deficit, wake expansion, and turbulence levels. A better understanding of wake behaviour can aid in the design of wind farm layouts. In addition, the behaviour of the wake when yawed was an interesting development to the research of wind turbine wakes. A wake deflection was clearly seen when the turbine was yawed at 30°, which appeared to reach a constant position as the flow moved downstream.

References

[1] A. Abdelrahman. Development of a wind turbine test rig and rotor for trailing edge flap investigation. Master's thesis, University of Waterloo, 2014.

[2] U.S. Energy Information Administration. Levelized cost and levelized avoided cost of new generation resources in the annual energy outlook 2018. Technical Report March, U.S. Energy Information Administration, 2018.

[3] J. F. Ainslie. Development of an eddy viscosity model for wind turbine wakes. *British Wind Energy Association*, 1985.

[4] J. F. Ainslie. Calculating the flowfield in the wake of wind turbines. *Journal of Wind Engineering and Industrial Aerodynamics*, 27:213–224, 1988.

[5] J. F. Ainslie, U. Hassan, H. G. Parkinson, and G. J. Taylor. A wind tunnel investigation of the wake structure within small wind turbine farms. *Wind Engineering*, 14:24–31, 1992.

[6] P. H. Alfredsson and J. Å. Dahlberg. A preliminary wind tunnel study of windmill wake dispersion in various flow conditions. Technical report, Aeronautical Research Institute of Sweden, 1979.

[7] I. Ammara, C. Leclerc, and C. Masson. A viscous three-dimensional differential/actuator-disk method for the aerodynamic analysis of wind farms. *Journal of Solar Energy Engineering*, 124(4), 2002.

[8] J. D. Anderson Jr. *Fundamentals of Aerodynamics*. McGraw-Hill, New York, fifth edition, 2011.

[9] The Canadian Wind Energy Association. Wind energy in Canada. Available: http://www.canwea.ca, 2017. [Accessed: 2018-08-21].

[10] J. Bartl. Wake measurements behind an array of two model wind turbines. Master's thesis, KTH School of Industrial Engineering and Management, 2011.

[11] M. Bastankhah and F. Porté-Agel. A wind-tunnel investigation of wind-turbine wakes in yawed conditions. *Journal of Physics: Conference Series*, 625:1–10, 2015.

[12] M. Bastankhah and F. Porté-Agel. Experimental and theoretical study of wind turbine wakes in yawed conditions. *Journal of Fluid Mechanics*, 806:506–541, 2016.

[13] M. H. Beale, M. T. Hagan, and H. B. Demuth. *Neural Network Toolbox User's Guide*, 2018.

[14] L. H. Benedict and R. D. Gould. Towards better uncertainty estimates for turbulence statistics. *Experiments in Fluids*, 22:129–136, 1996.

[15] C. Best. Measurement of fuel regression rate of a pool fire in crosswind with and without a large downwind blocking object. Master's thesis, University of Waterloo, 2010.

[16] F. Bingöl. Adapting a doppler laser anemometer to wind energy. Master's thesis, Technical University of Denmark, 2005.

[17] F. Bingöl, J. Mann, and G. C. Larsen. Light detection and ranging measurements of wake dynamics part I: One-dimensional scanning. *Wind Energy*, 13:51–61, 2009.

[18] T. Burton, N. Jenkins, D. Sharpe, and E. Bossanyi. *Wind Energy Handbook*. John Wiley & Sons, Ltd, Chichester, England, second edition, 2011.

[19] Campbell Scientific. *CSAT3 Three Dimensional Sonic Anemometer Instruction Manual*, 2015.

[20] International Electrotechnical Commission. Section 415-01: Wind turbines and wind turbine generator systems. Technical report, International Electrotechnical Commission, Geneva, Switzerland, 1999.

[21] R. M. Young Company. Wind monitor. Available: http://www.youngusa.com, 2018. [Accessed: 2018-09-07].

[22] A. Crespo and J. Hernández. Turbulence characteristics in wind-turbine wakes. *Journal of Wind Engineering and Industrial Aerodynamics*, 61:71–85, 1996.

[23] A. Crespo, J. Hernández, and S. T. Frandsen. Survey of modelling methods for wakes and wind farms. *Wind Energy*, 2:1–24, 1999.

[24] R. Danielian, H. E. Jørgensen, J. Mann, F. Bingöl, M. Harris, and T. Mikkelsen. Surface-layer wind and turbulence profiling from LiDAR: Theory and measurements. *European Wind Energy Association*, 2006.

[25] C. B. Devaud, J. Weisinger, D. A. Johnson, and E. J. Weckman. Experimental and numerical characterization of the flow field in the large-scale UW Live Fire Research Facility. *International Journal for Numerical Methods in Fluids*, 60:539–564, 2008.

[26] A. Duckworth and R. J. Barthelmie. Validation of wind turbine wake models. *Wind Engineering*, 32(5):459–475, 2008.

[27] S. Frandsen and M. L. Thøgersen. Integrated fatigue loading for wind turbines in wind farms by combining ambient turbulence and wakes. *Wind Engineering*, 23(6):327–339, 1999.

[28] T. Gallant. Quantitative measurement techniques for wind turbine blade aerodynamic performance. Master's thesis, University of Waterloo, 2017.

[29] B. Gaunt. Power generation and blade flow measurements of a full scale wind turbine. Master's thesis, University of Waterloo, 2009.

[30] Enola Gaye. Pyrotechnics. Available: https://wwwenolagaye.com. [Accessed: 2018-08-13].

[31] D. Gertz. An evaluation testbed for wind turbine blade tip designs winglet results. Master's thesis, University of Waterloo, 2011.

[32] D. Gertz and D. A. Johnson. An evaluation testbed for wind turbine blade tip designs baseline case. *International Journal of Energy Research*, 35:1360–1370, 2011.

[33] Google. Google Maps. Available: https://www.google.ca/maps, 2017. [Accessed: 2017-12-04].

[34] Pattern Energy Group. Harvesting the wind for Ontario. Available: http://k2wind.ca, 2018. [Accessed: 2018-08-21].

[35] M. M. Hand, D. A. Simms, L. J. Fingersh, D. W. Jager, J. R. Cotrell, S. Schreck, and S. M. Larwood. Unsteady aerodynamics experiment phase VI: Wind tunnel test configurations and available data campaigns. Technical Report NREL/TP-500-29955, National Renewable Energy Laboratory, Golden, Colorado, 2001.

[36] M. Harris, W. Barker, E. Burin des Roziers, M. Pitter, R. Scullion, and C. Slinger. Lidar calibration and performance validation process. Technical report, Natural Power, 2012.

[37] C. G. Helmis, K. H. Papadopoulos, D. N. Asimakopoulos, P. G. Papageorgas, and A. T. Soilemes. An experimental study of the near-wake structure of a wind turbine operating over complex terrain. *Solar Energy*, 54(6):413–428, 1995.

[38] G. V. Iungo and F. Porté-Agel. Volumetric lidar scanning of wind turbine wakes under convective and neutral atmospheric stability regimes. *Journal of Atmospheric and Oceanic Technology*, 31:2035–2048, 2014.

[39] D. A. Johnson, A. Abdelrahman, and D. Gertz. Experimental indirect determination of wind turbine performance and blade element theory parameters in controlled conditions. *Wind Engineering*, 36(6):717–737, 2012.

[40] I. Katić, J. Højstrup, and N. O. Jensen. A simple model for cluster efficiency. *European Wind Energy Association*, 7-9:407–410, 1986.

[41] P. Krogstad and M. S. Adaramola. Performance and near wake measurements of a model horizontal axis wind turbine. *Wind Energy*, 15:743–756, 2011.

[42] V. Lam. Development of wind resource assessment methods and application to the Waterloo region. Master's thesis, University of Waterloo, 2013.

[43] G. C. Larsen. A simple stationary semi-analytical wake model. Technical report, Risø National Laboratory, 2009.

[44] G. C. Larsen, J. Højstrup, and H. Aagaard Madsen. *Wind Fields in Wakes*, pages 764–768. H.S. Stephens & Associates, 1996.

[45] S. E. Larsen, S. E. Grying, N. O. Jonson, H. F. Jørgensen, and J. Mann. Mean wind and turbulence in the atmospheric boundary layer above the surface layer. In *Wind Energy: Proceedings of the Euromech Colloquim*. Springer, Berlin, Germany, 2007.

[46] A. Lewis. ZephIR Lidar, 2018. [Private communication].

[47] ZephIR Lidar. *ZephIR CSV Files User's Guide*, 2014.

[48] ZephIR Lidar. *Waltz User's Guide*, 2015.

[49] Magnetic-Declination.com. Magnetic declination angle in Kitchener, Canada. Available: http://www.magnetic-declination.com/Canada/Kitchener/335775, 2015.

[50] M. McKinnon and D. A. Johnson. Wind turbine wake effect visualization and LiDAR measurement techniques. In *CSME International Congress*, Toronto, Canada, May 27 – 30, 2018.

[51] M. McKinnon and D. A. Johnson. Experimental considerations of the wake effects of wind turbines. In *Canadian Congress of Applied Mechanics*, Victoria, Canada, May 29 – June 1, 2017.

[52] D. Medici. Experimental studies of wind turbine wakes - power optimisation and meandering. Technical report, KTH Mechanics, Royal Institute of Technology, Stockholm, Sweden, 2005.

[53] J. Medley. ZephIR Lidar, 2018. [Private communication].

[54] Air Movement and Control Association International. Field performance measurement. Technical report, Air Movement and Control Association International, Inc., Arlington Heights, IL, 2011.

[55] National Energy Board of Canada. Canada's energy future 2017: Energy supply and demand projections to 2040. Technical report, National Energy Board of Canada, 2017.

[56] Natural Power. *ZephIR z150 Operations & Maintenance Manual*. Ledbury, UK, 2009.

[57] A. Niayifar and F. Porté-Agel. A new analytical model for wind farm power prediction. *Journal of Physics: Conference Series*, 625:1–10, 2015.

[58] University of Waterloo Weather Station. UW Weather station. Available: http://weather.uwaterloo.ca, 2018. [Accessed: 2018-09-01].

[59] D. C. Quarton and J. F. Ainslie. Turbulence in wind turbine wakes. *Wind Engineering*, 14:15–23, 1990.

[60] Renewable NRG Systems. *Symphonie PLUS3® Data Logger and Accessories User's Manual*. Hinesburg, Vermont, 2015.

[61] B. Sanderse. Aerodynamics of wind turbine wakes: Literature review. *Energy research Centre of the Netherlands*, pages 1–46, 2009.

[62] J. G. Schepers. ENDOW: Validation and improvement of ECN's wake model. Technical report, ECN, 2003.

[63] Setra Systems. *Model 267*, 2017.

[64] C. Slinger and M. Harris. Introduction to continuous-wave doppler LiDAR. Technical report, Natural Power, Ledbury, UK, 2012.

[65] D. M. Somers. S833, S834, and S835 airfoils. Technical Report August, National Renewable Energy Laboratory, Port Matilda, Pennsylvania, 2005.

[66] R. J. A. M. Stevens and C. Meneveau. Flow structure and turbulence in wind farms. *Annual Review of Fluid Mechanics*, 49:311–339, 2016.

[67] NRG Systems. NRG 40C anemometer. Available: https://www.nrgsystems.com, 2018. [Accessed: 2018-09-07].

[68] Vestas Wind Systems. Turbines. Available: http://www.vestas.com, 2018. [Accessed: 2018-08-21].

[69] S. Tavoularis. *Measurements in Fluid Mechanics*. Cambridge University Press, Cambridge, 2005.

[70] L. Tian, W. Zhu, W. Shen, N. Zhao, and Z. Shen. Development and validation of a new two-dimensional wake model for wind turbine wakes. *Journal of Wind Engineering and Industrial Aerodynamics*, 137:90–99, 2015.

[71] I. Troen and E. Lundtang Petersen. *European Wind Atlas*. Risø National Laboratory, Roskilde, Denmark, 1989.

[72] J. Trujillo, F. Bingöl, G. C. Larsen, J. Mann, and M. Kühn. Light detection and ranging measurements of wake dynamics. part II: two-dimensional scanning. *Wind Energy*, 14:61–75, 2010.

[73] L. J. Vermeer, J. N. Sorensen, and A. Crespo. Wind turbine wake aerodynamics. *Progress in Aerospace Sciences*, 39:467–510, 2003.

[74] N. Vermeer. A review of wind turbine wake research at TU DELFT. *American Institute of Aeronautics & Astronautics*, 2001.

[75] P. E. J. Vermeulen. An experimental analysis of wind turbine wakes. *International Symposium on Wind Energy Systems*, pages 431–450, 1980.

[76] U. Wandinger. Introduction to Lidar. In C. Weitcamp, editor, *Lidar*, chapter 1, pages 1–18. Springer-Verlag, New York, 2005.

[77] J. Weisinger. Characterization of the University of Waterloo Live Fire Research Facility Wind Generation System. Master's thesis, University of Waterloo, 2004.

[78] C. Werner. Doppler wind Lidar. In C. Weitcamp, editor, *Lidar*, chapter 12, pages 325–354. Springer-Verlag, New York, 2005.

[79] F. M. White. *Fluid Mechanics*. McGraw-Hill, New York, seventh edition, 2011.

[80] D. Wood. *Small Wind Turbines*. Springer, London, 2011.

APPENDICES

Appendix A

Experimental Uncertainty

A.1 LiDAR Verification Uncertainty Calculations

During the LiDAR verification process, the LiDAR measurements were compared to a cup and vane anemometer for wind speed and direction, as described in Section 4.2.1. The uncertainty of the measurements for the cup anemometer, vane anemometer, and LiDAR are detailed in the following sections.

A.1.1 Cup Anemometer

The uncertainty in the cup anemometer velocity measurements is due to random error, shown in Eq. A.1, and instrument precision. The NRG cup anemometer has a precision uncertainty, Δu_{NRGcup}, of ± 0.5 m/s [67].

$$\Delta u_{RMS} = \pm \frac{2\sigma}{\sqrt{N}} \tag{A.1}$$

Therefore, the total uncertainty for the cup anemometer is calculated as:

$$\Delta u_{cup} = \pm \sqrt{\Delta u_{RMS_{cup}}^2 + \Delta u_{NRGcup}^2} \tag{A.2}$$

A.1.2 Vane Anemometer

Similarly, the vane anemometer also has uncertainty due to random error and instrument precision, with the added uncertainty due to the velocity direction correction and fit error, R^2, from Figure 5.19. The RMY vane anemometer had an instrument precision uncertainty, $\Delta u_{RMY\,vane}$, of $\pm 3°$ [21].

Therefore, the uncertainty of the vane anemometer is calculated as:

$$\Delta u_{vane} = \pm\sqrt{\Delta u_{RMS_{vane}}^2 + \Delta u_{RMY\,vane}^2} \tag{A.3}$$

Including the direction correction and fit error, the uncertainty becomes:

$$\Delta u_{vane_{actual}} = \pm\sqrt{\left(\frac{\partial \theta_{actual}}{\partial \theta_{vane}}\Delta u_{vane}\right)^2 + (\theta_{vane}(1-R^2))^2} \tag{A.4}$$

This equates to:

$$\Delta u_{vane_{actual}} = \pm\sqrt{(0.7724\Delta u_{vane})^2 + (\theta_{vane}(1-0.9789))^2} \tag{A.5}$$

A.1.3 LiDAR

The LiDAR uncertainty was calculated from the random error due to the standard deviation in the velocity and directions, as calculated used Eq. A.1.

A.2 Wake Measurement Uncertainty Calculations

The wake measurements, outline in Section 4.4, used the Pitot Tree from Section, sonic anemometer, and LiDAR to take measurements in the wake of the UW WEG turbine. Details on the Pitot Tree, sonic anemometer, and LiDAR are given in Sections 3.2, 3.3, and 3.4 respectively. The uncertainty associated with each device is given in the following sections.

A.2.1 Pitot Tree

Velocity

Uncertainty in the velocity measurements are a result of the instrument precision, including the DAQ resolution, transducer accuracy, and calibration, and the random error of measurements.

The DAQ has a 32 bit resolution and a 0-10 V range of the Setra 267 pressure transducer. Therefore, the uncertainty in the DAQ, Δu_{DAQ}, is calculated as follows:

$$\Delta u_{DAQ} = \pm \frac{10[V]}{2^{32-1}} \tag{A.6}$$

The Setra 267 transducer has range of 0-10 V and an accuracy of 1% full scale. Therefore, the uncertainty in the transducer, $\Delta u_{Transducer}$, is calculated from the following:

$$\Delta u_{Transducer} = \pm 10[V] \times 0.01 \tag{A.7}$$

Combing the uncertainty of the DAQ and transducer results in the instrument precision uncertainty, Δu_{E_0}.

$$\Delta u_{E_0} = \pm \sqrt{\Delta u_{DAQ}^2 + \Delta u_{Transducer}^2} \tag{A.8}$$

The instrument precision uncertainty is converted to pressure from the calibration measurements in Section 3.2.2. The calibration slope, $\frac{\partial P}{\partial E}$, is obtained from Table 3.5.

$$\Delta u_{P_0} = \pm \frac{\partial P}{\partial E} \Delta u_{E_0} \tag{A.9}$$

The instrument precision uncertainty can therefore be derived for the velocity calculations. The final uncertainty in the instrument for the Pitot Tree velocities, Δu_{v_0}, is therefore calculated as below:

$$\Delta u_{v_0} = \pm \frac{\partial v}{\partial P} \Delta u_{P_0} = \pm \frac{1}{2} \sqrt{\frac{2}{\rho P}} \Delta u_{P_0} \tag{A.10}$$

Random error, Δu_{RMS}, from the measurements is calculated with a 95% confidence as shown below, where σ is the standard deviation of the velocity and N is the sample size of measurements.

$$\Delta u_{RMS} = \pm \frac{2\sigma}{\sqrt{N}} \tag{A.11}$$

The combined uncertainty due to random error and the transducer, $\Delta u_{\bar{v}_0}$, is therefore:

$$\Delta u_{\bar{v}_0} = \pm \sqrt{\Delta u_{v_0}^2 + \Delta u_{RMS}^2} \tag{A.12}$$

An average of the upstream measurement was calculated by taking the average all 16 transducer readings, where $\Delta u_{v_{N_T}}$, is the error of the velocity from each transducer with N_T representing the transducer number. Therefore, the upstream uncertainty, Δu_{U_0}, results in:

$$\Delta u_{U_0} = \pm \frac{1}{2} \sqrt{\Delta u_{v_1}^2 + \ldots + \Delta u_{v_{16}}^2} \tag{A.13}$$

Using the upstream error, the non-dimensionalized velocity uncertainty, $\Delta u_{\frac{v}{U}}$, is calculated as the following, where v is the local velocity and U_0 is the upstream velocity:

$$\Delta u_{\frac{v}{U}} = \pm \sqrt{\left(\frac{\partial v}{\partial \frac{v}{U}} \Delta u_{\bar{v}_0}\right)^2 + \left(\frac{\partial U}{\partial \frac{v}{U}} \Delta u_{U_0}\right)^2} \tag{A.14}$$

Therefore, the derived formula is calculated as:

$$\Delta u_{\frac{v}{U}} = \pm \sqrt{\left(\frac{\Delta u_{\bar{v}_0}}{U_0}\right)^2 + \left(\frac{\Delta u_{U_0} v^2}{{U_0}^2}\right)^2} \tag{A.15}$$

Turbulence Intensity

Uncertainty in the random error of the variance, $\Delta u_{v_{RMS}}$, is calculated using a 95% confidence interval and assuming a normal distribution [14].

$$\Delta u_{v_{RMS}} = \pm \frac{2\sigma}{\sqrt{2N}} \tag{A.16}$$

The turbulence intensity is calculated from the variance of the velocity over the local mean velocity, as shown in Eq. 2.25. Therefore, the total uncertainty of the turbulence,

Δu_I, is a combination of the random error of the variance, $\Delta u_{v_{RMS}}$, and local velocity uncertainty, $\Delta u_{\bar{v}_0}$. The total uncertainty of the turbulence is derived as follows:

$$\Delta u_{\frac{v}{U}} = \pm\sqrt{\left(\frac{\partial I}{\partial \sigma}\Delta u_{v_{RMS}}\right)^2 + \left(\frac{\partial I}{\partial v}\Delta u_{\bar{v}_0}\right)^2} \tag{A.17}$$

This equates to:

$$\Delta u_I = \pm\sqrt{\left(\frac{\Delta u_{v_{RMS}}}{v}\right)^2 + \left(\frac{\Delta u_{\bar{v}_0} I}{v^2}\right)^2} \tag{A.18}$$

Position

The Pitot tube position uncertainty is a result of the manufacturing of the Pitot Tree to position the pitot tubes and place the Pitot Tree in the measurement location. This results in an estimated uncertainty of ±1.4 cm in the x, ±1 cm in the y-direction, and ±1.1 cm in the z-direction.

A.2.2 Sonic Anemometer

Velocity

The instrument error was determined to be ±8 cm/s due to the offset error.

Therefore, the total uncertainty of the sonic anemometer velocity measurements are a combination of the instrument error, $\Delta u_{\bar{v}_0}$, and random error, Δu_{RMS}:

$$\Delta u_{\bar{v}_0} = \sqrt{\Delta u_{\bar{v}_0}^2 + \Delta u_{RMS}^2} \tag{A.19}$$

The Pitot tree was used to provide the average upstream wind velocity to non-dimensionalize the measurements. Therefore, the total non-dimensionalized velocity uncertainty, $\Delta u_{\frac{v}{U}}$, of the sonic anemometer is:

$$\Delta u_{\frac{v}{U}} = \pm\sqrt{\left(\frac{\partial v}{\partial \frac{v}{U}}\Delta u_{\bar{v}_0}\right)^2 + \left(\frac{\partial U}{\partial \frac{v}{U}}\Delta u_{U_0}\right)^2} \tag{A.20}$$

which equates to:

$$\Delta u_{\frac{v}{U}} = \pm\sqrt{\left(\frac{\Delta u_{\bar{v}_0}}{U_0}\right)^2 + \left(\frac{\Delta u_{U_0} v^2}{{U_0}^2}\right)^2} \tag{A.21}$$

Position

Alignment to the direction of the flow was neglected since the average of all velocity components was used in the calculations. Therefore, the sonic anemometer had an uncertainty of ±1 cm in the x and y-directions for positioning the sonic anemometer in the measurement location. An error of ±0.5 cm in the z-direction is a result of position the sonic anemometer head at hub height..

Turbulence Intensity

The turbulence intensity was calculated as in the Pitot tree analysis, with the uncertainty of the variance a result of random error, as calculated the same as the Pitot Tree in Eq. A.16, and the uncertainty in velocity measurements taken from the total uncertainty of sonic anemometer velocity, $\Delta u_{\bar{v}_0}$.

A.2.3 LiDAR

The main error of the LiDAR uncertainty is a result of the location of measurements due to alignment of the laser, positioning the LiDAR, and area of the laser focal point.

The velocity and turbulence intensity uncertainty are only a result of the random error of measurements. The calculation can be seen in the Pitot tree uncertainty analysis from Eq. A.11 and Eq. A.16 respectively.

Position

The LiDAR measurement position is related to angle of the LiDAR directed at the flow and the measurement distance of the laser focal point from the LiDAR. Alignment of the laser with determined to have an error of ±2.5 cm in the x and y-direction, which equates to a rotation error of ±0.1° to position the LiDAR measurement location. In addition, the LiDAR focal length changes based on the measurement distance [24]. From Danielian et

al. [24] it was determined that the focal length, L_F, can be calculated from the fit function in Eq. A.22, where H_m is the line-of-sight distance of the focal point from the LiDAR. The maximum laser focal width was 1 mm, which was insignificant in comparison to the focal length [24].

$$L_F = 0.0024H_m^2 + 0.0055H_m \tag{A.22}$$

The LiDAR measurement position uncertainty in the z-direction is a result of uncertainty in the leveling of the LiDAR, which was estimated to be ±0.5°. Therefore, the measurement height is also a function of the focal distance from the LiDAR.

The maximum and minimum uncertainty values for the measurement position of the LiDAR are therefore shown in Table A.1. The uncertainty in all directions increases as the focal distance from the LiDAR increases. The maximum uncertainty occurs at the furthest line-of-sight distance of 17.4 m and the minimum at the closest distance of 11.6 m.

Table A.1: LiDAR position uncertainty values

Direction	Max Uncertainty	Min Uncertainty	Source
x	±0.41 m	±0.17 m	Estimate / specifications [24]
y	±0.31 m	±0.04 m	Estimate / specifications [24]
z	±0.15 m	±0.10 m	Estimate

A.2.4 Density

The air density was calculated using the temperature readings from a digital thermometer and atmospheric pressure taken from the UW Weather Station [58]. The temperature was seen to vary within ±5° during the measurement day. The error is pressure, $\Delta u_{P_{atm}}$, was estimated to by ±80 Pa [32]. Therefore, the uncertainty, Δu_ρ, in density is determined from the equation:

$$\Delta u_\rho = \pm\sqrt{\left(\frac{\partial\rho}{\partial T}\Delta u_T\right)^2 + \left(\frac{\partial\rho}{\partial P}\Delta u_{P_{atm}}\right)^2} \tag{A.23}$$

The derived equation is as follows, where R_{air} is the gas constant:

$$\Delta u_\rho = \pm\sqrt{\left(\frac{P}{R_{air}T^2}\Delta u_T\right)^2 + \left(\frac{1}{R_{air}T}\Delta u_P\right)^2} \tag{A.24}$$

The uncertainty in density was calculated to be ± 0.02 kg/m^3 for each measurement.

A.2.5 Tip Speed Ratio

The tip speed ratio is calculated using Eq. 2.8. The error in tip speed ratio, Δu_λ, is therefore a result of uncertainty in the rotational speed, Δu_Ω, blade radius, Δu_R, and incoming velocity measurements from the Pitot Tree, Δu_{U_0}. The uncertainty of the tip speed ratio is therefore calculated from:

$$\Delta u_\lambda = \pm\sqrt{\left(\frac{\partial\lambda}{\partial\Omega}\Delta u_\Omega\right)^2 + \left(\frac{\partial\lambda}{\partial R}\Delta u_R\right)^2 + \left(\frac{\partial\lambda}{\partial U_0}\Delta u_{U_0}\right)^2} \tag{A.25}$$

The derived formula is therefore:

$$\Delta u_\lambda = \pm\sqrt{\left(\frac{R}{U_0}\Delta u_\Omega\right)^2 + \left(\frac{\Omega}{U_0}\Delta u_R\right)^2 + \left(\frac{\Omega R}{U_0^2}\Delta u_{U_0}\right)^2} \tag{A.26}$$

The error in rotational speed was determined to be negligible due to the controller feedback system described in Section 3.1.2. The blade radius error was estimated by Gertz [32] to be ± 0.005 m. Therefore, the uncertainty in the tip speed ratio was determined to be ± 0.32 for a tip speed ratio of 3.6 and ± 0.49 for a tip speed ratio of 4.1.

A.2.6 Thrust Coefficient

The thrust coefficient uncertainty, Δu_{C_T}, is due to the error associated with measuring the axial induction factor as shown in Eq. 2.12. Therefore the derived uncertainty is:

$$\Delta u_{C_T} = \pm\frac{\partial C_T}{\partial a}\triangle u_a \tag{A.27}$$

This equates to:

$$\Delta u_{C_T} = \pm 4(1-2a)\triangle u_a \tag{A.28}$$

The uncertainty of the axial induction factor was determined from the measurements by Johnson et al. [39]. This was determined to by ± 0.03 for both a tip speed ratio of 3.6 and 4.1. Therefore, the uncertainty in thrust coefficient is ± 0.06.

Appendix B

Wind Facility Velocity Uniformity Characterization

It was determined that there is non-uniformity of the velocity profile in the Controlled Wind Facility seen at the wind turbine location. This non-uniformity is problematic to perform accurate experiments inside of the facility. Therefore, the following sections look at the work completed to the explore and correct potential causes. Evidence of the non-uniformity was provided by Gallant [28], Best [15], and Weisinger [77].

B.1 Fan Position Representation

When referring to data representation of each fan, the tables are formatted to represent the position of each fan from the view inside the Wind Generation Facility. Therefore, the position of the data in each table representing the fan layout will correspond to the fans as shown in Table B.1.

Table B.1: Fan Position Representation

Top South	Top Middle	Top North
Bottom South	Bottom Middle	Bottom North

B.2 Fan Characteristics

The first attempt to troubleshoot the issue was to look at the current output of the fans running at 30 Hz and 60 Hz. The current readings of the fans at both frequencies are shown in Table B.2 and B.3.

Table B.2: Current readings of fans running at 30 Hz

33 A	34 A	33 A
34 A	36 A	37 A

Table B.3: Current readings of fans running at 60 Hz

72 A	80 A	73 A
72 A	70 A	72 A

The current was seen to vary between each fan, but there was no significant difference that could be corrected right away and it was unknown how much the current difference affected the flow out of each fan if any.

B.3 Fan Blade Angles

The angles of the fan blades were measured to determine if the fan blade angles were constant within each fan and across all fans, which may be a cause of possible flow rate variation among the fans. Each fan consists of 16 blades. The angle of each blade was measured with respect to the line of rotation of the fans. The angles were then averaged to get a single value for each fan for comparison.

B.3.1 Results

The results of the fan angle measurements are shown in Table B.4.

Table B.4: Fan blade angles with respect to the line of rotation

15.0°	15.7°	15.4°
14.4°	15.0°	15.1°

It can be seen that the fan with the highest angle is the top middle fan and the fan with the lowest blade angle is the bottom south fan. The difference of the fan angles is a possible contributor to the uneven flow, however it is unknown how much of an impact the angle difference has on the velocity profile.

B.4 Back Draft Dampers

Each of the six fans in the facility had a back draft damper installed at the outlet to prevent back draft from occurring. Over time the dampers became corroded and fixed in an open position. However, each damper was fixed with a different opening amount. The next steps were to adjust each of the dampers to ensure consistent opening amount between all the fans.

Threaded rods held on to the dampers by clamps were attached and adjusted so that the opening of each fan was equal. The fixed damper can be seen in Figure B.1. Due to placement of the blocks to prevent the dampers from opening too much, the top middle fan damper had to be fixed with less of an opening amount than the rest of the fans. The angle on each side of the damper was made constant by placing metal brackets between the blocks and the damper, however.

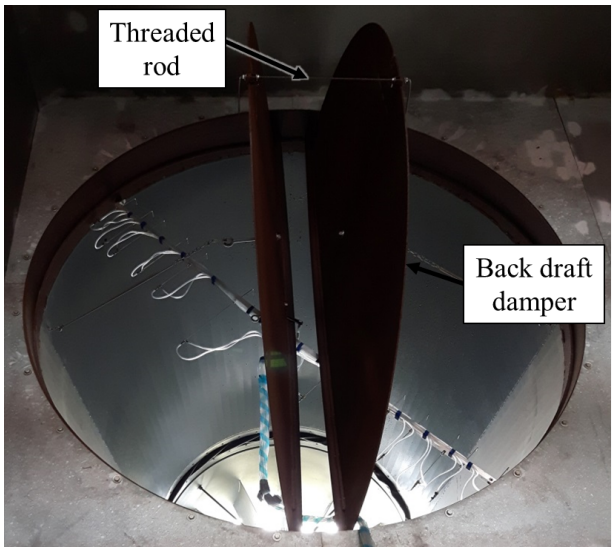

Figure B.1: Fixed back draft damper for the top south fan

B.5 Wind Turbine Velocity Profile

The velocity profile in front of the wind turbine was measured to more accurately determine the location of the velocity discrepancy.

B.5.1 Experimental Setup

A pitot tube array was designed to place in front of the turbine and measure the velocity at various heights, see Figure B.2. Four pitot tubes were positioned in a vertical direction along the pitot tube array. The pitot tube array was traversed in front of the wind turbine to obtain a velocity profile for the area. The pitot tubes were spaced at a distance of 91 cm (36") apart and the first pitot tube was located at 127 cm (54") from the ground, then raised to 183 cm (72") from the ground to obtain 8 different vertical heights. The pitot tube array and distances are shown in Figure B.3.

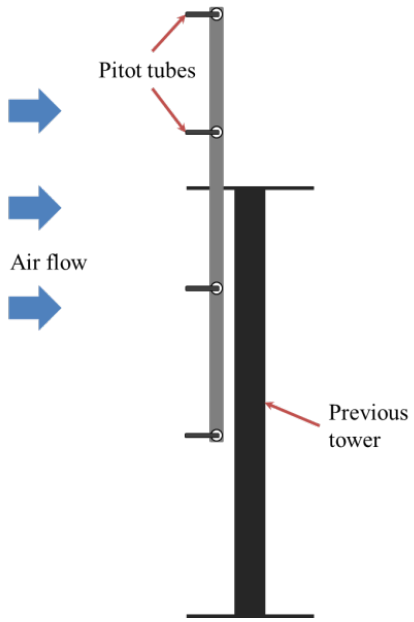

Figure B.2: Pitot tube array design

The pitot tubes were attached to four Setra 267 pressure transducers and relayed the data to a DAQ via WiFi connection. The sonic anemometer was positioned upstream and on the south side of the fans to provide a consistent velocity reading. Figure B.4 shows the positions of the pitot tube array and sonic anemometer in the measurement setup.

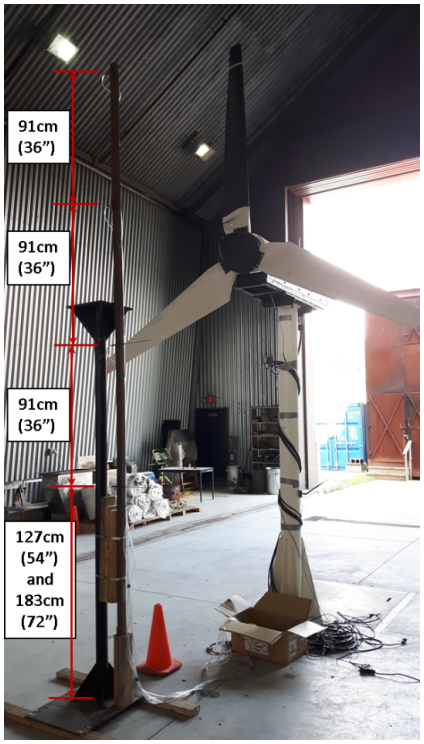

Figure B.3: Pitot tube array and pitot tube positions

B.5.2 Measurements

During the measurements, the pitot tube array was placed 1.5 m upstream of the base of the turbine and moved 50 cm north and south from the middle position of the turbine to a maximum of 150 cm in each direction. The total corresponding distances of each of the measurements are as follows:

Vertical distances from floor [cm]: 127, 173, 228, 274, 320, 366, 411, 457

Horizontal distances from turbine middle [cm]: -150, -100, 50, 0, 50, 100, 150

where positive position represents north and negative is south. The fans were run at 2 frequencies of 30 Hz and 60 Hz for each measurement. The data was taken at 10,000 Hz for a sample size of 1,200,000 data measurement points.

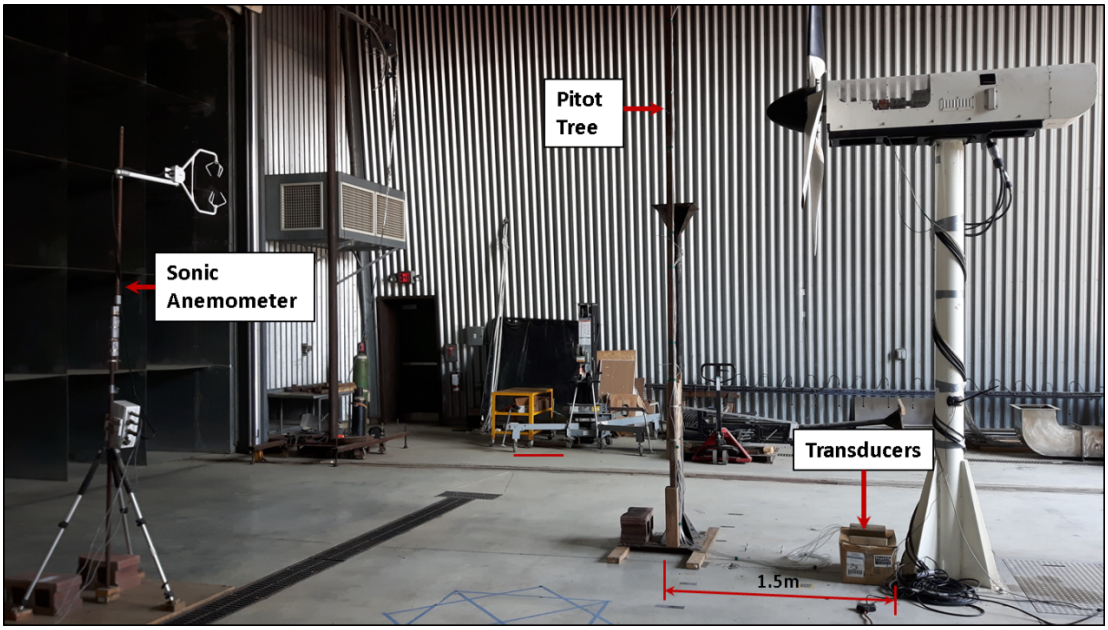

Figure B.4: Measurement setup

B.5.3 Results

After the measurements were taken, the data was adjusted based on the calibration of the transducers and analyzed to provide a velocity contour, as shown in Figure B.5. The velocity contour values were non-dimensionalized based on the velocity readings of the sonic anemometer.

It can be seen from the results of the velocity measurements that there is an increase in velocity in the upper north corner and a decrease in the upper middle region. The decrease is possibly due to the turbine blade blocking the flow, which was positioned in that region.

B.6 Fan Flow Rate Comparison

The flow rate of each fan was determined to compare each fan. The results were used to determine if there was any difference between the fan outputs that could contribute to the downstream non-uniformity of the velocity profile

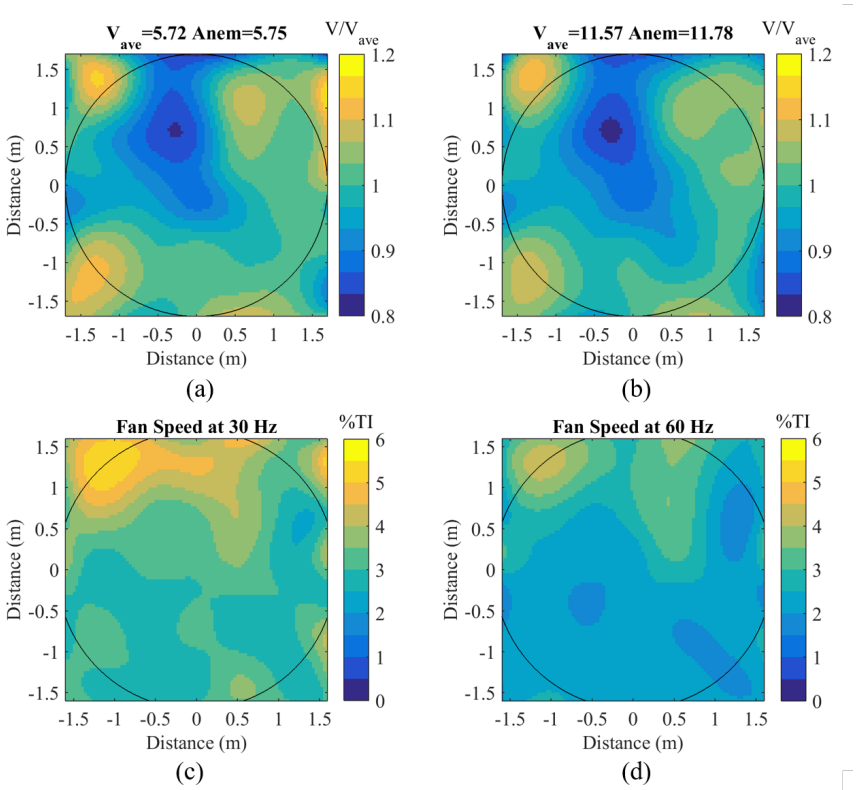

Figure B.5: Upstream profile in front of the UW WEG turbine for (a) velocity contour at fan frequencies of 30 Hz, (b) velocity contour at fan frequencies of 60 Hz, (c) turbulent intensity at fans frequencies of 30 Hz, and (d) turbulent intensity at fans frequencies of 60 Hz

B.6.1 Experimental Setup

A Pitot tube traverse structure was built to hold 12 pitot tubes in place across the diameter of the fan outlet to measure the pressure differential across the traverse. The structure was held in place with adjustable legs on either end and clamped to the back draft dampers located at the outlet of each fan. Figure B.6 shows the pitot tube traverse structure in place on one of the fans in position 1.

The Pitot tubes were positioned based on the AMCA standard for measuring the flow rate of a fan for a fan size between 8 and 12 [54]. The corresponding Pitot tube positions are as follows:

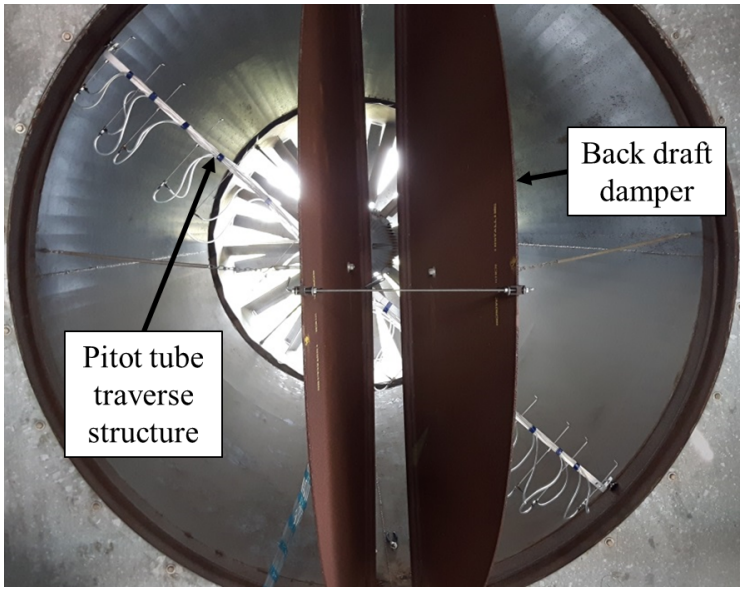

Figure B.6: Pitot tube traverse structure in position 1

Pitot tube position measured from north wall of fan outlet [cm]: 3.5, 18.9, 28.7, 46.0, 60.6, 94.1, 157.4, 190.9, 205.4, 222.8, 232.6, 248.0

The structure was placed at 2 positions at the outlet of the fan:

Position 1: 45 clockwise from horizontal position in the direction facing the fan

Position 2: 45 counterclockwise from horizontal position in the direction facing the fan

The pitot tubes were attached to Setra 267 pressure transducers and the data relayed to a DAQ via WiFi connection. The fans were run at 2 frequencies of 30Hz and 40Hz for each measurement. The data was taken for a sample size of 1,200,000 data measurement points.

B.6.2 Results

After the measurements were taken, the data was adjusted based on the calibration of the transducers and analyzed to provide a plot of each fan traverse and the calculated flow rate. Figure B.7 shows the velocity across each fan for each position and frequency. The distance of the diameter is increasing from south to north in the traverse plots.

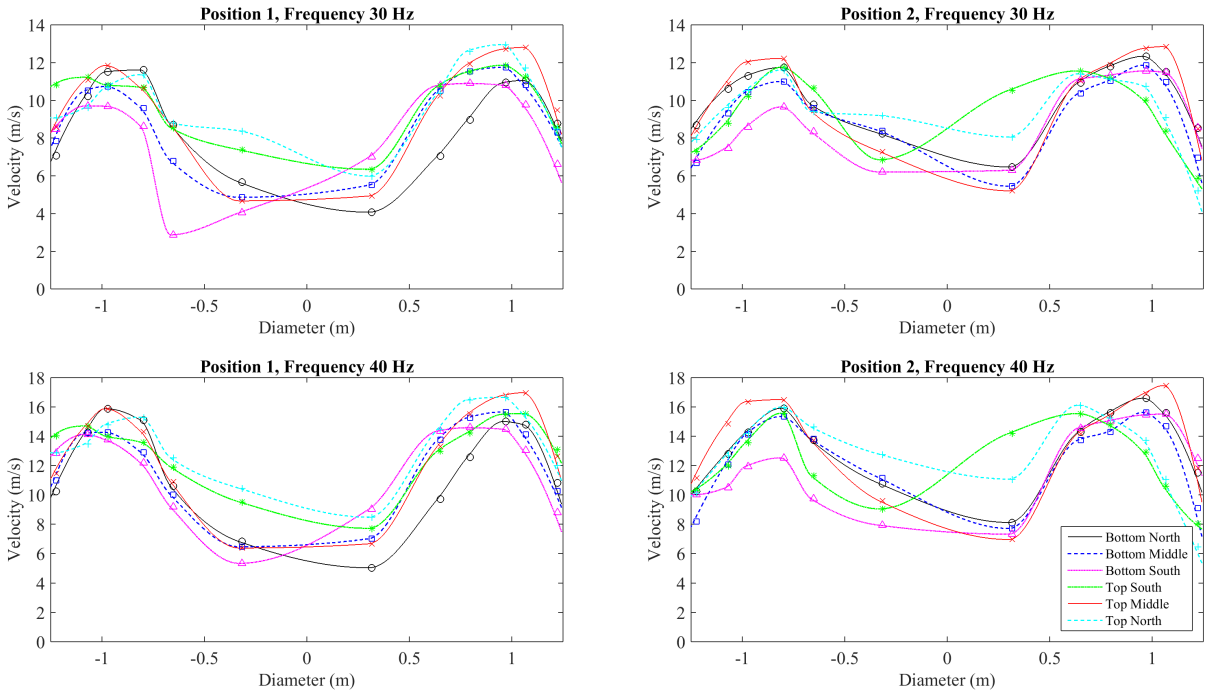

Figure B.7: Fan traverse for position 1 and 2, and frequency of 30 Hz and 40 Hz

It can be seen from the results of the velocity traverse that the top south and top north fans show higher velocities. The traverses for each fan are plotted in Figure B.8 and Figure B.9 with both positions of the pitot tube traverse structure for each frequency. Note that the position of each plot represents the position of the corresponding fan described in Section 1.3. The traverse for position 1 and position 2 do not tend to align with each other for the same fan. However, the traverse pattern and discrepancy between each position is consistent between a frequency of 30 Hz and 40 Hz. It is possible that the discrepancy is a result of the incoming wind direction when taking the measurements.

The results are better shown when comparing the calculated flow rate for each fan. Table B.5 shows the flow rates and the percent difference from the average flow rate of all the fans. The table is ordered based on the view of the fans from inside the facility as described in Section B.1.

From the results of the flow rate comparison it can be seen that for each frequency the top north and top south fans have the highest flow rate, while the bottom south fan has the lowest.

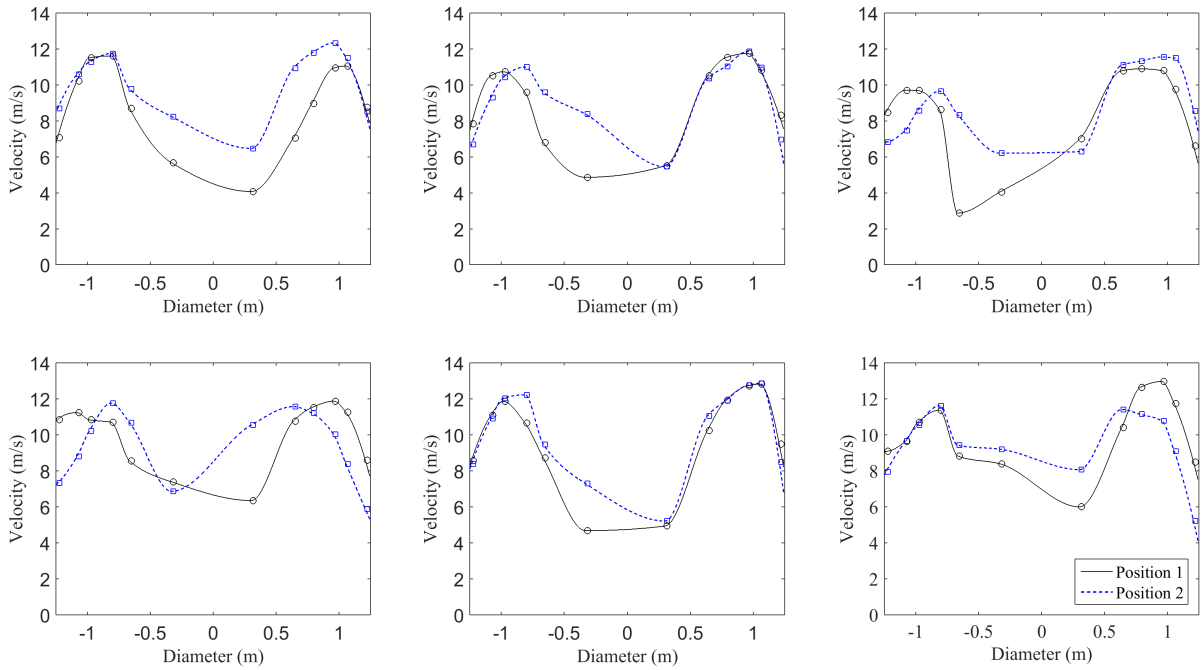

Figure B.8: Fan Traverse for each fan with both positions for a frequency of 30 Hz

Table B.5: Flow rates and the percent of the total average for each fan averaged for both positions

	30 Hz			40 Hz		
Flow rate	45.1	41.9	45.5	58.2	56.1	62.3
[m^3/s]	35.8	40.0	41.9	49.3	54.1	54.5
Percent of	108%	100%	109%	104%	101%	112%
average	86%	96%	100%	88%	97%	98%

B.6.3 Results Confidence

Additional comparisons of both positions of the traverse, seen in Table B.6 and B.7, show that position 2 consistently has a higher flowrate for each fan.

During the measurements the outside wind speed varied significantly with direction coming from the east. Therefore, it is possible that the results of the measurements were affected by this condition. Due to complications in the measurements, some of measure-

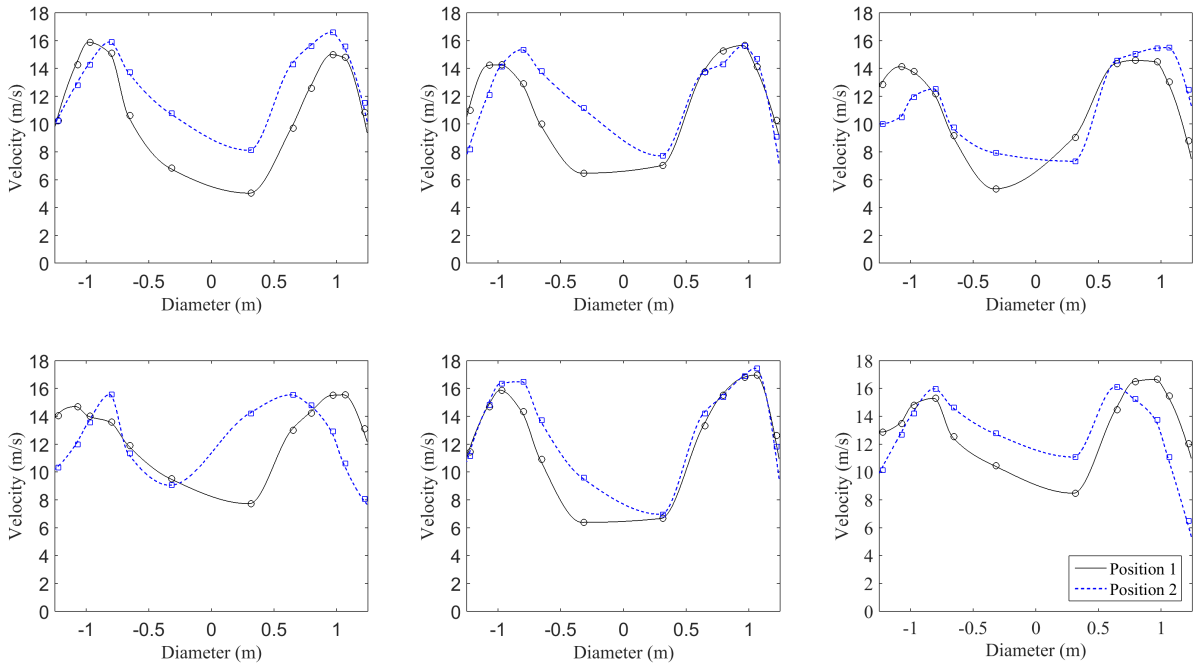

Figure B.9: Fan Traverse for each fan with both positions for a frequency of 40 Hz

Table B.6: Flow rates and the percent of the total average for each fan averaged for 30 Hz

	Position 1			Position 2		
Flowrate	44.2	39.6	44.2	46.0	44.2	46.9
[m^3/s]	33.7	37.3	38.0	37.9	42.7	45.8
Percent of	112%	100%	112%	105%	101%	107%
average	85%	95%	96%	86%	97%	104%

Table B.7: Flow rates and the percent of the total average for each fan averaged for 60 Hz

	Position 1			Position 2		
Flowrate	56.9	52.5	59.8	59.5	59.7	64.8
[m^3/s]	49.7	50.4	49.6	48.9	57.8	59.4
Percent of	107%	99%	113%	102%	102%	111%
average	93%	95%	93%	84%	99%	102%

ments were taken twice and are used to compare the effects of the varying wind speed. The repeated measurements were for the top middle fan in position 1 and 30 Hz, and the bottom north fan in both positions and 30 Hz. The plots of the compared repeated measurements are shown in Figure B.10 to B.12. The measurements for the bottom north fan were taken at different days and the measurements for the top middle fan were taken during periods of different outside wind speeds. The blue line represents the repeated variable for each case and the red values were using in the initial analysis. In the case of the top middle fan, the repeated measurement was measured when the outside wind speed was higher than the analyzed measurement.

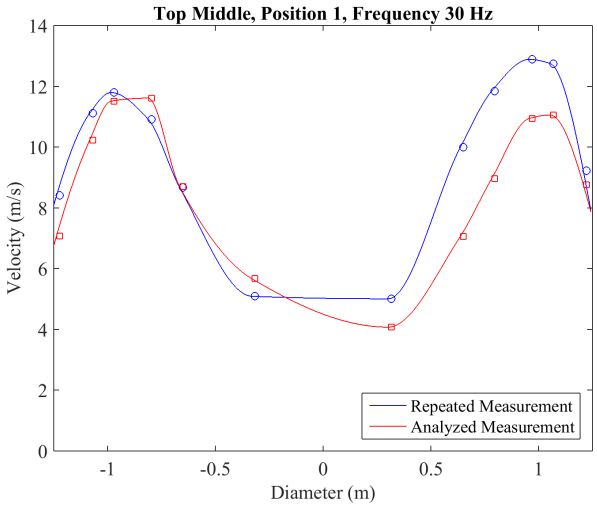

Figure B.10: Comparison of repeated measurements for top middle fan in position 1 and 30 Hz

The results show a similar correlation between the repeated measurements. Table B.8 shows the calculated flow rates for each repeated measurement and the percent difference for the analyzed value. It can be seen that the incoming wind speed did not have a significant effect on the measurements as seen in the top middle measurements, however there is some variability between fan measurements themselves. This was concluded due to the fact that the bottom north fan measurements were each taken during relatively low wind speeds with the repeated measurement was taken at a lower outside wind speed than the analyzed measurement, which show a higher flow rate contradictory to the assumption that the outside wind speed would increase the flow rate of the fans.

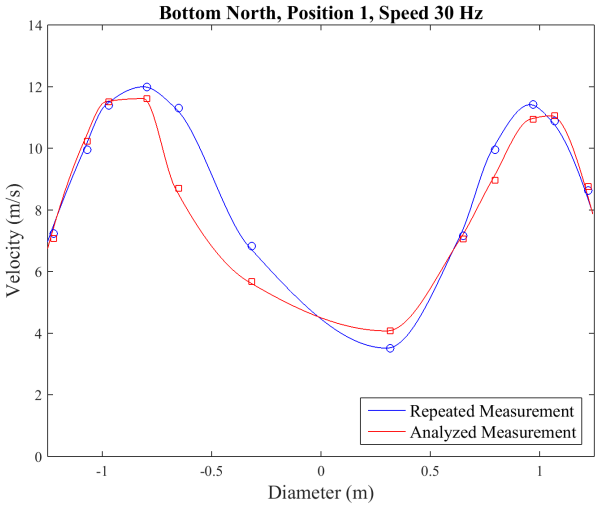

Figure B.11: Comparison of repeated measurements for bottom north fan at 30 Hz in position 1

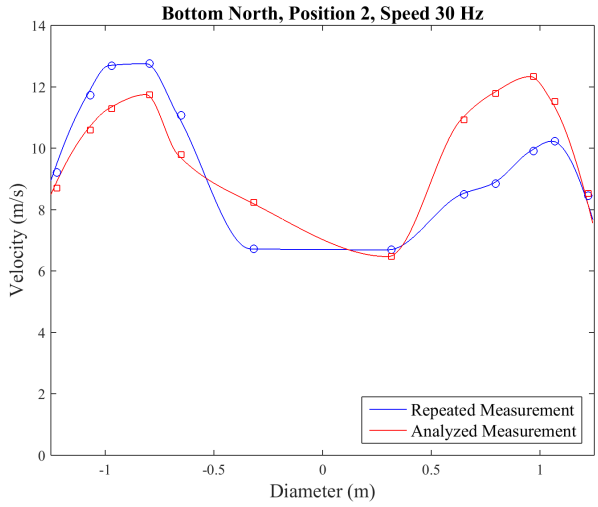

Figure B.12: Comparison of repeated measurements for bottom north fan at 30 Hz in position 2

Table B.8: Comparison of repeated measurement flow rates

Fan Measurement	**Repeated [m^3/s]**	**Analyzed [m^3/s]**	**%Difference**
Top Middle	40	40	1.4%
Bottom North, Position 1	41	38	7.9%
Bottom North, Position 2	46	46	0.8%

B.7 Initial Fan Frequency Adjustment

Based on the results of the fan flow rate comparison in the previous section, the fans were adjusted to attempt to equalize the flow rate based on the frequency setting.

B.7.1 Measurements

It was determined that the velocity of the fans is linearly proportional to the frequency set point. Therefore, the frequencies in Table B.9 were tested to equalize the flow rates. The frequency set points were determined to get an average constant flow rate out of each fan for a specific frequency.

Table B.9: Frequency Set Points of each fan for an average frequency of (a) 30 Hz, (b) 40 Hz, and (c) 53 Hz

(a)

28 Hz	30 Hz	27 Hz
34 Hz	31 Hz	30 Hz

(b)

38 Hz	40 Hz	35 Hz
45 Hz	41 Hz	41 Hz

(c)

50 Hz	53 Hz	47 Hz
60 Hz	55 Hz	53 Hz

The pitot tube array was modified to hold an additional 4 pitot tubes as to not change the position of the bar during the traverse. Therefore, only one traverse across the wind turbine was needed. The positions and other measurement parameters are the same as in Section B.5.2.

B.7.2 Results

The results for the velocity profile of each average frequency are shown in Figure B.13. The plot contour shows a slight variance between the heights of the pitot tubes for every second

position in the vertical direction. The cause of this discrepancy is unknown, however the velocities can still be compared in the horizontal direction.

Compared to the results of Figure B.5, it seems the flow profile has changed, however the velocity deficit is still present. It can therefore be determined that the frequency adjustment did not solve velocity uniformity. The interaction between the flow out of each fan and how it translates downstream is a complex problem. From this experiment it is unlikely to be able to correlate a calculated frequency adjustment to get a uniform flow even if this method was a certain solution.

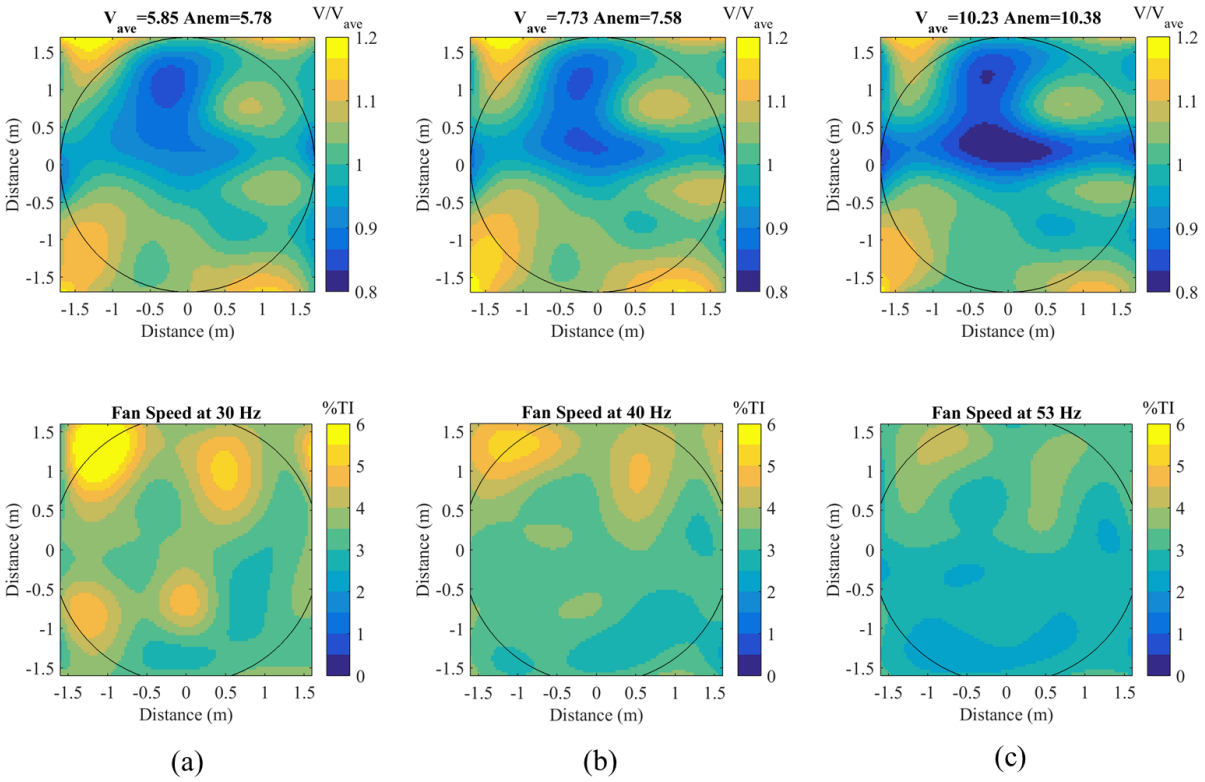

Figure B.13: Velocity contour and turbulent intensity at average fans frequencies of (a) 30 Hz, (b) 40 Hz, and (c) 53 Hz

B.7.3 Fan Characteristics

The current output on the fans were also obtained for an average frequency of 53 Hz. The current outputs of the fans are shown in Table B.10.

Table B.10: Current readings of fans running at an average frequency of 53 Hz

61 A	70 A	53 A
72 A	59 A	58 A

The results show an even larger discrepancy between the fan current readings for the adjusted frequency experiment compared to a constant frequency setting measured in Table B.2 and B.3.

B.8 Fan Frequency Adjustment Test Cases

The fan frequency test cases completed in Section 4.1.1 are given in Figures B.14 to B.16 with the corresponding fan orientation as shown in Table B.1.

B.9 Fan Frequency Adjustment Results

The averaged non-dimensional velocity profiles from the fan test settings from Section B.8 are given in Table B.11. The corresponding average velocities are given in Table B.12.

Test 1

30	30	30
30	30	30

Test 2

28	30	27
34	31	30

Test 3

29	28	29
30	29	28

Test 4

30	36	25
25	30	30

Test 5

31	31	31
25	31	31

Test 6

29	35	29
29	29	29

Test 7

29	29	25
25	29	29

Test 8

28	32	26
28	29	28

Test 9

30	31	26
26	29	29

Test 10

30	33	26
26	29	29

Test 11

28	30	27
26	29	29

Test 12

31	30	31
26	29	29

Test 13
[Test 2]

Test 14

28	35	26
25	29	29

Test 15

31	30	31
28	29	28

Test 16

30	30	30
34	31	30

Test 17

30	30	30
30	29	28

Test 18
[Test 3]

Test 19

28	29	31
25	29	28

Test 20

28	30	27
34	31	28

Test 21

28	30	27
36	31	30

Test 22

28	30	27
40	31	30

Test 23

28	30	27
40	27	30

Test 24

30	30	27
40	27	30

Test 25

30	30	27
36	27	30

Test 26

28	30	27
36	27	30

Test 27
[Test 25]

Figure B.14: Fan frequency test settings at an average of 30 Hz (all units in Hz)

Test 28

40	40	40
40	40	40

Test 29

40	40	26
48	26	40

Figure B.15: Fan frequency test settings at an average of 40 Hz (all units in Hz)

Test 30

50	50	50
50	50	50

Test 31

50	50	45
60	45	50

Test 32

50	50	47
56	47	50

Figure B.16: Fan frequency test settings at an average of 50 Hz (all units in Hz)

Table B.11: Non-dimensional velocity readings from Pitot Tree during fan frequency adjustment tests

Test	**Transducer Number**															
	1	**2**	**3**	**4**	**5**	**6**	**7**	**8**	**9**	**10**	**11**	**12**	**13**	**14**	**15**	**16**
1	1.04	0.92	1.00	0.98	0.85	1.13	1.05	0.95	0.89	1.04	1.09	0.98	0.97	1.01	1.02	1.08
2	0.98	0.92	0.98	0.92	0.86	1.10	1.01	0.94	0.93	1.05	1.12	1.01	1.00	1.00	1.07	1.12
3	1.02	0.93	1.00	0.95	0.86	1.11	1.02	0.95	0.91	1.04	1.11	1.00	0.98	0.99	1.05	1.11
4	1.17	1.05	1.06	1.01	0.87	1.31	1.07	0.88	0.96	0.91	0.95	0.89	0.98	0.99	0.90	1.00
5	1.04	0.95	1.01	0.96	0.83	1.16	1.09	0.96	0.88	0.99	1.07	0.95	0.97	1.04	1.01	1.11
6	1.17	1.03	1.05	1.02	0.86	1.29	1.09	0.88	0.95	0.94	0.99	0.91	0.97	0.98	0.92	0.98
7	1.03	0.93	1.03	0.95	0.83	1.14	1.05	0.95	0.90	0.99	1.09	0.97	0.98	1.03	1.02	1.11
8	1.13	0.98	1.03	1.00	0.86	1.20	1.04	0.91	0.93	0.96	1.05	0.94	0.97	0.99	0.98	1.04
9	1.10	0.95	1.04	0.99	0.84	1.16	1.03	0.94	0.91	1.01	1.07	0.96	0.97	1.01	0.98	1.05
10	1.13	0.99	1.04	1.01	0.86	1.24	1.07	0.90	0.93	0.96	1.00	0.92	0.98	1.00	0.94	1.03
11	1.03	0.99	1.00	0.93	0.85	1.21	1.05	0.93	0.93	0.95	1.06	0.96	1.00	1.02	1.01	1.11
12	1.06	0.99	1.02	0.94	0.85	1.19	1.07	0.95	0.92	1.00	1.06	0.95	0.96	0.99	0.98	1.08
13	0.97	0.92	0.96	0.91	0.87	1.11	1.00	0.96	0.94	1.05	1.13	1.00	1.01	0.99	1.06	1.13
14	1.11	1.07	1.01	0.96	0.88	1.34	1.09	0.87	0.99	0.89	0.96	0.91	1.00	0.99	0.91	1.03
15	1.04	0.97	1.01	0.95	0.85	1.17	1.07	0.95	0.93	1.02	1.08	0.97	0.96	0.98	1.00	1.06
16	0.97	0.95	0.98	0.90	0.87	1.11	1.01	0.96	0.95	1.04	1.11	1.00	1.00	0.98	1.05	1.13
17	0.99	0.97	0.99	0.92	0.87	1.18	1.05	0.95	0.95	1.03	1.07	0.97	0.99	0.98	1.01	1.08
18	0.99	0.98	0.99	0.91	0.87	1.18	1.06	0.96	0.95	1.04	1.07	0.97	0.98	0.97	1.00	1.08
19	1.01	0.97	0.98	0.92	0.84	1.19	1.11	0.93	0.93	0.96	1.06	0.97	0.99	1.02	1.01	1.12
20	0.96	0.93	0.97	0.90	0.87	1.12	1.00	0.96	0.95	1.03	1.13	1.02	1.00	0.97	1.07	1.14
21	0.99	0.93	0.97	0.90	0.88	1.09	1.00	0.96	0.94	1.05	1.12	1.01	0.99	0.98	1.07	1.13
22	0.98	0.93	0.96	0.90	0.88	1.05	0.98	0.96	0.93	1.11	1.14	1.04	0.99	0.96	1.10	1.10
23	0.97	0.96	0.96	0.90	0.89	1.11	1.03	0.95	0.96	1.10	1.10	0.96	1.00	1.01	1.07	1.04
24	1.03	0.94	1.00	0.94	0.88	1.10	1.02	0.97	0.94	1.14	1.08	0.96	0.96	0.99	1.05	1.02
25	1.03	0.97	1.01	0.93	0.88	1.13	1.03	0.96	0.95	1.10	1.07	0.95	0.97	1.01	1.00	1.03
26	1.02	0.97	0.97	0.91	0.88	1.15	1.04	0.94	0.96	1.08	1.06	0.96	0.99	1.02	1.01	1.05
27	0.98	0.97	0.98	0.91	0.90	1.15	1.03	0.95	0.97	1.10	1.07	0.93	0.98	1.00	1.04	1.04
28	0.97	0.95	1.00	0.93	0.87	1.17	1.07	0.94	0.95	1.00	1.08	0.96	1.00	1.02	1.01	1.10
29	0.99	0.95	1.00	0.94	0.88	1.15	1.05	0.95	0.95	1.09	1.05	0.94	0.99	1.02	1.02	1.02
30	1.01	0.94	1.01	0.97	0.87	1.15	1.06	0.95	0.93	1.05	1.07	0.96	0.97	1.01	0.99	1.06
31	1.02	0.94	1.02	0.96	0.89	1.14	1.04	0.95	0.95	1.13	1.05	0.93	0.97	1.01	1.01	1.01
32	1.04	0.94	1.03	0.97	0.88	1.15	1.03	0.94	0.94	1.09	1.05	0.94	0.98	1.01	0.98	1.03

Table B.12: Velocity readings from Pitot Tree during fan frequency adjustment tests [m/s]

Test	Transducer Number															
	1	**2**	**3**	**4**	**5**	**6**	**7**	**8**	**9**	**10**	**11**	**12**	**13**	**14**	**15**	**16**
1	31.3	27.5	30.1	29.5	25.5	33.8	31.6	28.5	26.8	31.1	32.7	29.4	29.1	30.4	30.6	32.5
2	31.8	29.7	31.8	29.9	28.0	35.8	32.7	30.6	30.1	33.9	36.2	32.6	32.4	32.3	34.5	36.4
3	28.5	26.2	27.9	26.6	24.2	31.1	28.5	26.6	25.6	29.3	31.0	27.9	27.5	27.7	29.3	31.0
4	34.7	31.2	31.4	30.1	25.8	39.0	31.8	26.1	28.5	27.0	28.3	26.6	29.0	29.4	26.7	29.7
5	30.2	27.5	29.4	28.0	24.0	33.8	31.8	27.8	25.6	28.9	31.2	27.7	28.2	30.2	29.3	32.2
6	36.2	31.8	32.4	31.6	26.6	39.9	33.7	27.3	29.4	29.1	30.8	28.1	29.9	30.5	28.4	30.4
7	26.7	24.0	26.5	24.5	21.6	29.6	27.1	24.6	23.3	25.7	28.3	25.0	25.4	26.6	26.3	28.6
8	31.7	27.4	28.9	27.9	24.1	33.6	29.0	25.6	26.0	27.0	29.4	26.4	27.0	27.7	27.6	29.0
9	30.3	26.1	28.5	27.2	23.1	32.0	28.2	25.9	25.0	27.7	29.4	26.4	26.7	27.7	27.0	28.9
10	31.3	27.5	28.7	28.0	23.9	34.3	29.6	25.0	25.7	26.5	27.5	25.4	27.1	27.7	26.0	28.5
11	27.0	25.9	26.3	24.5	22.2	31.7	27.5	24.3	24.3	24.8	27.8	25.0	26.3	26.6	26.4	29.0
12	28.7	26.9	27.6	25.6	23.0	32.3	29.1	25.8	25.0	27.2	28.9	25.7	26.2	27.0	26.7	29.2
13	30.9	29.3	30.7	29.0	27.6	35.4	32.0	30.5	29.9	33.5	36.0	32.0	32.1	31.7	33.7	36.0
14	30.7	29.6	28.1	26.6	24.3	37.3	30.3	24.1	27.4	24.7	26.5	25.2	27.8	27.5	25.2	28.6
15	29.0	27.1	28.3	26.5	23.8	32.7	29.9	26.7	25.9	28.5	30.2	27.0	26.8	27.3	27.9	29.6
16	31.6	30.7	31.7	29.1	28.3	36.0	32.8	31.1	30.7	33.7	36.1	32.5	32.3	31.7	33.9	36.6
17	27.7	27.1	27.7	25.7	24.5	33.1	29.5	26.5	26.6	28.7	30.1	27.3	27.8	27.4	28.1	30.3
18	28.1	27.8	28.2	25.9	24.6	33.7	30.3	27.2	27.2	29.5	30.5	27.5	27.9	27.6	28.5	30.8
19	25.3	24.5	24.7	23.2	21.1	29.8	27.9	23.5	23.5	24.0	26.7	24.4	25.0	25.6	25.4	28.3
20	30.2	29.4	30.5	28.3	27.4	35.3	31.5	30.2	29.8	32.6	35.7	32.1	31.6	30.4	33.7	35.8
21	32.7	30.8	31.9	29.9	28.9	36.1	32.9	31.6	31.0	34.8	36.9	33.5	32.8	32.5	35.2	37.4
22	33.8	32.1	33.4	31.3	30.5	36.5	34.0	33.4	32.4	38.4	39.6	35.9	34.2	33.4	38.0	38.3
23	32.1	32.0	31.8	29.8	29.5	36.8	34.2	31.5	32.1	36.6	36.4	32.1	33.2	33.7	35.5	34.7
24	35.9	32.9	34.9	32.7	30.7	38.5	35.6	33.7	32.7	39.7	37.8	33.4	33.6	34.7	36.5	35.6
25	32.2	30.1	31.3	29.1	27.3	35.3	32.1	29.8	29.5	34.3	33.2	29.5	30.2	31.5	31.0	32.1
26	30.4	29.0	29.0	27.3	26.5	34.3	31.2	28.2	28.8	32.3	31.7	28.6	29.5	30.6	30.1	31.4
27	30.4	30.1	30.5	28.4	27.8	35.8	31.9	29.3	30.0	34.2	33.2	29.0	30.5	31.1	32.2	32.2
28	50.5	49.8	52.0	48.4	45.3	61.1	55.9	49.3	49.4	52.4	56.2	50.4	52.3	53.3	52.9	57.4
29	55.8	53.5	56.6	53.1	49.7	64.8	59.0	53.2	53.5	61.4	59.3	52.8	56.0	57.5	57.2	57.6
30	83.4	77.4	83.5	79.8	71.9	95.2	87.4	78.8	77.1	87.0	88.3	79.6	80.4	83.0	81.9	87.6
31	88.9	82.7	89.0	84.3	77.7	99.5	91.2	83.3	83.1	98.8	91.9	81.0	85.2	88.5	88.4	88.0
32	90.0	81.3	88.7	83.9	76.1	99.1	89.3	81.1	81.4	94.2	90.4	81.1	84.5	87.4	84.4	89.3

Appendix C

Preliminary Flow Visualization

A preliminary smoke visualization experiment was conducted for the experiments outlined in Section 4.3. The experiments used the blade ignited smoke visualization technique to obtain qualitative and quantitative measurements of the wake behind the UW WEG turbine.

C.1 Setup

Blade ignited flow visualization was conducted on the UW WEG turbine inside the Wind Generation Facility. The experiment attached an Enola Gaye smoke emitter to a single blade of the turbine. The smoke emitter was attached to the tip of the blade and ignited through the wire pull ignition of the smoke emitter.

The experiment was performed with an upstream wind speed of 6 m/s as measured by the sonic anemometer. The turbine rotated at a constant 100 RPM rotational speed, which was determined to effectively visualize the smoke in the wake of the turbine without causing too much dispersion.

The setup of the experiment is shown in Figure C.1. A wide angle camera was used at the side view of the experiment to capture to flow of the smoke with the wake as it moves downstream. Two DSLR were positioned at the side view directed at the turbine blade and in a crosswise view. A reference marker was placed on the side to obtain quantitative measurements from the photos.

Several smoke colours were tested to determine which colour stands out against the

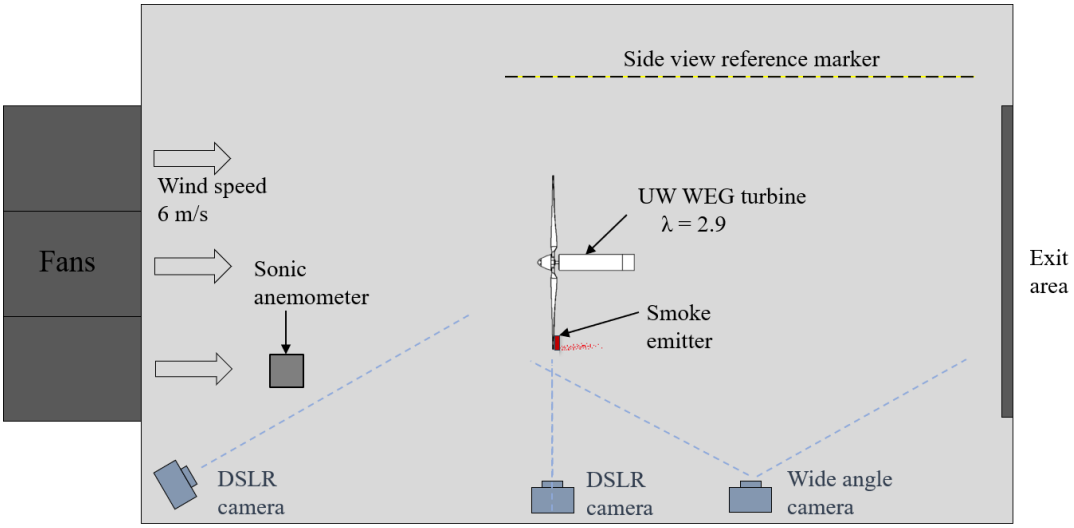

Figure C.1: Preliminary smoke visualization experimental setup

background the best. Additionally, the lighting was adjusted to attempt to enhance the smoke in the pictures by orientating spotlights directed at the flow.

C.2 Results

A progression of the blade tip smoke visualization as the blade rotates can be seen in Figure C.2. The smoke provides a visualization of the flow coming off of the blade tip and how it propagates downstream. Further downstream of the turbine the smoke begins to dissipate into a less concentrated form.

Looking at a single time frame of the tip smoke visualization in Figure C.3 it can be seen that the wake follows the typical helical vortex wake distribution. Vortex cylinders are shed from the blades of the turbine and then follow the helical path downstream of the turbine. Additionally, wake expansion can be seen from the experiment, however a frontal view of the flow will allow a better visualization of this characteristic.

From the angle of the smoke leaving the turbine blade, the helix angle, ϕ, also known as the flow angle at the blade tip, can be determined [18]. This angle can be used to determine the direction of the vortex cylinder parallel to the axis of rotor rotation. The helix angle from the experiment can be seen from a close-up image of the blade shown in Figure C.4. The helix angle was therefore measure to be 25°.

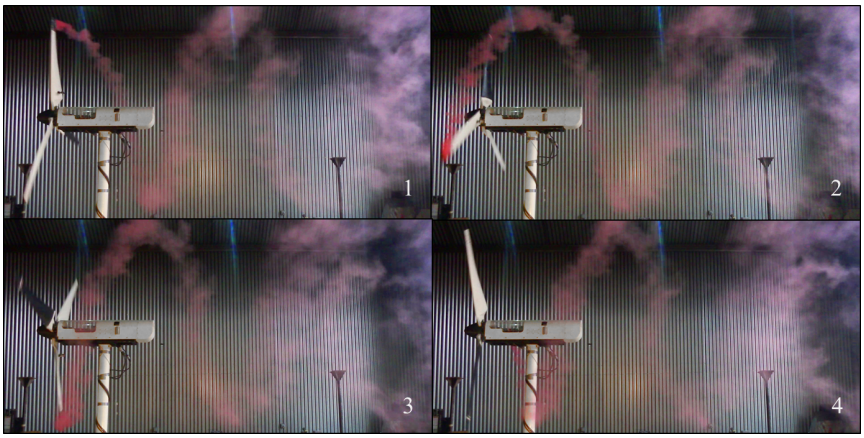

Figure C.2: Tip smoke visualization progression of the UW WEG turbine for $\lambda = 1.7$

Figure C.3: Blade tip smoke visualization of the UW WEG turbine for $\lambda = 1.7$

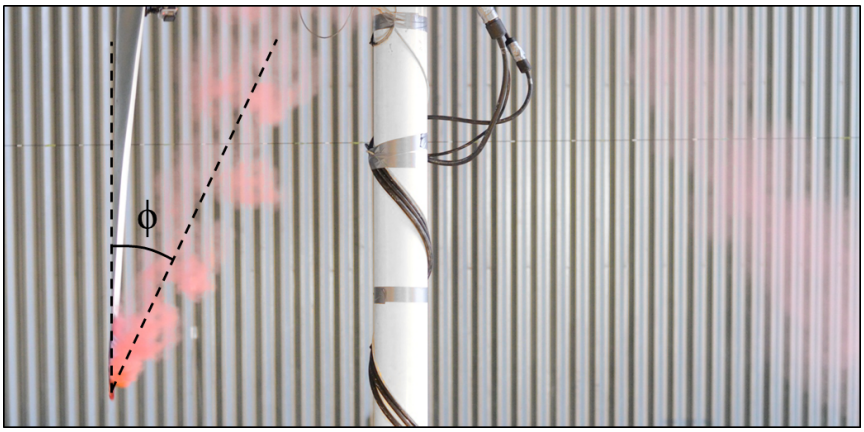

Figure C.4: Helix angle of the UW WEG turbine for $\lambda = 1.7$

Appendix D

LiDAR Measurement Points

The following points in Tables D.1 to D.3 were taken inside the Wind Generation Facility during the LiDAR wake measurements described in Section 4.4.3. The measurements were taken at z/D of 1.1. Tables D.1 to D.3 show the measurement points taken for each LiDAR measurement distance setting, H_m. The measurements for y/D were offset due to the change in hub position when the UW WEG Turbine was in the yawed direction as seen by the difference in positions from Tables D.2 and D.3 for yaw angles of 0° and 30° respectively.

Table D.1: LiDAR measurement point positions for x/D

$\mathbf{H}_m$	11.6 m	12.8 m	13.9 m	15.1 m	16.2 m	17.4 m
x/D	1.74	1.13	2.46	2.00	3.18	2.82
	1.71	1.22	2.44	2.07	3.17	2.87
	1.68	1.31	2.41	2.14	3.15	2.92
	1.65	1.39	2.39	2.20	3.14	2.96
	1.61	1.47	2.36	2.26	3.12	3.00
	1.56	1.55	2.33	2.32	3.10	3.04
	1.52	1.62	2.29	2.38	3.08	3.08
	1.46	1.69	2.26	2.43	3.06	3.12
	1.41	1.75	2.22	2.48	3.04	3.16
	1.35	1.81	2.17	2.53	3.01	3.19
	1.28	1.86	2.13	2.57	2.98	3.23
	1.22	1.91	2.08	2.61	2.96	3.26
	1.15	1.96	2.03	2.65	2.93	3.29
	1.07	2.00	1.98	2.69	2.90	3.32
	1.00	2.04	1.92	2.72	2.87	3.35
	0.92	2.07	1.86	2.75	2.83	3.37
	0.83	2.10	1.80	2.77	2.80	3.40
	0.75		1.74	2.80	2.76	3.42
	0.66		1.67	2.82	2.73	3.44
			1.60		2.69	3.46
			1.54		2.65	3.48
					2.61	3.50
					2.57	3.51
					2.52	3.53
					2.48	
					2.43	

Table D.2: LiDAR measurement point positions for y/D at $\gamma = 0°$

$\mathbf{H}_m$	11.6 m	12.8 m	13.9 m	15.1 m	16.2 m	17.4 m
y/D	0.88	-1.03	0.88	-1.08	0.93	-1.11
	0.76	-0.93	0.77	-0.98	0.84	-1.03
	0.64	-0.82	0.66	-0.88	0.76	-0.95
	0.52	-0.72	0.55	-0.78	0.67	-0.87
	0.41	-0.61	0.45	-0.68	0.59	-0.78
	0.29	-0.50	0.34	-0.57	0.50	-0.70
	0.18	-0.38	0.24	-0.46	0.42	-0.62
	0.07	-0.26	0.13	-0.36	0.34	-0.54
	-0.04	-0.15	0.03	-0.25	0.25	-0.45
	-0.15	-0.02	-0.07	-0.14	0.17	-0.37
	-0.25	0.10	-0.17	-0.03	0.09	-0.28
	-0.36	0.22	-0.27	0.08	0.01	-0.19
	-0.46	0.35	-0.37	0.20	-0.07	-0.11
	-0.55	0.48	-0.47	0.31	-0.15	-0.02
	-0.65	0.61	-0.56	0.43	-0.47	0.07
	-0.74	0.74	-0.66	0.54	-0.39	0.16
	-0.83	0.87	-0.75	0.66	-0.31	0.25
	-0.92		-0.84	0.78	-0.23	0.33
	-1.00		-0.93	0.90	-0.55	0.42
			-1.02		-0.62	0.51
			-1.10		-0.70	0.60
					-0.78	0.69
					-0.85	0.79
					-0.93	0.88
					-1.00	
					-1.07	

Table D.3: LiDAR measurement point positions for y/D at $\gamma = 30°$

$\mathbf{H}_m$	11.6 m	12.8 m	13.9 m	15.1 m	16.2 m	17.4 m
y/D	0.76	-1.15	0.76	-1.20	0.80	-1.23
	0.64	-1.05	0.65	-1.10	0.72	-1.15
	0.52	-0.95	0.54	-1.00	0.63	-1.07
	0.40	-0.84	0.43	-0.90	0.55	-0.99
	0.29	-0.73	0.33	-0.80	0.47	-0.91
	0.17	-0.62	0.22	-0.69	0.38	-0.82
	0.06	-0.50	0.12	-0.59	0.30	-0.74
	-0.05	-0.39	0.01	-0.48	0.22	-0.66
	-0.16	-0.27	-0.09	-0.37	0.13	-0.57
	-0.27	-0.15	-0.19	-0.26	0.05	-0.49
	-0.37	-0.02	-0.29	-0.15	-0.03	-0.40
	-0.48	0.10	-0.39	-0.04	-0.11	-0.31
	-0.58	0.23	-0.49	0.08	-0.19	-0.23
	-0.68	0.36	-0.59	0.19	-0.28	-0.14
	-0.77	0.49	-0.68	0.31	-0.35	-0.05
	-0.86	0.62	-0.78	0.42	-0.43	0.04
	-0.95	0.75	-0.87	0.54	-0.51	0.12
	-1.04		-0.96	0.66	-0.59	0.21
	-1.12		-1.05	0.77	-0.67	0.30
			-1.14		-0.75	0.39
			-1.22		-0.82	0.48
					-0.90	0.57
					-0.97	0.66
					-1.05	0.76
					-1.12	
					-1.19	

Appendix E

LiDAR Modifications

The ZephIR z150 LiDAR was modified to convert the LiDAR's conical laser sweep to line-of-sight (LOS) measurements. This was achieved by removing the LiDAR's rotating prism lens that deflect the laser to obtain the conical measurement pattern. The steps to remove the lens are outlined below. The LiDAR manual states that a locking mechanism will activate if the lens is removed so careful considerations were taken to override the mechanism [56]. This was achieved by replacing any removed sensor equipment.

The lens is located in the optics pod of the LiDAR. A cover protects the components and lens inside of the optics pod. Figure E.1 shows a view of the lens through the optics pod cover before any modifications were made. The cover was removed, the bolts were unscrewed and the cover lifted off. Figure E.2 shows the internal components underneath the cover. The wedge was located on the rotating mechanism as shown in Figure E.3.

The wedge position was indicated using a black mark down the side of the lens, brass gear, and base to ensure proper realignment if necessary. The bolts were removed on the wedge base and the wedge pried off using a screwdriver due to the tight fit. Figure E.4 shows the rotating assembly after the removal of the wedge. A position indicator was attached to the rotating wedge lens, seen in Figure E.5. The position indicator passes through two strips to determine the rotating position.

A replacement position indicator was made to be installed on the rotating mechanism without the lens to take precautions in preventing the activation of locking mechanism. The replacement position indicator is shown in Figure E.6. The replacement position indicator was made to have the same dimensions as the original. It was ensured that the indicator had enough clearance to move through the two strips without any interference so

Figure E.1: Optics pod top view before modification

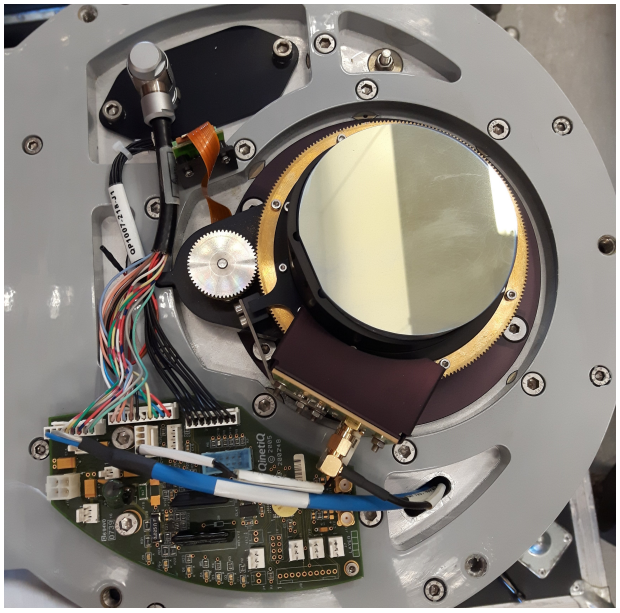

Figure E.2: Internal components beneath optics pod cover

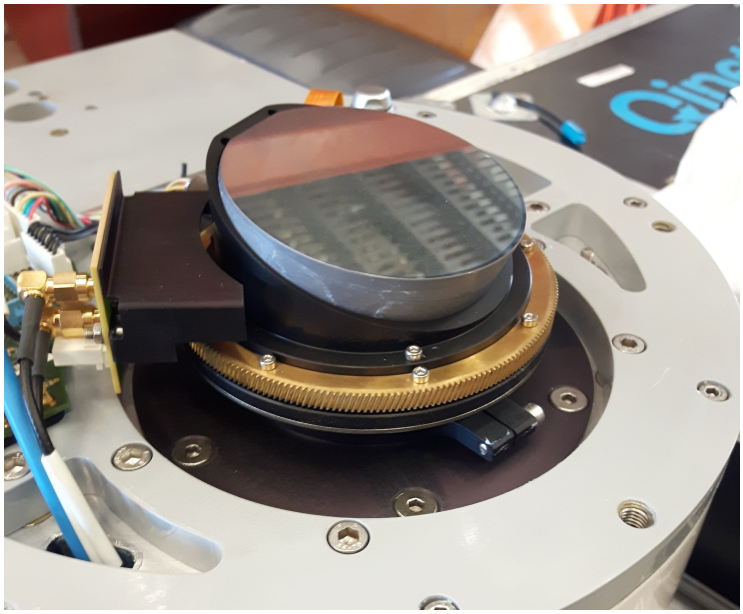

Figure E.3: Rotating wedge assembly

to not damage the device when the device is running. Figure E.7 shows the replacement position indicator moving through the two strips with enough clearance.

The optics pod cover includes an O-ring to ensure a proper seal when the cover is closed. O-ring lubricant was used on the O-ring when the cover was previously closed. During reassembly, the O-ring and cover surface were cleaned and new O-ring lubricant was applied. Figure E.8 shows the optics pod cover with the O-ring inserted in the groove. The optics pod cover was then placed on the optics pod and the bolts were reinserted. Figure E.9 shows the top view of the optics pod after the reassemble and with the modification.

The LiDAR was tested outside of the WEG laboratory on March 1, 2018. The test setup is shown in Figure E.10. The test verified that the LiDAR turns on successfully, the lens rotating mechanism had no interference, the laser enabled properly, and readings were taken. Issues did arise when downloading wind data, however the raw data was able to download suggesting that the issue being a possible software problem. This issue did not occur with later operations of the LiDAR.

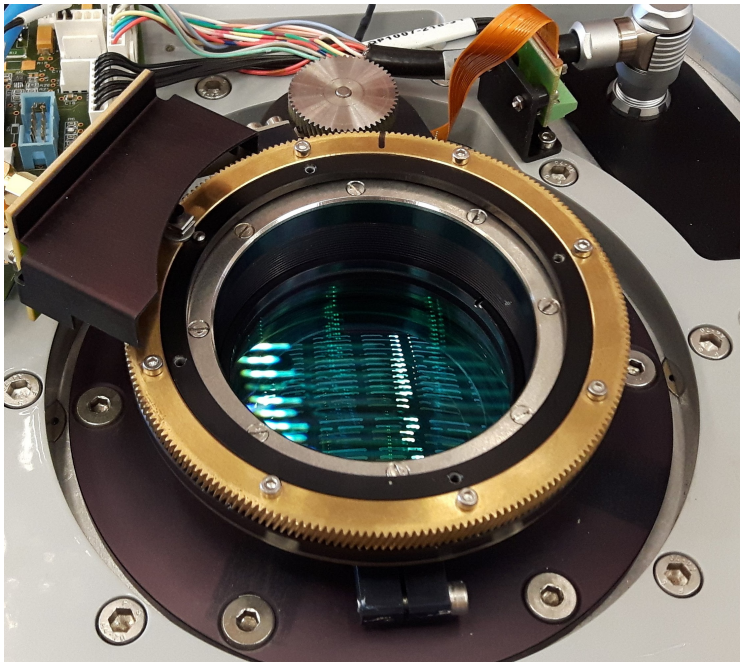

Figure E.4: Rotating assembly after wedge removal

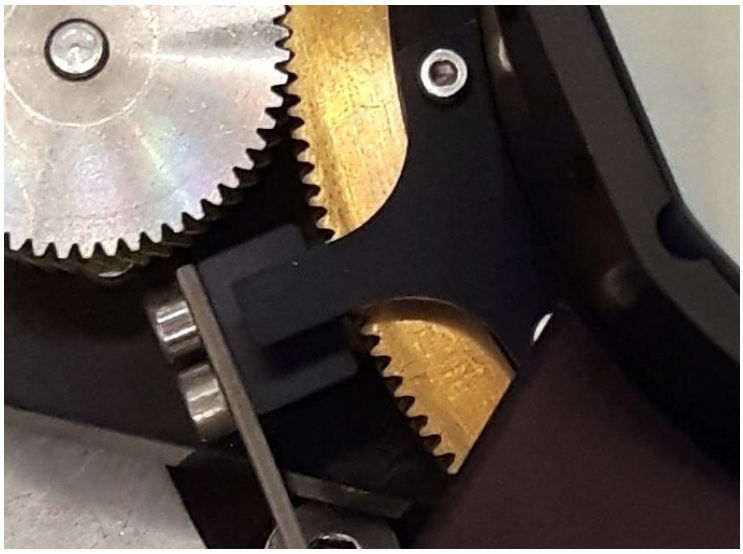

Figure E.5: Wedge position indicator

Figure E.6: Replacement position indicator

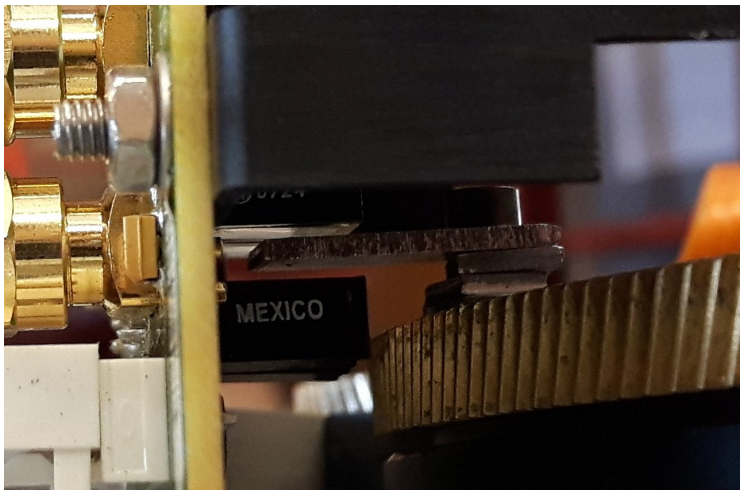

Figure E.7: Clearance of the replacement indicator

Figure E.8: Bottom of optics pod cover showing O-ring inserted

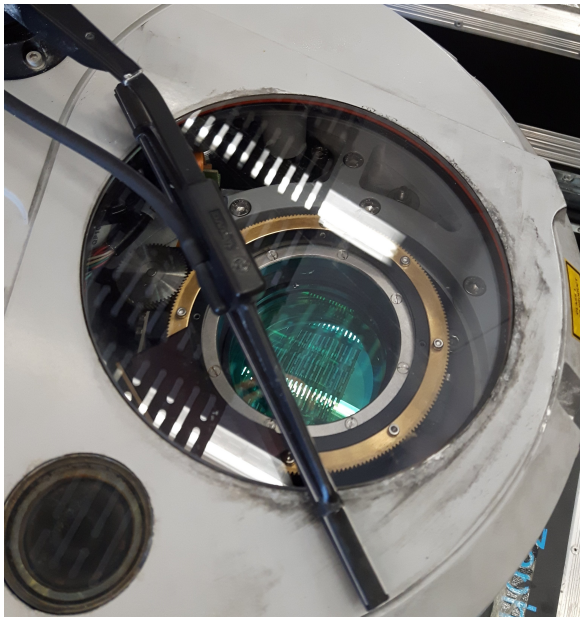

Figure E.9: Optics pod top view after modification

Figure E.10: Verification test setup outside of the WEG laboratory